Summer 2019

Explaining the physics behind regional peak flow equations using the scaling theory of floods and river network descriptors

Gabriel Jaime Perez Mesa
University of Iowa

Recommended Citation

Perez Mesa, Gabriel Jaime. "Explaining the physics behind regional peak flow equations using the scaling theory of floods and river network descriptors." PhD (Doctor of Philosophy) thesis, University of Iowa, 2019.
https://doi.org/10.17077/etd.dabq-5b5d

EXPLAINING THE PHYSICS BEHIND REGIONAL PEAK FLOW EQUATIONS
USING THE SCALING THEORY OF FLOODS
AND RIVER NETWORK DESCRIPTORS

by

Gabriel Jaime Perez Mesa

A thesis submitted in partial fulfillment
of the requirements for the Doctor of Philosophy
degree in Civil and Environmental Engineering in the
Graduate College of
The University of Iowa

August 2019

Thesis Supervisors: Assistant Professor Ricardo Mantilla
                       Professor Witold Krajewski

To my mother and father

"They say there's no such place ... as Paradise. Even if you search to the ends

of the Earth, there's nothing there. No matter how far you walk, it's always the

same road. It just goes on and on. But, in spite of that ... why am I so driven to

find it? A voice calls to me ... it says, 'Search for Paradise.'"

Wolf's Rain
Keiko Nobumoto

ACKNOWLEDGEMENTS

I am grateful for the unconditional support of many people who have made my PhD journey an unforgettable experience. I would especially like to thank my advisors: Professor Ricardo Mantilla, who showed me the joy of an inquiring mind, and Professor Witold Krajewski, who inspired me to address my scientific questions with discipline and passion. I want to thank the University of Iowa and the Iowa Flood Center for providing the perfect environment for a scientific mindset.

ABSTRACT

The development of regional flood-frequency equations is a key component of engineering infrastructure design and flood risk assessment at ungauged sites. These equations are constructed based on regression analysis techniques to study the connection between peak flow observations and different explanatory variables. However, many regions of the world remain poorly gauged or have experienced dramatic changes in land use or climate that make past observations less useful. To remedy this situation, we need to interpret and construct these regional equations based on physical principles of water movement and general knowledge of the geographic and geomorphologic setting of the upstream catchment at the location of interest. Several studies have examined these regional equations through the scaling theory of floods, making physical interpretations of the equation parameters (or scaling parameters) with respect to rainfall properties and geomorphologic variables. However, despite the advances of these previous works, the scaling theory of floods must be concerted with different, well-known problems in statistical hydrology for a proper engineering application in flood regionalization. These problems can vary from limitations in peak flow observations (sampling errors) to selection of an inadequate model structure of peak flows (epistemic errors). I present a series of studies based on hydrologic simulations and peak flow observations that illustrate several aspects related to the application and use of the scaling theory of floods, which include the following: (1) description of spatial patterns of scaling parameters; (2) inclusion of river network descriptors in flood frequency equations; and (3) evaluation of sampling errors and epistemic errors in the construction of flood frequency equations. The results presented in this dissertation contribute to the development of a more complete regional flood frequency analysis framework that leverages the physics of peak flow scaling and river network descriptors.

PUBLIC ABSTRACT

The estimation of extreme peak flows at sites where no streamflow data are available is a key component of engineering infrastructure design and flood risk assessment. The most common technique to estimate peak flows where no streamflow data are available is the construction of empirical regional flood frequency equations. These equations use explanatory variables that are easily obtained at any site of interest. However, dramatic changes in land use or climate incorporate new physical conditions that make the use of these equations less useful. To remedy this situation, we need to interpret and construct these equations based on physical principles of water movement and general knowledge of the geographic and geomorphologic setting of the upstream catchment for the location of interest. Several studies have examined these regional equations through the scaling theory of floods, making physical interpretations of the equation parameters with respect to rainfall properties and geomorphologic variabilities. However, the testing of the scaling theory of floods needs to be concerted with limitations in peak flow observations for a proper engineering application in flood regionalization. I present a series of studies based on simulations and observations of peak flow data to expose the dynamic of the scaling theory of floods from river network structures to include the density of streamflow gauges. The results of this dissertation contribute to the development of a more adequate regional flood frequency analysis framework that leverages the physics of peak flow scaling and river network descriptors.

TABLE OF CONTENTS

LIST OF TABLES

LIST OF FIGURES

xiii

xv

CHAPTER 1: INTRODUCTION

1.1. Motivation

Estimation of peak flows at ungauged sites where no streamflow data are available is a crucial task in engineering practice, particularly for structural design and floodplain management. Inadequate understanding of extreme peak flows at ungauged sites results in the incorrect estimation of flood risk with important societal consequences. When streamflow data are available, an "at-site" flood frequency analysis can be developed using probability distribution fitting techniques to extract peak flow quantiles associated with small exceedance probabilities. In contrast, peak flow quantiles at ungauged sites are regularly estimated with a regional statistical analysis of peak flow quantiles from neighboring gauged sites. This regional statistical analysis is part of the framework of the Regional Flood Frequency Analysis (RFFA), which uses regression analysis techniques to study the connection between peak flow quantiles and different explanatory variables to develop empirical regional flood-frequency estimation equations. This methodology depends on observations of annual maximum flows over homogeneous regions (e.g., Smith et al. 2015; Srinivas et al. 2008; Haddad et al. 2012; Wan et al. 2012). However, many regions of the world remain poorly gauged or have experienced dramatic changes in land use or climate that make past observations less useful. To remedy this situation, we need methodologies to estimate flood frequencies based on physical principles of water movement and general knowledge of the geographic and geomorphologic setting of the upstream catchment for the location of interest.

When making the leap from RFFA to physics-based estimations of flood frequencies, it is important to identify the scaling patterns revealed by data in the physical system where floods occur (i.e., watersheds and river networks). We can study these scaling patterns by means of

1

power laws describing the change of peak flows with respect to a length scale (e.g., drainage area). Then we can interpret the power law structure in peak flows as the systematic increase in the maximum discharge (Q) for a specific recurrence interval or quantile (p) as a function of the drainage area (A), which implies that $Q_p = \alpha_p A^{\Theta_p}$. This scaling feature arises from scale-invariant systems with self-similarity properties (Gupta, et al., 2007) and it seems to reflect a fundamental symmetry of nature (Schroeder, 2012). Two scaling parameters control the change of peak flows: the intercept (α) and the scaling exponent (Θ). Basically, an understanding of the factors governing α and θ is crucial for the development of regional equations to estimate peak flows at ungauged sites, and to meet our increasing need to understand how to adapt these regression parameters in future climatic scenarios (Burns, et al., 2015; Gupta et al., 2007).

Fuller (1914) was the first to connect the power-scaling structure to a statistical framework for peak flow data for the United States; however, significant questions have emerged, and many remain unanswered with regard to the physical controls and hydrologic variables governing power law–scaling structure in peak flows. Dawdy et al. (2012) provided a detailed explanation of the origins and early developments of flood-scaling methods. Most of the progress in our understanding of the scaling structure of peak flows has focused on quantifying the variables that control the value of α and Θ. For instance, a number of researchers have quantified the role of rainfall properties, such as instensity, duration, and spatial coverage, as key players in determining the scaling parameter values (e.g., Gupta et al. 1996; Jothityangkoon & Sivapalan 2001; Mandapaka et al. 2009; Robinson & Sivapalan 1997). Mantilla et al. (2006) studied flood scaling in real river networks, generalizing the results of previous studies (Gupta & Waymire 1998; Menabde & Sivapalan 2001; Morrison & Smith 2001). Furey et al. (2007) evaluated the flood-scaling dynamic for 148 rainfall-runoff events, demonstrating the strong

2

influence of depth, duration, and spatial variability of excess rainfall on the scaling parameters. These results encorruraged new studies to more deeply explore the scaling structure vis-à-vis rainfall properties. Examples of this include: Ayalew et al. (2014a); Ayalew et al. (2014b) and Ayalew et al. (2015), which demonstrated clear connections between rainfall properties and scaling parameters at different spatial scales. Ayalew et al. (2014a) used rainfall-runoff model simulation results to study how the rainfall intensity, duration, hillslope overland velocity, and channel flow velocity affect the scaling parameters in three small basins (252, 520, and 1082 km^2, respectively) in a spatial scale study of the Cedar River basin, which has a drainage area of ~17,000 km^2. In a subsequent study, Ayalew et al. (2015) analyzed actual data and showed the interplay between duration and depth of excess runoff with scaling parameters for 51 rainfall-runoff events at the mesoscale Iowa River basin, which has a drainage area of 32,400 km^2. This study demonstrated that even at this large scale, flood scaling still dominates. In a more extensive study of the scaling parameters structure, Kroll (2014) showed the scaling exponent structure in the United States, defining 18 water regions. In a further exploration of this course of study, Medhi and Tripathi (2015) explained the connections between basin attributes and scaling exponents, defining homogenous regions based on the region-of-influence method and showing evidence of simple-scaling for regions where snowfall dominates the total precipitation. In addition, these results suggest small flood-scaling exponents for regions with large soil moisture storages and high evapotranspiration losses, as well as significant overland flow fractions when compared to base flow. These studies represent an outstanding advance in the understanding of the flood-scaling structure for several spatial domains, a range of basin sizes, and their connection to rainfall and catchment properties.

Despite the contributions of the previous studies to our understanding of the physical controls behind the flood-scaling parameters, the scaling theory of floods needs to be used in concert with several well-known problems in statistical hydrology to achieve a proper engineering application in flood regionalization. These problems can vary from limitations in peak flow observations (sampling errors) up to selection of an inadequate model structure for peak flows (epistemic errors). In this dissertation, I examine these aspects in five specific studies (Chapter 2 to Chapter 6). A summary of each chapter is presented in the following section.

1.2. Overview of Thesis Chapters

1.2.1. Spatial Patterns of Peak Flow Quantiles Based on Power-Law Scaling in the Mississippi River Basin

This chapter introduces the scaling variability of peak flows by means of a spatial analysis of these peak flows for different drainage area sizes in the Mississippi River Basin (MRB), based on the power law relation between flood quantiles (Q_p) and drainage areas (A), expressed as $Q_p = \alpha_p A^{\theta_p}$. This chapter addresses three specific objectives:

(1) Characterize the spatial structure in α and Θ within the MRB.

(2) Evaluate the changes in α and Θ for different flood frequencies and spatial regions.

(3) Unmask regional differences in flood magnitudes and flood frequency signatures for specific drainage areas.

To meet these specific objectives, I used data from 5,137 streamflow gauges with peak flow records and the USGS Hydrologic Unit Code (HUC) catchment organization framework to estimate the scaling parameters (α_p and θ_p) at multiple spatial disaggregation levels, including: the complete Mississippi River Basin (MRB), six major MRB sub-regions (HUC-2), and finally, 84 medium-scale catchments (HUC-4). The analysis at the HUC-4 level exposed remarkable

4

regional flood patterns in θ_p and α_p, which I used to estimate peak flows at the 2.33- and 100-year return periods at multiple spatial scales, including 1-, 100-, 1,000-, and 10,000-km^2 drainage areas. The results expose a peak flow quantile relation that varies as a function of region and drainage area, demonstrating that regions with higher peak flow quantiles vary with respect to the watershed size in the MRB. Mainly, I found that the cluster of higher floods extends from the center to the eastern MRB for drainage areas from 1 km^2 to 10,000 km^2. Conversely, the clusters of lower 2.33-year floods are preserved in the western MRB for the same range of drainage areas. The results presented in this chapter demonstrate that the flood-producing mechanisms vary with respect to drainage area size and region. This provides a starting point for quantitative description of the physical processes that dominates the variability of flood-producing mechanisms, such as river network structures.

1.2.2. The Influence of Spatial Variability of Width Functions on Regional Peak Flow Regressions

This chapter studies the relationship between the variability in river network structure and the regional variability of peak flows. I define three specific objectives in this chapter:

(1) Capture the variability of the river network structure by means of Width Function Descriptors (WFDs).

(2) Identify the WFDs that explain the regional peak flow variability of synthetic uniform rainfall events.

(3) Explore the WFDs as explanatory variables in regional regressions of peak flow quantiles.

To address these specific objectives, I explored 34 WFDs to represent the river network structure, in addition to drainage area, as potential candidates to explain the regional peak flow

variability. First, I used hydrologic simulations of uniform rainfall events with variable rainfall duration and constant rainfall intensity for 147 watersheds across the state of Iowa. I demonstrated that WFDs can explain the spatial variability of peak flows for individual rainfall-runoff events under idealized physical conditions. This theoretical exercise indicates that the inclusion of WFDs should drastically improve regional peak flow estimates, reducing the Root Mean Square Error (RMSE) by more than half compared to a regression model based on drainage area only.

I followed the simulation with an analysis of estimated peak flow quantiles from 94 stream gauges in Iowa to determine if the WFDs have a similar explanatory power. The correlations between WFDs and peak flow quantiles are not as high as those for simulated events. This indicates that results from event-scale simulations do not translate directly to peak flow quantiles. Other physical and statistical aspects, including sampling errors and the number of streamflow gauges, influence the spatial variability of peak flow quantiles. I will explore this last finding in more detail in the following chapter.

1.2.3. Examining Observed Rainfall, Soil Moisture, and River Network Variabilities on Peak Flow Scaling of Rainfall-Runoff Events with Implications on the Regionalization of Peak Flow Quantiles

This chapter examines the flood scaling of observed peak flows associated with a probability of exceedance (Q_p) or a specific rainfall-runoff event (Q_R), with respect to drainage area (A) in a framework of peak flow regionalization. I explored the effects of actual rainfall and soil moisture variabilities, as well as the effect of the river network structure, on the scaling of peak flows for 85 rainfall-runoff events and peak flow quantiles from the Partial Duration Series observed at 43 streamflow gauges in the Iowa River Basin. I established empirical evidence to address two questions:

(1) What controls the performance of scaling relations for observed Q_R?

(2) What is the interplay between sampling error and the selection of explanatory variables in the construction of regional regression models for Q_R and Q_p?

For the first question, I found that the magnitude of slope in the scaling of the rainfall intensity fields with respect to A controls the scaling performance of Q_R. Regarding the second question, I demonstrated that the inclusion of river network descriptors must improve the regional equations to estimate peak flow quantiles; however, this result could be rejected because of sampling errors in the regression analysis.

1.2.4. Using Physically-Based Synthetic Peak Flows to Assess Local and Regional Flood Frequency Analysis Methods

This chapter evaluates the role of sampling errors and epistemic errors associated with local and regional methods to estimate peak flow quantiles (PFQs). I used regional peak flow distributions derived from a combined framework of observation-driven Stochastic Storm Transposition and a distributed hydrologic model. I evaluated four common PFQ estimation methods using synthetic peak flows at 5,000 sites in the Turkey River Watershed. I first used at-site flood frequency analysis employing the Pearson Type III distribution with L-moments and Method of Moments. Then I pooled regional information using: the index flood method, quantile regression, and parameter regression. This experiment allowed me to quantify the error components stemming from epistemic assumptions, parameter estimation methods, sample size, and, in the regional approaches, the number of "pooled" sites. The specific objectives of this chapter are as follows:

(1) Compare the estimates of peak flow quantiles (PFQs) between the at-site flood frequency analysis (ASFFA), the Index Flood Method (IFM), the quantile regression technique (QRT), and the parameter regression technique (PRT).

(2) Evaluate the epistemic errors in the PFQ estimation for the four techniques, and of sampling errors as a function of sample size and the number of pooled sites for IFM, QRT, and PRT.

(3) Evaluate the impact of different intersite peak flow dependency structures in the sampling of peak flows for the estimates of PFQs based on IFM, QRT, and PRT.

(4) Explore the different geomorphologic factors to explain the regional variability of skewness.

The results demonstrated that for regional methods, the inability to capture the spatial variability of the skewness of the peak flows dominates epistemic error. The study also demonstrated that this variability could be partially explained by river network structure and the predominant orientation of the watershed.

1.2.5. Estimation of Historical-Annual and Historical-Monthly Scale-Invariant Flow Duration Curves: With Implementation for the State of Iowa

This chapter presents an extension of flood scaling theory as applied to streamflow distributions for the construction of historical-annual and historical-monthly flow duration curves (FDC) for agricultural, unregulated, and ungauged sites. The specific objectives in the construction of the proposed FDCs are as follows:

(1) Estimate FDCs with a single explanatory variable for an easy implementation.

(2) Fit a continuous and monotonic FDC for a representative range of quantiles.

8

(3) Estimate FDCs for both historical and monthly scales to capture the seasonal streamflow variability.

I explored the performance and the regional dependence of four different regression models to estimate daily flow quantiles (Q_p), with probabilities of exceedance (p) ranging from 0.01 to 0.99. I based the construction and analysis of the four regression models on scale-invariance of Q_p with respect to drainage area (A) or mean annual flow ($\bar{Q}$). I implemented the procedure using data from 74 gauged sites in Iowa. The results demonstrate that the multi-scaling framework of Q_p with respect to $\bar{Q}$ provides the most accurate FDC estimates that are region-independent within Iowa's physical characteristics. I developed a piecewise continuous function to estimate the scaling parameters as a function of p, allowing estimations of continuous FDCs using independent estimates of $\bar{Q}$. A validation test using data from 40 gauges (not employed in developing the regression equations) shows that the methodology performs similarly for historical-annual FDC estimates when compared to the methodology that the U.S. Geological Survey (USGS) developed for Iowa. For discharges with p values larger than 0.6, the proposed methodology exhibits lower, but still acceptable, performance. Two features make the proposed methodology attractive for FDC estimation: first, it is simpler to use and implement than the USGS methodology because it only requires estimates of $\bar{Q}$; and second, it provides reliable FDC estimates at monthly scales that are otherwise unavailable. I present an example in which we used FDC estimates at ungauged sites to create streamflow frequency maps to categorize flows predicted in real time by a distributed hydrologic model implemented for Iowa.

2.1. Introduction

I start examining the Regional Flood Frequency Analysis (RFFA) to estimate flood quantiles at ungauged sites by means of a power law model with respect to drainage area. This power law (see Equation 2-1) represents the systematic increase in the maximum discharge (Q) for a specific quantile (p) as a function of the drainage area (A) as,

$$Q_p = \alpha_p A^{\Theta_p} \qquad\qquad \text{Equation 2-1}$$

The rate of increase is controlled by two scaling parameters: the intercept (α_p) and the scaling exponent (Θ_p). As was mentioned in the Chapter 1, Multiples studies have explored different approaches to quantifying the variables that control the value of α and Θ. These studies represent an outstanding advance in the understanding of the flood scaling structure for several spatial domains, range of basin sizes, and their connection with rainfall and catchment properties; however, none of them have demonstrated how the differences of scaling parameters are controlling the flood magnitude for different drainage size areas in a specific large spatial domain such as the Mississippi River Basin (MRB).

This chapter addresses three specific aspects: (1) characterize the spatial structure in α and Θ within the MRB; (2) evaluate changes in α and Θ for different quantiles and spatial regions; and (3) unmask regional differences in flood magnitudes and flood frequency signatures for specific drainage areas.

Regarding (1) researchers have explored in depth the existence of flood scaling for flood quantiles and flood events in different basin sizes (Furey et al. 2007; Ayalew et al. 2014a; Ayalew et al. 2014b; Ayalew et al. 2015; Medhi & Tripathi 2015), but the power law structure

for flood quantiles in a large domain such as the MRB is still unknown. Therefore, research is needed to determine the upper bound, if exists, in the spatial limit over the watershed domain.

Regarding (2) the understanding of the characterization of α and Θ across space need to be improved. Although, the scaling parameters change across different hydrologic conditions (Medhi and Tripathi 2015), we want to determine if these changes exhibit gradual or abrupt shifts in space thus enabling possible connections between scaling parameters and spatial patterns in hydrologic signatures.

Regarding (3), the flood scaling framework allows us to analyze floods in specific drainage areas; therefore, I will use the different values of α and Θ across the spatial domain to compare the flood changes among spatial locations, drainage areas, and flood quantiles. These results should help to identify the spatial locations and drainage area magnitudes in which flood quantiles are more extreme.

The rest of this chapter is organized as follows. A section describing the study area and peak flow data, including the hydrologic variability in the region, watershed boundaries and spatial units of analysis, number of peak flow gauges, and the type of regression analysis to estimate the scaling parameters. Consecutively, I present the different methods for revealing flood patterns, testing of regional homogeneity, and identification of simple-scaling or multi-scaling structures in the MRB. Subsequently, I report and discuss results, emphasizing characteristics of flood scaling across scales for different sub-regions, and provide insights into regional homogeneity based on flood scaling, and flood patterns for different watershed sizes. I conclude addressing the importance and consequences of the main findings of this chapter, proposing future work around the connections between scaling parameters and mechanistic processes behind floods.

2.2. Peak Flow Data in the Mississippi River Basin

One of the largest continental basins in the world, the MRB, is characterized by diverse hydrologic, climatic, and geomorphologic settings. The MRB drains an area of almost 3 million km^2 and is significantly impacted by human activity due to industrial and agricultural practices. From a hydroclimatological perspective, there are strong gradients in rainfall, snowfall, evapotranspiration, and temperature across the watershed at multiple temporal scales. These geophysical properties make the MRB a good candidate to understand the spatial variability in the scaling structure of floods. This study includes only those stream gauge locations that drain watersheds smaller than 10,000 km^2 to guarantee that the information represents the flood diversity inside a particular HUC partition, avoiding biases introduced by gauges in large rivers that flow through a HUC (e.g. the Mississippi River) that may be influenced by large scale regulation and with flow regimes that result from integrating multiple climate regimes.

Streamflow in the MRB are routinely estimated at 7,587 gauged locations that record peak flows, managed by the U.S. Geological Survey (USGS). The USGS peak flow data is easily accessible by web services (http://nwis.waterdata.usgs.gov/usa/nwis/peak). The USGS records maximum annual floods at specific gauge sites, which are the inputs for the quantile estimation related to different probabilities of exceedance (also expressed as the "return period"). I used the guidelines for determining peak flow frequency outlined in the USGS Bulletin 17B. This procedure uses the probability distribution Log Pearson Type 3 with the incorporation of outlier treatments, flows affected by regulation in dams, estimation of the regional skew, and historical flood information. The complete method is incorporated in the software PeakFQ (Flynn et al. 2006). I used the PeakFQ software to estimate the peak flow quantiles for each location. I exclude peak flow data affected by dams or gauges with annual peak flow records reported as zero. This last condition arose because some gauges present long records of annual

12

floods, but some have values equal to zero. These could be a consequence of long dry periods in small basins or instrument errors. For the regression analysis section, I only considered the gauges with more than 10 years of record period which gives a total of 5,137 gauges.

In order to analyze the variability of scaling parameters α and θ over different spatial scales and quantiles, I segmented the Mississippi River basin. For this purpose, three levels of spatial discretization are used. I used the spatial hydrological units (HUC), defined by the USGS (Seaber et al. 1987). The largest spatial unit is the complete Mississippi River basin. The second is the HUC-2 level with six sub-regions, and finally the HUC-4 level which partitions the MRB into 84 sub-regions. Figure 2-1 shows the spatial definition of the three levels of analysis and Figure 2-2 illustrates an example of the spatial segmentation in the flood scaling from Level 1 to Level 3.

2.3. Scaling Patterns of Flood Data

I selected two methods to describe spatial patterns of scaling in peak flows in the MRB. First, I calculated a flood Severity Index (SI), defined as the ratio between the peak flows with a return period of 100 years and the mean annual flood. In this calculation the mean annual flood is represented as the peak flow with a return period of 2.33 years. I used these results as the starting point in creating the relationship between the spatial pattern of floods, physical controls, and hydrologic conditions across space.

Second, I fitted a power law function between peak flows and drainage using a Weighted Least Square (WLS) regression in each of the regions defined by the HUC partitions of the MRB. The WLS reduced the uncertainty in the estimation of the scaling parameters, because peak flow gauges with few records will have larger uncertainty in the estimation of peak flow quantiles in comparison with peak flow gauges with larger records. Therefore, the length of the

13

peak flow record is used as weight in the WLS regression. To illustrate the effect of considering the WLS rather than a standard Ordinary Least Square (OLS) regression, the Figure 1-3 show the comparison of scaling parameters (α and θ) for the 84 sub-regions at HUC-4 Level for the 2.33 and 100 years of return period. Although Figure 1-3 show small changes in α and θ between WLS and OLS, these could be translated as important differences in the estimation of the peak flow quantiles along the MRB. For this reason, it is important to use the WLS regression in order to reduce the uncertainty introduced by peak flow gauges with few records. The regression for the entire MRB included all 5,137 gauges. The number of gauges in the HUC-2 decomposition, which defines six sub-regions of the MRB, ranges from 338 to 1,601. Finally, the number of gauges defined by the HUC-4 decomposition with 84 sub-regions ranges from 6 to 195, with 90% of the sub-regions containing more than 20 gauges.

I conducted a separate analysis to explore the variability of peak flows and regional homogeneity across space. I calculated the residuals from the power law function for the three analysis levels and displayed them spatially. These residuals were organized according to their signs (positive or negative residuals). This approach helped us recognize the existence of spatial clusters in the distribution of peak flows, caused by regions with higher or lower floods. This procedure provides a qualitative method to assess the regional homogeneity of floods in which the flood scaling is described only by drainage area (Gupta et al. 1995).

I mapped the values of θ_p and α_p for the 84 sub-regions to reveal the spatial patterns behind the scaling parameters for the 2.33- and 100-year return periods. These plots represent the spatial signatures of floods synthetized in two parameters (θ and α) across the drainage areas and return periods. In particular, I used the estimated power law formulas for each HUC-4 partition to estimate peak flow quantiles of 2.33- and 100-year return period for drainage areas of 1, 100,

14

1,000 and 10,000 km^2. Finally, I estimated the flood SI for the same range of drainage area based on the power law formulas. These results allow us to analyze the spatial shifts of floods for different flood quantiles and spatial scales.

2.4. Identifying the Type of Scaling

Gupta (1995) defines simple-scaling when the scaling exponent in the power law regression between flood quantiles and upstream area remains constant for all flood quantiles, and multi-scaling when the scaling exponents change. I used the Potthoff analysis (Potthoff, 1966) in order to test the null hypothesis $H_0: \theta_{2.33} = \theta_{100}$. The Potthoff analysis identifies if there is a significant difference in the regression exponents when data are separated in different groups. This analysis requires to perform a multiple linear regression to compare the regression coefficients for different peak flow quantiles.

With a significance level of 5%, we can conclude that if the p-value is less than 0.05 the null hypothesis of simple scaling is rejected. But, if the p-value is greater than 0.05 we cannot reject the null hypothesis, leaving open the possibility of simple-scaling in the data. The test relies on three equations,

$$Y^{[i]} = ln(Q_{2.33}) = ln(\alpha_{2.33}) + \theta_{2.33}ln(A) \qquad \text{Equation 2-2}$$

$$Y^{[j]} = \ln(Q_{100}) = \ln(\alpha_{100}) + \theta_{100}\ln(A) \qquad \text{Equation 2-3}$$

$$Y^{[i,j]} = a + bX^{[i,j]} + cG^{[i]} + dG^{[i]}X^{[i,j]} \qquad \text{Equation 2-4}$$

where X is the vector of drainage area repeated twice, since the drainage area is the same for Equation 2-2 and Equation 2-3. G is the dichotomous grouping variable (Dummy variable) coding one for the region i and zero for the region j. The coefficients in Equation 2-4 evaluate the difference in coefficients for Equation 2-2 and Equation 2-3. The coefficient d determines differences between $\theta_{2.33}$ and θ_{100}; therefore, I estimate the p-value for the coefficient d to test

15

the null hypothesis $H_0: \theta_{2.33} = \theta_{100}$. Then, if the p-value is less than 0.05 (significance level of 5%), the null hypothesis of simple scaling is rejected. But, if the p-value is greater than 0.05 the null hypothesis cannot be rejected, speculating a possible simple-scaling feature.

2.5. Testing Regional Homogeneity

I assessed regional homogeneity using the Moran spatial autocorrelation (Moran, 1950) for the residuals of the scaling power law in space. I group the residuals of the power law regression as HOT: Positive residuals, and COLD: Negative residuals. Mainly, the Moran spatial autocorrelation evaluates if a pattern of a spatial variable is clustered, dispersed, or random based on the null hypothesis that the variable (residuals in our case) is randomly distributed in the space.

I hypothesize that, if there is regional homogeneity over the scaling of peak flows the groups HOT-COLD should be randomly distributed in the watershed, showing that the floods in the region have a similar hydrologic response. But, if there are strong differences of flood responses along the watershed, HOT and COLD clusters will start to arise, breaking the regional homogeneity assumption in the flood scaling theory. The significance of the test is evaluated with a Z-score in which a Z-score of 1.96 rejects the null hypothesis with a significance level of 5%, in such case the existence of a clustering pattern of residuals in the space is assumed and therefore the regional homogeneity is not reached. The Moran statistic is based on neighboring elements which are defined with a specific buffer distance. I evaluate the Z-score for a search distance between 100 km and 200 km assuming that this range is enough to consider the inclusion of different peak flow gauges at the watershed level of HUC-4.

16

2.6. Discussion and Analysis of Results

2.6.1. First Insight of Spatial Pattern in Peak Flows

Figure 2-4 shows the SI for all 5,137 peak flow gauges. The map shows a spatial pattern over the MRB that reveals strong differences between the eastern and western parts of the basin. This variability is attributed to the differences in precipitation and runoff generation mechanisms across the large spatial domain. In particular, western areas present SIs between 6 and 10, with a cluster in the northwest border with values around 2.

Although the current study focuses on identifying flood patterns across the spatial scales and flood quantiles rather than explaining the processes that govern these patterns, I discuss some insights behind the spatial structure of the SI. Higher SI values in the west are connected to differences in flood mechanisms behind the frequent floods (i.e. the 2.33-year flood) and the infrequent ones (i.e. 100-year flood). In general, floods in this region are described with a combination of snowmelt in the winter season and higher precipitation in the spring season. The occurrence of periodic floods is more interconnected to one of these processes rather than both of them simultaneously. However, the 100-year flood (low probability of occurrence) could be connected to combinations of extreme conditions of these processes. An example of this dynamic are the floods in Montana, in which the periodic floods are related to only heavy rainfall in the spring; but the higher floods (with a return period greater than 50 years) are a result of a long period of snow accumulation without intermediate melting time, in conjunction with a high soil moisture content and a high rainfall in the region (Parrett et al. 1984). We could link the western cluster with SI values of 2 by the strong orographic controls in the southwest region of Montana. This control incentivizes convection of moisture, generating more rainfall in the area; becoming the dominant flood generation process. Consequently, the magnitude in the mean annual flood and the 100-year flood in this region is not very different (a flood severity index from 1 to 2).

17

Quantification of the relative role of these mechanisms would require the implementation of physics-based models to confirm or reject the hypothesis.

In contrast, eastern Mississippi presents index values around 2 and 3; moving toward the center of the basin the dispersion increases, showing values between 2 and 5. This increase in SI allows us to speculate about a mix of processes behind the mean annual flood and the 100-year flood in the eastern region. Some findings reported by (Lavers et al. 2013; Villarini et al. 2014) have shown that climatological signatures from tropical cyclones and atmospheric rivers play an important role in the flood structure in the east and central part of the basin. Note that the central region of the MRB presents a high variance in SI values, with a transition between low values in the eastern region to high values in the western region.

The results from examining the SI show a certain degree of spatial structure. Nevertheless, the analysis mixes peak flow gauges draining different watershed drainage areas, which can conceal scale dependent differences in a region. To reveal it, in the following sections, I analyze the power law structure between drainage area and flood quantiles described by power-law scaling to expose the spatial structure of floods across watershed scales.

2.6.2. Representations of Patterns in Flood Scaling

The results for the 2.33-year flood at the MRB level show $\alpha_{2.33}$ equal to 1.97 and $\theta_{2.33}$ equal to 0.60. On the other hand, at the HUC-2 level, the $\alpha_{2.33}$ ranges from 0.85 to 5.13, and the $\theta_{2.33}$ ranges from 0.53 to 0. 71 (see Figure 2-5). At the HUC-4 level, the $\alpha_{2.33}$ and $\theta_{2.33}$ values vary in the ranges of 0.11 to 8.83, and 0.18 to 0.91, respectively.

Figure 2-6 shows the distribution of the scaling parameters for the 2.33- and 100-year return period, which leads us to use simple-scaling as our null hypothesis for scaling in peak flow quantiles in the MRB for the HUC-4 Level. Gupta (1995) defines simple-scaling when the

18

scaling exponent remains constant through the quantiles, and multi-scaling when the scaling exponents change for different quantiles. In general, we could presume that the simple scaling dominates in the MRB, by the similarity of distribution of the scaling exponents presented in Figure 2-6. A rigorous statistic test must be performed in order to evaluate the statistically significant difference between the scaling exponents of the 2.33- and 100-year return period. For this purpose the Potthoff analysis (Potthoff, 1966) is performed in order to identify the type of scaling in each sub-region at HUC-4 Level in the MRB testing the null hypothesis $H_0: \theta_{2.33} = \theta_{100}$. Figure 2-7 presents the estimated p-value for the 84 sub-regions at HUC-4 Level. Based on this result, I found 17 sub-watersheds with multi-scaling with clusters on the western and eastern Mississippi; and 67 sub-watershed with possible simple-scaling with a predominance in the center of Mississippi.

I assessed the performance of the power law function for the three levels of analysis using the adjusted coefficient of determination (R^2) (see Figure 2-2 for the MRB, Figure 2-5 for the HUC-2 level, and Figure 2-8 for the HUC-4 level). For the 2.33-year floods in the MRB I obtained an R^2 of 0.58; at the HUC-2 level (six sub-regions), the R^2 varies from 0.53 to 0.88; and at the HUC-4 level (84 watersheds), the R^2 shows a range from 0.15 to 0.98, with a mean and standard deviation of 0.79 and 0.16 respectively. On the other hand, for the 100-year floods in the MRB the model has an R^2 of 0.61; at the HUC-2 level the R^2 varies from 0.50 to 0.84; and at the HUC-4 level (84 watersheds), the R^2 shows a range from 0.17 to 0.95, with a mean and standard deviation of 0.74 and 0.17 respectively. In general, the HUC-4 decomposition provides a better performance of the power laws in explaining the scaling structure of floods. Figure 2-9 shows six of the 84 regressions obtained for the 84 sub-regions at the HUC-4 level for the 2.33-year flood. I found that only 11 of the 84 sub-regions show an R^2 less than 0.3. I hypothesize that

19

the poor values of R^2 (less than 0.3) presented at the HUC-4 level were caused by different hydrologic conditions generating flood in the sub-regions. I explore this further in the following sub-section.

2.6.2.1. Spatial Clustering of Residuals from Power Law Functions for Different Decomposition Levels

The determination (or lack) of regional homogeneity is essential to characterize flood producing mechanisms. I propose a strategy to determine homogeneity that follows the fundamental idea given by Gupta (1994), in which catchment size is the only variable needed to describe the flood scaling. I use the power law function between flood quantiles and drainage area to group the peak flow residuals as HOT (peak flow above the linear regression) and COLD (peak flow below the linear regression). This notation is associated with overestimation or underestimation of flood values by the regression. I hypothesize that, if the watershed is homogeneous with respect to the flood producing mechanism, the HOT and COLD gauges should be randomly distributed in the watershed, showing that the all floods are correctly represented by the parameter of drainage area in the power law function. Contrarily, if there is a strong difference in flood responses inside the watershed, HOT and COLD clusters will be apparent, representing different hydrologic conditions inside the watershed. Figure 2-10 shows the scaling plot where gauges are classified as having HOT or COLD residuals for the regression analysis at the full MRB level.

I mapped the HOT-COLD classification in the three levels of analysis in Figure 2-11. The spatial structure at the MRB level, essentially the eastern region has higher floods than the western regions in any range of drainage area. Clearly, this pattern exists because of the strong difference in hydrologic conditions in the two regions. The HOT-COLD results at HUC-2 Level displays more mixed HOT and COLD patterns than for the full MRB; however, there are still

20

strong clusters of HOT and COLD floods in each of the six sub-regions. Finally, the HUC-4 level, with 84 sub-regions, shows a more evenly spread pattern in the spatial distribution of HOT and COLD sites; however, a close inspection of patterns in the HUC-4 units reveals some units with significant HOT-COLD clusters. Even if at HUC-4 level basins are still presenting a degree of non-homogeneity, the number of gauges inside the basins is limited, therefore it is not possible to go to a more refined level of analysis. In order to make more evident the existence (or non-existence) of HOT-COLD clusters.

I test the homogeneity assumption based on the spatial autocorrelation Moran in the randomness evaluation of the power-law residuals in the space for each of the sub-regions HUC-4 Level at the MRB. The spatial structure of the Z-score presented in Figure 2-12 demonstrates that the regional homogeneity is independent of frequency in some regions, showing watersheds with Z-score higher than 1.96 for the 2.33-year floods, but lower than 1.96 for the 100-year floods. Also, the results show a dominant pattern of non-homogeneity in the MRB at the HUC-4 level, suggesting that a more refined spatial scale is necessary to obtain a more accurate representation of peak flows through scaling of floods. Figure 2-13 shows 6 examples of the classification of regional homogeneity based on the Z-score. Note that the HUCs 1010, 1029, and 510 have Z-score less than 1.96 which is related to a regional homogeneity feature (randomness in the HOT-COLD residuals), concluding that the flood scaling on these watersheds is well represented. However, the HUCs 1027, 508, and 1114 have Z-score higher than 1.96 in which is obvious the clustering of the HOT-COLD residuals in the space. Therefore, these watersheds must be refined based on the HOT-COLD clusters to properly capture the regional signature of floods across the scales

2.6.3. Spatial Flood Patterns Based on Power Law Formulas

In this section, I use the scaling parameters to explore regional flood differences and similarities as these values synthesize the flood processes in a scale-dependent quantity. The spatial structure in the α and θ values for the return period of 2.33 and 100 years for each HUC-4 level is shown in Figure 2-14. Assuming a drainage area equal to 1 km^2, Equation 2-1 gives Q_p values equal to α_p. Therefore, the α_p value can be interpreted as the flood quantile for the unitary drainage area (1 km^2). Consequently, these values describe the pattern of floods for small watersheds with 1 km^2 of drainage area along the Mississippi watershed. The α patterns in the west and central part of the Mississippi watershed show strong differences, with $\alpha_{2.33}$ values closer to 1 and 5, respectively, and α_{100} values closer to 10 and 55 in the west and central part, respectively. These results suggest that the 2.33-year floods for a watershed with a size of 1 km^2 in the central region of the Mississippi River basin are five times stronger in magnitude that the floods in the western part of the basin. The question that remains is if this spatial pattern is preserved for different watershed sizes, this will be addressed in the following section.

The θ values represent the slope between drainage areas and floods in the log space, connecting the power rate in the flood increments across drainage areas. As we mentioned earlier, α is controlling floods with a unitary drainage area, however, changes in the α values are also impacting the other spatial scales. This means that a displacement in the intercept will modify the flood magnitude in direct proportion to the A^θ value. In contrast, the θ magnitude affects the flood magnitude differently across the scales. The spatial patterns in α are completely different from the spatial structure of θ. An example are clusters of high θ values found in the west, east, and north of the basin. These values show a transition to

22

lower values towards the center of the basin, locating finally the lowest cluster of θ in the Midwest with θ values close to 0.2.

2.6.3.1. Flood Patterns for Different Watershed Sizes

The final step is to explore regional flood patterns combining θ and α. To reveal regional flood patterns along the Mississippi River basin, I normalized the peak discharges at the HUC-4 level, with the highest peak discharge over the 84 sub-regions for each quantile analyzed. Figure 2-15 shows the regional flood pattern for drainage areas of 1, 100, 1,000 and 10,000 km^2 for the 2.33-, and 100-year flood. The maps reveal different regional flood patterns for different watershed sizes and flood frequencies. Note that the regional flood patterns revealed at the 2.33-year flood and different values of drainage area (see Figure 2-15): the western floods remain stable across the range of drainage areas; however, the cluster of larger floods expands from the center to the eastern MRB for the drainage area from 1 km^2 to 10,000 km^2. These results confirm the differences in flood producing mechanisms across drainage areas and across regions in the Mississippi River Basin. In the 100-year flood, we find similar spatial patterns with the presence of a cluster of maximum values in the center of the basin for drainage areas of 100, 1,000 and 10,000 km^2. At the same time, in the eastern part of the MRB, a cluster of high floods emerges in the transition from 1 km^2 to 10,000 km^2.

To highlight the variability of these regional flood patterns with respect to the drainage area, I grouped the HUC-4 Level in the Top 20 sub-regions with higher floods and the Top 20 sub-regions with lower floods. Figure 2-16 shows the transition in space of the Top 20 sub-regions with higher 2.33- and 100-year floods respect to the watershed size, with a displacement from the center to the eastern Mississippi from 1 km^2 to 10,000 km^2. Looking at the Top 20 of the lower 2.33-year floods the cluster in the northwestern Mississippi is preserved in the different

23

ranges of watershed sizes. However, the spatial pattern exhibited by the Top 20 of lower 100-year floods is more dispersed with respect to the 2.33-year flood pattern. These results demonstrate that the flood producing mechanisms change not only in region, but also in drainage area magnitudes.

2.6.3.2. Severity Index with Flood Scaling

To improve the description of regional flood patterns for different frequencies and drainage areas, I calculated the severity index using the power law formulas calculated for each one of the 84 HUC-4 sub-regions. The severity index is referred to as the ratio between the 100-year flood and the 2.33-year flood. Figure 2-17 presents the SI variability in the drainage area across the Mississippi River Basin described by the scaling parameters. Examining the results, we find that for a watershed size of 1 km^2 there is a clear pattern of the index over space, with higher values of around 10 in the west, with a transition moving toward the center of the basin with index values of 4 and 7, and finally decreasing to values of 2 and 5 in the east. In addition, the increasing drainage area begins to transform the cluster of higher severity index values found in the west, showing more dispersion in this region. In contrast, the eastern cluster is more consolidated with the increasing of the drainage area, structuring a cluster with values around 2 and 3. This result dissects the analysis of severity index calculated for each gauge in Figure 2-4 by presenting patterns in flood ratios across sizes of drainage area. These results highlight the importance of discerning the watershed size from the smallest (1 km^2), to medium-sized (100<A<1,000 km^2), to largest (>10,000 km^2) watersheds in flood estimation.

2.7. Conclusions

The flood scaling analysis performed in this chapter reveals a diversity of regional flood patterns using scaling parameters (θ and α) of the 2.33- and 100-year floods for different

drainage area values. I show that at HUC-4 Level of decomposition the power laws represent a satisfactory representation of peak flows; although the HOT-COLD pattern suggests that in some sub-regions the analysis can be improved with a refined level of analysis (e.g. HUC-6 Level). The number of gauges inside the basins is a limitation to evaluate a more refined scale.

A remarkable result is the shift of regional flood patterns for different drainage sizes and for the 2.33- and 100- years flood at HUC-4 Level, in which the relative flood magnitude depends of the catchment size, showing a dynamic dependence of floods related to drainage area and spatial location. This result is especially strong in the spatial transition of the Top 20 regions with higher 2.33- and 100-year from the center to the eastern Mississippi. The results of this analysis provide clear signatures in flood producing mechanisms that should be explained from physical considerations.

Several caveats are recognized in our study. I presented spatial patterns only up to watersheds smaller than 10,000 km^2. This threshold was defined to guarantee the flood diversity inside of a particular HUC-4, eliminating the influence of gauges over large rivers that integrate different climate regimes and are more likely to be affected by regulation. In addition, the use of a different probability distribution could change the outcome of the flood quantiles estimations. I decided on using the standard methodology proposed by the USGS in the Bulletin 17B based on the probability distribution Log Pearson Type 3 as the best option for the flood quantile estimation because it is easily replicable thanks to the USGS PeakFQ software.

This chapter represents an effort to quantify the structure of flood scaling in a range of drainage areas and flood quantiles. Most of the HUC-4 Level units present a satisfactory peak flow scaling, however, even in these units of analysis there are peak flow variabilities that cannot be explained just by the drainage area. Therefore, further analysis needs to be conducted in order

25

to capture this remaining variability, either by physical controls such as river network structures or statistical controls such as sampling errors and number of streamflow gauges used in the regression analysis. These aspects are explored with more detail in the following chapters.
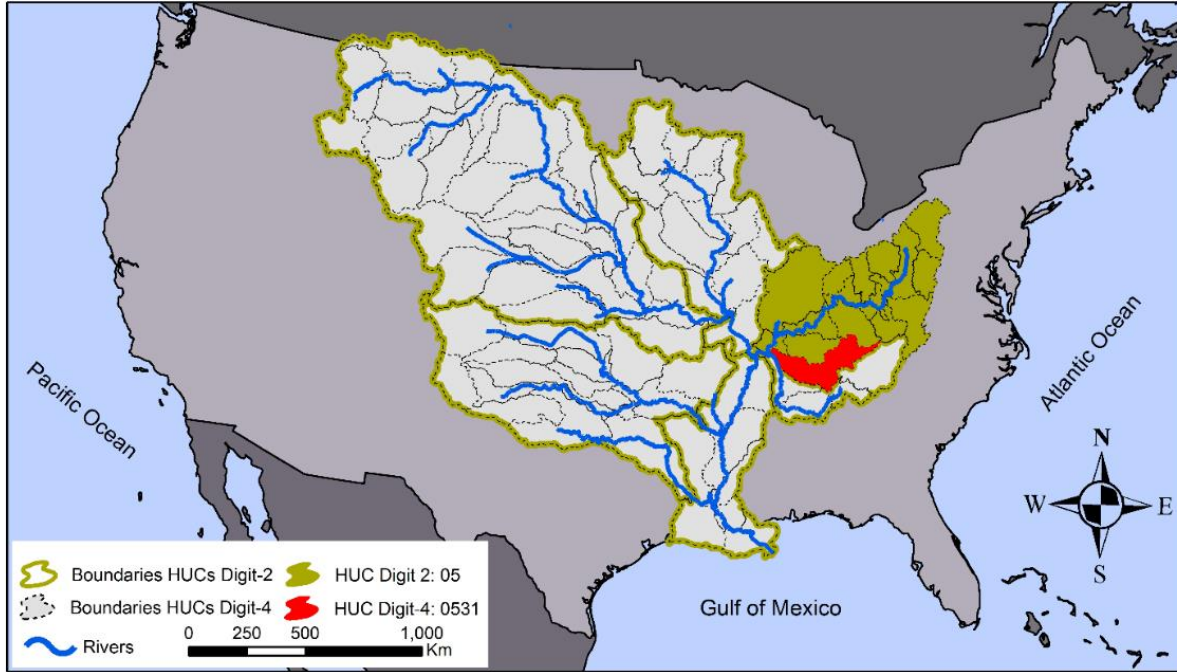
Figure 2-1. Location of the units of analysis: Complete MRB, six major MRB sub-regions (HUC-2) and 84 HUC-4 sub-regions. Location of HUC 2-Digits 2:05 and HUC 4-Digits: 0531 related to the flood scaling in Figure 2-2.
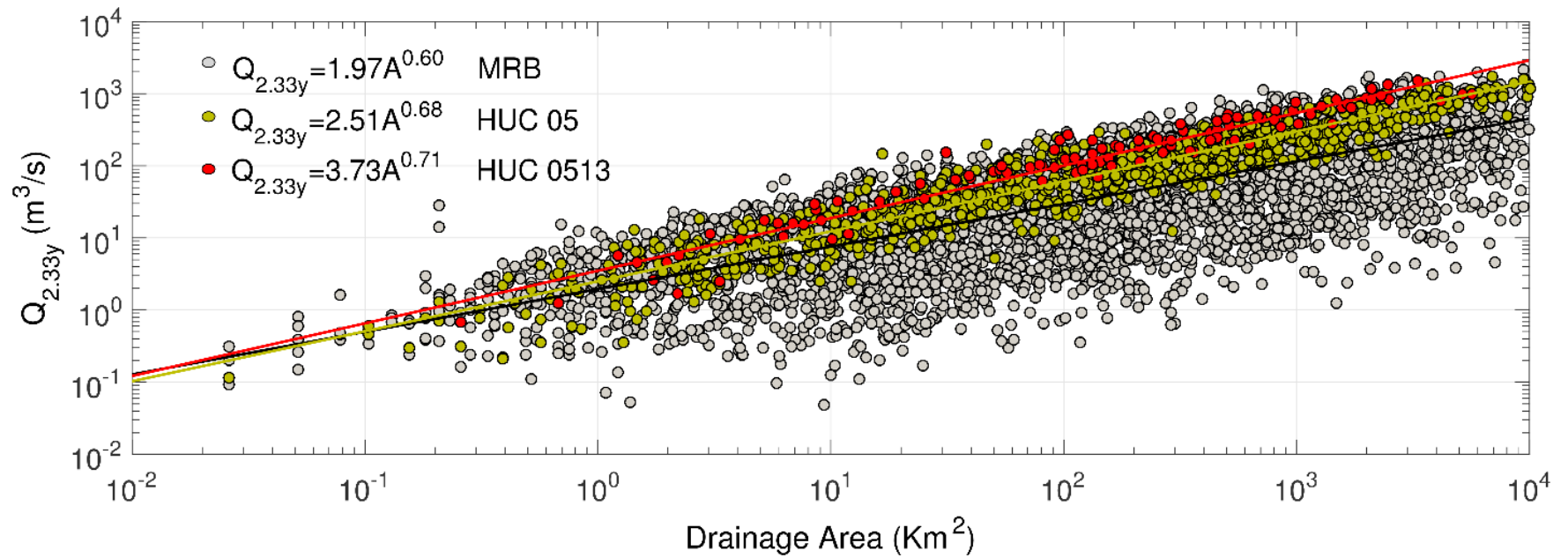
Figure 2-2. Disaggregation in the flood scaling from the complete MRB to HUC-2 level (HUC- 2 – Digits: 05) to HUC-4 level (HUC 4 –Digits: 0531); the regressions have 5136, 1029 and 110 peak flow gauges and R^2 values of 0.27, 0.88 and 0.93 respectively.
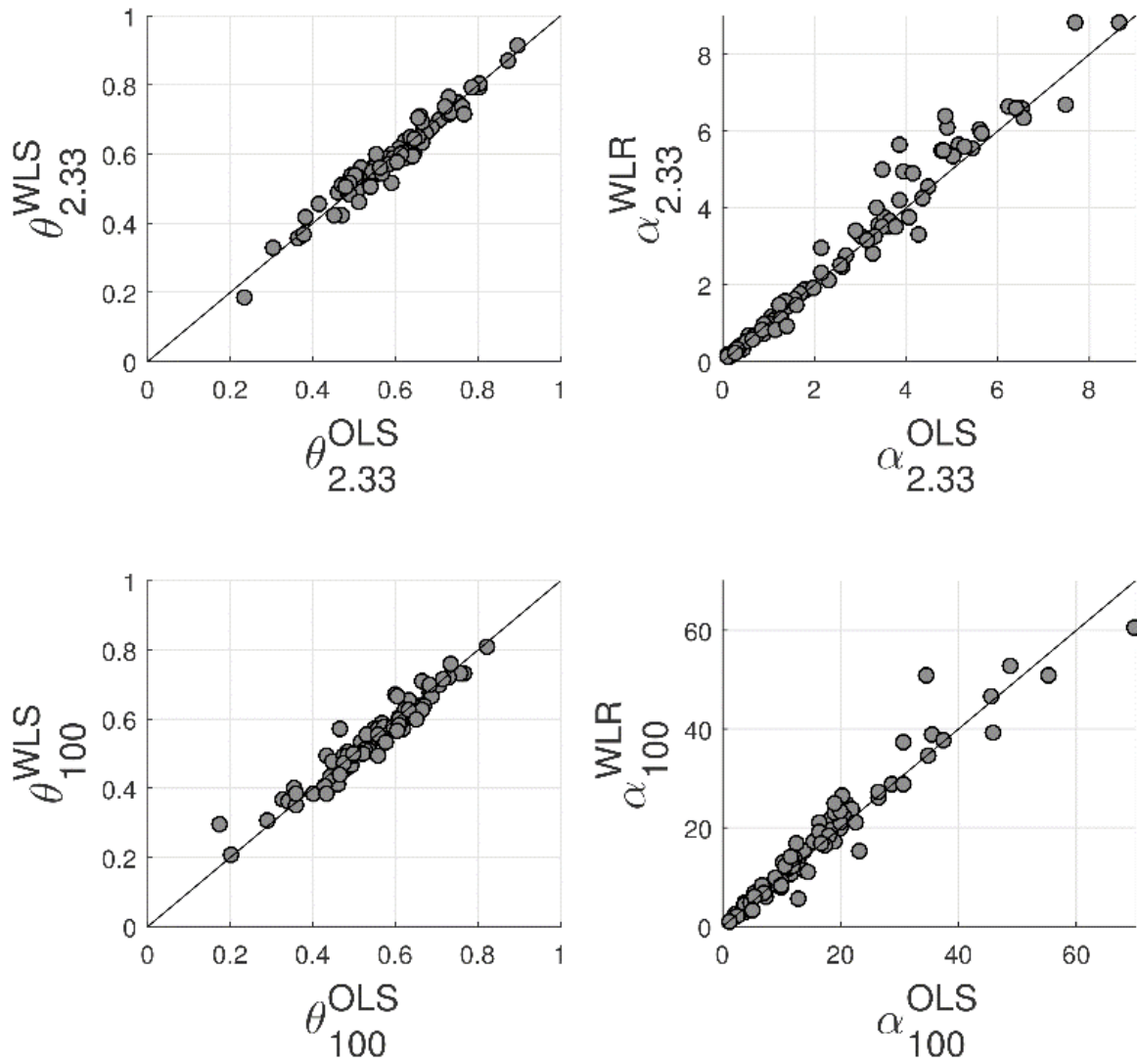
Figure 2-3. Comparison of scaling parameters between WLS and OLS regressions.
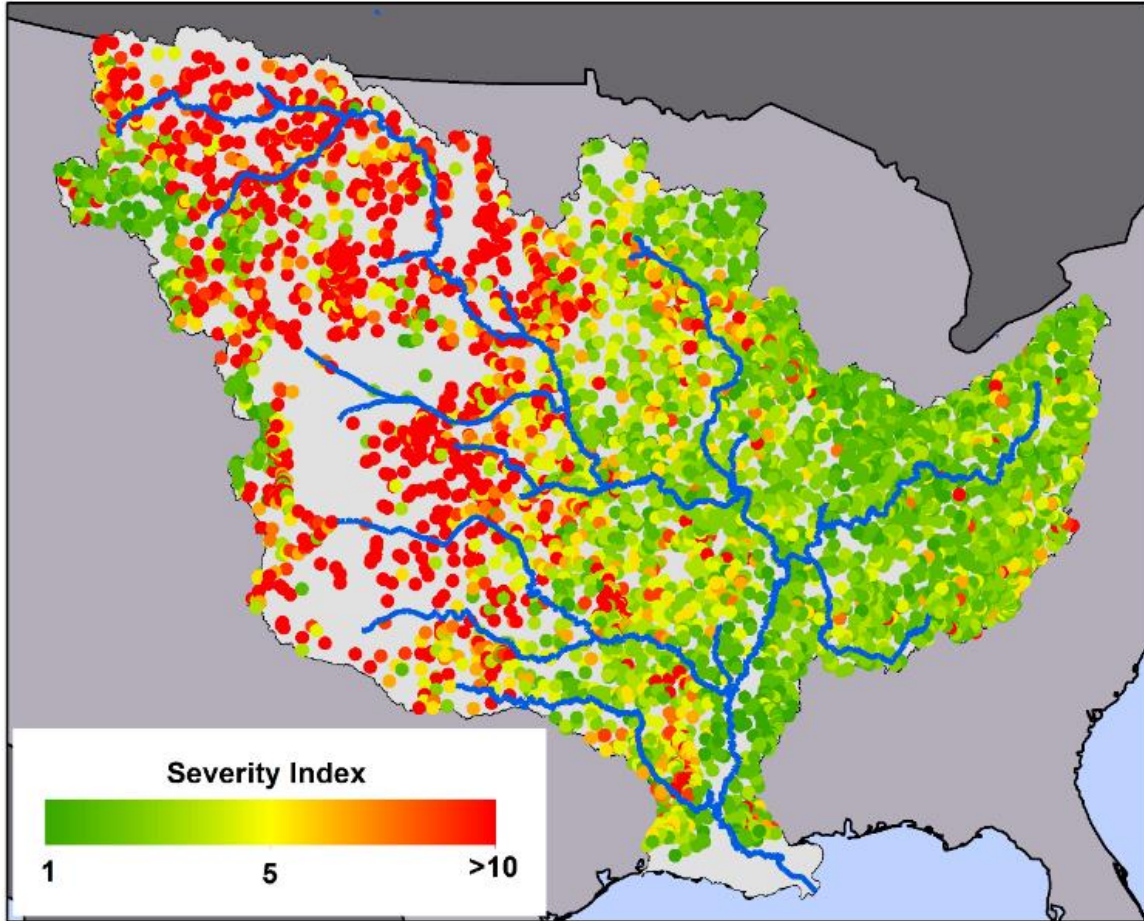
Figure 2-4. Flood severity Index for the 5,137 peak flow gauges.
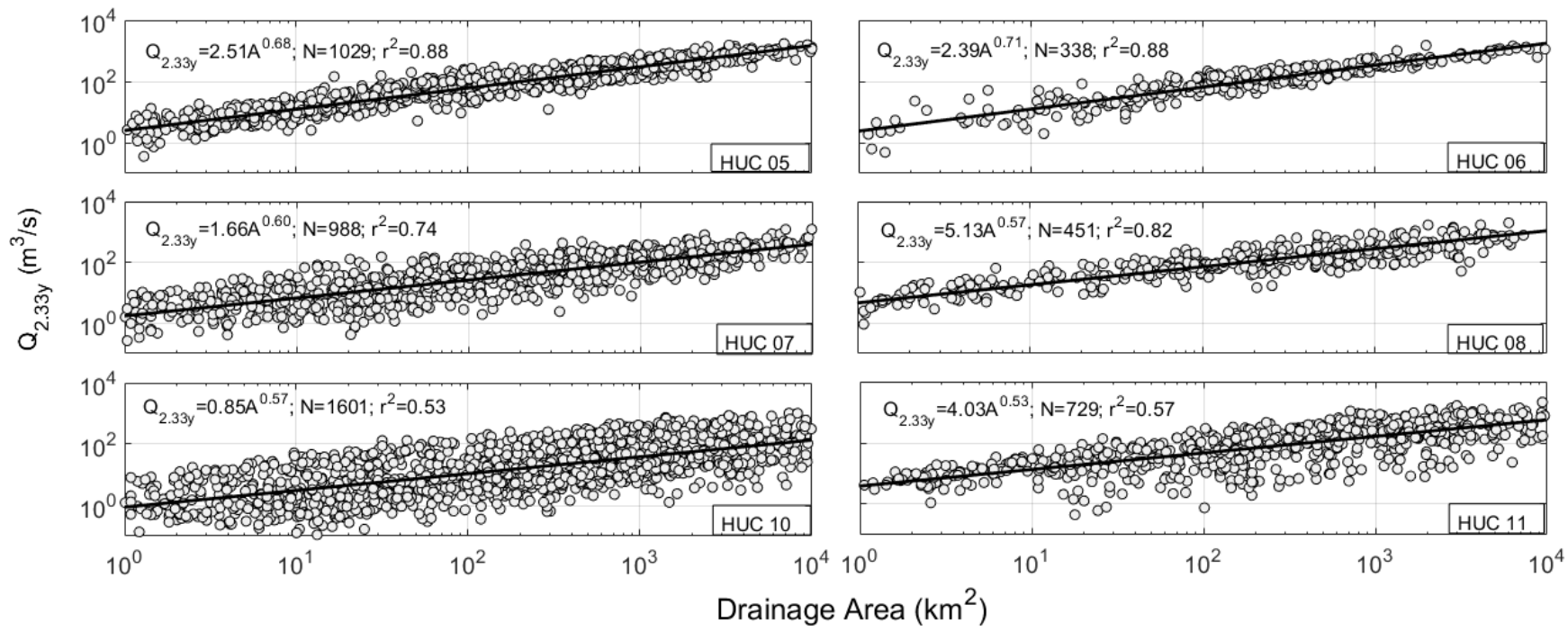
Figure 2-5. Power law regression at spatial domain HUC-2 level (six sub-regions)
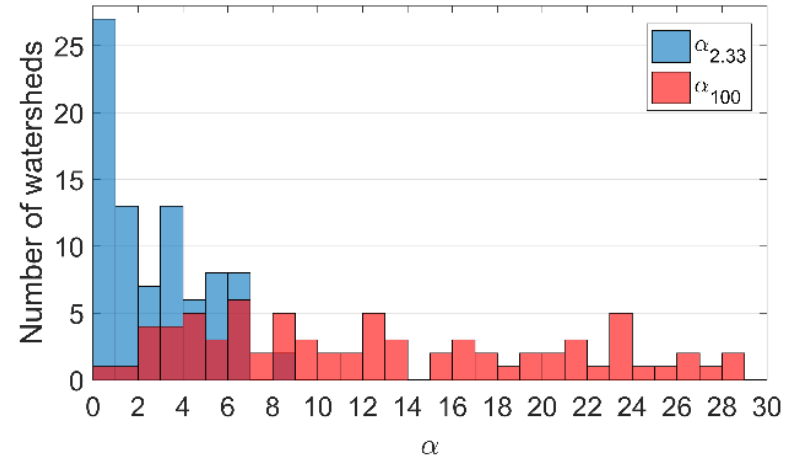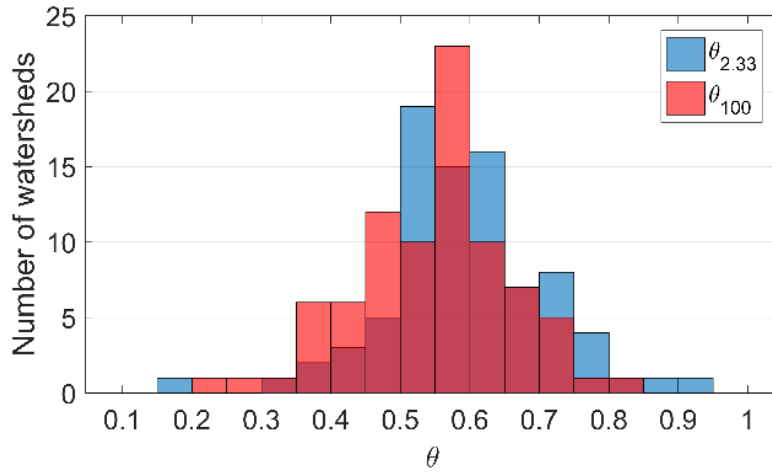
Figure 2-6. Histogram of scaling exponents and intercepts for the peak flow of 2.33 years and 100 years of return period at the HUC-4 level.
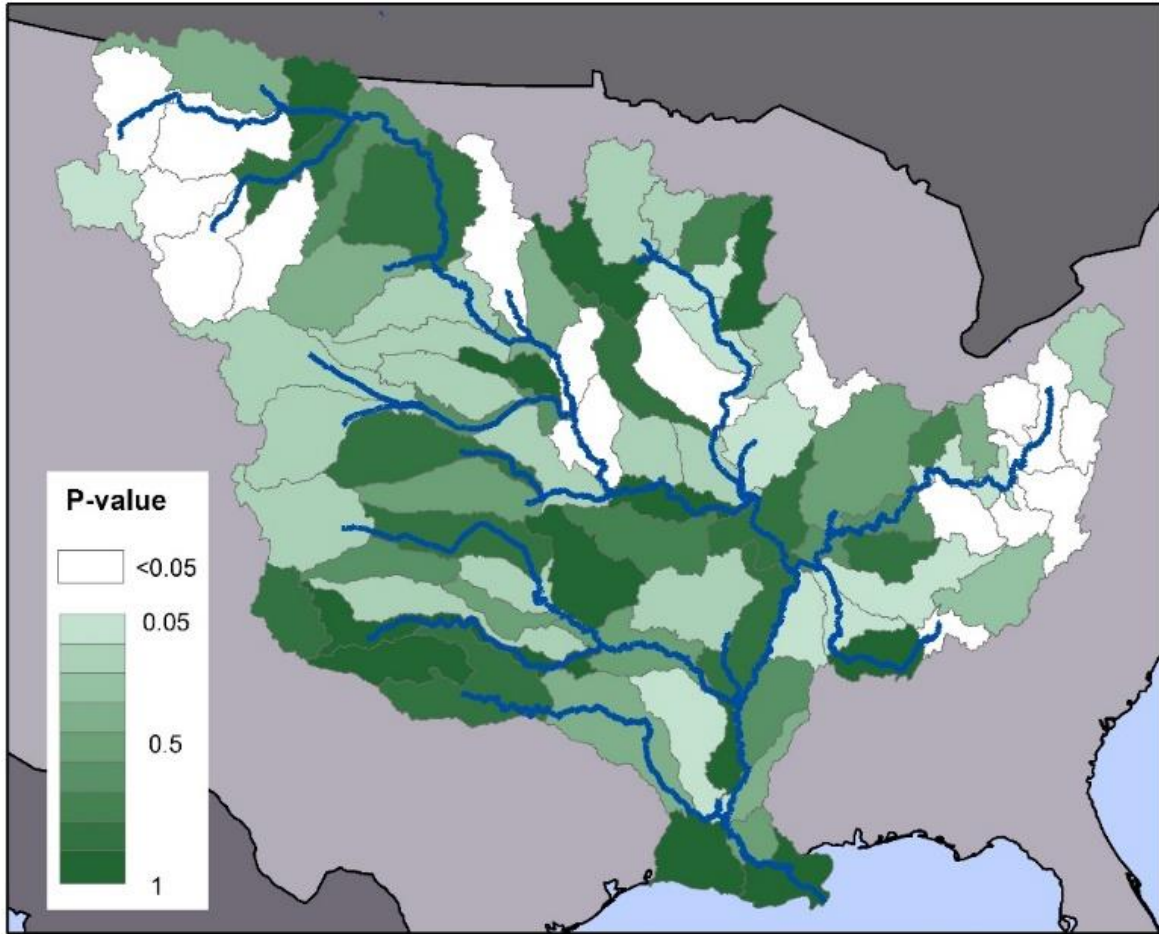
Figure 2-7. Spatial pattern of the p-value to test the null hypothesis $H_0: \theta_{2.33} = \theta_{100}$ in the 84 sub-watershed.
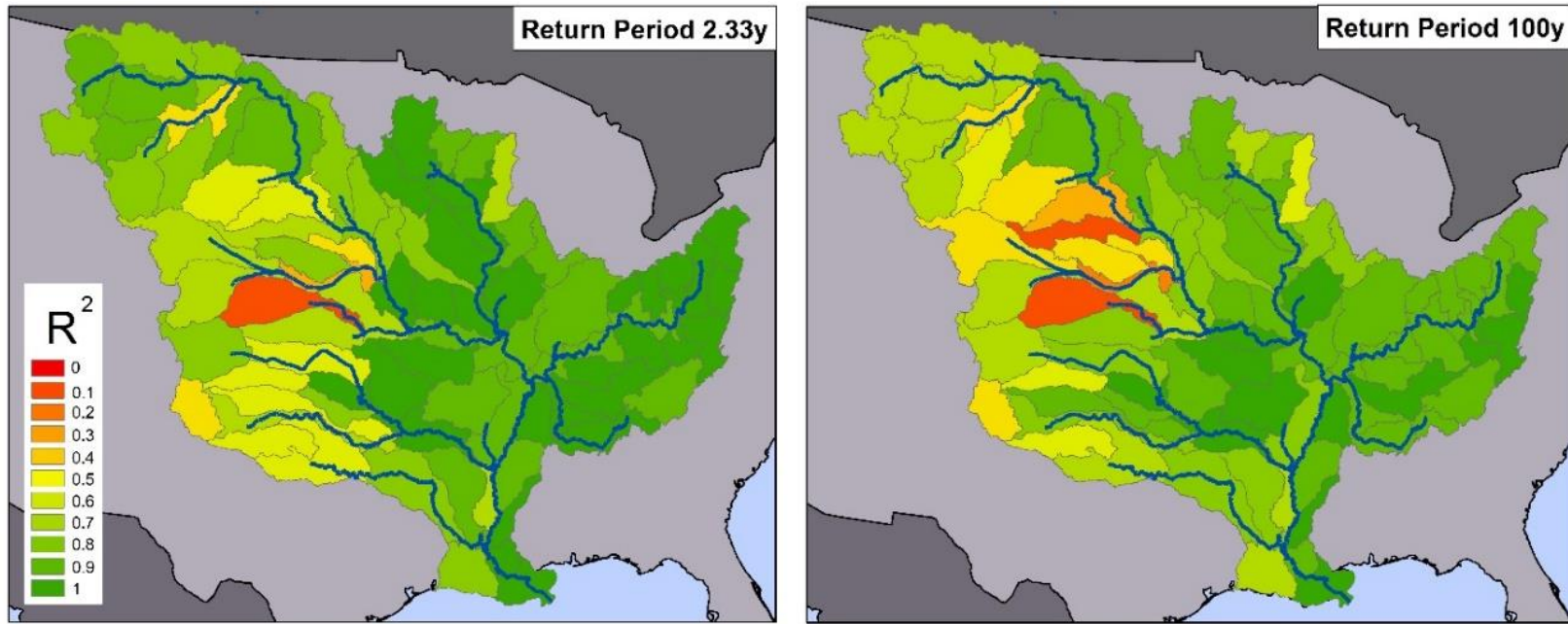
Figure 2-8. Adjusted coefficient of determination (R^2) for the power law with 2.33-year floods (left) and 100-year floods (right) at the HUC-4 level.
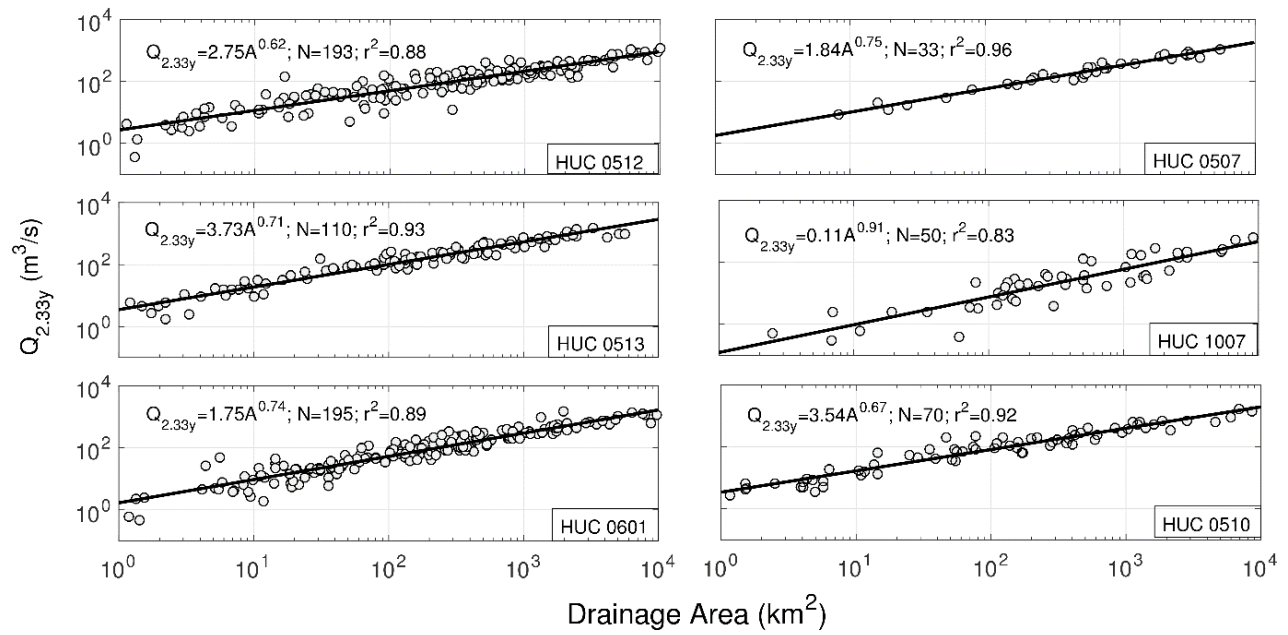
Figure 2-9. Power law in six HUC-4 sub-regions (HUC 4-Digits: 0512, 0513, 0601, 0507, 1007, and 0510).
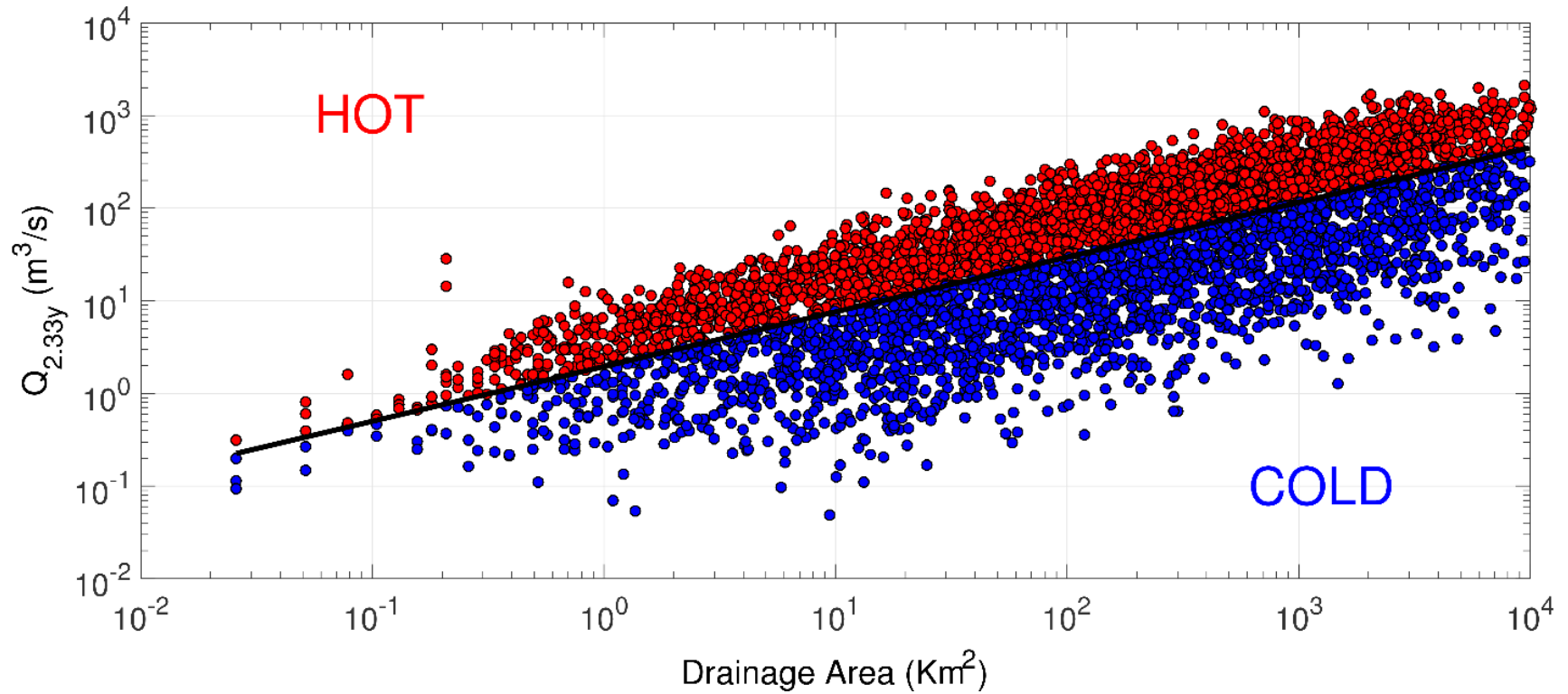
Figure 2-10. HOT-COLD plot of the power law with the 5,137 peak flow gauges located in the complete MRB. Red points identify the peak flow values above the regression and blue points identify the peak flow values below the regression.
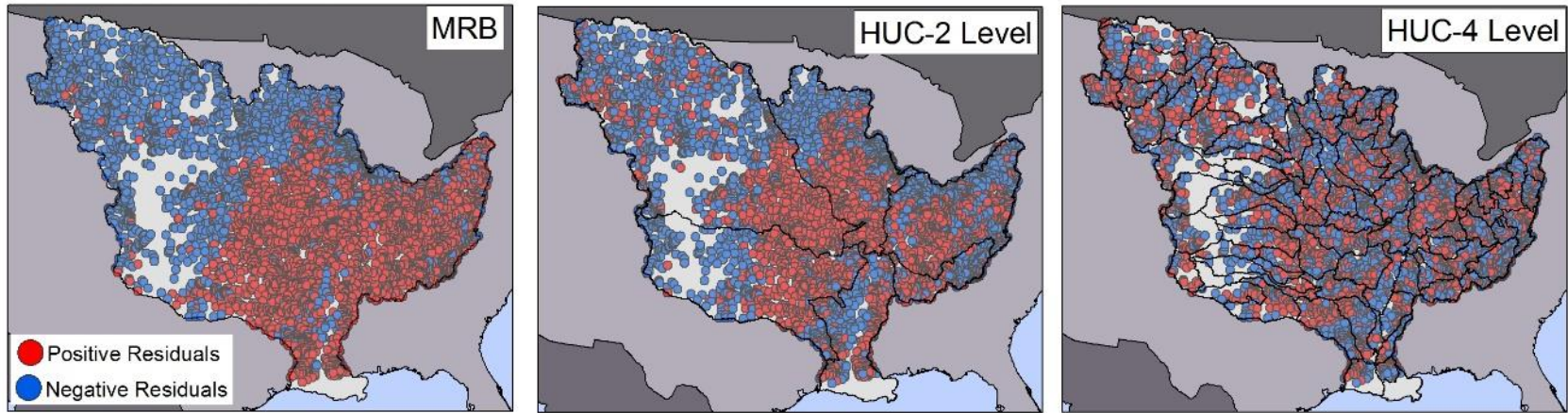
Figure 2-11. Spatial pattern for the HOT-COLD analysis in the complete MRB, HUC-2 Level, and HUC-4 Level. Red points identify the peak flow values above the regression and blue points identify the peak flow values below the regression.
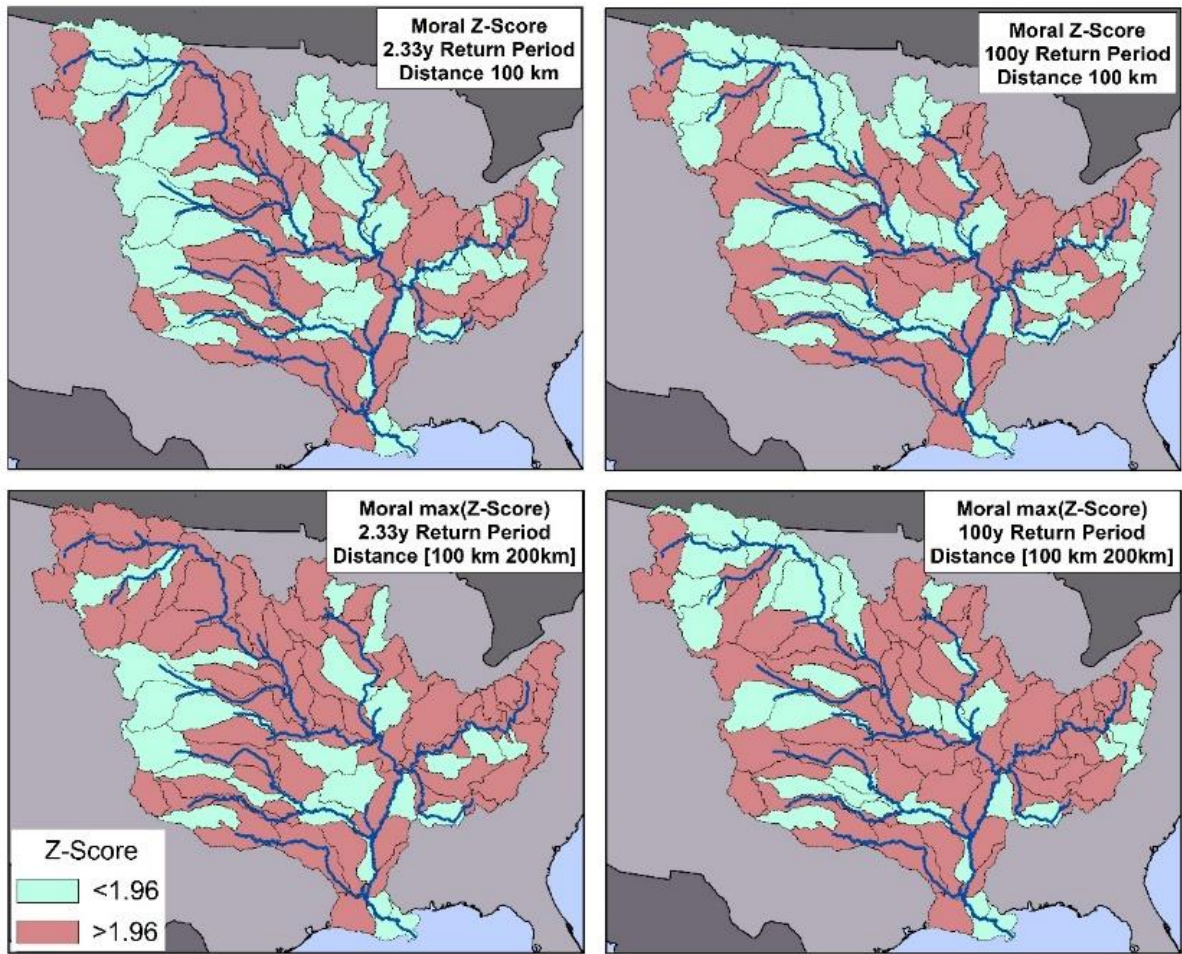
Figure 2-12. Map of the Z-Score in the 84 sub-watersheds for the 2.33 and 100 year of return period.
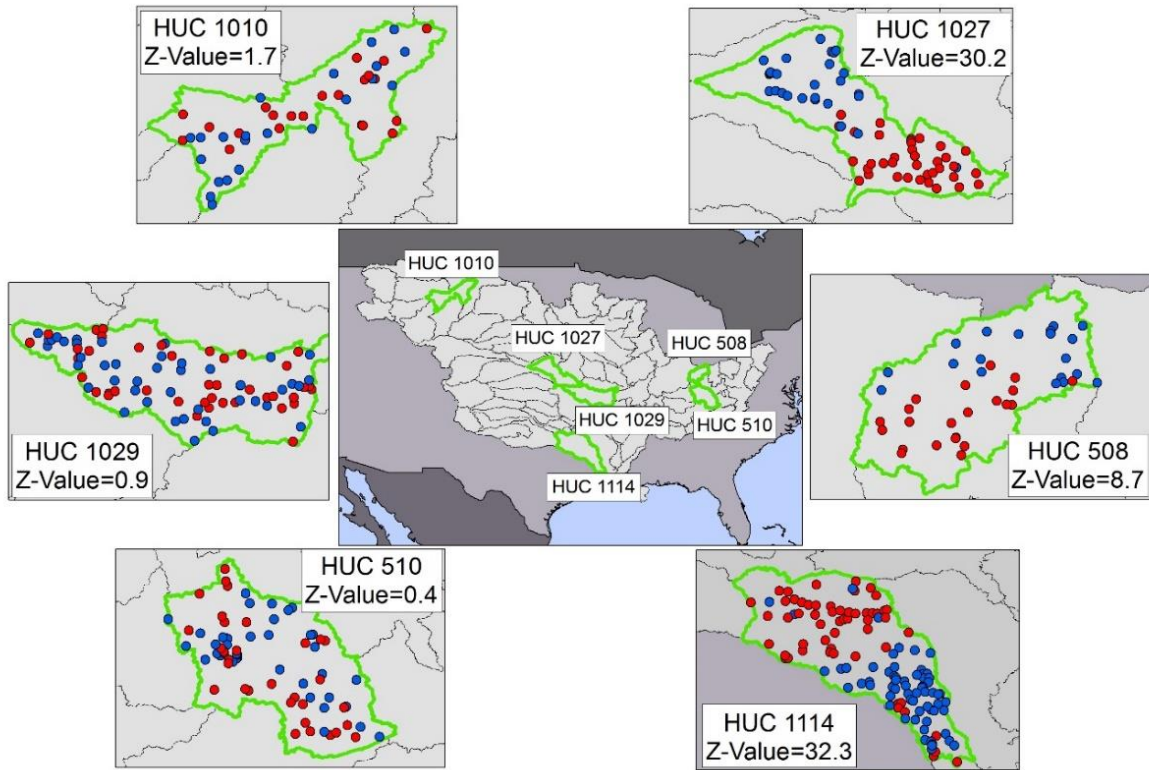
Figure 2-13. Examples of regional homogeneity and non-homogeneity based on the Z-score in 6 sub-watersheds in the MRB.
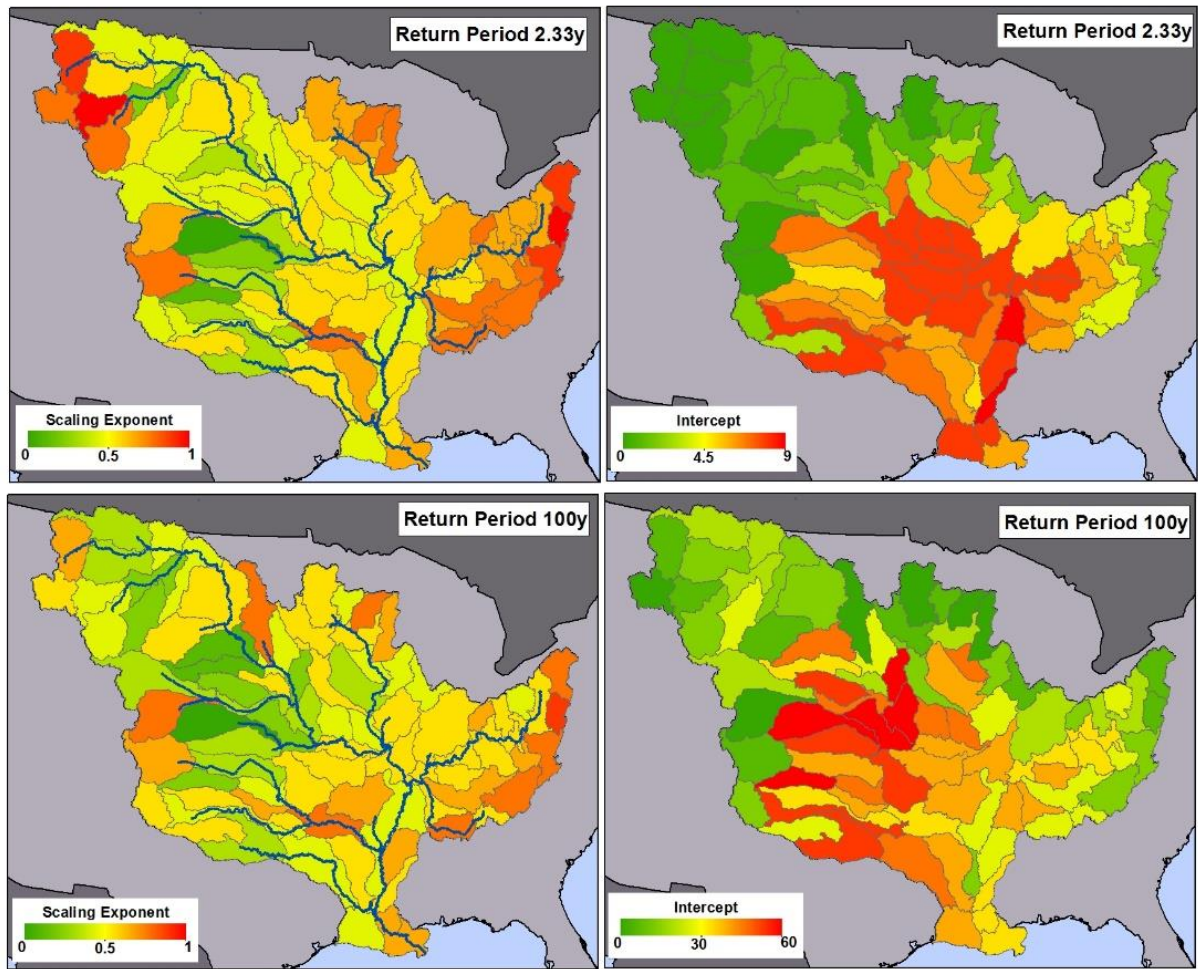
Figure 2-14. Scaling exponent and intercept at HUC-4 level for peak flows with return periods of 2.33 and 100 years.

40
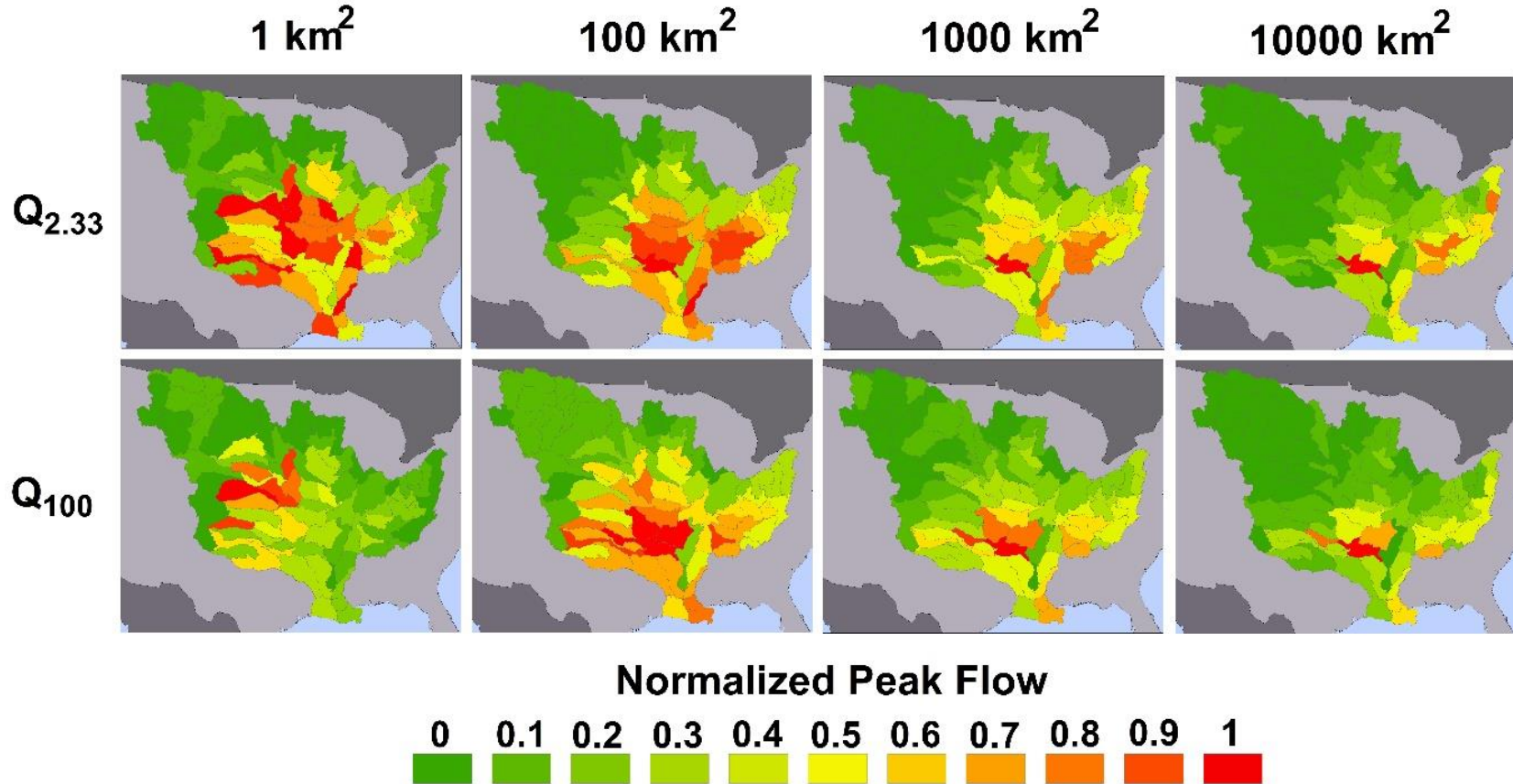
Figure 2-15. Normalized peak flows estimated with the power-law model for different return periods (rows) and magnitudes of drainage area (columns) at the HUC-4 level of analysis.
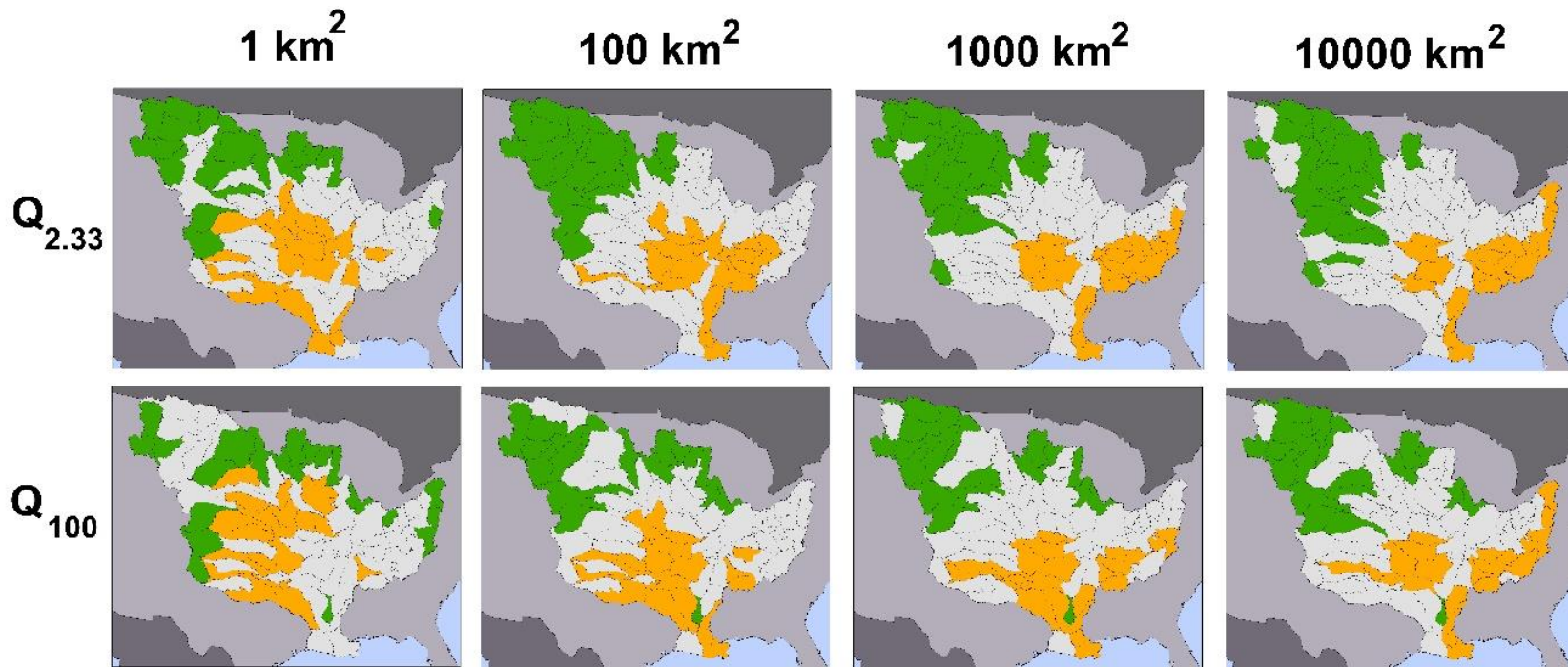
Figure 2-16. Top 20 sub-regions with higher (orange) and lower (green) peak flows for specific drainage area sizes and return period of 2.33 and 100 years at the HUC-4 level of analysis.
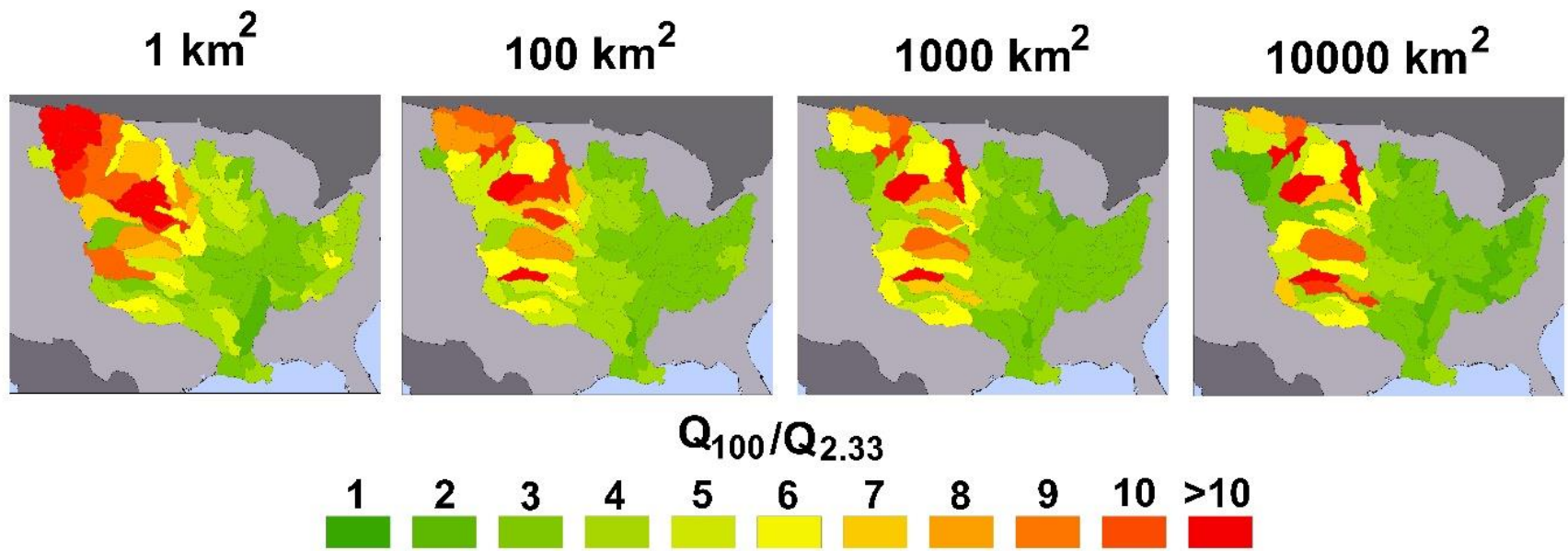
Figure 2-17. Flood severity index generated with the power law model for different magnitudes of drainage area at the HUC-4 level of analysis.

CHAPTER 3: THE INFLUENCE OF SPATIAL VARIABILITY OF WIDTH FUNCTIONS ON REGIONAL PEAK FLOW REGRESSIONS [2]

3.1. Introduction

The development of the regional flood-frequency equations can be described in four major steps: (1) estimation of "at-site" flood quantiles, (2) delineation of homogeneous regions, 3) definition of explanatory variables, and 4) estimation of regression equations between peak flow quantiles and the explanatory variables over the regions (Eash et al., 2013). The USGS is the agency in charge of the development of regional flood-frequency equations for the entire United States (e.g., Eash et al., 2013; Mastin et al., 2016; Parrett et al., 2010). A detailed explanation of the origins and early developments of the RFFA in the United States is summarized in Dawdy et al. (2012). Multiple regionalization studies have identified drainage area (A) as the most important variable in the construction of these regional equations, which is consistent with the findings of Fuller (1914), who first identified the connection between peak flows and A by means of power laws. In addition to A, other explanatory variables such as mean annual precipitation, base flow index, basin perimeter, average basin slope, drainage density, and percentage of area underlain by a specific soil type are sometimes used in regional flood-frequency equations.

Ayalew & Krajewski (2017) indicated that only few states include the shape of the watershed as a variable in the development of regional flood-frequency equations. Then, most states are using regional flood-frequency equations assuming that catchments with the same A, but different shape and drainage network geometry are expected to have the same peak flow quantiles. This practice is in stark contrast to the long-standing research in hydrology that shows how the shape of a watershed and drainage network structure affects the streamflow fluctuations,

44

including the magnitude of the peak flow (Horton, 1932; Morisawa, 1958; Rinaldo et al., 1995; Sherman, 1932; Strahler, 1964; Taylor & Schwarz, 1952). However, the exclusion of the drainage network geometry can be explained because the peak flow quantiles used in regional flood frequency equations are a statistical characterization of a cumulative distribution function. Therefore, they are disconnected from the physical processes that occur during individual flood-generating rainfall-runoff events (Dawdy et al., 2012; Furey et al., 2016; Wright et al., 2014). This motivates the need to study the relation of peak flow quantiles and peak flows from rainfall-runoff events, with respect to the explanatory variables that capture the spatial distribution of the drainage network.

This chapter explores the inclusion of Width Function Descriptors (WFDs) in the construction of regional peak flow equations. I derived 34 WFDs to study their relations with two types of peak flows. The first type comprised peak flows generated by a uniform rainfall-runoff event via hydrologic simulations. The second type comprised peak flow quantiles derived by fitting probability distributions to actual annual peak flow observations. I demonstrated that WFDs can explain the regional peak flow variability from synthetic rainfall-runoff events but not for peak flow quantiles derived from annual peak flow observations, which may explain why most of the regional flood frequency equations for the United States do not include descriptors of the drainage network as explanatory variables.

This chapter is organized as follows. The first section describes the study area and data used for the generation of WFs. This is followed by a detailed description of the 34 WFDs based on the geometric WF and two different WF normalizations. Subsequently, I describe the use of a hydrologic simulation framework to make connections between WFDs and peak flows for different rainfall durations and constant rainfall intensity. I explain the implications of these

45

results in a discussion section. The next section replicates the same analysis and discussion done for peak flow from rainfall-runoff events using observations-based peak flow quantiles. Finally, I summarize the main findings in a conclusion section.

3.2. Study Area and Data Sources

To investigate the interplay between the drainage network and peak flows, I used the drainage network for all the watersheds that drain into Iowa excluding the Mississippi and Missouri rivers, which respectively form the eastern and western boundaries of the state. The characterization of the drainage network topology is a key ingredient in the construction of the WFDs developed in Section 3.3. It also supports the structure of the hydrologic modelling framework used in this chapter, which I explain in Section 3.4.1. I used data provided by the National Hydrograph Dataset Plus Version 2 (NHDPlusV2) (Horizon System Corporation, 2016) for the extraction of the drainage network. The digital elevation model (DEM) provided by NHDPlusV2 is the National Elevation Dataset (NED) with a resolution of 1-arc-second (approximately 30-m). This DEM is a resampling from the higher-resolution NED of 1/3-arc-second (approximately 10-m). To ensure hydrologic consistency and agreement with the observed drainage network, the NHDPlusV2 products include a flow accumulation grid and flow direction grid derived from a DEM "burned" with the existing hydrography.

The conversion from an accumulation grid to a meaningful drainage network is an ongoing research subject for hydrologists. The conventional approach is to use a unique contributing area or slope-area threshold, beyond which the hydrographical network is chosen (Sofia et al., 2011; Tarboton et al., 1991). Alternative approaches use the physical locations of the observed channel heads on the field (Orlandini et al., 2011), or morphological reasons to establish the headers of the drainage networks (Heine et al., 2004). I decided to use the traditional approach with a

46

unique contributing area threshold for the definition of the drainage network. I selected the threshold to maximize the drainage network density but at the same time to conserve an average hillslope area close to 0.4 km^2, which we can consider a reasonable scale for development of surface processes at hillslope scale (Quintero & Krajewski, 2018; Quintero et al., 2016). I selected a minimum contributing area threshold of 0.2 km^2 (222 cells), resulting in 409,756 stream links with an average length of 620 m and an average hillslope area of 0.41 km^2. Although the drainage network is sensitive to the threshold method, we can consider the drainage network derived with the previous parameters is accurate enough to capture the main structure of the spatial configuration of the drainage network across Iowa.

For the extraction of WFs, 147 watersheds with outlets at USGS stream gauges and drainage areas ranging from 6.6 km^2 up to 20,168 km^2 are selected. These watersheds are distributed throughout Iowa (Figure 3-1); therefore, we can expect to capture many different drainage structures and WF forms. This variability is illustrated by selecting six watersheds grouped in three pairs (Figure 3-1). Each pair represents a different spatial watershed scale with respect to drainage area *A*. I used these three pairs to show how watersheds with similar drainage area but a different drainage network structure (Figure 3-2) can be expected to have different peak flow responses.

The first pair has the same *A* of 521 km^2 and consists of for the watersheds of Salt Creek (USGS Code: 05452000) and Old Man's Creek (USGS Code: 05455100). Using the Bransby-Williams equation (Martin et al., 1996), the time of concentration is equal to 1 day for Salt Creek and 1.4 days for Old Man's Creek. These two watersheds were studied by Ayalew & Krajewski (2017), who found the watersheds are similar in terms of rainfall, land cover, and soil type characteristics, but different in terms of geometry of watershed shape. Old Man's Creek is

47

elongated compared to Salt Creek, which has a more circular shape. The second pair represents an increase in the spatial scale; the watersheds of the North Raccoon River (USGS Code: 05482300) and the Thompson River (USGS Code: 06898000) have A and time of concentration of 1,813 km^2 and 2 days, and 1,816 km^2 and 3.4 days, respectively. The third pair represents the largest spatial scale formed by the watershed of the Cedar River (USGS Code: 05464000) with A of 13,328 km^2 and time of concentration of 5.2 days, and the watershed of the Des Moines River (USGS Code: 05481300) with A of 14,120 km^2 and time of concentration of 8.3 days. Although there is a 6% difference in drainage area for the last pair, it is still reasonable to compare them. Note that the watershed form of the second and third pairs can be considered a rescaled version of the first pair of watersheds. For instance, the watersheds of Old Man's Creek, Thompson River, and Des Moines River are more elongated than their counterparts in terms of A which are the watersheds of Salt Creek, North Raccoon River, and Cedar River, respectively.

3.3. Width Function

The hydrologic literature includes a long list of descriptors of the morphometric variability of a watershed. For instance, Moussa (2003) shows that the geometric characteristics of a watershed represented by an equivalent ellipse can explain part of the peak flow variability for seven watersheds located in France. The study by Rai et al. (2017) compiles 36 morphometric parameters that had been previously explored by different authors (Black, 1972; Hack, 1957; Horton, 1932; Melton, 1957; Miller, 1953; Muelle, 1968; Schumm, 1956; Smart & Surkan, 1967; Strahler, 1964). The best known morphometric descriptors are the Bifurcation Ratio, Area Ratio, Length Ratio, Basin Length, Basin Width, Basin Parameter, Elongation Ratio, Stream Density, and Main Channel Sinuosity. Although these descriptors contain important geomorphological information about the watershed form and drainage network characteristics,

48

none of them provides complete information about the complex distribution of the drainage network within a watershed.

One of the most robust ways to represent the spatial distribution of a drainage network is by using the width function (WF) (Lee & Delleur, 1976). Several studies have confirmed the relation between WF and streamflow response (e.g., Vijay et al., 1988; Vijay et al., 1998; Ignacio Rodríguez-Iturbe, 2001; Mesa & Mifflin, 1986; Moussa, 1997; Naden, 1992; Rinaldo et al., 1991; Snell & Sivapalan, 1994; Troutman & Karlinger, 1985; Veitzer & Gupta, 2001). For instance, the WF is easily connected to the peak flow response using the geomorphological instantaneous unit hydrograph (GIUH) (Bras and Ignacio Rodriguez-Iturbe, 1989; Vijay et al., 1980; Kirshen & Bras, 1983; Rodríguez-Iturbe & Valdes, 1979; Rigon et al., 2001). The hydrograph generated by the GIUH under idealized conditions in which the surface water flows at constant speed without infiltration or other losses will match the WF form. This result demonstrates that the WF contains valuable information about the variability of peak flows from one watershed to another.

The WF gives the number of links located at a flow distance "x" from the outlet and represents the essential features of the drainage network structure within a watershed (Shreve, 1969). The WF has captured the interest of geomorphologists and hydrologists who study the interplay between drainage network structures and hydrologic responses. Various authors have focused on describing the WF using different approaches, such as iterated random pulse (Veneziano et al., 2000), deterministic fractal-multifractal (Puente & Sivakumar, 2003), and topologic and morphometric properties (Moussa, 2008), which have been used in similarity indices for channel network comparison and regionalization. For this study, I defined 34 WFDs which can be easily extracted from the WF. The 34 WFDs come from three different WF

49

formulations. The first type is based on the classic formulation of a geometric WF of stream links, and I refer to it as WF. The second type normalizes the WF with its base; I call this WF-at-site. The third type normalizes the WF with respect to a regional WF as a function of A. This last normalized WF is referred to as WF-at-region.

3.3.1. Descriptors of the WF

The WF of a watershed in a discrete case can be defined as

$$W(x) = Count(x - \Delta x < D(C_L) < x) \qquad \text{Equation 3-1}$$

where $Count(\mathrm{X})$ is the count of stream links that satisfy the condition X, C_L is the unique identification tag of a stream link, $D(C_L)$ is the distance from the link C_L to the outlet of the basin, x is the distance to evaluate the WF, and Δx is the width interval in x. The drainage network derived from NHDPlusV2 for the state of Iowa has an average stream link length of 620 meters; therefore, I decided to use a Δx equal to 1 km to provide a continuous representation of the count of stream links along the WF. Considering Δx equal to 1, and the distance x limited to the longest stream link distance to the outlet, the Equation 3-1 can be rewritten as

$$W(x) = Count(x - 1 < D(C_L) < x) \; with \; x \; \epsilon \; [1,2, \dots, D_B] \qquad \text{Equation 3-2}$$

where D_B is the longest stream link distance to the outlet. We can easily obtain the WF defined by Equation 3-2 from a histogram function with bin size equal to Δx and vector input equal to the distances of the stream links to the outlet in km. Characteristics such as the maximum of the WF are connected to streamflow response in idealized conditions (e.g., GUIH with instantaneous injection of rainfall and constant velocity on the stream channel). This type of connection suggests that other WF descriptors could provide more insights about the variability of the peak flow response. I defined 12 descriptors for the WF derived from the Equation 3-2 that we can considered representative features of the WF structure and that can be connected to peak flow

50

responses. Most of these descriptors are based on three characteristic points of the WF: (1) the maximum of the WF and its corresponding location; (2) the centroid of the WF and its corresponding location; and (3) the right tail of the WF where the WF is equal to zero (i.e., maximum distance to the outlet). Figure 3-3A shows the location of these critical points for the WFs of Salt Creek and Old Man's Creek.

The 12 descriptors are as follows: (1) the maximum of the WF (W_{max}); (2) the distance to the maximum ($D(W_{max})$); (3) the base of the WF (D_B), which is the same that the longest stream length in the watershed; (4) the mass of the WF (M), which can be interpreted as the area under the WF; (5) the center of mass in d-direction ($\bar{d}$); (6) the center of mass in W-direction ($\bar{W}$); (7) the volume of revolution with respect to the W-direction (V_W); (8) mass of WF from 0 up to the distance to the maximum ($M_{[0,D(W_{max})]}$); (9) mass of WF from the maximum up to the longest distance in the network ($M_{[D(W_{max}),D_B]}$); (10) number of stream links per kilometer (T_D); (11) rectangular area defined by the vertices (0,0) and ($D(W_{max}), W_{max}$) (M_{WD}); and (12) the rectangular area defined from the vertices (0,0) and ($\bar{d}, \bar{W}$) ($M_{\overline{WD}}$). For the mathematical formulation of these descriptors, see the Appendix.

The main purpose of the WFDs is to identify the variability of different drainage network structures that are not captured by *A*. For instance, the 12 WFDs above are shown in Table 3-1 for Salt Creek and Old Man's Creek. Both watersheds have the same *A* of 521 km^2 and approximately the same number of stream links. However, the WF for Salt Creek is close to a Gaussian shape, while the WF for Old Man's Creek has a rectangular shape. The strong difference in WF is evident in at least nine of the descriptors presented in Table 3-1. For instance, the descriptors W_{max}, $\bar{W}$, T_D, M_{WD}, and $M_{\overline{WD}}$ represent a relative difference between 29% and 58%, and the descriptors $D(W_{max})$, D_B, $\bar{d}$, V_W represent a relative difference between -

51

59% and -36% between the two watersheds. The mass of WF up to $D(W_{max})$ is almost the same; therefore, the differences between $M_{[0,D(W_{max})]}$ and $M_{[D(W_{max}),D_B]}$ are close to zero. Strong relative differences for the other two sets of watersheds are also found. For the North Raccoon River and Thompson River pair, the pattern is similar to that of the Salt Creek and Old Man's Creek pair, with the exception that the descriptors $M_{[0,D(W_{max})]}$ and $M_{[D(W_{max}),D_B]}$ show relative differences of 29% and -19%, respectively. The Cedar River and Des Moines River pair have a different pattern in the relative difference when compared to the other two pairs of watersheds; this is because the Des Moines River watershed has a higher number of links than the Cedar River watershed, which influences most of the descriptors defined in Table 3-1.

3.3.2. Descriptors of the WF-at-site

The 12 descriptors derived from the geometric WF illustrate the remarkable differences between watersheds with the same *A*, capturing part of the drainage network structure that is not represented by *A*. However, notice that most of these 12 descriptors have a strong dependence on *A*. For instance, if we increase *A*, the number of stream links (T_L) and D_B will increase as well. Therefore, the descriptors related to D_B, such as M, $\bar{d}$, $\overline{W}$, V_W, $M_{[D(W_{max}),D_B]}$, T_D, and $M_{\overline{WD}}$ will represent a dependence on *A*. The consideration of this scale dependence is important because in Section 3.4 the WFDs are used as explanatory variables in regional peak flow equations; strong dependence among explanatory variables will lead to collinearity problems in the regression analysis. Therefore, I decided to normalize the WF to avoid such collinearity problems. The distance of each stream link to the outlet ($D(C_L)$) is normalized with respect to D_B. Recall that C_L represents a tag to identify a specific channel, and if this tag starts from 1 with unitary increments up to T_L, the vector of the normalized distance of each stream link to the outlet can be defined as

$$D^{[N]}(C_L) = \frac{D(C_L)}{D_B}, with \ C_L \ \epsilon \ [1,2,3,...,T_L]$$

Equation 3-3

and the $D^{[N]}(C_L)$ can be used to estimate the normalized width function WF-at-site as

$$W\left(\frac{x}{D_B} = x^{[N]}\right) = Count\left(x^{[N]} - \frac{1}{D_B} < D^{[N]}(C_L) < x^{[N]}\right),$$

$$with \ x^{[N]} = [\frac{1}{D_B}, \frac{2}{D_B}, ..., 1]$$

Equation 3-4

where the super index N is referred to as Normalized. The WF-at-site provides a more robust structure without scale dependence because the base of the WF-at-site is equal to 1. The vector $D^{[N]}(C_L)$ will range from 0 to 1 for all the WFs-at-site. Therefore, I decided to extract 10 descriptors of the WF-at-site based on analogous quantities related to probability distributions, such as moments and quantiles over the vector $D^{[N]}(C_L)$. These statistics are the mean ($\overline{D^{[N]}}$), variance ($Var(D^{[N]})$), skewness ($Sk(D^{[N]})$), kurtosis ($K(D^{[N]})$), first quartile ($q_{25}(D^{[N]})$), second quartile or median ($q_{50}(D^{[N]})$), and third quartile ($q_{75}(D^{[N]})$). For this set of descriptors, I also included the descriptors $D_{W_{max}}^{[N]}, M_{[0,D_{W_{max}}^{[N]}]}^{[N]}$, and $M_{[D_{W_{max}}^{[N]},1]}^{[N]}$, which are related to the location of the maximum of WF-at-site. $D_{W_{max}}^{[N]}$ is the normalization of $D_{W_{max}}$ with respect to D_B, $M_{[0,D_{W_{max}}^{[N]}]}^{[N]}$ is the area of WF-at-site from 0 up to $D_{W_{max}}^{[N]}$, and $M_{[D_{W_{max}}^{[N]},1]}^{[N]}$ is the area of WF-at-site from $D_{W_{max}}^{[N]}$ up to 1. Figure 3-3B shows the location of the quartiles and $D_{W_{max}}^{[N]}$ for the WF-at-site of Salt Creek and Old Man's Creek. See the Appendix for the mathematical formulation of these descriptors.

Table 3-2 shows the values of these 10 descriptors of the WF-at-site for the six watersheds used as example cases. These descriptors show significant relative differences for each of the pairs of watersheds, proving that these WFDs can explain the WF variability without the scale dependence with *A*. For instance, the Salt Creek and Old Man's Creek pair has relative

53

differences between 4% and 113% for the descriptors of $\overline{D^{[N]}}$, $Sk(D^{[N]})$, $K(D^{[N]})$, $q_{25}(D^{[N]})$, $q_{50}(D^{[N]})$, and $M^{[N]}_{[D^{[N]}_{W_{max}},1]}$. For the descriptors $Var(D^{[N]})$, $q_{75}(D^{[N]})$, $D^{[N]}_{W_{max}}$, and $M^{[N]}_{[0,D^{[N]}_{W_{max}}]}$, the relative differences are between -85% and -6%.

3.3.3. Descriptors of the WF-at-region

The WF-at-site is convenient because the scale dependence on *A* is removed. However, valuable information about the WF is excluded because the base of the WF-at-site is always equal to 1. This means that the variability of the longest stream length in the watershed, which is a strong descriptor related to the watershed shape (Horton, 1932; Schumm, 1956), is removed. Hence, I proposed an approach to normalize the WF by removing the scale dependence with respect to *A* and at the same time preserving the differences in the base of the WF for the same spatial scale. This normalized WF is based on an average WF estimated over a region, based on analysis of WFs from several watersheds. I call this normalized Width Function the WF-at-region.

The average (expected) WF is defined by two variables, the expected base of the WF ($E(D_B)$) and the expected number of stream links per kilometer ($E(\overline{W})$); both variables are defined with respect to *A*. I estimated the values of $E(D_B)$ and $E(\overline{W})$ with independent regression analysis using the WFs for the 147 watersheds across Iowa. The left panel in Figure 3-4 shows results of these two regressions. Using these regressions, we can construct the expected WF for any site if we know the upstream area *A*. For instance, the right panel in Figure 3-4 shows the expected WF for Salt Creek and Old Man's Creek in green. These two expected WFs are equal because *A* is the same in both watersheds. The expected WF can be used as a reference to build the WF-at-region as

$$D^{[NS]}(C_L) = \frac{D(C_L)}{E(D_B)}$$
<div style="text-align: right">Equation 3-5</div>

$$W^{[NS]}(x) = \frac{W(x)}{E(\overline{W})}$$
<div style="text-align: right">Equation 3-6</div>

with $W(x)$ defined as Equation 3-2. The superscript NS denotes Normalized in Space. Figure 3-3C shows an example of the final form of WF-at-region for the watersheds of Salt Creek and Old Man's Creek. The reader should notice two characteristics about the WF-at-region. First, the bases of these WF at-region ($D_B^{[NS]}$) are different from 1. Second, the WF-at-region contains information about the residuals of the regression of $E(D_B)$ and $E(\overline{W})$ with respect to A. Therefore, the WF-at-region is independent of A and still represents variability over the $D_B^{[NS]}$. For instance, for Salt Creek the value of $D_B^{[NS]}$ is 0.7, which means that the D_B is 30% lower than the $E(D_B)$. On the contrary, Old Man's Creek has a $D_B^{[NS]}$ of 1.1; therefore, the D_B for Old Man's Creek is 10% bigger than the $E(D_B)$ for watersheds within Iowa with A equal to 521 km^2.

I described this WF-at-region in the same fashion as we did in the geometric WF. Three characteristic points are located on the WF-at-region: (1) peak of the WF-at-region; (2) centroid of the WF-at-region; and (3) extreme on the right tail of the WF-at-region. Figure 3-3C shows the location of these critical points for the WF-at-region of Salt Creek and Old Man's Creek. I extracted 12 descriptors from the WF-at-region: (1) the maximum of the WF-at-region ($W_{max}^{[NS]}$); (2) the distance to $W_{max}^{[NS]}$ ($D(W_{max}^{[NS]})$); (3) the area ratio (A_r) between the expected WF and the geometric WF; (4) the base of WF-at-region ($D_B^{[NS]}$); (5) the mass of WF at-region ($M^{[NS]}$); (6) mass of WF-at-region from 0 up to $D(W_{max}^{[NS]})$ ($M^{[NS]}{}_{[0,D(W_{max}^{[NS]})]}$); (7) mass of WF-at-region from $D(W_{max}^{[NS]})$ up to $D_B^{[NS]}$ ($M_{[D(W_{max}^{[NS]}),D^{[NS]}{}_B]}$); (8) the center of mass in d-direction ($\overline{d^{[NS]}}$); (9) the center of mass in W-direction ($\overline{W^{[NS]}}$); (10) volume of revolution with respect to W-direction

$(V_W^{[NS]})$; (11) rectangular area defined by the vertices (0,0) and $(D(W_{max}^{[NS]}), W_{max}^{[NS]})$ $(M_{WD}^{[NS]})$; and (12) the rectangular area defined by the vertices (0,0) and $(\overline{d^{[NS]}}, \overline{W^{[NS]}})$ $(M_{\overline{WD}}^{[NS]})$. See the Appendix for the mathematical formulation of these descriptors.

Table 3-3 shows the values of the 12 descriptors of the WF-at-region for the six watersheds used as example cases. The high relative differences in Table 3-3 verify that this approach can still be used to distinguish between WF structures without the scale dependence with *A* and preserves the variability in the bases of the WFs. For the pair of Salt Creek and Old Man's Creek, the descriptors of $W_{max}^{[NS]}$, $\overline{W^{[NS]}}$, $M_{WD}^{[NS]}$, and $M_{\overline{WD}}^{[NS]}$ represent relative differences between 32% and 57% and for the descriptors $D(W_{max}^{[NS]})$, $D_B^{[NS]}$, $\overline{d^{[NS]}}$, and $V_W^{[NS]}$, the relative differences are between -59% and -36%. The number of stream links and the mass of WF-at-region up to $D\left(W_{max}^{[NS]}\right)$ are almost the same in these two watersheds; therefore, the differences among descriptors $M^{[NS]}$, $M^{[NS]}_{[0,D(W_{max}^{[NS]})]}$, and $M_{[D(W_{max}^{[NS]}), D_B^{[NS]}]}$ are close to zero. These descriptors also show a significant relative difference for the pairs of North Raccoon and Thompson rivers, as well as the Cedar and Des Moines rivers.

3.4. Connections between WFDs and Peak Flows

In this section, I explore whether the WFDs can capture the variability of peak flows across the scales more accurately than can drainage area alone. I will explore two types of peak flows: (1) from hydrological simulations of rainfall-runoff events, and (2) quantiles derived from annual peak flow observations.

3.4.1. WFDs and Peak Flows from Rainfall-Runoff Events

I used the hydrologic distributed Hillslope Link Model (HLM) adopted at the Iowa Flood Center (IFC) for the state of Iowa (e.g., Krajewski et al., 2017; Mantilla & Gupta, 2005; Quintero

56

et al., 2016). The key features of HLM is the decomposition of the landscape into hillslope-channel-link components, and the use of the mass and momentum conservation equations at the hillslope-channel-link scale. The model describes changes in storage components using a system of non-linear ordinary differential equations that are solved using a parallel implementation of Runge-Kutta methods that allow for asynchronous integration (Small et al., 2013). This hydrologic model is ideally suited for our simulation exercise because it makes predictions of streamflow fluctuations for every link in the river network. The river network matches the NHDPlusV2 dataset. I used a simplified setup for the rainfall-runoff events with a constant runoff coefficient of 0.3, constant hillslope overland flow velocity of 0.01 m/s, constant subsurface flow velocity of 0.005 m/s, and nonlinear streamflow routing described by Quintero et al. (2016). The initial states of the model are all equal to zero, which means that channel discharge, water ponded on the hillslope surface, and effective water depth in the hillslope subsurface are initialized to zero. The interested reader can refer to Quintero et al. (2016) for further details of the HLM construction.

I applied uniform rainfall inputs with constant intensity of 6.35 mm/hr (1/4 inch per hour), and different rainfall durations of 5 min, 15 min, 30 min, 1 hr, 3 hr, 6 hr, 12 hr, 1 day, 2 days, and 10 days. The total depth for each rainfall duration is 0.53, 1.58, 3.17, 6.35, 19.05, 38.10, 76.20, 152.40, 304.80, and 1,524.00 mm, respectively. I conducted these hydrologic simulations for the entire state of Iowa, which includes the 147 watersheds of interest. The peak flows are extracted from the hydrographs obtained from the hydrologic simulations and used them as response variables for a posterior regression analysis with respect to the 34 WFDs and A. I used a multiple linear regression model with Ordinary Least Square (OLS) regression with a maximum of three explanatory variables to avoid overfitting. In addition, an exhaustive search

method to select the final set of explanatory variables based on the Akaike Information Criteria with correction (AICc) is used. The selected explanatory variables must be statistically significant at the 95% confidence level. I investigated the correlation between the explanatory variables to assess potential multicollinearity problems. I used a Variance Inflator Factor (VIF) greater than 3 to remove variables with strong correlations.

3.4.1.1. Results and Discussions: WFDs and Peak Flows from Rainfall-Runoff Events

For uniform rainfall events over a watershed, rainfall duration controls the proportion of the watershed that is contributing to the peak flow response. This control can be understood in terms of two end members. The first end member occurs when the rainfall duration is greater than the time of concentration of a watershed. In this case, the entire watershed contributes to the peak flow response, and A is sufficient to explain the regional peak flow variability. The second end member occurs when the rainfall duration is instantaneous; here, the dominant control in the peak flow response is the structure of the drainage network (Mandapaka et al., 2009). In fact, for the case of a constant streamflow-channel velocity and without losses by infiltration or evaporation, the shape of the streamflow hydrograph is controlled by the WF. Therefore, the hydrologic simulations with different rainfall durations capture the variability between these two end members in which the drainage network structure and A have a role in controlling the peak flow response. Figure 3-5 shows the hydrographs obtained for four different rainfall durations over the six watersheds used as example cases. Note that the two hydrographs of each panel come from watersheds with similar A. These simulated hydrographs show that for rainfall durations shorter than the time of concentration, the drainage network influences the regional peak flow variability. However, the hydrographs get closer as the rainfall duration increases, which means that the control of the drainage network structure over the peak flow variability is

58

being reduced and the *A* is more dominant. Figure 3-6 quantifies the relative differences between the peaks of the hydrographs. For the Salt Creek and Old Man's Creek pair, and the North Raccoon River and Thompson River pair, we saw a clear decreasing trend of the relative difference with respect to the increase of the rainfall duration. For instance, the Salt Creek and Old Man's Creek pair starts with a relative difference of 125% in the peak flow for rainfall duration of 5 minutes, and it reaches 1% for rainfall duration of 5 days. The Cedar River and Des Moines River pair shows a different trend in which the relative difference remains close to the value of 30% for rainfall durations from 5 minutes up to 2 days. I presume that this difference remains around 30% because the rainfall duration from 5 minutes up to 2 days does not represent a large variability with respect to the longer times of concentration of 5.2 days for Cedar River and 8.3 days for Des Moines River. Note that for 5 and 10 days, the Des Moines River has a bigger peak flow, and therefore the relative difference is around -6%. This makes sense because most of the watershed is contributing to the peak flow, and the Des Moines River has a bigger *A*.

Figure 3-7 shows the peak flows from the simulation with rainfall durations of 30 minutes, 3 hours, 12 hours, and 5 days for the 147 sites across Iowa. These simulations reveal the strong relation between *A*, rainfall duration, and drainage network structure. Figure 3-7 shows the scale break of peak flows as a function of the rainfall duration. The scale break is explained by the previous argument that if the rainfall duration is larger than the time of concentration, drainage area is enough to explain the peak flow response in a regional domain. This argument is well illustrated for the peak flows with rainfall duration of 5 days, in which the drainage area is enough to explain the regional peak flow variability. However, for shorter rainfall durations such as 12 hours and watersheds with times of concentration longer than 12 hours, the drainage network will start to influence in the peak flow response. Therefore, for these cases, the regional

peak flow variability is not explained just by A. Visually, we found that the scale break is 500, 300, and 100 km^2 for the rainfall durations of 12 hours, 3 hours, and 30 minutes, respectively. The structure of the drainage network of each watershed causes the peak flow variability after this scale break. These results are consistent with previous findings reported by Mandapaka et al. (2009).

I argue that the peak flow variability after the scale break can be explained using WFDs. Regression analysis results support this statement. I found that the A, $q_{25}(D^{[N]})$ and $D_B^{[NS]}$ explain with much greater detail the variability of the regional peak flow response, rather than the use of the drainage area alone. Figure 3-8 shows the results of the regression model using only A, and the model using A, $q_{25}(D^{[N]})$ and $D_B^{[NS]}$ as explanatory variables. The model that includes WFDs demonstrates a significant improvement in capturing the regional peak flow variability, with a reduction of more than half for the Root Mean Square Error (RMSE). The model selection criteria AICc for the regression analysis after the scale break support the finding that the model with WFDs contains more information than the model using only A.

For a complete examination of the role of the different WFDs in the regression models, Figure 3-9 shows the RMSE for some combinations of one, two, and three explanatory variables in the construction of the regional regression models for the peak flow responses for a rainfall duration of 12 hours. For the model with two explanatory variables, I fixed the drainage area A in addition to a second explanatory variable; and for the model with three explanatory variables, I fixed A and $D_B^{[NS]}$ in addition of a third explanatory variable. For one explanatory variable, we can observe that the A, M, and $M_{\overline{WD}}$ have the lower RMSE of 156 m^3/s. For two variables, the RMSE for the model using A and $D_B^{[NS]}$ decreases up to 80 m^3/s; and for three variables, the

60

model with A, $D_B^{[NS]}$, and $q_{25}(D^{[N]})$ produces a reduction in the RMSE up to 58 m³/s. The selection of the best model was based on the AICc.

The finding in this regression analysis suggests that the descriptors $q_{25}(D^{[N]})$ and $D_B^{[NS]}$ contain valuable information on the WF, which is connected to the peak flow response. $D_B^{[NS]}$ can be interpreted as the residual of the Hack's law (Hack, 1957). In fact, I noticed that we can reconstruct a simplified version of the WF formed by two blocks using the A, $q_{25}(D^{[N]})$, $D_B^{[NS]}$, T_L, and the $E(D_B)$ obtained from the regional regression between D_B and A. This reconstructed WF has a base estimated from the product of $D_B^{[NS]}$ and $E(D_B)$. The total area of WF is equal to T_L, and this area can be distributed into two blocks delimited by $q_{25}(D^{[N]})$, with the first block having 25% of T_L, and the second block 75% of T_L. Examples of the reconstructed WF for the six watersheds used as example cases are shown in Figure 3-10.

3.4.2. WFDs and peak flow quantiles

Now, I investigate the connections between peak flow quantiles and WFDs. I selected 94 gauges with more than 30 years of continuous records from the initial 147. For each one of these gauges, I estimated peak flow quantiles using the USGS estimation procedure explained in Bulletin 17C (England et al., 2015). This procedure assumes a Log Pearson Type III distribution for the data and recommends use of the Expected Moment Algorithm (EMA) including historical records and at-station skew to determine distribution parameters. I excluded sites with regulation or diversion of any kind. I used the estimated peak flow quantiles to perform a regional regression analysis with respect to our 34 WFDs and A for two different regions. First, I selected a region that includes the 94 selected gauges for the entire state of Iowa. Second, I used a sub-region that includes the Iowa River Basin (see Figure 3-11), which contains only 25 peak flow

gauges with more than 30 years of records. I did this to determine if homogeneity in the region has a significant bearing in the results. The Iowa River Basin is chosen because it is contained in the Flood Region 2 of Iowa as defined by Eash et al. (2013), which to some extent, can be considered as a homogeneous in terms of hydrologic properties. The regression analysis procedure was the same as the one described in Section 3.4.1, but using the peak flow quantiles as dependent variables and the 34 WFDs and *A* as explanatory variables.

3.4.2.1. Results and Discussions: WFDs and Peak Flow Quantiles

The regional regression analysis for peak flow quantiles indicated that the WFDs explored in this study do not explain well the variability of peak flow quantiles in a regional domain. The best model selected in the exhaustive search with the different 34 WFDs uses only *A* as an explanatory variable (see Figure 3-12). We found this result for both the entire state of Iowa and for the Iowa River Basin. Iowa has large variability in soil types, land uses, and hydrologic responses (Eash et al., 2013). For that reason, I selected the Iowa River Basin to reduce these heterogeneities, and to be able to capture most of the influence of the drainage network structure over the response of peak flow quantiles. However, the regression analysis results demonstrate that the WFDs do not explain well the regional variability of the peak flow quantiles. We can rationalize this outcome as follows. First, the peak flow quantiles for different watersheds with the same probability of exceedance do not always come from the same rainfall-runoff events, therefore the connection of peak flow response through the drainage network is lost. Second, the estimation of peak flow quantiles is subjected to sampling errors (number of peak flow observations) and epistemic errors (e.g. selection of underlaying peak flow distribution). Third, physical variables such as soil type, land use, basin slope, and rainfall variability that also influence in the peak flow response are not captured by the WFDs. These

results support the notion that the peak flow quantiles are a statistical characterization and are disconnected from the physical processes controlling flood-generating rainfall-runoff events (Dawdy et al., 2012; Furey et al., 2016; D. Wright et al., 2014).

The hypothesis that WFDs would provide a more powerful descriptor for peak flow data was based on the theoretical evidence shown in Section 3.4.1 and the analysis of at-site records for pairs of gauged sites with similar area in Iowa. For instance, Figure 3-13 shows the peak flow quantiles for the six watersheds used as example cases. The watershed of Salt Creek has larger peak flows for every quantile than those for Old Man's Creek. This agree with the pattern observed in the results of hydrologic simulations with rainfall duration of less than 12 hours (top panel of Figure 3-5). It also agrees with results presented by Ayalew & Krajewski, (2017) indicating that because these two watersheds have similar rainfall, soil properties, and land use, the variations in the drainage network topology are the dominant factor generating differences in peak flow quantiles between the two watersheds. However, this is not true for results obtained for the other two pairs of watersheds. For instance, the Thompson River has larger peak flows quantiles than the North Raccoon River for all considered probabilities of exceedance, although we might expect otherwise. This result suggests that the drainage network is not the dominant factor over the regional variability of peak flow quantiles. In fact, there are larger differences in soil type and land use for the two watersheds. For instance, the North Raccoon River watershed is covered by the soil region number 4 (Loamy Wisconsin Glacial Till), and the Thompson River watershed is covered by the soil regions number 15 (Loess Ridges/Glacial Till-Southwest Iowa) and number 21 (Loess Ridges/Glacial Till Sideslopes) (Fenton et al., 1971). Another important factor to distinguish these two watersheds is drainage control by subsurface drainage systems (tiling) and spatial distribution of small dams. Some work suggests that for storms with higher

rainfall intensities, surface runoff is dominant and the tiles are not contributing significantly to the peak flows (Sloan, 2013). However, the influence of tile systems on the peak flow response is not yet completely understood. These subsurface drainage systems are incorporated into the soil to create more productive farmland, reducing the excess of water ponded over the croplands and in the unsaturated root zone. The tiles change the timing of the water delivery from hillslopes to streams. About 30% of Iowa is tiled (Schilling & Helmers, 2008). According to the Iowa Department of Natural Resources, the North Raccoon River watershed is part of a region completely controlled by tile systems managed by drainage districts. In contrast, there are no drainage districts in the Thompson River watershed. In addition, the spatial distribution of small dams could contribute to the difference of peak flow quantiles between watersheds. The National Inventory of Dams shows that the number of small dams between both watersheds is drastically different, with 4 and more than 100 small dams for the North Raccoon River and Thompson River, respectively. The difference in peak flow quantiles can be also attributed to the climatology in the North Raccoon River and Thompson River watersheds. For example, for different return periods, the rainfall frequency atlas for the Midwest shows that the North Raccoon River watershed has about 10% lower rainfall intensities than the Thompson River watershed does (Huff & Angel, 1992).

At the larger scale of the watersheds of Cedar River and Des Moines River, we could initially expected higher peak flow quantiles in the latter because of its larger drainage area. However, the results show that the peak flows quantiles in Cedar River are higher than for Des Moines River. I presume that the structure of the drainage network is not controlling the difference in peak flows for these two watersheds. Note that overall, the Des Moines River basin is elongated, but if we remove the upstream area from the "bottleneck," the shape of this

watershed is closer to circular. For this reason, the first part of the WF of Des Moines River is close to that of Cedar River. Regarding the anthropogenic factors, the subsurface drainage system is different for these two watersheds. The Des Moines River basin has extensive tile systems, while the Cedar River basin does not. I should point out, though, that in the past 10 years there has been an "explosion" of tiling taking place in Iowa without the establishment of new drainage districts. Despite the difference in tile systems between these watersheds, we can presume that rainfall variability is the dominant factor causing the large difference in the peak flow quantiles between them. At this large scale, we are unlikely to see rainfall events that cover the entire watershed. Therefore, rainfall characteristics such as direction, intensity, duration, and location in the watershed need to be studied together to understand the peak flow response at these large scales.

3.5. Conclusions

I showed that the WF is a powerful geomorphologic descriptor that allows researchers to distinguish different drainage network structures and their influence on peak flow magnitude. This is illustrated using three pairs of watersheds. While these basins have similar drainage area A, their specific drainage network structures influence peak flow response in a predictable way. I extracted 34 WFDs that provide contrasting measures from one catchment to another. The regression analysis between peak flows generated during rainfall-runoff events under simplified conditions indicates that A, $q_{25}(D^{[N]})$ and $D_B^{[NS]}$ are the descriptors that explain the most variance in the regional peak flow variability. I used this result to justify the use of WFDs in regional equations to estimate peak flows quantiles. I found, however, that the WFDs did not sufficiently explain the regional variability of the peak flow quantiles. I concluded that peak flow quantiles are difficult to explain from geomorphologic controls such as the drainage network

because these estimates are the result of a statistical characterization and are related to a more complex physical flood-generation processes, that cannot be well-explained by drainage network morphology/topology alone, whereas peak flow obtained from simulated uniform rainfall-runoff events is controlled by the drainage network structure. In overall, the results presented in this chapter will help us assess future investigations of the connections between WFDs and peak flows from observed rainfall-runoff events; and also, to narrow the number of variables influencing regional peak flow quantiles regressions. Further investigation needs to be done to understand the role of the sampling errors and epistemic errors in the estimation of peak flow quantiles in order to evaluate the benefit of using WFDs in the regional flood frequency equations. This last aspect is explored in the following chapter.

Table 3-1. Descriptors of the geometric WF for the six watersheds used as example cases. RD: Relative Difference between the pair.
#: Number of stream links

Name	Salt Creek	Old Man's Creek	RD (%)	North Raccoon River	Thompson River	RD (%)	Des Moines		
							Cedar River	River	RD (%)
USGS Code	5452000	5455100		5482300	6898000		5464000	5481300	
A [km^2]	521	521	0	1813	1816	0	13328	14121	-6
W_{max} [#]	80	34	58	112	56	50	195	217	-11
$D(W_{max})$ [km]	29	46	-59	60	75	-25	213	151	29
D_B [km]	48	68	-42	97	173	-78	288	482	-67
M [#]	1295	1307	-1	4671	4374	6	32484	35349	-9
$\bar{d}$ [km]	25	34	-36	57	92	-63	146	210	-44
$\bar{W}$ [#]	22	11	50	32	15	53	65	50	24
V_W [$\# \cdot km$]	2.E+05	3.E+05	-37	2.E+06	3.E+06	-53	3.E+07	5.E+07	-57
$M_{[0,D(W_{max})]}$ [#]	918	927	-1	2452	1744	29	25944	13106	49
$M_{[D(W_{max}),D_B]}$ [#]	377	380	-1	2219	2630	-19	6540	22243	-240
T_D [#/km]	27	19	29	48	25	47	113	73	35
M_{WD} [$\# \cdot km$]	2320	1564	33	6720	4200	38	41535	32767	21
$M_{\overline{WD}}$ [$\# \cdot km$]	550	374	32	1824	1380	24	9490	10500	-10

Table 3-2. Descriptors of the WF-at-site for the six watersheds used as example cases. RD: Relative Difference between the pair.

Name	Salt Creek	Old Man's Creek	RD (%)	North Raccoon River	Thompson River	RD (%)	Cedar River	Des Moines River	RD (%)
USGS Code	5452000	5455100		5482300	6898000		5464000	5481300	
$\overline{D^{[N]}}$	0.522	0.501	4	0.583	0.535	8	0.505	0.436	14
$Var\left(D^{[N]}\right)$	0.038	0.070	-85	0.047	0.064	-36	0.058	0.059	-1
$Sk\left(D^{[N]}\right)$	-0.264	0.034	113	-0.363	0.000	100	0.037	0.565	-1444
$K\left(D^{[N]}\right)$	2.798	1.815	35	2.236	2.002	10	1.958	2.361	-21
$q_{25}\left(D^{[N]}\right)$	0.391	0.279	29	0.420	0.345	18	0.301	0.262	13
$q_{50}\left(D^{[N]}\right)$	0.548	0.494	10	0.618	0.535	13	0.498	0.379	24
$q_{75}\left(D^{[N]}\right)$	0.640	0.730	-14	0.760	0.735	3	0.710	0.603	15
$D_{W_{max}}^{[N]}$	0.604	0.676	-12	0.619	0.434	30	0.740	0.313	58
$M_{[0,D_{W_{max}}^{[N]}]}^{[N]}$	0.647	0.682	-6	0.500	0.386	23	0.793	0.365	54
$M_{[D_{W_{max}}^{[N]},1]}^{[N]}$	0.353	0.318	10	0.500	0.614	-23	0.207	0.635	-206

Table 3-3. Descriptors of the WF-at-region for the six watersheds used as example cases. RD: Relative Difference between the pair.

Name	Salt Creek	Old Man's Creek	RD (%)	North Raccoon River	Thompson River	RD (%)	Cedar River	Des Moines River	RD (%)
USGS Code	5452000	5455100		5482300	6898000		5464000	5481300	
$W_{max}^{[NS]}$	3.980	1.692	57%	3.478	1.738	50%	2.850	3.103	-9%
$D\left(W_{max}^{[NS]}\right)$	0.460	0.729	-59%	0.437	0.546	-25%	0.448	0.307	32%
A_r	1.022	1.031	-1%	1.058	0.989	6%	0.999	1.026	-3%
$D_B^{[NS]}$	0.761	1.078	-42%	0.707	1.260	-78%	0.606	0.979	-61%
$M^{[NS]}$	1.022	1.031	-1%	1.058	0.989	6%	0.999	1.026	-3%
$M_{\left[0,D\left(W_{max}^{[NS]}\right)\right]}^{[NS]}$	0.724	0.731	-1%	0.555	0.394	29%	0.798	0.381	52%
$M_{\left[D\left(W_{max}^{[NS]}\right),D_B^{[NS]}\right]}^{[NS]}$	0.297	0.300	-1%	0.502	0.595	-18%	0.201	0.646	-221%
$\overline{d^{[NS]}}$	0.397	0.540	-36%	0.412	0.673	-63%	0.306	0.427	-39%
$\overline{W^{[NS]}}$	1.070	0.533	50%	1.006	0.469	53%	0.957	0.714	25%
$V_W^{[NS]}$	2.549	3.498	-37%	2.739	4.182	-53%	1.924	2.753	-43%
$M_{WD}^{[NS]}$	1.830	1.234	33%	1.521	0.950	38%	1.278	0.952	26%
$M_{\overline{WD}}^{[NS]}$	0.425	0.288	32%	0.415	0.316	24%	0.293	0.305	-4%
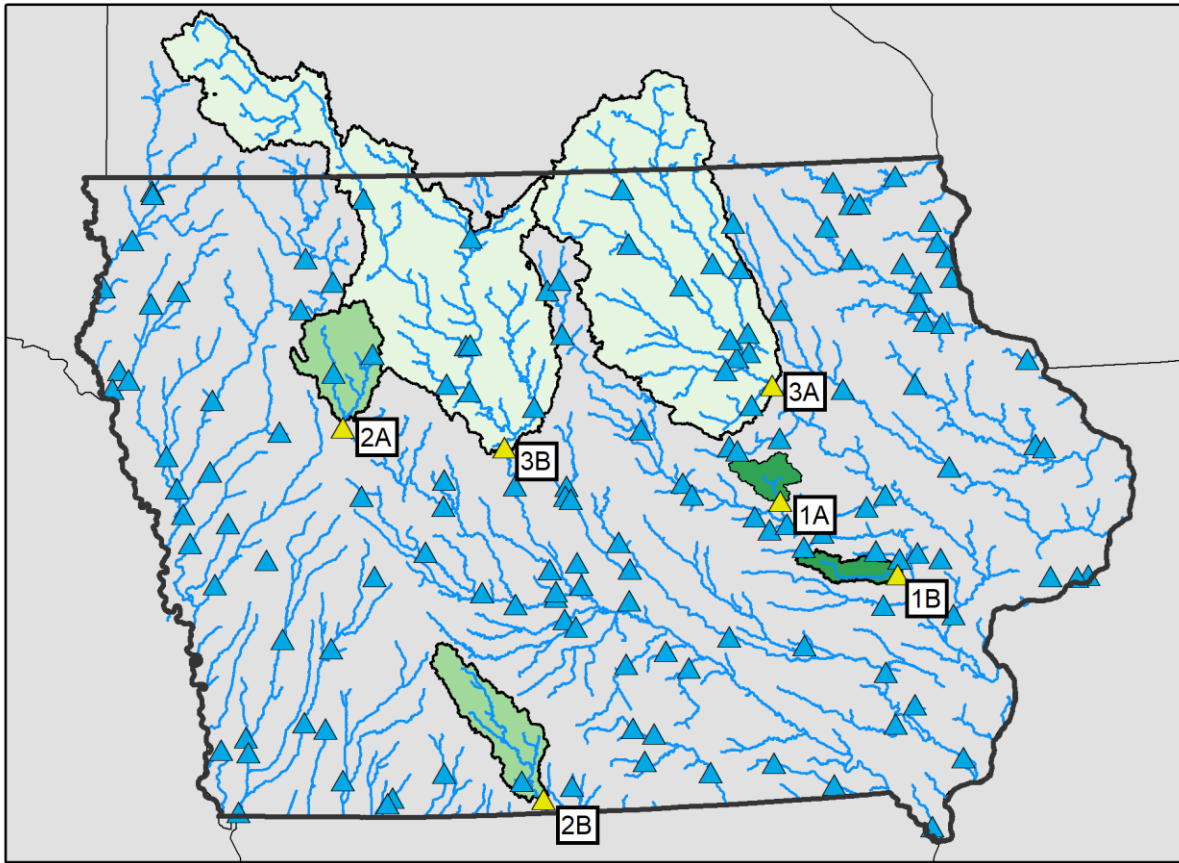
Figure 3-1. Location of the 147 peak flow gauges (triangles) used to delineate the watersheds in the characterization of WFs for the state of Iowa. The yellow triangles are the outlets of the six watersheds used as example cases for three different spatial scales. Small scale: 1A) Salt Creek – USGS Code 05452000 and 1B) Old Man's Creek – USGS Code 05455100. Medium scale: 2A) North Raccoon River – USGS Code 05482300 and 2B) Thompson River – USGS Code 06898000. Large scale: 3A) Cedar River – USGS Code 05464000 and 3B) Des Moines River – USGS Code 05481300. The drainage network in the figure is for spatial reference only.
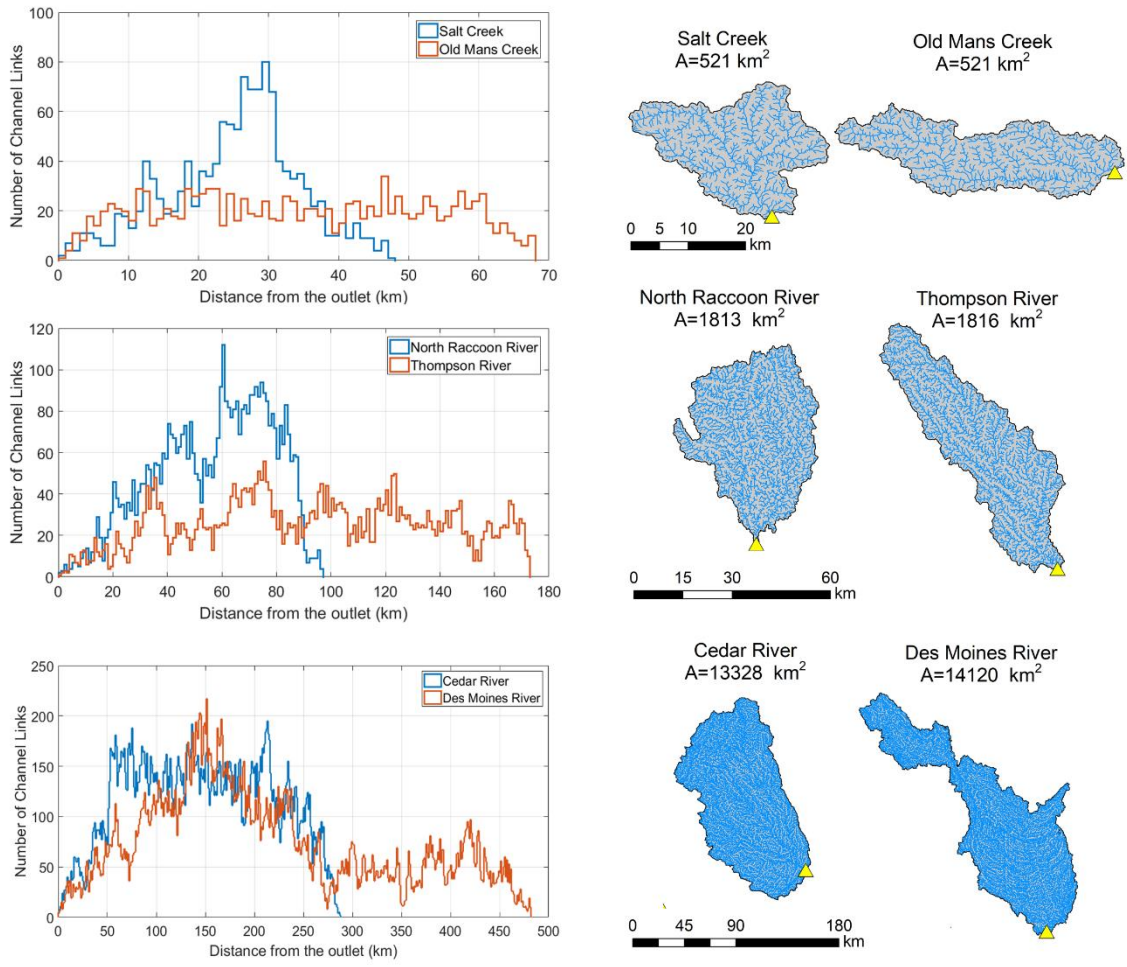
Figure 3-2. WFs for the six watersheds used as illustration cases. The watersheds have the drainage network derived from the NHDPlusV2 product.

www.manaraa.com
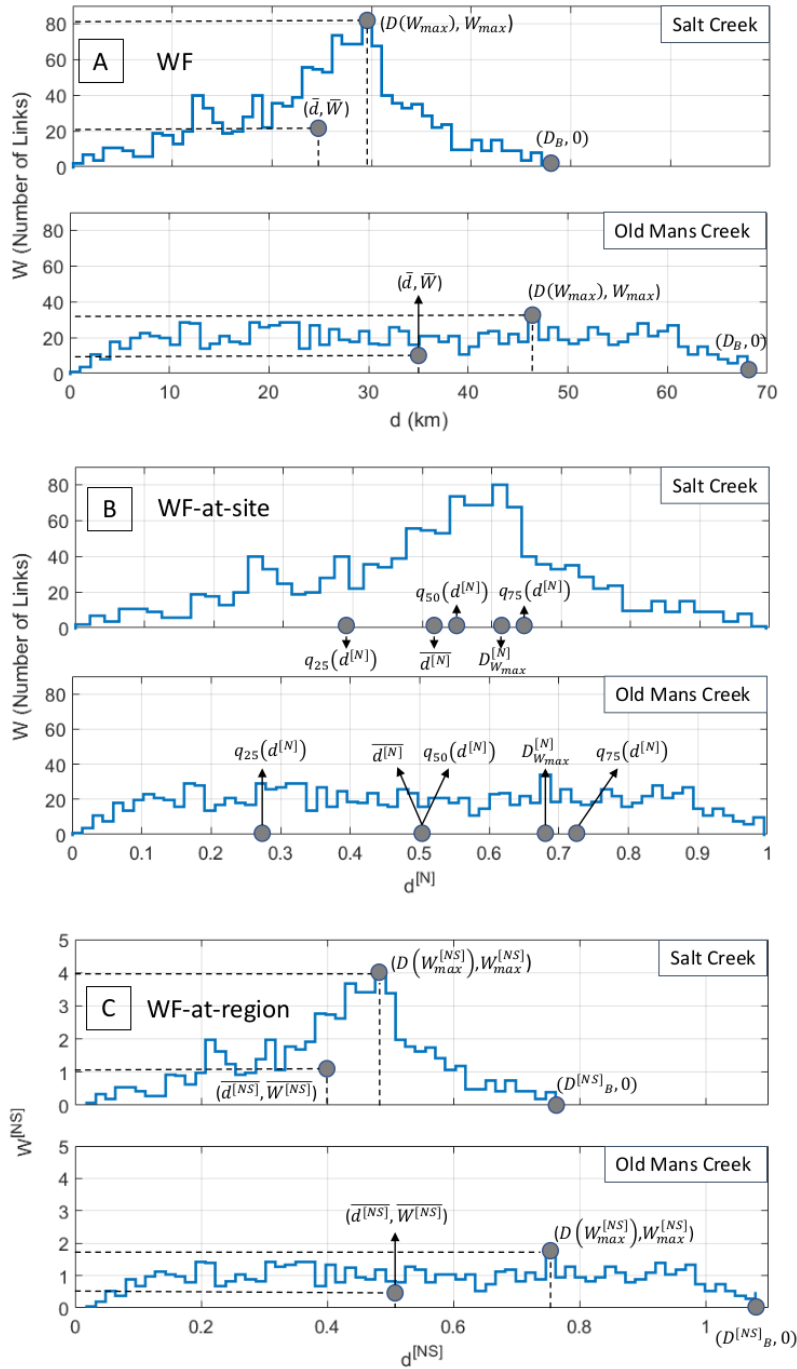
Figure 3-3. Location of the characteristic points used for the construction of WFDs for the watersheds of Salt Creek and Old Man's Creek: A) geometric WF, B) WF-at-site, and C) WF-at-region.

72
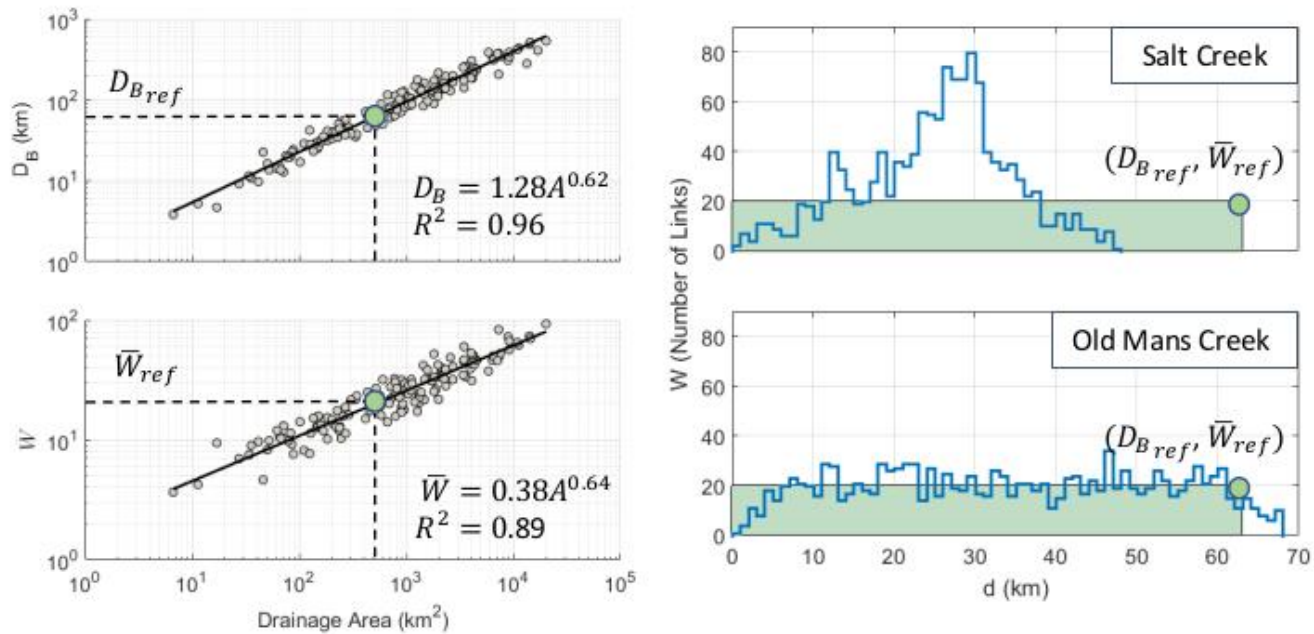
Figure 3-4. Construction of the expected WF based on the power law regression (left panel) of D_B and $\overline{W}$ with respect to the drainage area. The green rectangles in the right panel represent the expected WF obtained from this regression. The blue line is the observed WF.
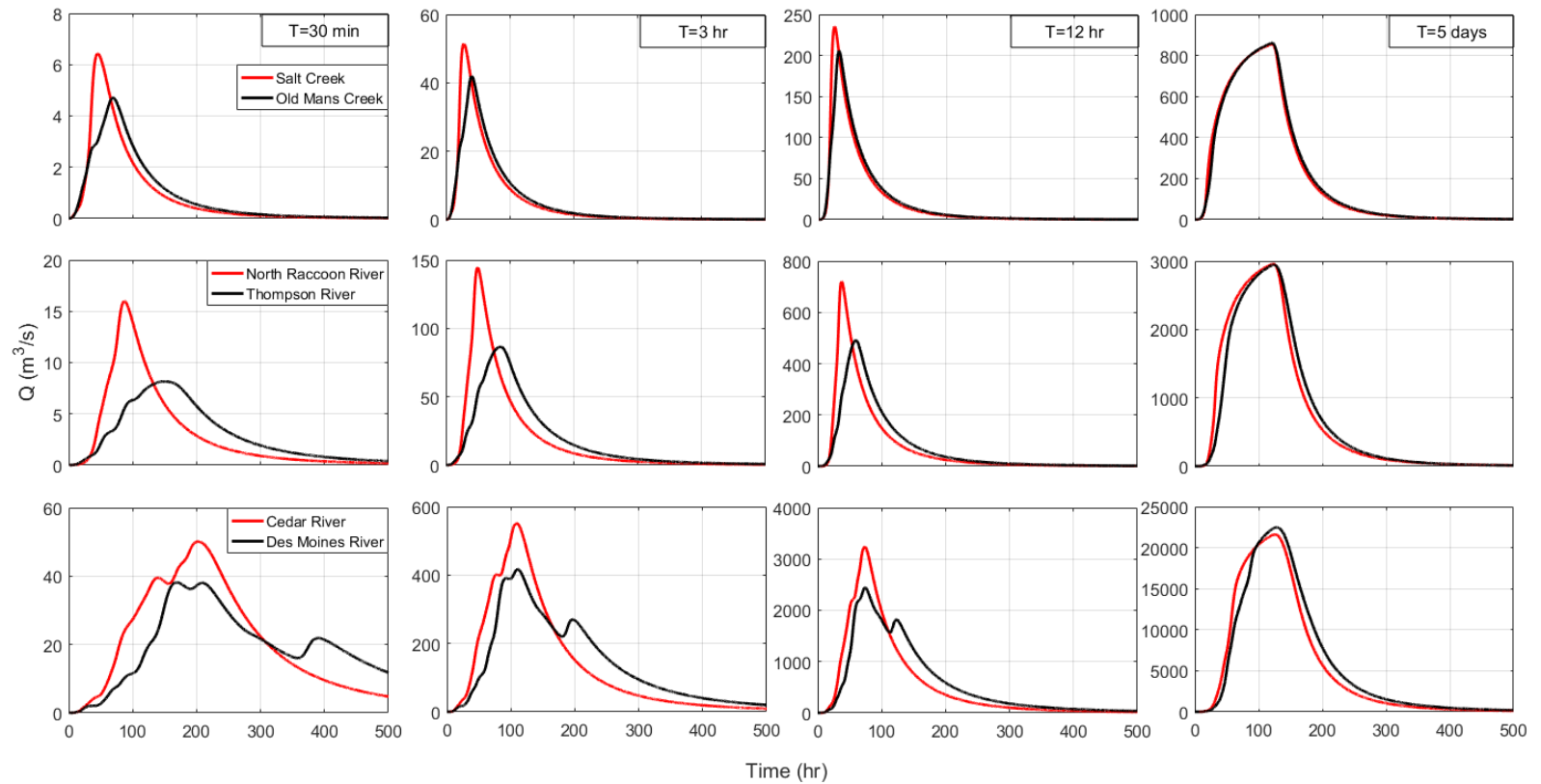
Figure 3-5. Hydrographs for the six watersheds with rainfall duration of 30 minutes, 3 hours, 12 hours, and 5 days. Each row represents an illustration case, and each column represents a rainfall duration with a constant rainfall intensity of 6.35 mm/hr (0.25 in/hr).
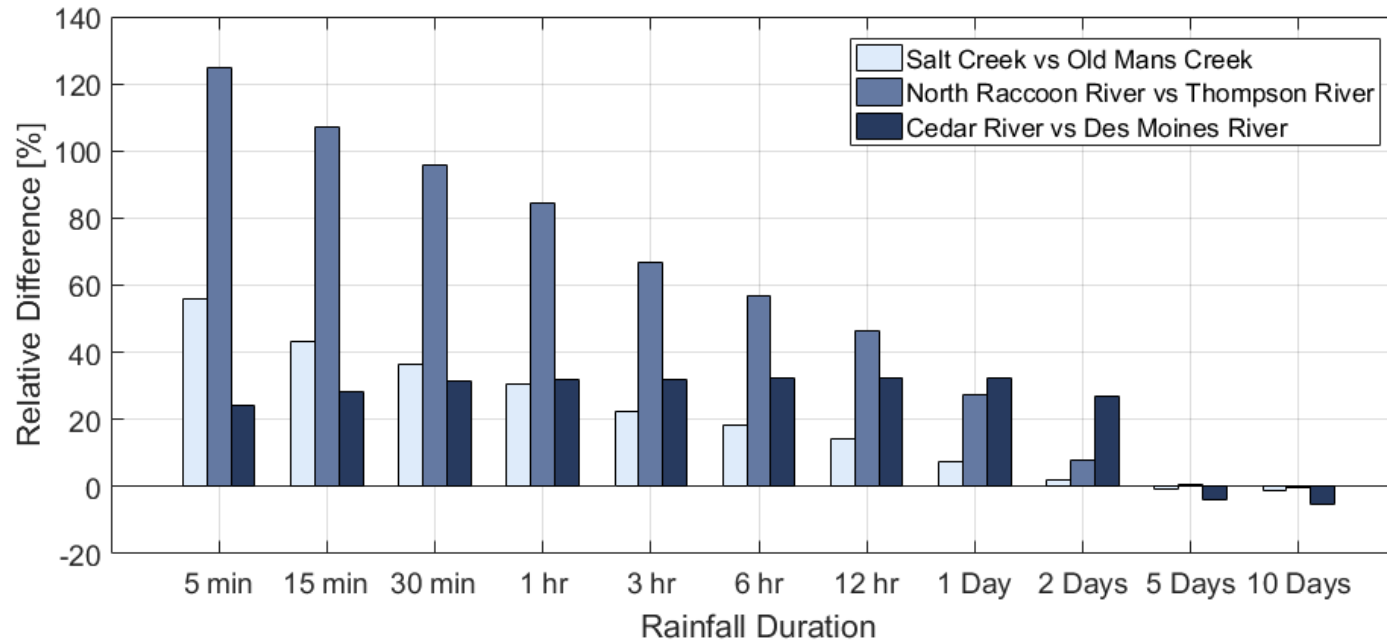
Figure 3-6. Relative difference of maximum discharge obtained from the hydrologic simulations for the three illustration cases.
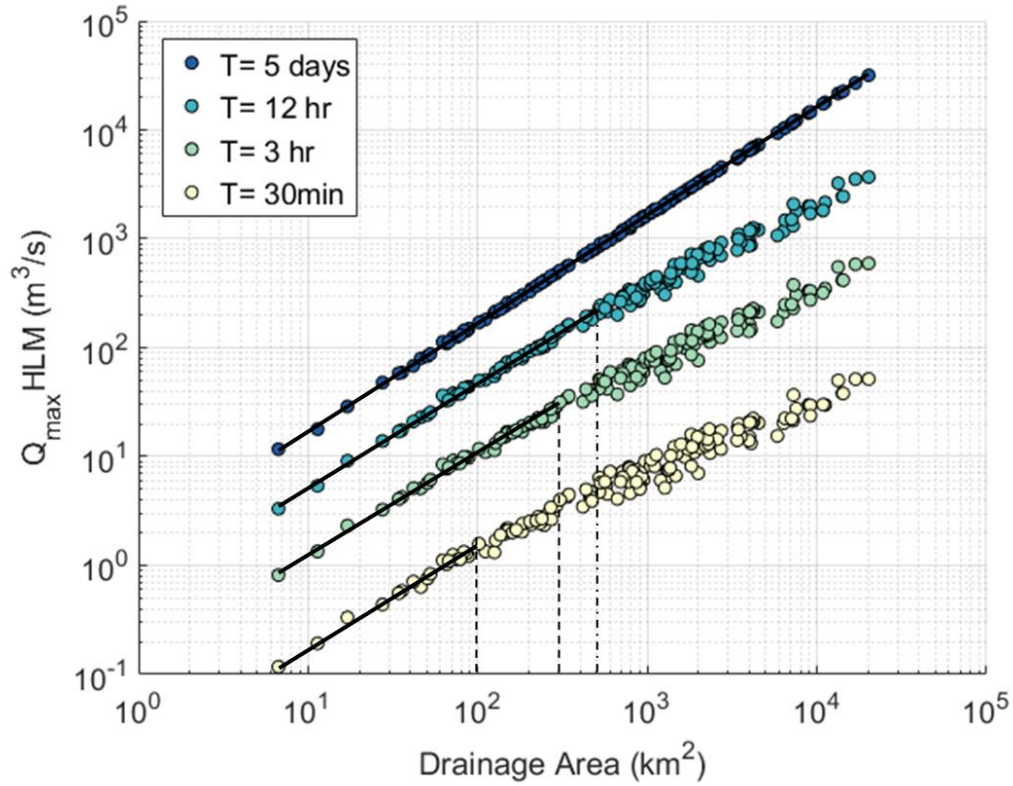
Figure 3-7. Comparison of the maximum discharge obtained from the hydrologic simulations on the 147 sites and 4 different rainfall durations. The dashed lines represent the break in scale in which the variability of peak flows is not fully explained by the drainage area.
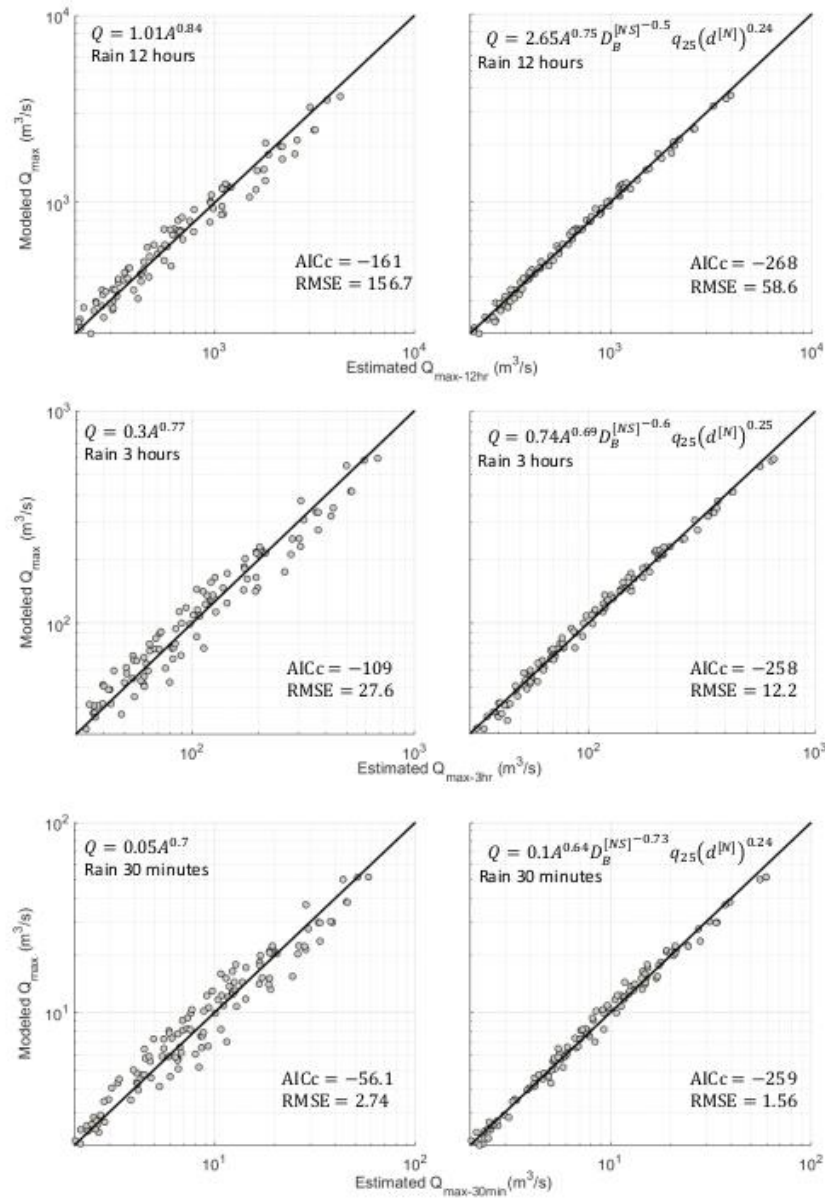
Figure 3-8. Comparison of the observed maximum discharge (based on hydrologic simulations) and the estimated maximum discharge (based on regression analysis) for rainfall durations of 30 minutes, 3 hours, and 12 hours. The left panels show the regression results using only the drainage area as an explanatory variable. The right panels use the A, $q_{25}(d^{[N]})$, and $D_B^{[NS]}$ as explanatory variable.
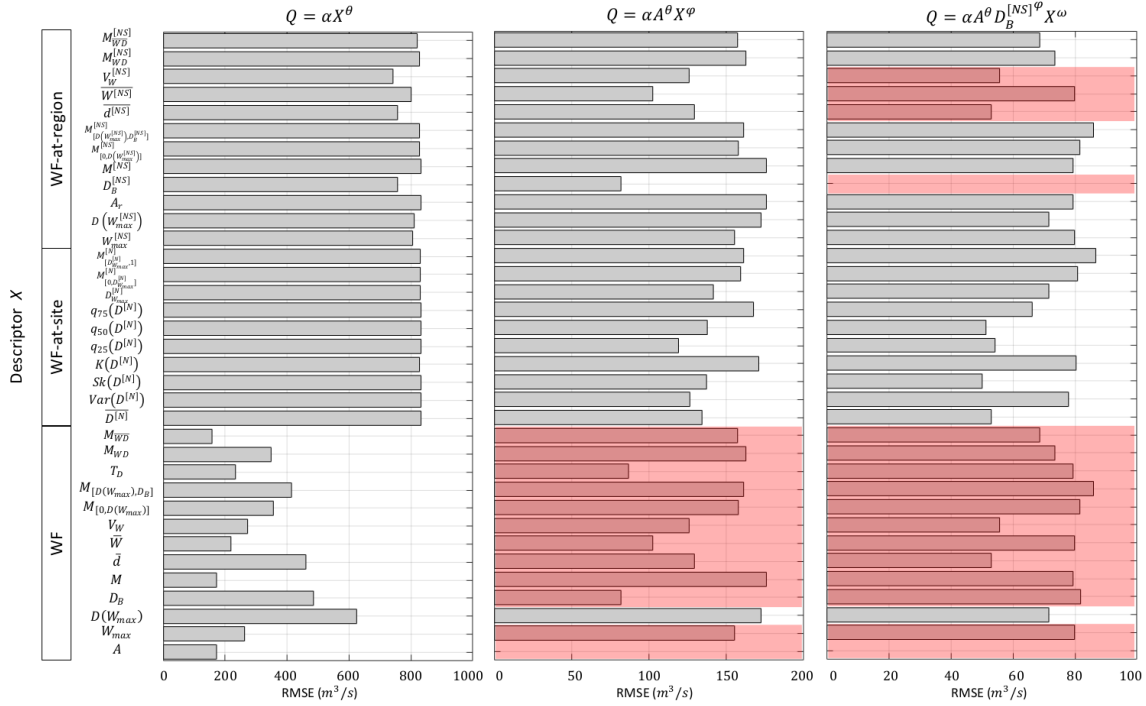
Figure 3-9. RMSE for some combinations of one, two, and three explanatory variables in the construction of the regional regression models for the peak flow responses from rainfall duration of 12 hours. The shaded red regions represent models with VIF greater than 3.
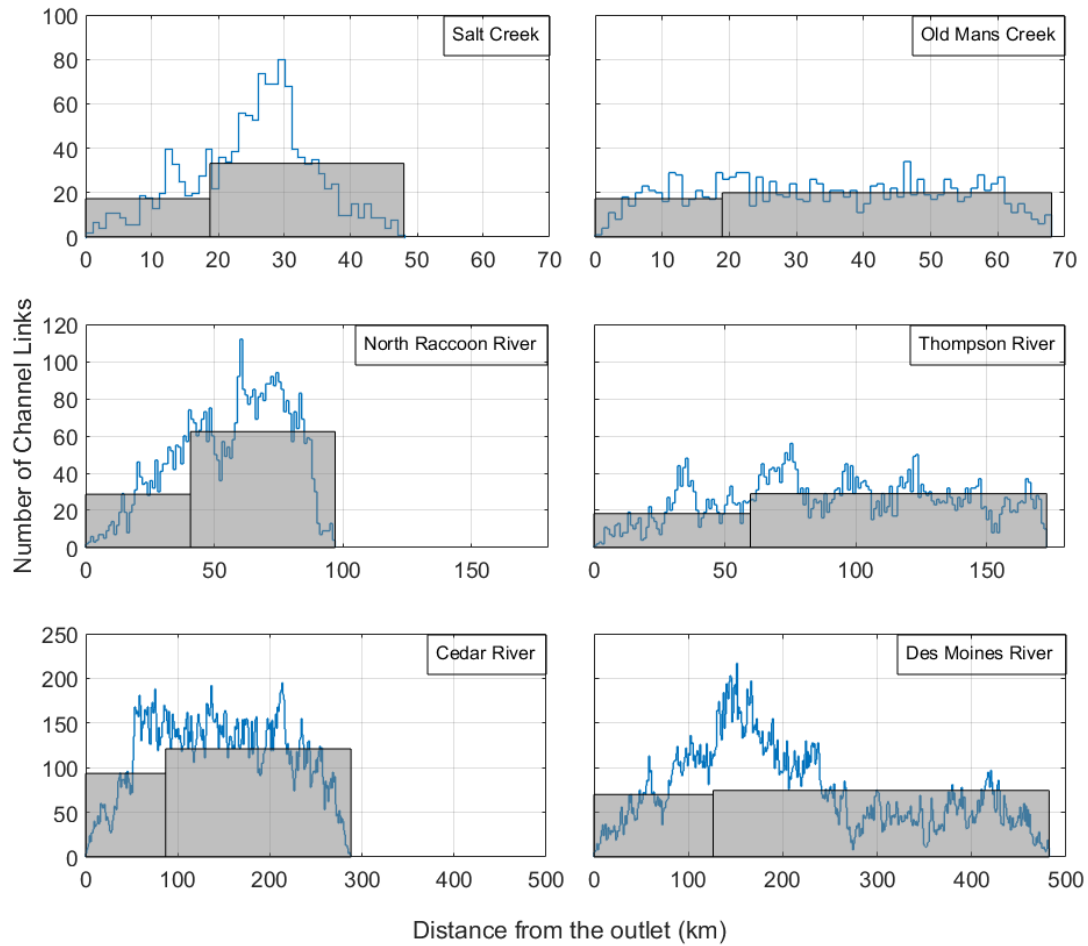
Figure 3-10. Reconstruction of the WD based on the WF descriptors $q_{25}(d^{[N]})$, and $D_B^{[NS]}$ for the six watersheds used as illustration cases.
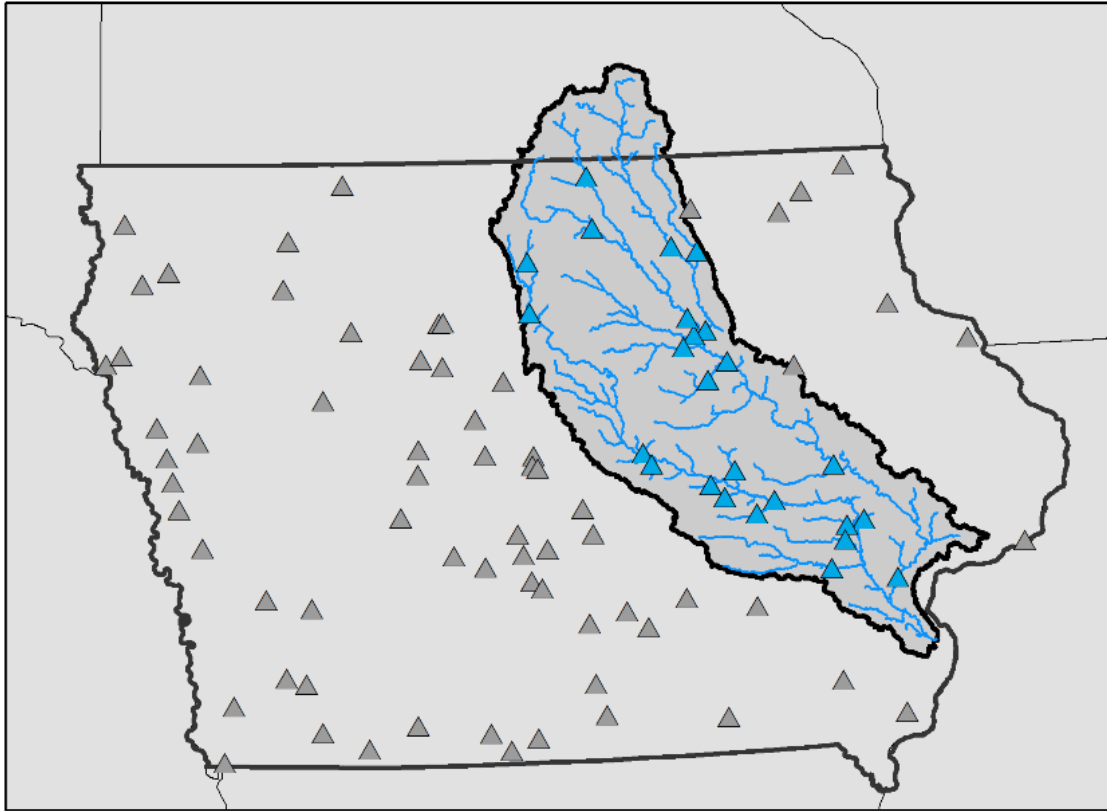
Figure 3-11. Location of the Iowa River Basin containing the 25 peak flow gauges (blue triangles) used in the regional flood frequency regressions. The gray triangles are the other peak flow gauges used for regional flood frequency regressions for the entire state of Iowa.
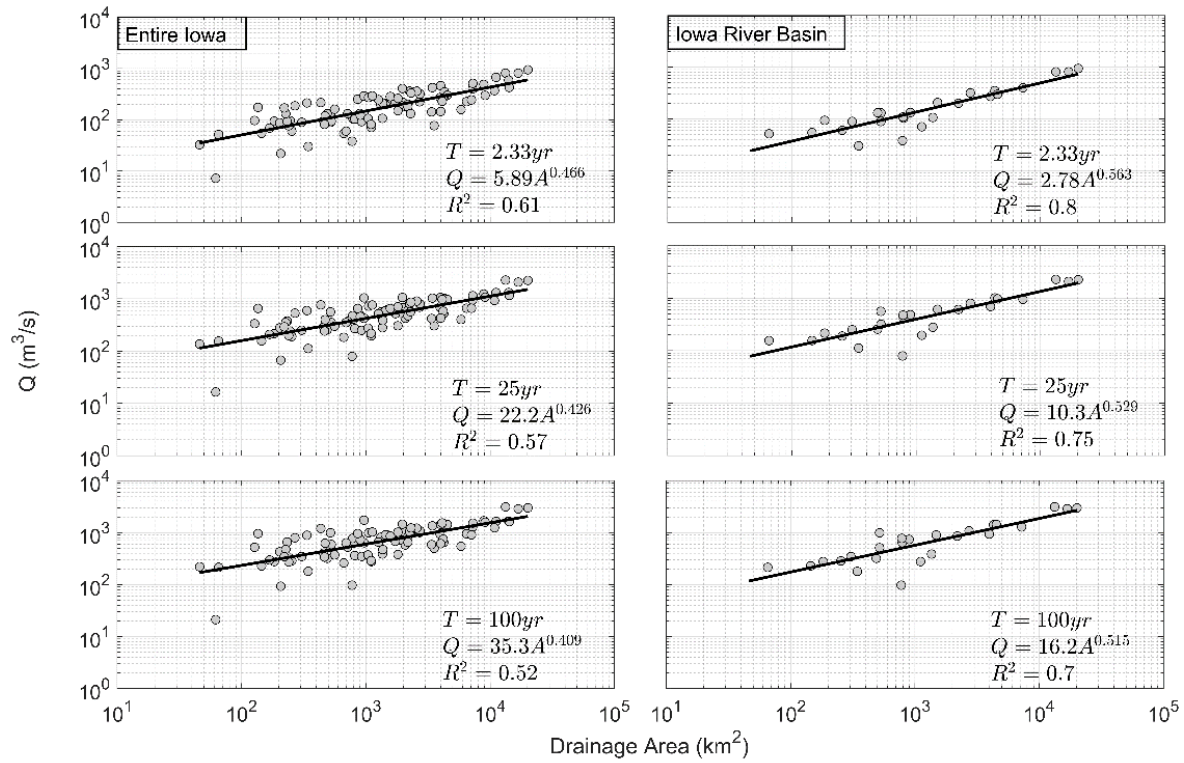
Figure 3-12. Power law regression between the drainage area and peak flow quantiles for the entire state of Iowa (left panel) and the Iowa River Basin (right panel).
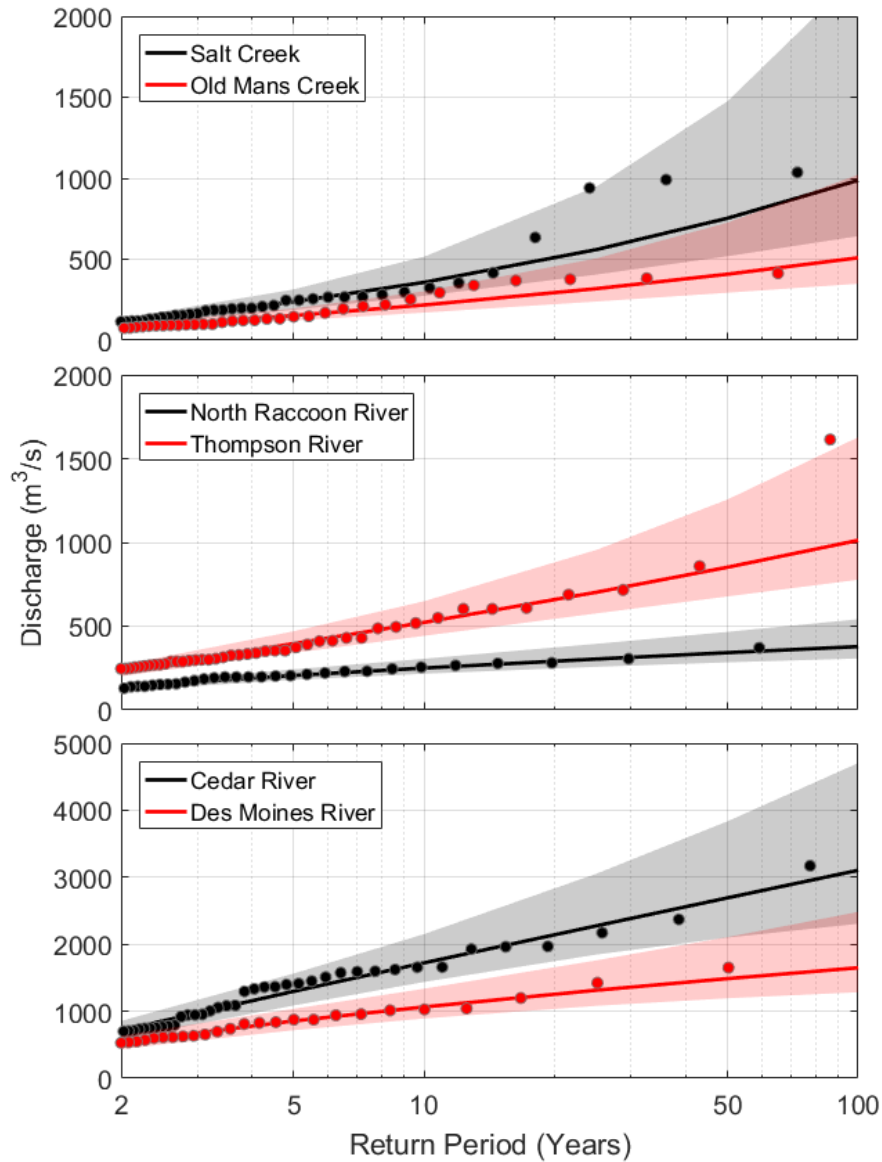
Figure 3-13. Estimation of the peak flow quantiles for the six watersheds used as illustration cases. The solid lines are the peak flow quantiles estimated with the USGS' Bulletin 17C methodology. The shaded regions represent the 95% confidence intervals. The points are empirical probabilities based on the Weibull plotting position formula.

CHAPTER 4: EXAMINING OBSERVED RAINFALL, SOIL MOISTURE, AND RIVER
NETWORK VARIABILITIES ON PEAK FLOW SCALING OF RAINFALL-RUNOFF
EVENTS WITH IMPLICATIONS ON REGIONALIZATION OF PEAK FLOW
QUANTILES[3]

4.1. Introduction

Previous studies of peak flow scaling have focused in two types of peak flows: Peak

flows resulting from individual rainfall-runoff events (Q_R), and peak flows related to recurrence

intervals, also known as peak flow quantiles (Q_p). Regarding the scaling of Q_R, several studies

have examined how rainfall properties, soil moisture conditions, and river network structure

explain the variability of α and θ. For instance, Furey & Gupta (2007) shows the robust

influence of depth, duration, and spatial variability of excess rainfall on the scaling parameters,

based on the analysis of 148 rainfall-runoff events. More recently Ayalew et al. (2014) showed

the influence of rainfall intensity, rainfall duration, hillslope overland velocity, and channel flow

velocity into the scaling parameters, by means of hydrologic simulations. On the other hand,

studying the scaling of Q_p requires estimating the statistical distribution of peak flows and to

make assumptions on how that distribution scales with respect to the drainage area. If the scaling

exponent of the power law of Q_p for different quantiles is independent of the recurrence interval

then the process is called simple-scaling, or multi-scaling otherwise (Gupta, et al., 1994). It is

important noting that the selection and fitting procedures of probability distributions incorporates

both, epistemic errors (the true probability distribution function is unknown), and sampling

errors (due to small sample sizes) to the estimation of Q_p, which could obscure the physical

interpretation of the scaling parameters. Different studies have investigated the parameters of the

scaling of Q_p. Furey et al. (2016) investigates the connections between scaling properties of Q_p

and Q_R, which suggest that the scaling exponents of Q_R are, on average, equivalent to the mean scaling exponent of Q_R. In general, the scaling analysis of Q_p and Q_R contain remarkable differences since Q_R is driven just by the hydrologic processes contained in a specific event, whereas Q_p is driven by statistical properties of the peak flow distribution which comprises the inclusion of sampling errors and epistemic errors.

The model $Q = \alpha A^{\theta}$ has been shown to capture the main scaling structure of the peak flows in a homogeneous region; however, this model does not cover the entire complex regional variability observed in actual peak flows. Different studies have explored alternative model structures to capture more complex natural variabilities that are not implicit in the drainage area. The more general example is the US Geological Survey (USGS) regional flood-frequency analyses for the estimation of Q_p for different recurrence intervals. Readers are referred to Dawdy et al. (2012) for further details about the origins of the regional flood-frequency equations in the United States. Usually, these equations incorporate the drainage area A and two additional explanatory variables for taking into account possible hydrologic variabilities; however, the selection of these explanatory variables are not necessarily supported by hydrologic justifications and are just following a statistical criterion in reducing the regression error residuals. This lack of hydrologic justifications leads to situations where different explanatory variables can be used for different recurrence intervals, making the understanding of the physical role of the explanatory variables with respect to the regional peak flow response difficult and obscure. One alternative to address this obstacle is to include explanatory variables based on hydrologic justifications which will help to facilitate the interpretation of regression parameters. For instance, I showed in Chapter 3 that the river network structure, represented by means of Width Function Descriptors, can be incorporated into the regional peak flow equations for

synthetic uniform rainfall events. Including river network descriptors in regional regression analysis line up with the long-standing research in hydrology that shows how the shape of a watershed, and the drainage network structure affects the streamflow fluctuations, including the magnitude of the peak flow (Horton, 1932; Morisawa, 1958; Rinaldo et al., 1995; Strahler, 1964).

I consider that establishing connections between scaling parameters and physics-based flood mechanisms is essential for developing flexible regional regression models to predict peak flows at ungauged sites. However, the presence of error components related to small sample sizes, number of streamflow gauges, and parameter estimation methods make it difficult developing these connections and makes the analysis of these regression models impractical. Hence, for addressing these concerns, this chapter investigates the following specific objectives.

1) Describe the scaling performance (e.g. coefficient of determination) of Q_R in terms of rainfall, soil moisture, and river network properties of observed rainfall-runoff events.

2) Evaluate the interplay between sampling error and the selection of explanatory variables in the construction of regional regression models for Q_R and Q_p.

The rest of this chapter is organized as follows. I start presenting a theoretical scenario based on the geomorphological instantaneous unit hydrograph (GIUH) to illustrate the interplay between rainfall properties and river network structure in the definition of model structures to represent regional variabilities of peak flows. This is followed by a general definition of regional equations for Q_R and Q_p with the different error components and scaling assumptions. The following section describes the study area and data sources including the data description of rainfall-runoff events, peak flow quantiles, radar rainfall fields, satellite soil moisture, and river network extraction. After this, I describe the methods to address the two specific objectives of

85

the present chapter. This is followed by a section of results, and a discussion section. Finally, I finish with a conclusions section.

4.2. Scaling and Model assumptions

4.2.1. Theoretical Illustration of a "True" and "Estimated" Regional Model

I present a theoretical case to illustrate the connections between peak flow scaling, rainfall properties, and river network structure. I clarify that this example is far from including all the complexities that exist in observed rainfall-runoff events or peak flow quantiles; however, this example provides elements to understand how the true regional model of peak flows is tied to variables different to drainage area. I start by defining a region which contains N number of streamflow gauges. Each gauge (or sub-watershed) is denoted by the sub-index e. The main goal is to find the "true" model that represents the regional variability of all N streamflow gauges under an idealized rainfall-runoff event. For this purpose, we use the GIUH under idealized conditions in which the surface water flows at a constant speed without infiltration or other losses (**Rigon, et al., 2016**). Now, two independent rainfall events are assumed. Event 1 has a long rainfall duration (larger than the concentration time of the larger basin of the region) and spatial uniform intensity, and Event 2 has an instantaneous rainfall duration with also spatial uniform intensity. Based on the GIUH we obtain that the regional peak flows of the Event 1 are directly proportional to drainage area, which agrees with the fact that the entire basin is contributing to the peak flow generation. Hence, for the Event 1, the true regional model is

$$Q_{R,e}^{[Event\ 1]} = \lambda_1 A_e \qquad \text{Equation 4-1}$$

where λ_1 is proportional to the spatial uniform intensity. Now, for the Event 2 (instantaneous rainfall event) the formulation of the regional model is different. One of the properties of the GIUH is that the hydrograph for instantaneous rainfall events will be proportional to the Width

Function (W) of the basin. The W gives the number of links located at a flow distance "x" from the outlet, which means that W can be easily extracted from the river network. This fact implies that the peak at each site e for the Event 2 is directly proportional to the maximum of W ($\max[W_e]$) extracted at each site e; therefore, the true regional model for the Event 2 is

$$Q_{R,e}^{[Event\ 2]} = \lambda_2 \cdot \max[W_e] \qquad \text{Equation 4-2}$$

where λ_2 is proportional to the spatial uniform intensity. Equation 4-1 and Equation 4-2 are the true models for the regional estimation of peak flows for Event 1 and Event 2 respectively, under the assumptions implied by the GIUH. Now, because of the scaling structure of the drainage network, different empirical studies corroborate that the expected value of $\max[W_e]$ scales with the drainage area (e.g. Veitzer & Gupta, 2001), which implies that

$$E(\max[W_e]) = \omega A_e^{\delta} \qquad \text{Equation 4-3}$$

with ω and δ as scaling parameters. Note that Equation 4-3 uses $E(\max[W_e])$ instead of $\max[W_e]$, which implies that there is variability that cannot be explained by just the drainage area. This natural variability is related to the intrinsic configuration of the river network at each subwatershed. We denote this remain variability as ψ_e, now Equation 4-2 can be rewritten in terms of Equation 4-3 and ψ as

$$Q_{R,e}^{[Event\ 2]} = \lambda_2(\omega A_e^{\delta} + \psi_e) \qquad \text{Equation 4-4}$$

From the previous arguments, I want to highlight the fact that both model structures of the regional peak flows from Event 1 and Event 2 include drainage area (see Equation 4-1 and Equation 4-4), but just the expression for Event 2 includes river network variabilities (ψ_e). This simple result shows that, at least in principle, the river network variability must be considered as a candidate to explain the regional variability of peak flow events. I illustrate this concept in Figure 4-2 showing an example of the scaling for two events with large durations (gray and black

87

lines) and two events with instantaneous durations (red and yellow lines) using 43 streamflow gauges located at the Iowa River Basin (see Figure 4-1). The synthetic intensities associated to each event are observed in the left panel of Figure 4-2. These intensities are calculated over the concentration time of each subwatershed, for that reason the instantaneous intensities decrease with respect to drainage area, since the concentration time increases with the drainage area. The regional peak flows are fitted based on the drainage area only. Then, as is expected, the events with large durations fits perfectly the Equation 4-1. On the other hand, the events with instantaneous duration fails to represent the entire regional peak flow variability that is caused for the exclusion of ψ_e in Equation 4-4.

This theoretical exercise is used as an argument to explore different model structures in the definition of regional peak flow equations. Three main aspects need to be questioned: 1) How can we describe the river network variability (ψ_e) from observed river network structures? 2) How dominant is ψ_e in the peak flow variability with respect to different sources of variabilities (e.g. soil moisture condition, rainfall structure) that are found in real rainfall-runoff scenarios? And 3) How can we extent this results to peak flow quantiles? We address these questions in the following sections.

4.2.2. Model Structure of Regional Peak Flow Equations for Q_R and Q_p.

I present regional equations with more general error structures. For rainfall-runoff events, we can assume that the true $Q_{R,e}$ for a site e is estimated by a power law model in function of drainage area as:

$$\hat{Q}_{R,e} = \alpha A_e{}^\theta \qquad \text{Equation 4-5}$$

$$Q_{R,e} = \hat{Q}_{R,e} + \eta_e \qquad \text{Equation 4-6}$$

88

where η_e is the model error which represent the failure of Equation 4-5 to represent the true $Q_{R,e}$. Note that η_e in Equation 4-6 is presented as an additive term; however, it could be multiplicative. For real scenarios of rainfall-runoff events, the η_e will depend on the different hydrologic processes interacting over the peak flow generation mechanisms such as rainfall structure, soil moisture conditions, land cover, river network structure, hydraulic geometry of river channels, etc. For the theoretical scenario of a GIUH with long rainfall durations, the η_e is equal to zero, and for instantaneous rainfall durations, η_e is equal to ψ_e. In practice, the parameters of Equation 4-5 are estimated based on regression techniques such as Ordinary Least Square (OLS) between drainage area and peak flow response for N sites in a region. An inconvenience is that the estimation of α and θ is sensitive to the size of N, therefore, in real cases, the estimation of $\hat{Q}_{R,e}$ will contain errors attributed to the number of sites used in the regional analysis. Then in a more general form, we can assume that

$$Q_{R,e} = \hat{\alpha}A_e{}^{\hat{\theta}} + \eta_e + \delta \qquad\qquad \text{Equation 4-7}$$

where δ is the error contribution due to the number of peak flow sites in the estimation of regression parameters in Equation 4-5. $\hat{\alpha}$ and $\hat{\theta}$ are the estimations of α and θ by means of OLS. I will explore in Section 4.4 the inclusion of river network descriptors in Equation 4-7 in order to reduce η_e.

Regarding $Q_{p,e}$, we need to consider the statistical procedure to estimate quantiles from a fitted probability distribution (F_e) for a correct depiction of error components. In real scenarios, F_e is derived from a sample of observed peak flows at the site e. Therefore, contrary to $Q_{R,e}$, the estimation of $Q_{p,e}$ will be subject to sampling errors (ε_e) caused by the limited sample of peak flows used to estimate the probability distribution F_e. Then, if we assume a power law model to

estimate $Q_{p,e}$ in a region, we will be subject to the same errors presented in Equation 4-7, in addition to ε_e.

$$Q_{p,e} = \hat{\alpha} A_e^{\hat{\theta}} + \eta_e + \varepsilon_e + \delta \qquad\qquad \text{Equation 4-8}$$

Equation 4-8 could include other error components related to the incorrect selection of a probability distribution function, or error related to the estimation method of distribution parameters (e.g. Method of Moments, Method of L-Moments, Maximum Likelihood); however for simplicity the empirical probability distribution will be used to exempt these type of errors.

The depiction of the different error components in the regional estimations of Q_R (Equation 4-7) and for Q_p (Equation 4-8) are key to understand the predictability limits reached with the regional regression equations. For instance, if the variability presented by ε_e and δ is larger than the physical variability explained just by the drainage area, then the regression analysis will show that the drainage area has no explanatory power with respect to Q_p, in other words, the regression parameter $\hat{\theta}$ will not be statistically significant. For this same reason, the inclusion of new explanatory variables (e.g. variables related to river network structure) in the regression models could be obscured by the error components of ε_e and δ. This aspect is evaluated in Section 4.4 and Section 4.5 with a Monte Carlo simulation experiment.

4.3. Study Area and Data Sources

The peak flows, rainfall fields, and soil moisture fields need to be collected over a "regional domain" in order to address the objectives of this chapter. The mesoscale Iowa River Basin with a drainage area of 32,700 km^2 can be considered as an ideal candidate, since it counts with a dense USGS monitoring streamflow network. The Iowa River Basin outlet in this study is determined by the USGS gauge Iowa River at Oakville (USGS code 05465700). It contains 43 embedded USGS instantaneous streamflow gauges with drainage area ranging from 6 to 32,700

90

km^2. The gauges record 15-minute streamflow data. The length of these streamflow records among sites ranges between 4 and 30 years, with average record length of 20 years per site (see Figure 4-1). Five gauges have some degree of regulation caused by dams (see Table 4-1). The 43 gauges were used for identification of rainfall-runoff events, however, just 38 unregulated sites were used for the scaling analysis of Q_R and Q_p. See Table 4-1 for a general description of the streamflow gauges used in this study. The USGS peak flow records at each of the 43 sites were used as well. The peak flow values are derived from instantaneous data.

4.3.1. Selection of Rainfall-Runoff Events (Q_R)

The method to identify rainfall-runoff events is subject to the type of properties to be explored from these events. The objectives of this study are directed to the scaling analysis of peak flows; therefore, the selected rainfall-runoff events must belong to the extreme flow population through the different spatial scales within the Iowa River Basin. This condition differs from previous studies that analyze the scaling of rainfall-runoff events (Furey & Gupta, 2005, 2007; Ogden & Dawdy, 2003). For instance, Ayalew et al. (2015) selected 51 rainfall-runoff events in the same domain of the Iowa River Basin in the period 2002-2013 ensuring that all the streamflow gauges exhibit a streamflow response. However, this streamflow response may not correspond to an extreme event. Then, as a countermeasure, I used peak flow thresholds for the selection of rainfall-runoff events. The selection is described as follows. I used the 15-minutes streamflow data to identify the rainfall-runoff events. The selected rainfall-runoff events must be independent amongst them; therefore, the concentration time of the Iowa River Basin is used as the minimum time window to separate events. For the concentration time, I use the same formulation as Ayalew et al. (2015) assuming channel flow velocity and hillslope overland flow velocity values of 0.5 and 0.02 m/s respectively, which provides a 15 day concentration time for

the Iowa River Basin. The concentration time is also calculated for each one of the 43 streamflow gauges. In order to guarantee that the observed rainfall-runoff event can be considered to be an extreme event, I select just the streamflow gauges that record a streamflow higher than a peak flow threshold defined at each site during a time interval of 15 days. Note that in order to guarantee a proper regression analysis, I limited the event selection to events that contain more than 20 streamflow gauges above the peak flow threshold defined at each site. The peak flow threshold is the minimum annual peak flow recorded at the USGS peak flow gauge. This minimum annual peak flow is considered part of the peak flow distribution; therefore, it is reasonable to assume that any other streamflow higher than this minimum peak flow can be considered to be part of the peak flow population.

4.3.2. Extraction of Peak Flow Quantiles (Q_p)

There are two common sampling methods to estimate peak flow quantiles: The first is the Annual Maximum Series also known as Annual Peak Flows, and the second is Partial Duration Series also known as Block Maxima or Peaks-Over-Threshold. The Annual Maximum Series uses the maximum instantaneous peak flow in a year; therefore, the peak flow sample is equal to the number of years recorded at the gauge. The shortcoming of this sampling method is the exclusion of possible high-flood events observed within a given year. On the other hand, Partial Duration Series selects peak flows above of a defined peak flow threshold. The selected peak flows need to be independent, for this reason, it is recommended to use a time window equal to the concentration time of the basin. In addition, literature recommends using the minimum annual peak flow in the observed record as peak flow threshold (Gado & Nguyen, 2016; Malamud & Turcotte, 2006; Mohssen, 2009). In this study I estimate the peak flow quantiles based on Partial Duration Series because a large sample of peak flows can be related to rainfall

and soil moisture observations. Once the peak flow sample is extracted at each gauge, the Weibull plotting position formula (Weibull, 1939) is used to estimate the peak flow quantiles with recurrence intervals of 50%, 20%, 10%, 4%, 2%, and 1%.

4.3.3. Rainfall Descriptors

Radar rainfall data is obtained from Stage-IV radar-rainfall products (Lin & Mitchell, 2005). The Stage-IV data is a national rainfall dataset distributed by the National Centers for Environmental Prediction, which provides multi-sensor rainfall data at 1-hour time resolution and a 4 x 4 km spatial resolution over the continental United States. I used this product starting on Jan-2002 up to Jan-2019. I characterized the spatial and temporal rainfall properties associated with each peak flow and gauge, either by rainfall-runoff events or Partial Duration series. The rainfall interval associated to an observed peak flow is defined based on the concentration time of each watershed. Then, if a peak flow is observed at a time t_f for a gauge e with concentration time T_e, the analyzed rainfall interval will start from an initial time t_0 equal to $t_f - T_e$ and will end at a time t_f.

I define the rainfall volume by unit area for each rainfall-runoff event k and basin e as

$$V_{e,k} = \sum_{t=t_0}^{t=t_f} \overline{i(t)}_{e,k} \Delta t \qquad \text{Equation 4-9}$$

where $\overline{i(t)}_{e,k}$ is the average intensity of the observed rainfall field in the event k in the basin e at the time t. Δt is the time interval in which the rainfall is measured (e.g. 1 hour for Stage-IV products). It is important to characterize the temporal variability of the observed rainfall fields; therefore, we can define the mean time of rainfall as

$$\mu_{e,k} = \frac{1}{V_{e,k}} \sum_{t=t_0}^{t=t_f} t \overline{i(t)}_{e,k} \Delta t \qquad \text{Equation 4-10}$$

93

The mean time of rainfall ($\mu_{e,k}$) varies from t_0 to t_f, in which t_0 is equal to $t_f - T_e$; therefore, in order to remove the scale dependence provided by the concentration time T_e, a normalized mean time of rainfall is defined as

$$\overline{\mu_{e,k}} = \frac{\mu_{e,k} - t_0}{T_e} \qquad \text{Equation 4-11}$$

then $\overline{\mu_{e,k}}$ ranges from 0 to 1. Now, the rainfall spread around the mean $\mu_{e,k}$ can be calculated as

$$\sigma_{e,k}^2 = \frac{1}{V_{e,k}} \sum_{t=t_0}^{t=t_f} (t - \mu_{e,k})^2 \overline{i(t)}_{e,k} \Delta t \qquad \text{Equation 4-12}$$

and the normalized rainfall spread around the mean $\overline{\mu_{e,k}}$ can be calculated as

$$\overline{\sigma_{e,k}}^2 = \frac{1}{V_{e,k}} \sum_{t=t_0}^{t=t_f} \left(\frac{t - t_0}{T_e} - \overline{\mu_{e,k}}\right)^2 \overline{i(t)}_{e,k} \Delta t \qquad \text{Equation 4-13}$$

I use $\overline{\mu_{e,k}}$ and $\overline{\sigma_{e,k}}^2$ to describe the temporal variability of a rainfall event k within a basin e. I remark that Ayalew et al., (2015) uses the descriptors $\mu_{e,k}$ and $\sigma_{e,k}^2$ (without normalization), but only for the outlet of the Iowa River Basin. The use of these descriptors at each basin will allow describing with more detail the observed rainfall structure at different watershed scales.

The rainfall fields used to estimate $\overline{i(t)}_{e,k}$ present spatial variability within the basin; therefore, I also describe the rainfall structure by means of the intrastorm rainfall variability. I use the same approach described by Smith et al. (2004). The intrastorm rainfall variability for an instant t, event k, and basin e is defined as

$$\sigma_{e,k,t}^* = \sqrt{\frac{\sum_{h=1}^{M} P_{t,h}^2}{M} - \frac{\left(\sum_{h=1}^{M} P_{t,h}\right)^2}{M^2}} \qquad \text{Equation 4-14}$$

where h represents a subregion (e.g. pixels in radar data) within the basin e which is constituted by M subregions (total pixels), and $P_{t,h}$ is the accumulated precipitation in a Δt equal to the temporal resolution of the rainfall field. Then, for a Δt equal to 1 hour, the $P_{t,h}$ can be interpreted

94

as the intensity of the rainfall field over 1 hour. Then, the intrastorm rainfall variability Index for a rainfall event k and basin e is defined as

$$I_{\sigma_{e,k}^*} = \frac{\sum_{t=t_0}^{t=t_f}\left(\sigma_{e,k,t}^* \sum_{h=1}^{M} P_{t,h}\right)}{\sum_{t=t_0}^{t=t_f} \sum_{h=1}^{M} P_{t,h}}$$

Equation 4-15

The descriptors $I_{\sigma_{e,k}^*}$, $\overline{\sigma_{e,k}}^2$, and $\overline{\mu_{e,k}}$ are gauge dependent (function of e) and event dependent (function of k). Therefore, in order to define a single descriptor for a specific event, the site dependence needs to be removed. For this reason, I calculate the expected value and standard deviation of $I_{\sigma_{e,k}^*}$, $\overline{\sigma_{e,k}}^2$, and $\overline{\mu_{e,k}}$ for all the sites (N) at the event scale. Then for instance for an event k the expected and variance of the normalized intrastorm rainfall variability Index is defined as

$$E(I_{\sigma_k^*}) = \frac{\sum_{e=1}^{N} I_{\sigma_{e,k}^*}}{N}$$

Equation 4-16

$$Var(I_{\sigma_k^*}) = \frac{\sum_{e=1}^{N}\left(I_{\sigma_{e,k}^*} - E(I_{\sigma_k^*})\right)^2}{N}$$

Equation 4-17

I also describe the scaling structure of each rainfall event. I explored the scaling dependence of the observed mean intensities $(\overline{i(t)}_{e,k})$ across basins in a particular event k. I estimate $\overline{i(t)}_{e,k}$ based on a fitted power law model with Ordinary Least Square and its performance is characterized by means of the coefficient of determination (R_i^2).

$$\widehat{\overline{i(t)}}_{e,k} = \alpha_{i_k} A_e^{\theta_{i_k}}$$

Equation 4-18

where α_{i_k} and θ_{i_k} are the scaling parameters of the rainfall fields for an event k.

4.3.4. Soil Moisture Descriptors

Soil moisture data was obtained from Soil Moisture Active Passive (SMAP) satellite products (Brown et al., 2013). The SMAP products provide soil moisture content at 9 x 9 km

grid size resolution and 12-hour temporal resolution. This data is retrieved from Jan-2015 to Jan-2019. The SMAP data is used to characterize the spatial variability of the antecedent soil moisture conditions prior to the arrival of the observed rainfall-runoff event. The SMAP data starts from Jan-2015, therefore just a few events can be described in terms of soil moisture conditions. I decided to describe the entire antecedent soil moisture condition for each event k, as the mean, standard deviation, and coefficient of variation of the soil moisture fields, calculated from the SMAP pixels intersected at the Iowa River Basin.

4.3.5. River Network Descriptors

I use the 34 Width Function Descriptors (WFDs) described in Chapter 3 for the representation of river network structure. As reminder, I show in Chapter 3 that the WFDs can be incorporated into regional peak flow equations with synthetic uniform rainfall scenarios, in which among the 34 WFDs, I found that the normalized base of the width function with respect to the expected width function base (D_B^{NS}) seems to explain part of the peak flow variability that is not explained by drainage area. It is important to note that D_B^{NS} can be interpreted as the residual of the Hack's law (Hack, 1957).

4.4. Methods

The scaling of Q_p and Q_R was explored with respect to the rainfall, soil moisture, and river network descriptors defined previously. I start evaluating the scaling performance of Q_R. The scaling performance is measured as the coefficient of determination (R_Q^2) in the log-log space of the linear relation between Q_R and A. Basically, I explore if there is any significant relation between R_Q^2 and the different rainfall and soil moisture descriptors defined for each rainfall event. The river network descriptors are used to evaluate different regional model

structures including WFDs. For this purpose, I use an exhaustive search method to select the final set of explanatory variables based on the Akaike Information Criteria (AIC).

Regarding Q_p, the evaluation is focused in three main parts. The first is to observe how is the scaling structure of the rainfall fields and soil moisture fields related to the empirical peak flow quantiles. The second is to evaluate if the inclusion of WFDs could improve the regional estimation of Q_p. And third, with a Monte Carlo simulation approach, I evaluate the influence of sampling errors in the selection of the model structures with WFDs as explanatory variables.

The following Monte Carlo simulation is used to show the control of sampling errors over the selection of explanatory variables in the regional equation. I start representing the peak flow as a random variable

$$Q_e \sim LP3(a_e, b_e, c_e) + \eta_e \qquad \text{Equation 4-19}$$

where LP3 represents the Log Pearson type III distribution with parameters a_e, b_e, and c_e for a site e, and, η represent the model error. Then, I assume that the peak flow quantiles in a region can be characterized by a model using A and an unknown river network descriptor χ, as

$$Q_{p,e} = \alpha A_e^{\beta} \chi_e^{\gamma} + \eta_e \qquad \text{Equation 4-20}$$

Since Equation 4-20 is assumed to be true, the use of a model criteria procedure based on AIC should confirm that a model with A and χ as explanatory variables outperform a model with just A. However, as was explained in the definition of Equation 4-8, the selection of the true regional model of peak flow quantiles could be flawed because of error components attributed to small sample sizes (ε) and the number of sites used in the regression analysis (δ). Then, Equation 4-20 can be rewritten as

$$Q_{p,e} = \hat{\alpha} A_e^{\hat{\beta}} \chi_e^{\hat{\gamma}} + \eta_e + \varepsilon_e + \delta \qquad \text{Equation 4-21}$$

97

The issue with Equation 4-21 is that, if $\varepsilon + \delta$ is too large, the model criteria procedure based on AIC could fail in the selection of χ as an explanatory variable. Therefore, in order to understand the control of ε and δ over the selection of χ, I generate random peak flow samples from regional peak flow distributions that satisfy Equation 4-19 and Equation 4-20. The definition of the "true" peak flow distribution at each site will be based on peak flow observations, and it will be described in the result section.

For each random sample, the peak flow quantiles are estimated based on a LP3 distribution. Note that I could assume a different distribution (e.g. GEV, Pearson 3, Weibull) in order to incorporate a new epistemic error. I used Monte Carlo simulations to create regional scenarios with a different number of peak flow gauges, and different number of observed peak flows at each gauge. The number of peak flow gauges varies from 25 to 38, and the number of observed peak flows varies from 10 to 100. I performed 1,000 iterations for each scenario, and for each of those I evaluated if the AIC prefers the model $Q_{p,e} = \hat{\alpha} A_e^{\hat{\beta}} \chi_e^{\hat{\gamma}}$ over the model $Q_{p,e} = \hat{\alpha} A_e^{\hat{\beta}}$ for different recurrence intervals p.

4.5. Results

4.5.1. Rainfall-Runoff Events and Rainfall Descriptors

I identified 85 rainfall-runoff events over the Iowa River Basin. The peak flow scaling of 25 of these rainfall-runoff events is observed in Figure 4-3. The scaling exponent (θ_Q) of these events ranges from 0.27 to 1.05, and the scaling intercept (α_Q) ranges from 0.03 to 9.28. The R_Q^2 for these events varies from 0.26 to 0.97, with a mean value of 0.80. I show in Figure 4-4 the scaling of rainfall-intensity fields with respect to drainage area for the 85 events. I found that the coefficient of determination R_i^2 of the scaling of intensity fields ranges from 0.14 to 0.93 with a

98

mean value of 0.63. The scaling intercept for the intensity fields (α_i) ranges from 1.01 to 71.93, and the scaling exponent (θ_i) ranges from -0.58 to -0.15. The interpretation of R_i^2, α_i, and θ_i is key to understand part of the rainfall structure of each rainfall event. For instance, a low R_i^2 (<0.4) will imply θ_i values closer to zero, which means that the observed rainfall field does not exhibit self-similar structure through different spatial scales. However, we can observe θ_i values closer to zero but with high R_i^2 (>0.4). For this case and any other case with high R_i^2, the magnitude of θ_i represents the change of intensity rate across the spatial scales, and in general, the higher intensities are expected in small basins rather than large basins. Therefore, the θ_i magnitude is expected to be always negative, which agrees with our observations. Also, note that we should expect a more uniform rainfall structure when θ_i is approaching to zero.

I found that the scaling exponents θ_i and θ_Q decay with respect to the scaling intercepts α_i and α_Q (see Figure 4-5). This is a common feature in scaling structures, which demonstrates the interplay between small and large scales that have been reported in different studies (Ayalew et al., 2015; Ogden & Dawdy, 2003). Regarding the comparison between scaling performances (R_i^2 and R_Q^2), I found cases where R_i^2 is low, but R_Q^2 still show good performance. For these cases, I presume that the scaling in peak flows is preserved because the aggregation processes across the river network are more dominant that the spatial variability presented by the intensity fields. Reversely, I found five events that have R_Q^2 lower than 0.5 and are related to R_i^2 higher than 0.5. This result could be caused by two reasons. First, due to a complex rainfall structure that is not captured by the scaling description of the intensity fields. And second, due to spatial variabilities induced by antecedent soil moisture conditions. I explore these two aspects with the analysis of soil moisture descriptors and different rainfall descriptors at the end of this section.

99

For a more detailed analysis, I divided the 85 events into three groups providing a similar number of rainfall events in function of ranges of R_Q^2 for a fair comparison. The first group are events with $R_Q^2 \leq 0.75$, the second group with $0.75 < R_Q^2 < 0.85$, and a third group with $R_Q^2 \geq 0.85$. The first, second and third group have 25, 26, and 34 rainfall-runoff events respectively. Figure 4-6 shows the values of θ_i and α_i for the three groups. This result shows a positive linear trend between θ_i and R_Q^2. Note also that the scaling intercept α_i tends to decay with the increasing of R_Q^2, which suggest that the peak flow scaling start to debilitate for events with higher intensities in small scales (related to higher α_i) and higher changes in intensity rates across the spatial scales (related to lower θ_i). The positive linear relation between θ_i and R_Q^2 implies that the scaling exponent of the rainfall fields controls the scaling performance of observed peak flows events. The implication of this result is examined in detail in the Discussion section.

I also inspected the behavior of rainfall descriptors $I_{\sigma_{e,k}^*}$, $\overline{\sigma_{e,k}}^2$, and $\overline{\mu_{e,k}}$ in relation to R_Q^2 in Figure 4-7. I found that these descriptors explain part of R_Q^2 variability between events. For instance, I found that the R_Q^2 increases with decreasing the expected value of $I_{\sigma_k^*}$, which means that the scaling of peak flows improves with more spatial uniform rainfall events. The larger $I_{\sigma_k^*}$, the higher the spatial variability of the observed rainfall event. This result is confirmed with the standard deviation of $I_{\sigma_k^*}$, which shows higher variabilities for events with lower R_Q^2. For the normalized mean time of rainfall $\overline{\mu_k}$, I found that almost all the rainfall events are concentrated in the range 0.4 to 0.5 with a spread ($\overline{\sigma_k}^2$) ranging from 0.02 to 0.04, which implies that most of the rainfall events are occurring at the middle of the window defined by t_0 and t_f.

4.5.2. Rainfall-Runoff Events and Soil Moisture Descriptors

Because of the short record length of SMAP product starting from 2015, I only could identify antecedent soil moisture conditions for 24 rainfall-runoff events out of the 85 initial events. I separated the 24 events into two groups based on R_Q^2 and a similar number of events. First group has $R_Q^2 < 0.85$ and it has 10 events, and the second group has $R_Q^2 \geq 0.85$ with 14 events. The most notable result is the coefficient of variation of the soil moisture fields between groups, which suggest that the higher R_Q^2 are related with more homogeneous soil moisture fields (see Figure 4-8). At the same time, this result implies that heterogeneity in soil moisture fields will generate more variabilities in the peak flow scaling. These results provide some insight of the importance in antecedent soil moisture, although, further analysis with large sample sizes or hydrologic simulations need to be tested in order to be confident of these findings.

4.5.3. Rainfall-Runoff Events and River Network Descriptors

The investigation of other model structures that include WFDs shows that 15 events are improved by using a model structure that accounts for drainage area and the width function descriptor D_B^{NS}. For the other 70 events, a model with only drainage area seems to be the best model based on the AIC (see Figure 4-9). Based on the theoretical argument presented in Figure 4-2, we were expecting to find model improvement with the inclusion of river network descriptors. I argue that this selection is partially controlled by the error contribution of the number of gauges (δ), which obscures the contribution of new explanatory variables such as D_B^{NS}. This feature is well represented in the boxplot of number of sites in Figure 4-9, which shows that the events with improved equations have in average more sites that the events that are not improving. The interplay between model structure and sampling error in the selection of

101

explanatory variables such as D_B^{NS} is explored in further detail for peak flow quantiles in the following section.

4.5.4. Connecting Peak Flow Quantiles to Rainfall and River Network Descriptors

I examined the rainfall properties of the individual rainfall events that are triggering the peak flow quantiles at different sites. Because of the statistical nature of the selection of peak flow quantiles at each site, there is no need for an agreement for a same rainfall event to generate a specific flood frequency across the entire domain. This result is observed in Figure 4-10 in which the peak flow quantiles at each site are caused by different rainfall events. I observed that the scaling exponents changes from 0.62 to 0.54 for $Q_{50\%}$ and $Q_{1\%}$ respectively (see Table 4-2), which agrees with the multi-scaling property found in previous studies (Gupta et al., 1994). Another interesting result is observed with the scaling of the rainfall-intensity fields associated with each of the events generating the peak flow quantiles. This result agrees with the well-known fact that the frequency of intensity fields decays with respect to the scale length (e.g. drainage area). In order to compare the results with the rainfall-runoff events, I plotted the intensity and peak flow scaling of the 85 rainfall-runoff events, and I superimposed the 1%, 4%, and 10% peak flow quantiles with their respective intensity scaling in Figure 4-11. I observed that the scaling of intensity fields of peak flow quantiles for lower frequencies are in the range in where the scaling performance of Q_R decreases (see Figure 4-6). Because of short record periods of soil moisture, I could not reconstruct the soil moisture fields for these regional peak flow quantiles.

A notable difference between the regression analysis of Q_R and Q_p is the number of gauges. For Q_p we have estimations for all the 38 sites, expect for the quantiles of 2% and 1% that have 37 and 35 sites respectively; however, for Q_R the number of gauges change from event

to event ranging from 20 to 38 sites. I found that all the regional regression models for Q_p improve with the inclusion of the width function descriptor D_B^{NS} with an average of 15% in reduction of the Root Mean Square Error (see Table 4-3). I argue that the disagreement of using D_B^{NS} in the estimation of Q_p and not in Q_R, is because of the difference of number of sites used in both analyses. This is demonstrated more clearly next with the results of the Monte Carlo simulations.

For the Monte Carlo simulation, I use the empirical evidence showing that peak flow quantiles can be represented by a regional model using A and D_B^{NS} as explanatory variables. Then, for the use of Equation 4-19 in the Monte Carlo simulation, I assume that a LP3 distribution fitted from the first three moments of the empirical peak flow distribution, is the "true" distribution, and for Equation 4-20 I assume that χ is represented by D_B^{NS}. Then, following the Monte Carlo simulation procedure explained in the Method section, we can explore the interplay between sample size, number of gauges, and selection of D_B^{NS} as an explanatory variable.

In Figure 4-12, we observe the results of the Monte Carlo simulation. It is notable the large influence of the number of peak flows and number of sites for the selection of the model structure. For instance, if we reduce the number of sites from 38 to 25, we expect to select just 40% of the cases the true model (a model with A and D_B^{NS}) over a model just with drainage area for any given recurrence interval. Regarding sample sizes, with more peak flow samples it is more likely to select the right model, which agrees with the reduction of sampling error. Also, note that the lower frequencies (e.g. 1%, and 2%) are more sensitive to sampling errors, therefore as we observed in Figure 4-12, the percentage of simulations showing improvement, decreases with the decrease of the probability of exceedance.

103

4.6. Discussion

The evaluation of R_Q^2 was based on a model using just the drainage area. Therefore, the understanding of the controls behind R_Q^2 will provide guidance for a better development of empirical regional flood frequency models. I found that the rainfall structure and soil moisture variability explain part of the peak flow scaling performance. More specifically, I found that the scaling exponent of rainfall-intensity fields explain part of the scaling performance of peak flows. This result agrees with the results showed in the theoretical scenario in which the scaling structure of the intensity fields is controlling the amount of explanatory power of the drainage area and geomorphologic variabilities such as river network structure. This result contains a strong indication for the analysis of peak flow quantiles. It suggests that for θ_i closer to zero the drainage area is enough to explain the regional variability of peak flows, and for θ_i away from zero (e.g. -0.5) the river network plays a more relevant role in the regional variability. I found for the scaling of intensities fields associated to peak flow quantiles that θ_i is around -0.4, which suggest that, although there is not spatial connectivity between the quantiles, there is a scaling organization in intensity fields that could create a physical control that determines the role of the river network structure as a source to explain the regional peak flow variability.

The theoretical regional variability of peak flows presented in Figure 4-2 illustrates the interplay between rainfall properties and river network structure with respect to the regional peak flow variabilities. In this theoretical scenario, the regional peak flow variability is caused by just the interplay between rainfall duration and river network structure. Therefore, a power law model with just A is insufficient to represent the regional peak flows. This theoretical scenario provides physical arguments to explore if river network descriptors could improve estimates of real peak flow variabilities, either in rainfall-runoff events or peak flow quantiles. I demonstrate

104

in Chapter 3 that the WFDs can improve regional equations for simulated uniform rainfall events. For rainfall-runoff events, I found that just 15 out of 85 events improve with WFDs. And although this finding could be attributed to the regional variabilities of other processes such as soil moisture fields, I argue that this is partially caused by the number of sites used in the regression analysis, since the improved events exhibit more sites with respect to those who do not improve. The argument that the number of sites controls the inclusion of WFDs is supported in the analysis of the regional peak flow quantiles. In the peak flow quantiles, I observed that all the explored frequencies were improved by the D_B^{NS}, in which a total of 38 sites are used for the regressions, except for the frequencies of 2% and 1% which have 37 and 35 sites respectively (see Table 4-2). In fact, the Monte Carlo simulation demonstrates that the selection of D_B^{NS} as an explanatory variable is very sensitive to the number of sites used in the regression analysis. I found in Chapter 3 for the Iowa River Basin that the WFDs do not improve the regional models of peak flow quantiles in comparison to a regional model with only drainage area. The results of this current chapter explain the findings of Chapter 3, since in Chapter 3 I use only 25 sites in the Iowa River Basin for the estimation of the regional models. The main reason that I use only 25 sites is because I estimate the peak flow quantiles using annual peak flows with sites with more than 30 years of records.

4.7. Conclusions

For the proper use of a scaling theory of floods in flood regionalization, the scaling theory needs to be concerted with the different well-known problems in statistical hydrology related to the development of regional regression equations. The findings of this study contribute to the following specific points

105

1) The performance of the peak flow scaling of 85 rainfall-runoff events with respect to drainage is linked to scaling properties of rainfall-intensity fields. This finding helps us to presume that part of the peak flow variability that is not explained by the power law with drainage area, is a consequence of variabilities in river network structure.

2) The spatial variability of soil moisture fields as antecedent conditions of 24 rainfall-runoff events is linked to the performance of the scaling structure of rainfall-runoff events. I found that more homogeneous soil moisture fields are related to rainfall-runoff events with better scaling.

3) Although in principle the scaling of peak flow quantiles does not come from the same rainfall-runoff events, I found a well-organized structure of the rainfall-intensity fields associated to the peak flow quantiles, suggesting that the river network structure could be used as an explanatory variable for the definition of regional regression equations.

4) I found that the integration of river network structure by means of Width Function Descriptors in regional regression equations improves the peak flow quantile estimations with an average of 15% in reduction of the Root Mean Square Error. I demonstrated that selection of Width Function Descriptors in regional equations are subject to the sampling errors incorporated by short sampling records of peak flows and number of streamflow gauges.

An exhaustive hydrologic simulation analysis needs to be conducted in order to test our findings. For instance, different rainfall fields with different θ_i under different soil moisture conditions can be evaluated in order to observe the change in R_Q^2, and subsequently, investigate if the Width Function Descriptors can improve this variability. With respect to peak flow quantiles, a rainfall generator method can be used to create different rainfall samples in order to investigate

106

if the regional variability of peak flows quantiles can be explained by width function descriptors. In the following chapter, I used exhaustive hydrologic simulations in order to explore with more detail the contribution of sampling errors and model structures in the estimation of peak flow quantiles

Table 4-1. Description of the streamflow gauges. $N_{Annual\ peaks}$ is the number of annual peak flows recorded by USGS peak flow gauge. N_{15-min} is the number of peak flows extracted from the Partial Duration series using the USGS 15-minutes streamflow data.

ID	USGS Code	Area [km^2]	$Q_{Threshold}$ [m3/s]	$N_{Annual\ peaks}$	N_{15-min}	Regulated
1	5465700	32712	784	9	44	Yes
2	5465500	32375	191	115	194	Yes
3	5465000	20168	155	78	170	No
4	5464780	18324	668	5	14	No
5	5464500	16861	93	116	220	No
6	5464420	16426	276	8	70	No
7	5464315	15644	309	8	59	No
8	5464000	13328	88	79	191	No
9	5463050	12261	575	5	15	No
10	5455700	11119	129	61	145	Yes
11	5454500	8472	45	117	226	Yes
12	5453520	8068	99	25	141	Yes
13	5453100	7236	94	62	115	No
14	5451770	4874	77	6	48	No
15	5462000	4522	35	65	166	No
16	5458500	4302	31	97	179	No
17	5458300	4007	72	17	88	No
18	5451500	3968	37	101	144	No
19	5460400	3240	90	6	32	No
20	5457700	2730	17	63	185	No
21	5458900	2191	11	73	190	No
22	5457505	2173	65	6	39	No
23	5455500	1487	27	79	109	No
24	5459500	1362	10	85	160	No
25	5449500	1111	8	76	146	No
26	5457000	1033	15	117	113	No
27	5463000	899	5	72	186	No
28	5458000	793	10	64	127	No
29	5463500	785	6	60	169	No
30	5464220	774	18	19	77	No
31	5451210	580	22	22	66	No
32	5452000	521	14	73	83	No
33	5455100	521	11	67	110	No
34	5453000	490	15	72	96	No
35	5451700	306	4	69	132	No
36	5454300	254	8	65	97	No
37	5452200	184	4	68	104	No
38	5454220	151	10	23	72	No
39	5451900	145	3	68	118	No
40	5454000	66	5	80	74	No
41	5451080	31	4	12	11	No
42	5454090	23	7	11	39	No
43	5464942	7	1	18	47	No

108

Table 4-2. Results for the regression analysis for the model $Q_p = \alpha A^\theta$

p [%]	α [m³/s]	p-value	θ	p-value	AICc	RMSE [m³/s]	adj-R²	N_{sites}
50%	0.71	2.76E-01	0.62	2.74E-16	56.89	137	0.85	38
20%	2.20	8.96E-03	0.58	6.84E-17	52.47	245	0.86	38
10%	4.07	5.22E-06	0.55	2.36E-17	46.15	291	0.86	38
4%	5.52	4.38E-09	0.57	4.01E-20	33.52	283	0.90	38
2%	9.04	1.89E-12	0.54	2.95E-20	23.31	277	0.91	37
1%	10.61	1.42E-11	0.54	9.37E-18	28.58	263	0.89	35

Table 4-3. Results for the regression analysis for the model $Q_p = \alpha A^\theta D_B^{NS\,\beta}$

p [%]	α [m^3/s]	p-value	θ	p-value	β	p-value	AICc	RMSE [m^3/s]	adj-R^2	N_{sites}
50%	0.72	2.73E-01	0.62	1.48E-16	-0.89	4.22E-02	54.71	120	0.87	38
20%	2.24	5.05E-03	0.57	2.99E-17	-0.89	2.79E-02	49.51	221	0.87	38
10%	4.14	2.07E-06	0.54	1.29E-17	-0.78	3.79E-02	43.76	266	0.88	38
4%	5.62	5.14E-10	0.56	6.31E-21	-0.83	7.15E-03	27.92	216	0.92	38
2%	9.34	1.69E-13	0.54	6.07E-21	-0.73	8.12E-03	17.94	211	0.93	37
1%	10.60	1.05E-11	0.54	8.86E-18	-0.53	1.05E-01	28.05	228	0.90	35
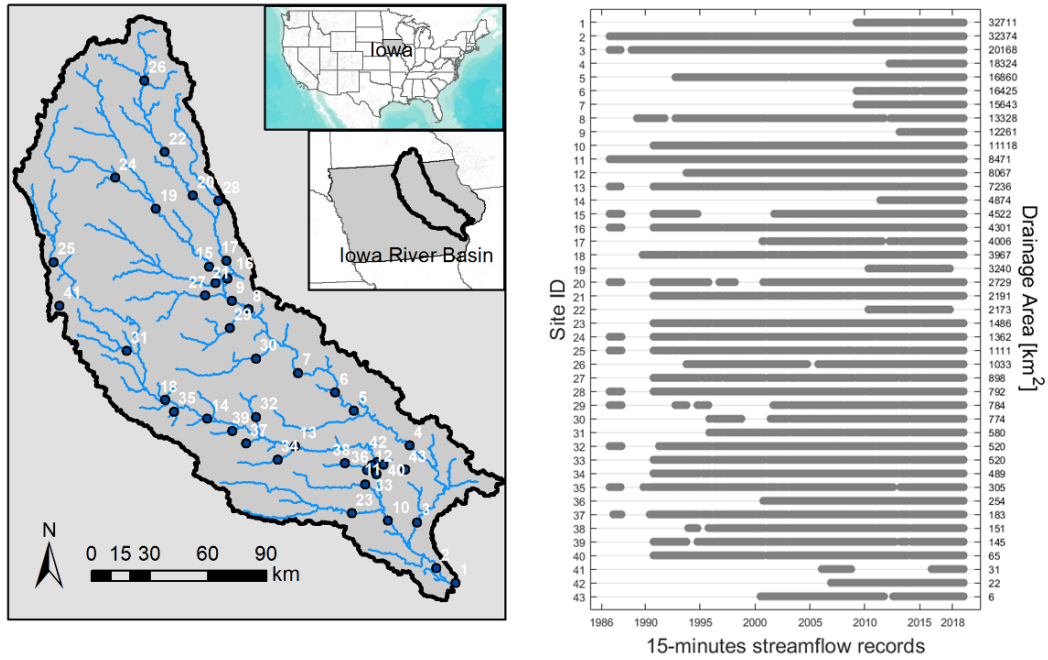
Figure 4-1. Location of the streamflow gauges within the Iowa River Basin (left panel) and length of the 15-minutes streamflow records (right panel).
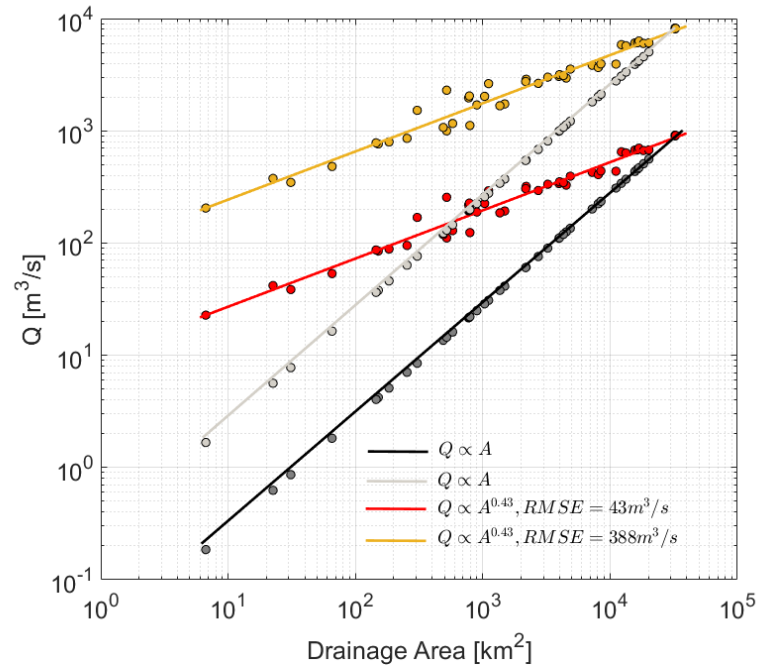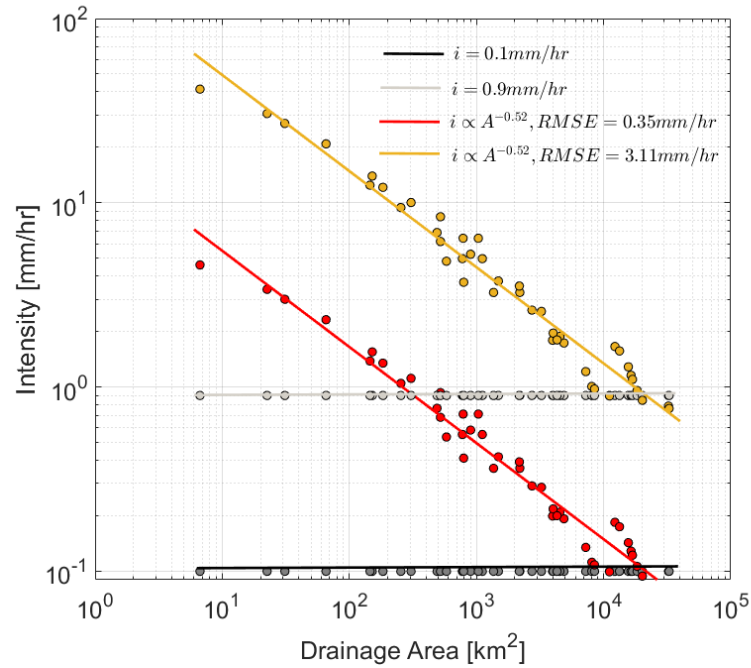
Figure 4-2. Translation of scaling properties from rainfall fields to peak flows in the Iowa River Basin in theoretical scenarios with spatial uniform rainfall fields with large durations (gray and black lines) and instantaneous durations (red and yellow lines).
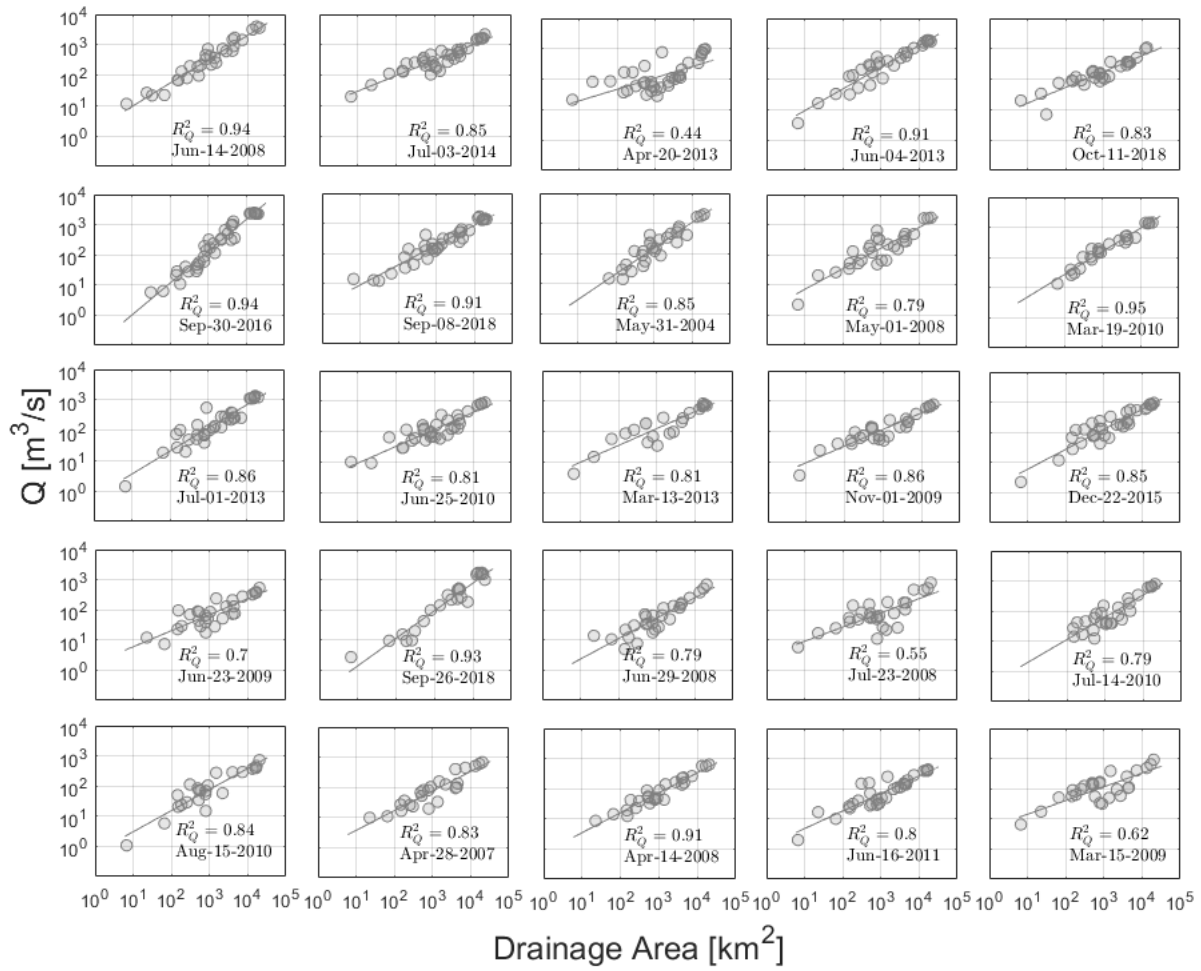
Figure 4-3. Example of 25 peak flow scaling of observed rainfall-runoff events over the Iowa River Basin.
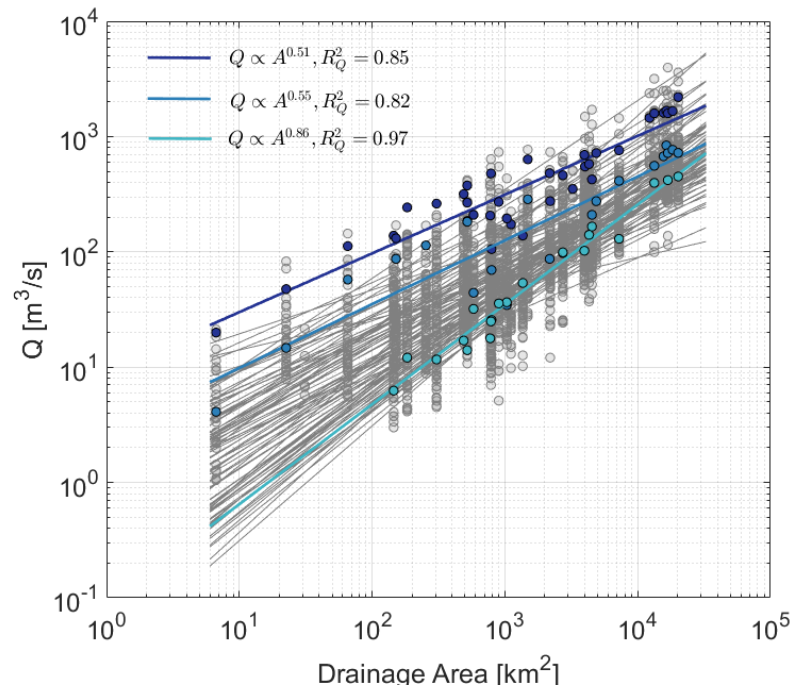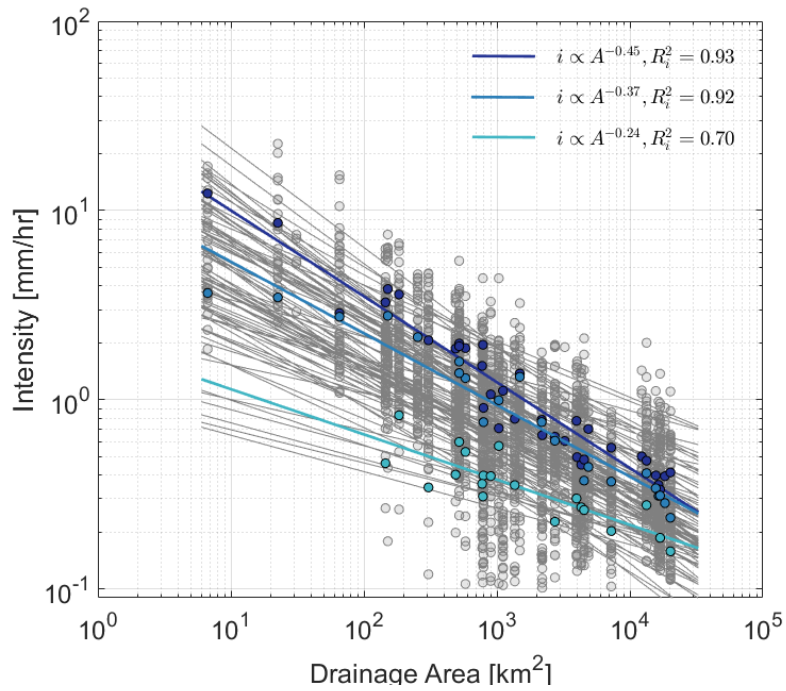
Figure 4-4. Scaling of the observed rainfall intensity fields (left panel) and associated peak flows (right panel). The gray lines represent all the 85 rainfall-runoff events. The three lines with shades of blue represents three different events.
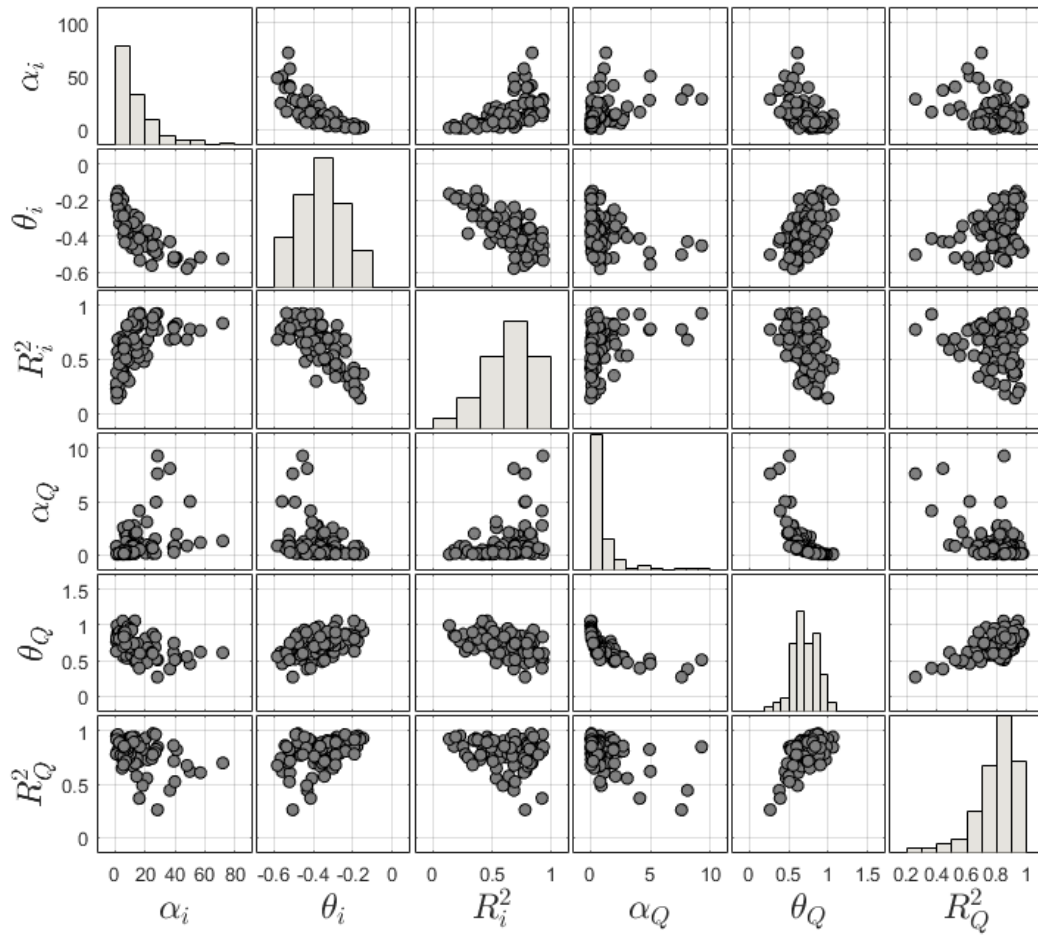
Figure 4-5. Scatter plots showing the relation of scaling parameters between rainfall intensity fields and peak flows of rainfall-runoff events.
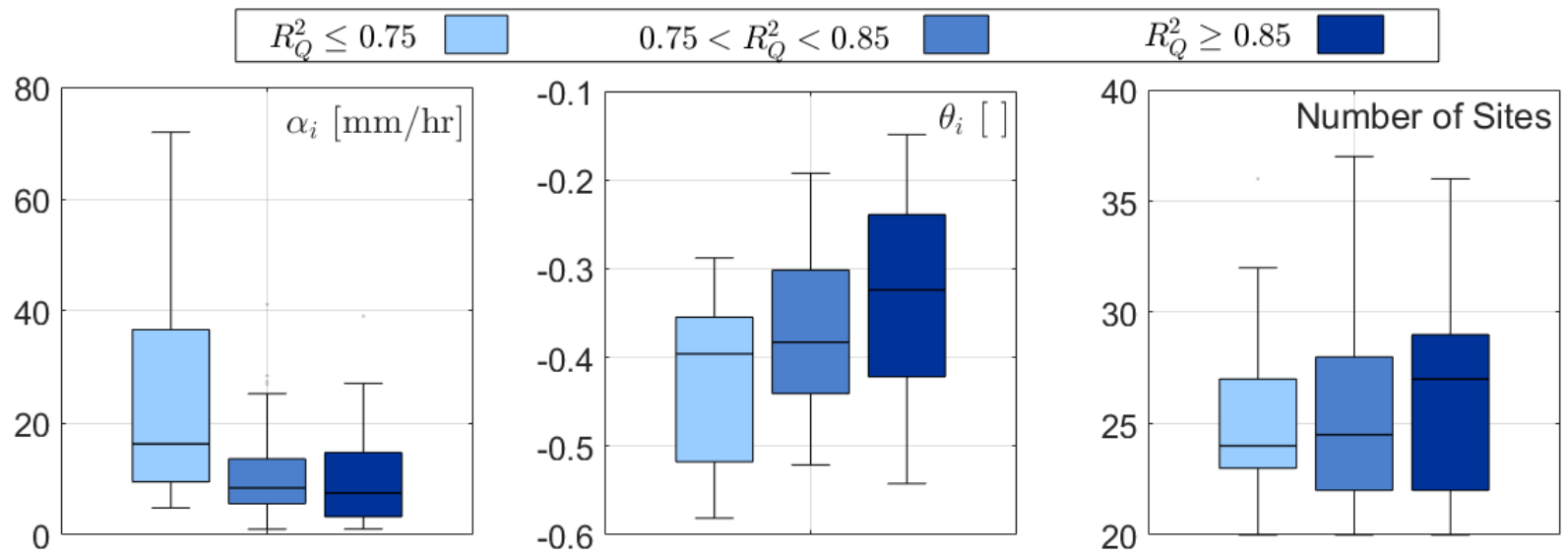
Figure 4-6. Boxplots of the scaling parameters of rainfall intensity fields and number of sites with respect to the performance of the peak flow scaling. Each of groups $R_Q^2 \leq 0.75$, $0.75 < R_Q^2 < 0.85$, and $R_Q^2 > 0.85$ contain 25, 26, and 34 rainfall-runoff events respectively.
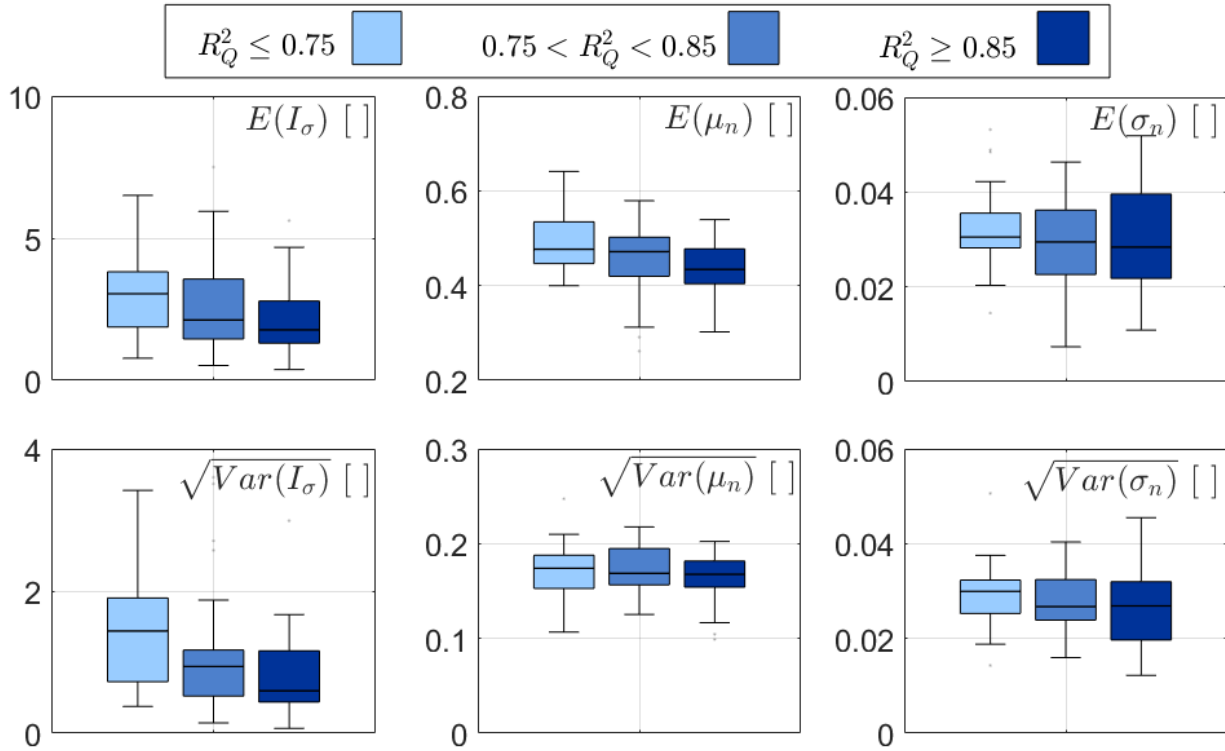
Figure 4-7. Boxplots of rainfall properties with respect to the performance of the peak flow scaling. Each of groups $R_Q^2 \leq 0.75$, $0.75 < R_Q^2 < 0.85$, and $R_Q^2 > 0.85$ contain 25, 26, and 34 rainfall-runoff events respectively.
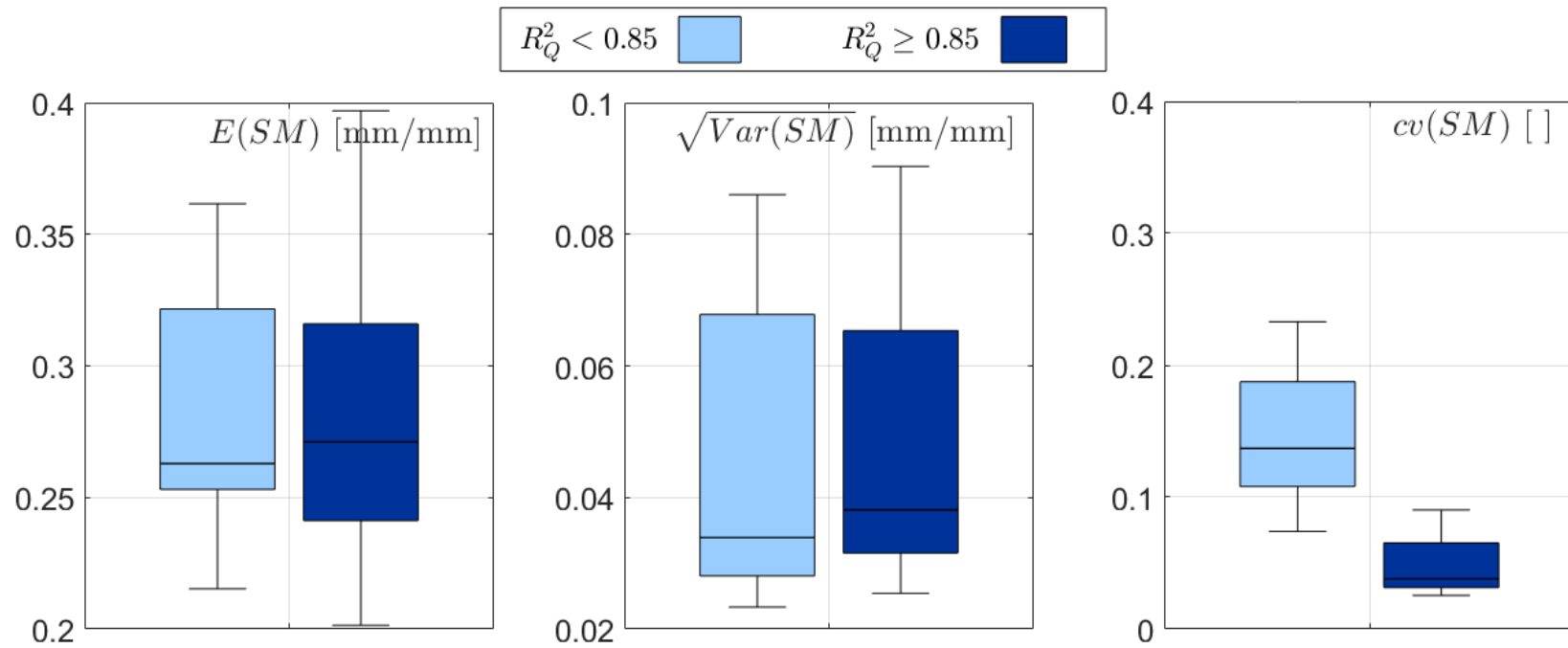
Figure 4-8. Boxplots of soil moisture properties with respect to the performance of the peak flow scaling. Each of groups $R_Q^2 < 0.85$, and $R_Q^2 > 0.85$ contain 10, and 14 rainfall-runoff events respectively.
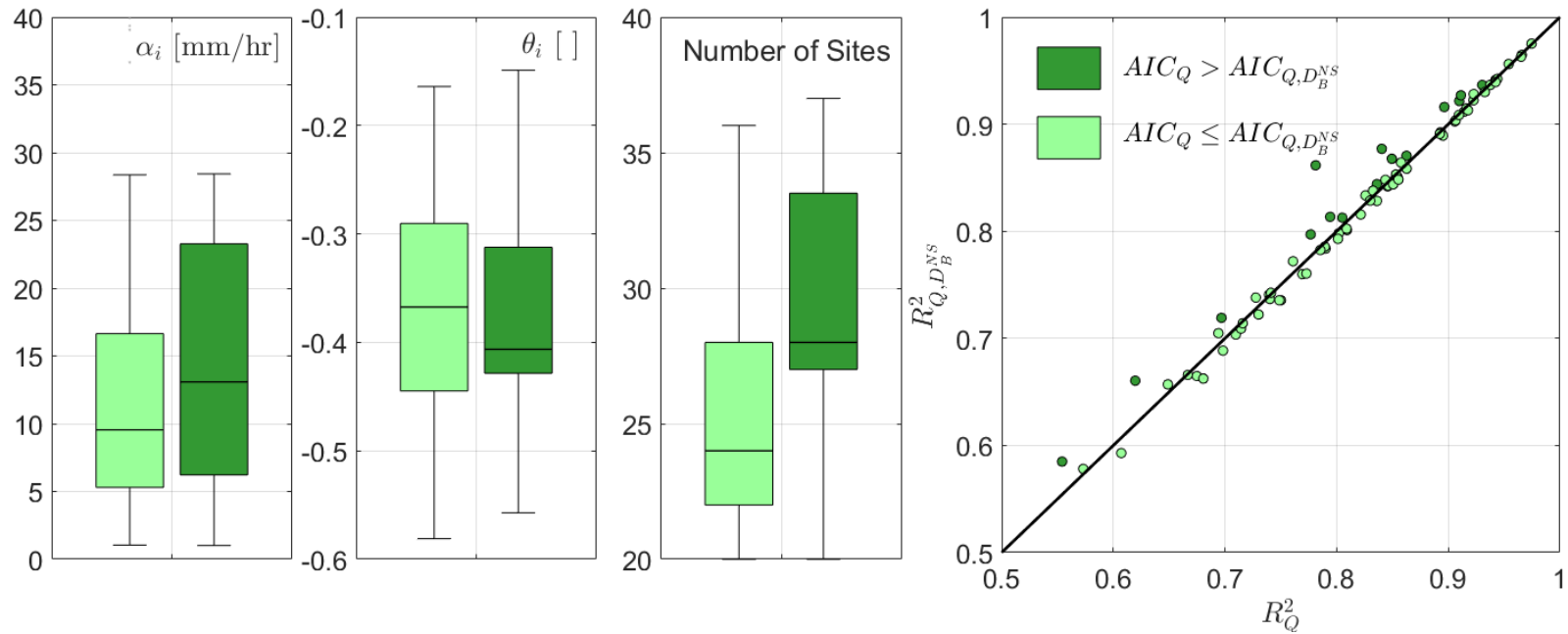
Figure 4-9. Boxplots of the scaling parameters of rainfall intensity fields and number of sites with respect to the best model selected via AIC. The group $AIC_Q > AIC_{Q,D_B^{NS}}$, contains 15 rainfall-runoff events and $AIC_Q > AIC_{Q,D_B^{NS}}$ contains 70 rainfall-runoff events. The sub-index Q represent the model $Q_R = \alpha A^\theta$, and the sub-index Q, D_B^{NS} represent the model $Q_R = \alpha A^\theta D_B^{NS\beta}$.
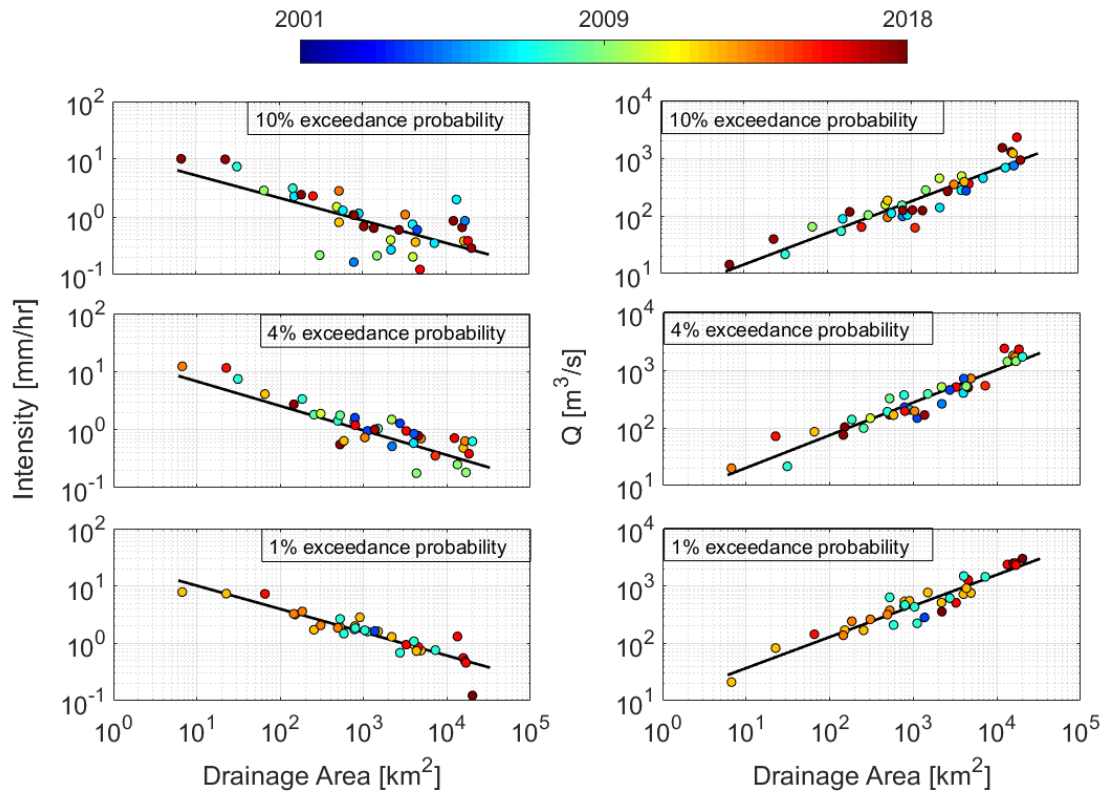
Figure 4-10. Scaling of empirical peak flow quantiles (right panel) and their respective rainfall intensities (left panels) for the probability of exceedance of 10%, 4%, and 1%. The colors show when the rainfall-runoff event occurred.
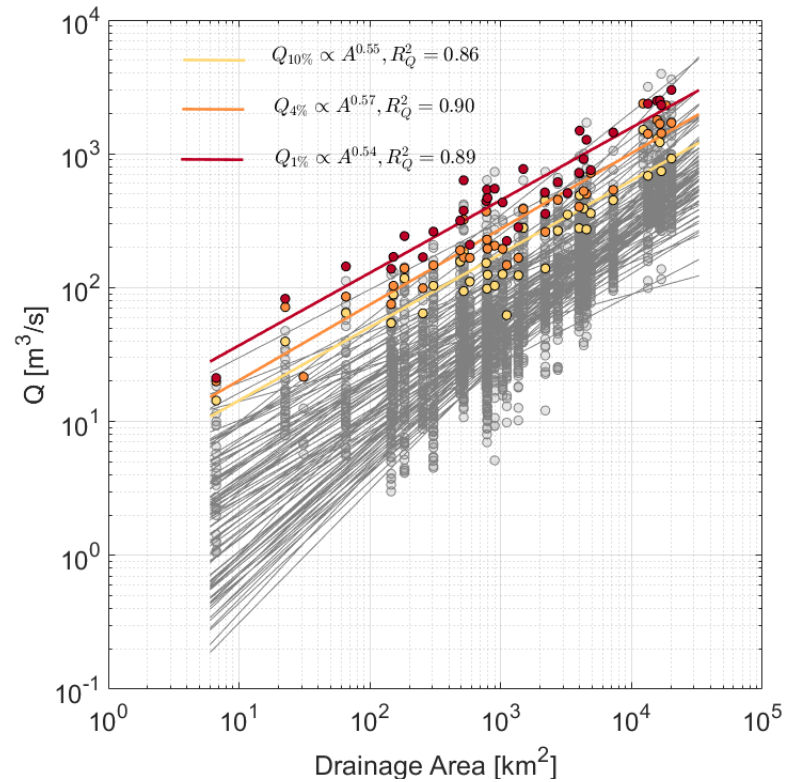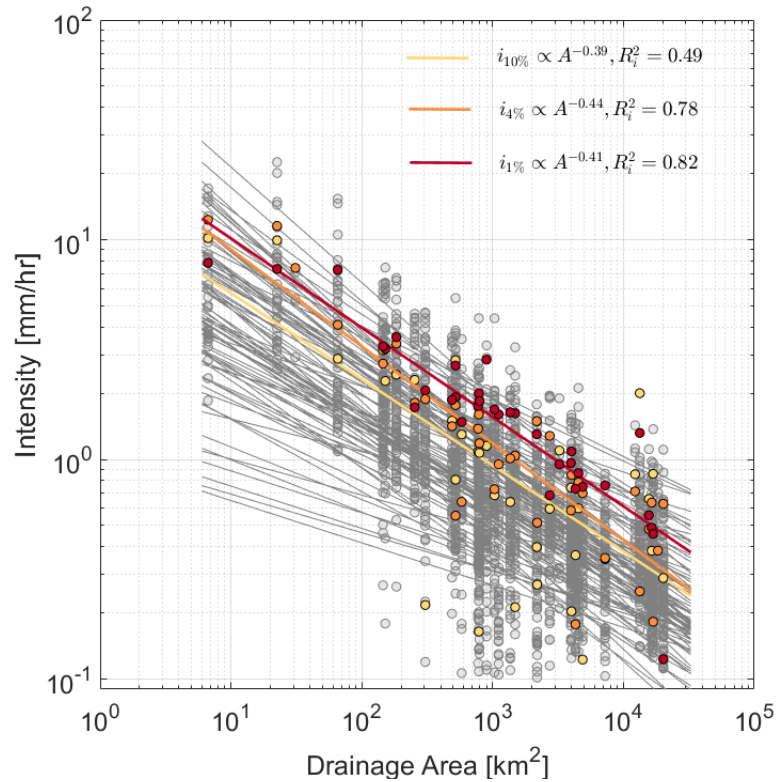
Figure 4-11. Scaling of empirical peak flow quantiles (right panel) and their respective rainfall intensities (left panels) for the probability of exceedance of 10% (yellow line), 4% (orange line), and 1% (red line). As reference the gray lines are the scaling of the observed 85 rainfall-runoff events.
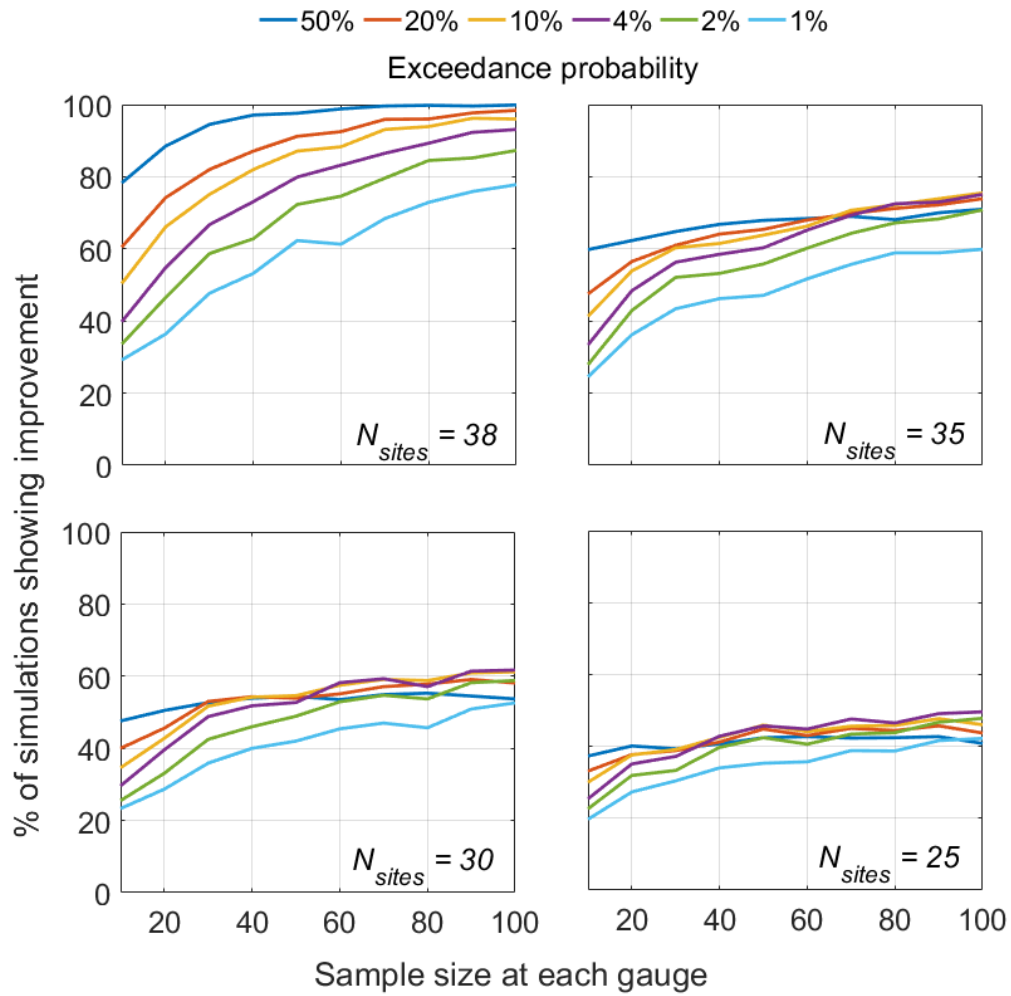
Figure 4-12. Results of the Monte Carlo simulation for the evaluation of the sensibility of model selection as function of exceedance probability, sample size, and number of streamflow gauges (N_{sites})

CHAPTER 5: USING PHYSICALLY-BASED SYNTHETIC PEAK FLOWS TO ASSESS LOCAL AND REGIONAL FLOOD FREQUENCY ANALYSIS METHODS [4]

5.1. Introduction

In situations in which flood peak observations are available, Peak flow quantile (PFQ) estimation is often based on one of two frameworks, both of which consist of fitting statistical distributions to these observations: At-Site Flood Frequency Analysis (ASFFA) and Regional Flood Frequency Analysis (RFFA). ASFFA uses observations at the (gauged) site of interest, while RFFA uses observations from a "homogeneous region" to estimate PFQ at either gauged or ungauged sites. Some of the most popular RFFA methods are the Index Flood Method (IFM) (e.g., Hailegeorgis & Alfredsen 2016; Hosking & Wallis 1997; Odry & Arnaud 2017; Saf 2009), the Quantile Regression Technique (QRT) (Ahn & Palmer 2016; Gupta & Dawdy 1995; Haddad et al. 2011), and the Parameter Regression Technique (PRT) (Ahn & Palmer 2016; Haddad et al. 2012; Malekinezhad et al. 2011). These methods are discussed in more detail in Section 5.3.

Relatively small samples of flood peak records (less than 100 years in most locations) can translate to large uncertainties because of sampling size limitations (henceforth denoted by ε) in estimates of rare quantiles such as the 100- or 500-year flood, since these are estimated from the sample rather than the population. The main objective of RFFA is to reduce these sampling errors by pooling regional peak flow information from other sites. Epistemic error (henceforth denoted by δ), on the other hand, represents the failure of the chosen statistical model (i.e., distribution) to represent the true quantity to be estimated. The quantification of the epistemic error for quantile estimates is challenging since the "true" underlying distribution is unknown.

Synthetic peak flows can help elucidate sampling and epistemic errors associated with different ASFFA or RFFA methods because researchers can identify the underlying peak flow distribution beforehand and create large samples. The principle challenge of synthetic approaches is the need for a realistic representation of peak flow distribution parameters. A common example is to evaluate errors for a specific ASFFA distribution with specified parameters. Synthetic evaluation of RFFA techniques is more complex because it requires depiction of the spatial variability of peak flow distributions throughout the region.

Most synthetic studies that have examined errors in RFFA use explanatory variables such as drainage area to vary the distribution parameters within the region. For instance, Stedinger & Tasker (1985) used a Monte Carlo experiment to evaluate PFQ estimates produced by different regression analysis methods. They generated synthetic peak flows based on the first three moments of the peak flow series, they represent the mean, and standard deviation as a linear function of the logarithms of the drainage area, and a zero skewness. Follow-up work (Stedinger & Tasker 1986) used a Pearson Type III (P3) distribution for site i with mean μ_i, standard deviation σ_i, and nonzero skewness $\gamma_i \sim N[0, \sigma_\gamma^2]$, with $\sigma_\gamma^2 = 0.5$, corresponding to the variance of nationwide (U.S.) skewness. More recently, Micevski & Kuczera (2009) evaluated epistemic and sampling errors of QRT with synthetic samples for 80 sites using a true regional model $\theta_i \sim N(2 + 0.3z_i, \sigma_R^2)$ in which θ_i and z_i are the peak flow quantile and a catchment descriptor for each site i respectively, and σ_R^2 is the true epistemic error. Sveinsson et al. (2001) performed a synthetic evaluation of IFM using the Generalized Extreme Value (GEV) and Log Pearson Type III (LP3) distributions; they assumed that the skewness in the region was constant in order to preserve the homogeneity assumption implicit in IFM (see Section 5.3.2.2). Similarly, Nguyen et al. (2014) evaluated IFM using Monte Carlo simulations for the GEV distribution, including

124

cases without regional variability (constant skewness) and a degree of spatial variability. Halbert et al. (2016) also used a Monte Carlo simulation to evaluate the effects of sampling variability and the consequences of two forms of regional heterogeneity in IFM using synthetic data based on the GEV. The first form was in the Index Flood Factor (similar to Nguyen et al. (2014)), while the second was heterogeneity in the distribution parameters.

The scientific community is still debating how best to select a local or regional method to estimate PFQs. For instance, Odry & Arnaud (2017) evaluated the relative performance of ASFFA, PRT, IFM, and a process-based simulation approach using peak flow observations in France. Using the Gumbel distribution for ASFFA and the GEV distribution for PRT and IFM, they found that for the 10-year flood peak, ASFFA and PRT perform slightly better than IFM, while for longer return periods (e.g., 100-year), PRT performance decreased. Hailegeorgis & Alfredsen (2016) used ASFFA with the generalized logistic distribution and IFM; they found that the resulting uncertainty estimates failed to "cover" the at-site (i.e., ASFFA) estimates for some catchments in Norway. Haddad & Rahman (2012) compared PFQ estimates in eastern Australia using QRT and PRT with the LP3 distribution, concluding that the two show similar performance. Ahn & Palmer (2016) compared QRT and PRT for the Northeastern United States using the GEV, showing that QRT had slightly better performance than PRT. Malekinezhad et al. (2011) performed a comparison between IFM and QRT based on L-moments for peak flows in Iran. They concluded that the IFM gives more reliable estimates for a range of recurrence intervals. Halbert et al. (2016) compared PFQ estimates between ASFFA and IFM for peak flow observations in France using the GEV distribution; their study showed similar performance from both methods. This study is the only one we found that used synthetic cases with the inclusion of

125

heterogeneities in the parameters of the local distribution to evaluate the performance of the IFM.

This chapter seeks to address two issues that have not received enough attention in the aforementioned literature. First, while the existing literature examines sampling error and epistemic errors under idealized RFFA scenarios, it is unclear whether the spatial depictions of distribution parameters are realistic because peak flow distributions are controlled by regional rainfall and geomorphologic characteristics (Ayalew & Krajewski 2017; Black 1972; Mandapaka et al. 2009) that are not explicitly represented in prior studies. Second, a synthetic study comparing error components of PFQs induced by local and regional approaches as a function of sample size and, in the case of regional approaches, the number of pooled sites, has not yet been conducted. I did not find any synthetic studies using rainfall-runoff models for the evaluation of regional methods to estimate PFQs. Thus, the present study presents a unique contribution in the use of hydrologic simulations for the evaluation of RFFA methods.

The structure of this chapter is as follows: Section 5.2 describes the generation of synthetic peak flows in a watershed based on Stochastic Storm Transposition (SST) and hydrologic modeling. Section 5.3 describes the local and regional procedures used to estimate the PFQs, as well as the epistemic error estimation and Monte Carlo simulation procedures to evaluate sampling errors. Section 5.4 presents results and discussion, including a subsection that provides insights into the controls of the regional peak flow variability through the regional skewness. Finally, I finish with a section of conclusions with final remarks.

5.2. Physically-Based Synthetic Peak Flows

Physically-realistic synthetic rainfall and resulting flood peaks for the Turkey River watershed (4,385 km^2), located in northeast Iowa in the midwestern United States (Figure 5-1) are simulated. I generated synthetic peak flows through a combined framework of stochastic storm transposition (SST), based on RainyDay (Wright et al. 2017), and the distributed hydrologic model Hillslope Link Model (HLM) (Krajewski et al. 2017; Mantilla & Gupta 2005; Quintero et al. 2016). We refer to this combined framework as RainyDay-HLM.

5.2.1. Observation-Driven Stochastic Storm Event Generation

RainyDay is an open-source software developed to couple SST with rainfall remote sensing data for observation-driven rainfall and flood frequency analysis Wright et al. (2017). The objective of SST is to increase the extreme rainfall records by means of temporal resampling and spatial transposition of storms from the surrounding region (e.g., Alexander (1963); Fontaine & Potter (1989); Foufoula-Georgiou (1989); Franchini et al. (1996)). RainyDay's SST methodology has five main components: (1) identification of a geographic transposition domain *A'* that encompasses the watershed of interest *A*; (2) creation of a "storm catalog" of the largest *m* temporal non-overlapping storms in *A'* from an *n*-year rainfall remote sensing dataset, in terms of rainfall accumulation of duration *t* and with the same size, shape, and orientation of watershed *A;* (3) random generation of annual storm frequency *k* (Poisson-distributed); (4) random selection of *k* storms from the storm catalog; and (5) random transposition of the rainfall fields associated with each storm in east-west and north-south distance. In this step, the largest (in terms of rainfall intensity) rainfall event over *A* is retained and can be understood as a "synthetic" annual rainfall maxima. Steps 3 and 4 are repeated with a user-specified T_{max}, the number of annual rainfall maxima to be synthesized for *A*. The selection of *A'* requires an

127

understanding of spatio-temporal features of the regional rainfall patterns (Pavlopoulos and Krajewski, 2014; Thorndahl et al., 2014). As mentioned in Wright et al. (2017) the method would be limited to small and flat regions far from topographic features. See Wright et al. (2017) for a more detailed description of limitations and advantages of RainyDay.

For the Turkey River Basin case study, a domain A' covering most of Iowa, southwestern Wisconsin, and southeastern Minnesota was used (see Figure 5-1 – Panel B). The April-November Stage IV rainfall data, which are based on weather radar and rain gauge observations (Lin & Mitchell 2005), for the years 2002-2016 is used to identify 300 storms in A' with the same size, shape, and orientation as A. The number of storms per year is Poisson-distributed with rate parameter of 20 storms per year (300 storms divided by 15 years). A T_{max} equal 10,000 is selected, meaning that we used 10,000 rainfall events and their associated hourly, 4 km rainfall fields for the rainfall-runoff modeling described in Section 4.2.2. Each rainfall event is at most 72 hours long, with 14 days of "spin-up" pre-pended to initialize seasonally-appropriate initial conditions as described in Wright et al. (2017).

5.2.2. Rainfall-Runoff Hydrologic Modeling

The 10,000 rainfall events generated in the previous subsection are used as inputs for the hydrologic distributed model HLM, which has been adopted at the Iowa Flood Center (IFC) at the University of Iowa. HLM's key features include the decomposition of the landscape into hillslope-channel-link components and the use of the mass and momentum conservation equations at the hillslope-channel-link scale. The HLM model for Turkey River Basin comprises 237,000 hillslope-link units with an average hillslope area of 0.018 km^2, which are extracted from a one-meter resolution LiDAR Digital Elevation Model. The model describes changes in storage components using a system of non-linear ordinary differential equations, which are

solved using a parallel implementation of Runge-Kutta methods that allow for asynchronous integration (Small et al. 2013). The resulting peak flows from each simulation at 5,000 sites across the Turkey River Basin are extracted. The 5,000 sites are randomly selected in order to cover all the ranges of drainage area from 1 to 4,385 km^2 (see Figure 5-1 – Panel A).

The HLM model has been used and validated in different studies in Iowa (Cunha et al., 2012; Krajewski et al., 2017; Ricardo Mantilla et al., 2012; Quintero et al., 2018; Seo et al., 2018; D. B. Wright et al., 2017). Most notable, Wright et al. (2017) present a flood frequency analysis for the Turkey River Basin using 500 rainfall scenarios from RainyDay with the hydrologic model HLM. Their results show that the HLM is able to replicate not just the hydrographs to different spatial scales in the Turkey River Basin, they also show that the peak flow quantiles estimated using RainyDay-HLM are higher than the USGS estimation. Wright et al. (2017) also demonstrated that the coupling of RainyDay and HLM can produce realistic flood frequency results, often superior to traditional RFFA estimates in Turkey River because of hydrologic nonstationarities in that watershed, assuming that the nonstationarities results are consequence of a trend of rainfall, then recent rainfall remote sensing record should be considered as more relevant information for flood frequency estimation. Here, I assumed that the synthetic sample of 10,000 flood peaks represents annual maxima flows at each site which is representing the underlying population distribution. Therefore, we could calculate the exceedance probability p for each peak in the dataset as $p = j/(1 + T_{max})$, where j is the rank of the peak.

5.3. Methods

5.3.1. Error Components

I extended the regression error component formulation of Kjeldsen & Jones (2009) to also examine statistical distributions. For this statistical analysis, I consider $Q_i(p)$ as the true population value of the PFQ with a probability of non-exceedance p for a site i. Let $\Theta_i(p)$ be the sample estimate of $Q_i(p)$; therefore,

$$Q_i(p) = \Theta_i(p) + \varepsilon_i \qquad \text{Equation 5-1}$$

where, ε_i is the sampling error. Let $\hat{Q}_i(p)$ be the estimated value of $\Theta_i(p)$, proffered by a fitted function $\Psi_i^p(X)$ where X can be the parameters of the function (e.g., drainage area or mean flood if $\Psi_i(X)$ is a regression model, or a distribution's parameters if $\Psi_i(X)$ is a probability density function (PDF)). $\Theta_i(p)$ can be expressed as

$$\Theta_i(p) = \hat{Q}_i(p) + \eta_i \qquad \text{Equation 5-2}$$

where η_i is the epistemic error, which represents the failure of $\hat{Q}_i(p)$ to represent $\Theta_i(p)$. Combining Equations 5-1 and 5-2, $Q_i(p)$ can be expressed in terms of sampling error and epistemic error:

$$Q_i(p) = \hat{Q}_i(p) + \eta_i + \varepsilon_i \qquad \text{Equation 5-3}$$

In the following subsections, we describe $\Psi_i^p(X)$ for different methods to estimate peak flow quantiles $\hat{Q}_i(p)$.

5.3.2. Local and Regional Flood Frequency Analysis Approaches

5.3.2.1. At-Site Flood Frequency Analysis (ASFFA)

The basis of ASFFA is to fit and select the best PDF of peak flows from a set of candidate distributions, with the assumption that the peak flow observations are independent and

130

identically distributed (i.i.d.). ASFFA has well-known limitations and challenges, including the validity of the i.i.d. assumption in the presence of nonstationarities, sampling errors, and parameter estimation challenges stemming from short time series (Strupczewski et al. 2011).

Studies by Beard (1974), Haktanir & Horlacher (1993), Hosking & Wallis (1997), Strupczewski et al. (2011), and Vivekanandan (2015) examined the Exponential, GEV, Generalized Pareto, Normal, Log-Normal, LP3, and P3 distributions in the United States and Europe. Beard (1974) (summarized in IACWD 1982) found that the LP3 distribution with a regional skew coefficient performed well for the United States. Griffis & Stedinger (2007) showed that the LP3 is very flexible and encompasses a wide range of reasonable models for log-space skews.

Various methods exist to estimate distribution parameters, including Maximum Likelihood Estimation, Method of Moments (MoM), L-moments, Probability Weighted Moments, and Expected Method of Moments (e.g., England et al. 2015; Greenwood et al. 1979; Hosking & Wallis 1997; Lim & Voeller 2009; Vivekanandan 2015; Vogel et al. 1993). Parameter estimates and epistemic errors depend on the method, and some methods are theoretically preferable to others. L-moments, for example, are in principle subject to lower biases than ordinary product-moments in small-sample situations (Hosking 1990; Hosking & Wallis 1997). Bulletin 17C recommends use of the Expected Method of Moments for the parameter estimation using an LP3 distribution for the peak flow distributions in the United States. (England et al. 2015; Paretti et al. 2014).

I explored four PDF candidate distributions: the Pearson-3 (P3), LP3, GEV, and 3 parameter Weibull. I used MoM and L-moments for distribution fitting and selected the "best"

131

distribution at each of the 5,000 simulation points based on the root-mean-square error between the theoretical and empirical cumulative density functions (CDFs).

As an example, $\Psi_i^p(X)$ for a site i can be prescribed from an assumed CDF $F(\hat{Q}_i|a_i, b_i, c_i)$ where a_i, b_i, c_i are the location, scale and shape parameters of the peak flow distribution estimated via MoM or L-moments. Then $\Psi_i^p(X) = G(a_i, b_i, c_i)$, with $G(a_i, b_i, c_i)$ representing the numerical estimate of $\hat{Q}_i$ for the case that $F(\hat{Q}_i|a_i, b_i, c_i) = p$, in which p is a specific probability of non-exceedance. Then, using $\Psi_i^p(X) = G(a_i, b_i, c_i)$ to estimate $\hat{Q}_i(p)$ in Equation 5-3, the peak flow quantile for a probability of non-exceedance p is given by

$$Q_i^{[ASFFA]}(p) = G(a_i, b_i, c_i) + \eta_i + \varepsilon_i \qquad \text{Equation 5-4}$$

where η_i is the epistemic error and ε_i is the sampling error for the estimates of $Q_i(p)$ from the assumed peak flow distribution. If a population is used to estimate the parameters, then ε_i is equal to zero and all error is attributed to η_i.

5.3.2.2. Index Flood Method (IFM)

IFM is a common approach to reduce the sampling error through the pooling of regional peak flow information from other sites and has been shown to improve at-site frequency estimation (Hosking &Wallis 1997; Odry & Arnaud 2017). IFM assumes that the peak flow data from pooled sites follow a common distribution, modified with an Index Flood Factor, which is a function of other characteristics, such as the mean annual flood. The presence of regional heterogeneity can reduce the performance of IFM (Halbert et al. 2016). I used the mean annual flood ($\bar{Q}$) as the Index Flood Factor, calculated as the arithmetic mean of the peak flow simulations.

132

As an example of the IFM, lets assume a regional CDF $F(Q^*|a^{[R]}, b^{[R]}, c^{[R]})$ where Q^* is a normalized peak flow with respect to the Index Flood Factor, and $a^{[R]}, b^{[R]},$ and $c^{[R]}$ are the weighted average of the distribution parameters of Q^* for all the sites within the homogeneous region. Then, $\Psi^*(X) = G(a^{[R]}, b^{[R]}, c^{[R]})$, in which $G(a^{[R]}, b^{[R]}, c^{[R]})$ represents the numerical estimate of Q^* for the case that $F(Q^*|a^{[R]}, b^{[R]}, c^{[R]}) = p$, in which p is a specific probability of non-exceedance. Using $\Psi_i^p(X) = \bar{Q}_i \Psi^*(X)$ to estimate $\hat{Q}_i(p)$ in Equation 5-3, the pth peak flow quantile estimated for site i is given by

$$Q_i^{[IFM]}(p) = \bar{Q}_i G(a^{[R]}, b^{[R]}, c^{[R]}) + \eta_i + \varepsilon_i \qquad \text{Equation 5-5}$$

5.3.2.3. Quantile Regression Technique (QRT)

QRT involves "regional regressions" between PFQs and a set of explanatory variables related to basin characteristics. These regressions can use ordinary least squares (OLS), weighted least squares (WLS), or generalized least squares (GLS). OLS assumes equal variance across all the sites, while WLS can account for the varying sampling errors in the at-site quantile estimators. GLS is the most appropriate because it can account for differing record lengths and cross-correlations between concurrent peak flow observations; it can also distinguish between sampling and epistemic errors (Haddad & Rahman 2012; Kroll 1998). GLS can produce regression coefficients with smaller errors and more accurate estimates than the competing OLS estimators (Stedinger & Tasker 1985). GLS, however, is beyond the scope of this chapter.

I implemented QRT using OLS and a single explanatory variable, either drainage area (A) or the mean annual flood ($\bar{Q}$). I explored two QRT models: QRT-A and QRT-$\bar{Q}$, that is,

$$\Psi_i^p(A_i) = \varphi(p) A_i^{\theta(p)} \qquad \text{Equation 5-6}$$

$$\Psi_i^p(\bar{Q}_i) = \varphi(p) \bar{Q}_i^{\theta(p)} \qquad \text{Equation 5-7}$$

133

Combining Equation 5-3 with the estimation of $\hat{Q}_i(p)$ using equations Equation 5-6 and Equation 5-7, the PFQ with a probability of non-exceedance p for any site i with its respective error components is given by

$$Q_i^{[QRT-A]}(p) = \varphi(p)A_i^{\theta(p)} + \eta_i + \varepsilon_i \qquad \text{Equation 5-8}$$

$$Q_i^{[QRT-\bar{Q}]}(p) = \varphi(p)\bar{Q}_i^{\theta(p)} + \eta_i + \varepsilon_i \qquad \text{Equation 5-9}$$

5.3.2.4. Parameter Regression Technique (PRT)

PRT consists of regional linear regressions between the distribution parameters of an assumed distribution with respect to explanatory variables. I singly consider A and $\bar{Q}$, then for instance the regression models using A are:

$$a_i^{[PRT-A]} = \varphi_a A_i^{\theta_a} \qquad \text{Equation 5-10}$$

$$b_i^{[PRT-A]} = \varphi_b A_i^{\theta_b} \qquad \text{Equation 5-11}$$

$$c_i^{[PRT-A]} = \varphi_c A_i^{\theta_c} \qquad \text{Equation 5-12}$$

where $\varphi_a, \varphi_b, \varphi_c, \theta_a, \theta_b,$ and θ_c are regression coefficients estimated by means of OLS. Then, $a_i^{[PRT-A]}$, $b_i^{[PRT-A]}$, and $c_i^{[PRT-A]}$ can be substituted into Equation 5-5 to get the PFQ with a probability of non-exceedance p:

$$Q_i^{[PRT-A]}(p) = G(a_i^{[PRT-A]}, b_i^{[PRT-A]}, c_i^{[PRT-A]}) + \eta_i + \varepsilon_i \quad \text{Equation 5-13}$$

A similar equation is obtained using $\bar{Q}$ as explanatory variable

$$Q_i^{[PRT-\bar{Q}]}(p) = G(a_i^{[PRT-\bar{Q}]}, b_i^{[PRT-\bar{Q}]}, c_i^{[PRT-\bar{Q}]}) + \eta_i + \varepsilon_i \quad \text{Equation 5-14}$$

5.3.3. Evaluation of Scenarios

I created different "scenarios" in terms of number of peak flows at each site (M) and number of pooled sites (N) to quantify the performance of the local and regional methods with respect to the "true" PFQs calculated from the empirical CDF using the 10,000 peak flows

derived from the RainyDay-HLM framework. I evaluated the scenarios based on a Monte Carlo simulation with a random sampling of *M* and *N*. Figure 5-2 shows a flow chart of this quantification.

Ten thousand rainfall events create 10,000 peak flows for each of the 5,000 sites in Turkey River. As an example, Figure 5-3 shows the precipitation depth and peak flows in the outlet of the Turkey River basin for 1,000 simulations of RainyDay-HLM. This dataset contains a strong dependence structure in the peak flows because of the aggregation and attenuation of runoff events through the river network. We can evaluate the influence of this dependence on PFQ estimates in IFM, QRT, and PRT via the inclusion (or exclusion) of dependent (or independent) peak flow values between sites. For that reason, the type of dependence in the random draw of peak flows in the Monte Carlo simulation needs to be established for each scenario. I defined three different types of dependencies between peak flows, as follows: (1) **Full Dependence**, in which the random draws of peak flows for different sites come from the same rainfall event; we should thus expect a non-negligible cross-correlation of peak flows; (2) **Full Independence**, in which the random draws of peak flows for different sites come from different rainfall events; and (3) **Partial Dependence**, a case that mimics real datasets, in which some portion of the various peak flow records comes from the same rainfall events.

The sampling schema for the Partial Dependence case is constructed as follows: for site *i*, we started with a with *N-1* sites selected randomly without repetition from the 5,000 sites. For the *N* sites (including site *i*), then an average value of M^* peak flows per site is fixed. Then, if we assume that in the last 10 years of records all the sites have peak flows, we will need at least 10 peak flows ($M^* \geq 10$) with Full Dependence structure between sites. Next, the remainder of the peak flows from an initial set with Full Dependence in peak flows of size $2(M^* - 10)$ is

135

selected. I assigned an order from 1 to $2(M^* - 10)$ to these peaks and performed a uniform random selection in the interval 1 to $2(M^* - 10)$ to define the number of new peaks assigned to each site. Note that the expected value of the number of random selections between 1 to $2(M^* - 10)$ is $M^* - 10$, and if we add the initial 10 peak flows in each site, we will have an expected value equal to M^*. This approach for the generation of random sites may be useful to create synthetic series with a spatial dependence that mimics that observed in real peak flow datasets.

I evaluated the effect of N, M, and the type of peak flow dependence on the error components for each of the local and regional methods for five cases. Case 1 used all the sites (N=5,000) with the peak flow population (M=10,000). The goal of the analysis of this case was to quantify the contribution of the epistemic error for the different estimation methods of PFQs. Here, the true PFQs with respect to PFQs obtained from ASFFA, IFM, QRT, and PRT are compared. Case 2 evaluated the sampling error for each site in the estimation of PFQs using the local and regional methods. For the PFQ estimates with ASFFA, M peak flows are used, and for the PFQ estimates with IFM, QRT, and PRT, the at-site data and regional data from N-1 pooled sites are used, with each site having M peak flows with full dependence in the random draw of the peak flow data. Then, for each site and each possible combination of N and M, I randomly drew a realization of peak flows (without replacement) from the peak flow population. I used $N = \{10, 20, 40, 60\}$ and $M = \{10, 20, \dots, 140, 150\}$, for a total of 56 possible combinations of N and M. A total of 1,000 Monte Carlo realizations were performed for each site i and combination of N and M. Case 3 is similar to Case 2, but it has a Full Independence feature in the random draw of the peak flow data. Case 4 is similar to Case 2, but it has a Partial Dependence feature in the random draw of the peak flow data. For Cases 2, 3, and 4, the mean annual flood $(\bar{Q})$ was

calculated as the mean of the peak flow sample, and for the Case 1 it was the mean of the population.

5.4. Results and Discussion

5.4.1. Distribution Selection

Case 1, fitting distributions to all 10,000 simulated flood peaks at all 5,000 sites in the Turkey River Basin, shows that P3 most accurately represents the simulated peak flow distributions. Figure 5-3 illustrates this result for four different sites with differing drainage areas. In the subsequent analyses, I thus used the P3 distribution as the "true" regional distribution to represent the PFQs. It is important to note that the P3 distribution is an emergent invariant for our synthetic hydrological system. Actual peak flow distributions in nature may follow heavy tail distributions (e.g. LP3), and in those cases the use of thin tailed distributions such as P3 distribution will underestimate the frequency and the magnitude of extremes. The determination of the character of the distribution of peak flows in natural rivers remains an open in very relevant question.

The adequacy of the fitted distribution depends on the parameter estimation method; Figure 5-4 presents the results based on L-moments. I considered MoM as well. I found a significant difference between MoM and L-moments, which I discussed further in Section 5.4.2. Figure 5-5 shows the mean (μ), standard deviation (σ), and skewness (γ) of the population (i.e., the 10,000 peaks) with respect to drainage area. The first and second moments show strong power law dependence with drainage area. However, the third moment (skewness) shows a weaker and more complex dependence structure. Figure 5-6 shows the spatial distribution of the skewness. The northwest part of the watershed exhibits higher skewness (around 3.5), while values elsewhere are around three. Note that the estimations of lower quantiles (i.e., higher return

137

periods) are very sensitive to the third moment; the performance of the local and regional methods, therefore, depends on the accuracy of its prediction. In Section 5.4.4, I provide insight into the geomorphologic properties that explain the spatial variability of the skewness.

5.4.2. Evaluation of Epistemic Error

I evaluated the epistemic errors associated with the four estimation methods using data obtained from the scenario described in Case 1. The epistemic error is represented as the relative bias (RB) calculated as the relative difference of the estimated PFQs by an estimation method (ASFFA, IFM, QRT, PRT) with respect to the true PFQs calculated from the empirical CDF. Figure 5-7 compares the estimation of the PFQs with 10-year, 100-year, and 1,000-year return periods using P3 fitted using MoM and L-moments. I analyzed the robustness of the MoM and L-moments by comparing the PFQ estimations using the entire peak flow population at each site, and also after removing the two highest peak flows at each site because P3-based PFQs estimates using MoM can be sensitive to the extreme values. Figure 5-7 - Column A shows this result; some sites have a relative error of approximately -50% for the 10-year PFQ, 25% for the 100-year PFQ, and 50% for 1,000-year PFQ. After the elimination of the two highest peak flows at each site (see Figure 5-7 - Column B), MoM epistemic errors become more stable, with a mean RB near zero. The L-moments, on the other hand, provide unbiased estimates for all the sites, highlighting its robustness to extreme values (Hosking 1990; Hosking & Wallis 1997). The mean (standard deviation) RB for the 5,000 sites using the P3 with L-moments and the entire flood peak population is -0.4% (1.3%) for 10-year PFQs, -0.3% (2.4%) for 100-year PFQs, and -3% (5%) for 1,000-year PFQs. Subsequent PFQs for ASFFA, IFM, QRT, and PRT will be based on the P3 distribution fitted using L-moments.

The evaluation of the epistemic error for the regional methods (IFM, QRT, and PRT) was based on the estimation of the peak flow quantiles using the peak flow population and the pooling of all 5,000 sites. Figure 5-8 shows the epistemic error as the RB for the IFM with respect to the drainage area. IFM uses the mean annual flood as the Index Flood Factor (i.e., scaling factor) to estimate the regional CDF. I found that the mean and standard deviation of the RB of the 10-year PFQ for the 5,000 sites are 0% and 3%, respectively. For the 100- and 1,000-year return periods, the variability of the RB increases, with means (standard deviations) of 0% and 4% (9% and 12%), respectively. In addition, a non-monotonic pattern in the epistemic error as a function of drainage area for the 100- and 1,000-year return periods is observed. We can attribute this to the fact that the regional variability of the skewness is not well explained by the regional CDF under IFM, which is a consequence of the Index Flood Factor's inability to explain all regional peak flow variability.

Figure 5-9 presents two versions of epistemic errors for the QRT and PRT. The first uses drainage area as the explanatory variable; the second uses the mean annual flood. I found that models using the mean annual flood are equivalent in terms of epistemic error with the results found in the IFM. For example, we found differences of less than 1% between both the means and the standard deviations of the RB from QRT, PRT, and IFM. QRT and PRT models using drainage area exhibit higher RB, which varies strongly by drainage area. For instance, the average RB of the 1,000-year quantiles from QRT using the drainage area is approximately 25% for subbasins with drainage areas of ~1 km^2, decreasing to -25% for subbasins around 100 km^2, before increasing to 40% for subbasins with drainage areas larger than 1,000 km^2.

These results highlight the fact that the epistemic error is lower in the ASFFA in comparison to regional approaches in which the entire population is used. RFFA methods should perform better in small sample situations, however, as considered in the next subsection.

5.4.3. Evaluation of Sampling Error

As described in Cases 2, 3, and 4 in Section 3.3, I used the Monte Carlo simulation to quantify the contribution of sampling error to the total error ($\eta + \varepsilon$) in the estimation of PFQs. The only difference among Cases 2, 3, and 4 is the type of random draw of peak flows from the peak flow population. I will start discussing the results for Case 4, since it represents partial dependence which is plausibly resembles the selection of peak flow samples of real data sets. Figure 5-10 shows an example for the Case 4 of the range of the total errors as RB in PFQ estimates from ASFFA, IFM, QRT, and PRT for an arbitrary site with a drainage area of 100 km^2. This illustrates the RB of the 10-year, 100-year, and 1,000-year PFQ estimates as a function of M and with N equal to 20. The 1,000 Monte Carlo simulations for each M allow estimation of the range of RB, shown in Figure 5-10 in the 0.05-0.95 quantile range. The results show that regional methods demonstrate a similar performance in terms of the 0.05-0.95 quantile range of RB. The influence of "pooling" in the regional methods improves the quantile estimation with respect to the ASFFA for longer return periods. For example, the 0.05-0.95 quantile range of RB of the 1,000-year quantile estimate of ASFFA for M equal to 50 is in the interval [-50%, +50%], whereas for the regional methods, the interval is [-45%, +25%].

The results presented in the Figures 5-11, 5-12, 5-13, and 5-14 are for all the sites. For this purpose, the results for all 5,000 sites are grouped into four drainage area "bins": Group 1 – sites with A between 1 and 10 km^2; Group 2 – sites with A between 10 and 100 km^2; Group 3 – sites with A between 100 and 1,000 km^2; and Group 4 – sites with A between 1,000 and 4,385

140

km^2. In Figure 5-11, I present the results for the Monte Carlo simulations for Case 4 using N=20 and M=30. These results are consistent with Figure 5-10. I found that the estimate for the 10-year quantile is similar among the four methods, while the 0.05-0.95 quantile range for the regional methods is smaller than ASFFA for longer return periods. Also, this result is consistent with the systematic bias in the epistemic error with respect to the drainage area (see Figure 5-8 and Figure 5-9). We can observed this bias along the mean of the boxplots from the Group 1 to Group 4 in Figure 5-11. Once again, the results show that the regional methods have similar performance in terms of the 0.05-0.95 quantile range of RB.

The previous results were based on 20 pooled sites (N=20) and M=30. Figure 5-12 shows the total error (as RB) for the estimation of the 100-year PFQ extracted from Case 4 using ASFFA for differing sample size (M), and spatial scale (From Group 1 to Group 4). Figure 5-13 shows the total errors for the estimation of the 100-year PFQ extracted from Case 4 using IFM, QRT, and PRT for 10 and 60 pooled sites (N) as a function of sample size (M) and spatial scale (From Group 1 to Group 4). The results from ASFFA show a reduction of the total error with increasing sample size and exhibit the aforementioned pattern in the bias on the mean error through the scales. The error distributions for IFM, QRT, and PRT are very similar for N=10 and N=60, likely attributable to the relatively limited variability presented in our (small) region (see Figure 5-6). It is quite likely that "real-world" RFFA, which typically pools data from larger regions and distinct watersheds, will exhibit stronger dependence on N.

The results for Case 2 (full dependence), Case 3 (full independence), and Case 4 (partial dependence) are used to evaluate the differences in total errors caused by concurrent peak flows between sites. I found no significant change between the error distributions among the different dependency structures (see Figure 5-14). This is because the RFFA methods used in this study

are not considering the correlation between sites. This result implies that the use of dependent data in regional methods that do not incorporate spatial correlations in the model structure will provide similar estimates to those using independent data. Therefore, the inclusion of techniques that take advantage of the peak flow dependencies between sites such as GLS or topological kriging should reduce the total error of regional methods for the estimation of PFQs (Archfield et al. 2013).

5.4.4. Insights into the Regional Variability of Skewness

The two methods for reducing total PFQ error are to lessen epistemic error or sampling error. Sampling error can be addressed in two ways: increased sample size through additional sites or additional years of observations (if available), or more robust parameter estimation methods. Epistemic error in RFFA is caused by failure of regional models to represent peak flow variability in the region, principally the skewness, which will control the right tail of the peak flow distribution. The regional models explored in this study are based on typical explanatory variables, such as drainage area or the mean annual flood. The epistemic errors presented in Figures 5-8 and Figure 5-9 demonstrate a systematic bias related to the inability of the regional models to capture the skewness shown in Figure 5-6. Therefore, physical reasoning to explain the spatial variability of skewness is crucial for future development of RFFA models.

I hypothesize four effects to explain the spatial variability of skewness presented in Figure 5-6: Hypothesis 1: heterogeneities in the runoff generation due to land cover. Hypothesis 2: sampling effects generated by the RainyDay data, assuming that 10,000 storms are not enough to capture the peak flow population. Hypothesis 3: attenuating influences of the river network structure. Hypothesis 4: watershed orientation relative to storm movement and shape. I examined the latter three hypotheses further.

142

We can discard Hypothesis 1 because our HLM configuration for the Turkey River used in this study does not consider differences in land use or land cover. I address Hypothesis 2 by using a second set of 10,000 rainfall events from RainyDay, generated using identical parameters. I calculated the ratios of moments and quantiles using the initial set (Set 1) and the new set (Set 2). Figure 5-15A shows that the ratios of these quantities are around 98%. In addition, Figure 5-16 shows that Sets 1 and 2 have very similar spatial patterns of skewness. Therefore, we can concluded that the sampling effect from RainyDay in our simulations fails to explain the regional variability on skewness.

Regarding Hypothesis 3—if we assume that each sub-basin is likely to observe the same rainfall events in the SST framework, then drainage network structure should partially control differences in peak flow skewness. One alternative to describe the river network structure within the watershed is by means of the Width Function. Multiples studies have confirmed the relation between Width Function and streamflow response (e.g., V. K. Gupta & Mesa, 2014; Moussa, 2008). To address this hypothesis, I evaluated linear and nonlinear regression models between skewness and 34 Width Function descriptors (WFDs), in addition to the drainage area and mean flood. The 34 WFDs are proposed and described in Chapter 3. Based on an exhaustive search and the Akaike Information Criteria (AIC), I found that a linear model including the drainage area and the Mass of the Width Function at region (M_{NS}) improves the adjusted coefficient of determination (i.e., adjusted R^2) from 0.22 to 0.34 with respect to a linear model with only drainage area (see Figure 5-15B). We can concluded that the WFDs cannot fully explain the skewness variability, but that this result could guide future attempts to relate regional variability of skewness to geomorphologic metrics.

Hypothesis 4 supposes that the relationship between basin orientation and the predominant orientation of rainfall events in the region could impact the skewness variability in the region. Figure 5-15C shows a directional histogram of skewness. The direction of each sub-basin is assigned as the dominant angle of the watershed measured counterclockwise with East at 0°.

I found that subbasins with the highest skewness have an orientation between 130° and 170°, though most of the subbasins within Turkey River Basin have a similar direction. Therefore, I performed a new set of RainyDay-HLM simulations in which I rotated the watershed 90° counterclockwise to evaluate the influence of watershed direction on skewness. Figure 5-16 shows that this rotation produces a new zone with higher skewness (around 3.5) near the watershed outlet. Therefore, we can surmise that the relationship between basin direction and storm motion (which is generally from the west-southwest in the state of Iowa, roughly speaking) exerts an important control on the spatial variability of skewness.

5.5. Conclusions

This study is the first to evaluate at-site and regional flood frequency analysis (RFFA) techniques using a physically-based synthetic framework based on distributed rainfall-runoff modeling. This approach has the advantage of providing physically plausible populations of flood flows at a large number of sites. Whether or not the peak flow distributions obtained by RainyDay-HLM adequately represent the "true" population of peak flows in the Turkey River is beyond the scope of this study. The findings of this study are pertinent, however, because the variability in the physically-based synthetic peak flow distributions modeled using RainyDay-HLM are "built" using real rainfall structures and geomorphologic characteristics that have not

been considered in previous synthetic studies of RFFA. The findings of this study help further the understanding of the following issues:

(1) Comparison of estimates of peak flow quantiles (PFQs) between the at-site flood frequency analysis (ASFFA), the Index Flood Method (IFM), the quantile regression technique (QRT), and the parameter regression technique (PRT).

(2) Evaluation of epistemic errors in the PFQ estimation for the four techniques, and of sampling errors as a function of sample size and number of pooled sites for IFM, QRT, and PRT.

(3) Evaluation of the impact of different intersite peak flow dependency structures in the sampling of peak flows for the estimates of PFQs based on IFM, QRT, and PRT.

(4) Exploration of different geomorphologic factors for explaining the regional variability of skewness.

The epistemic error analysis for ASFFA shows that the P3 using L-moments is an accurate representation of the PFQs for the 5,000 sites in the Turkey River Basin. The RFFA methods (IFM, QRT, and PRT) exhibit higher epistemic errors with respect to the epistemic error of ASFFA with P3 when the entire synthetic population is used for model fitting. The regional methods reduce the sampling error in scenarios with small samples of peak flows. This reduction makes them preferable for the estimation of peak flow quantiles in practice; the previous result is well-known in the literature. However, this study demonstrates that the distribution of errors for QRT, PRT, and IFM are very similar. I showed that the use of different explanatory variables for the construction of the QRT and PRT leads to strong differences in the model structure; in

145

general, I found that the mean annual flood is preferable to drainage area. In terms of the number of pooled sites in the regional methods, I found that the IFM, QRT, and PRT perform similarly with 10 to 60 pooled sites, a result that can be explained by the small variability in the synthetic peak flow distributions in the watershed. Also, the evaluation of the type of peak flow dependence between sites shows that the error distributions are similar in the three evaluated cases (Full Dependence, Partial Dependence, and Null Dependence). This result suggests that the estimation of PFQs can be improved with the implementation of estimation methods that take advantage of the dependence structure of peak flows between sites (e.g., GLS, topological kriging, max-stable process models). Finally, I found that river network structure and basin direction both help to partially explain the regional variability of the skewness.

The use of synthetic peak flows based on a combined framework of SST and a distributed hydrologic model that considers extreme rainfall and river network structure opens many avenues for study of peak flow estimation methods. This study covers only a small part of the large list of analyses that could be explored with this dataset. I believe that future studies based on this approach should address three main points: (1) the delineation of hydrologically homogeneous regions, including geomorphologic factors such as basin boundaries, river network characterization using Width Function Descriptors, and orientation of the watershed; (2) evaluation of PFQ estimation methods with statistical techniques that include the correlation of peak flows between sites; and (3) construction of regional models that capture more accurately the regional variability of skewness.

146
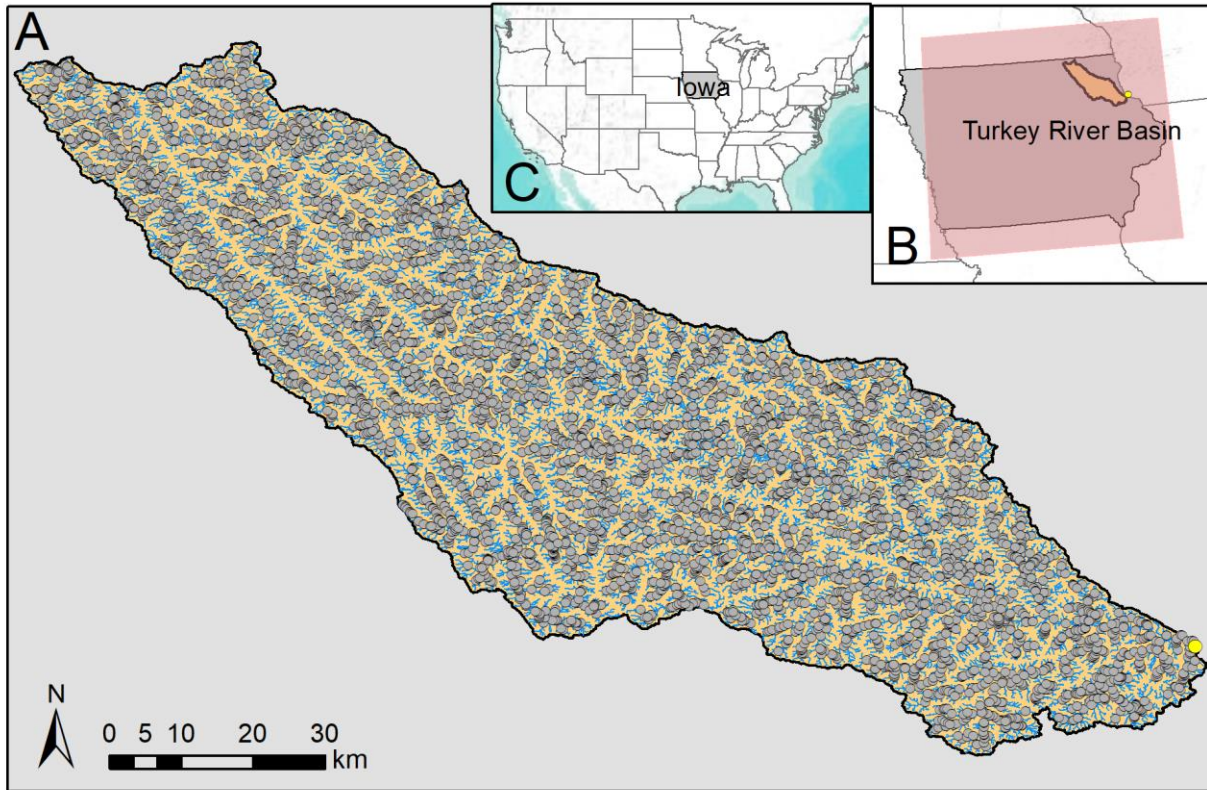
Figure 5-1. Location of the 5,000 simulated streamflow sites in Turkey River (black circles). The yellow circle indicates the basin outlet. The red polygon in panel B represents the transposition region used in the SST.
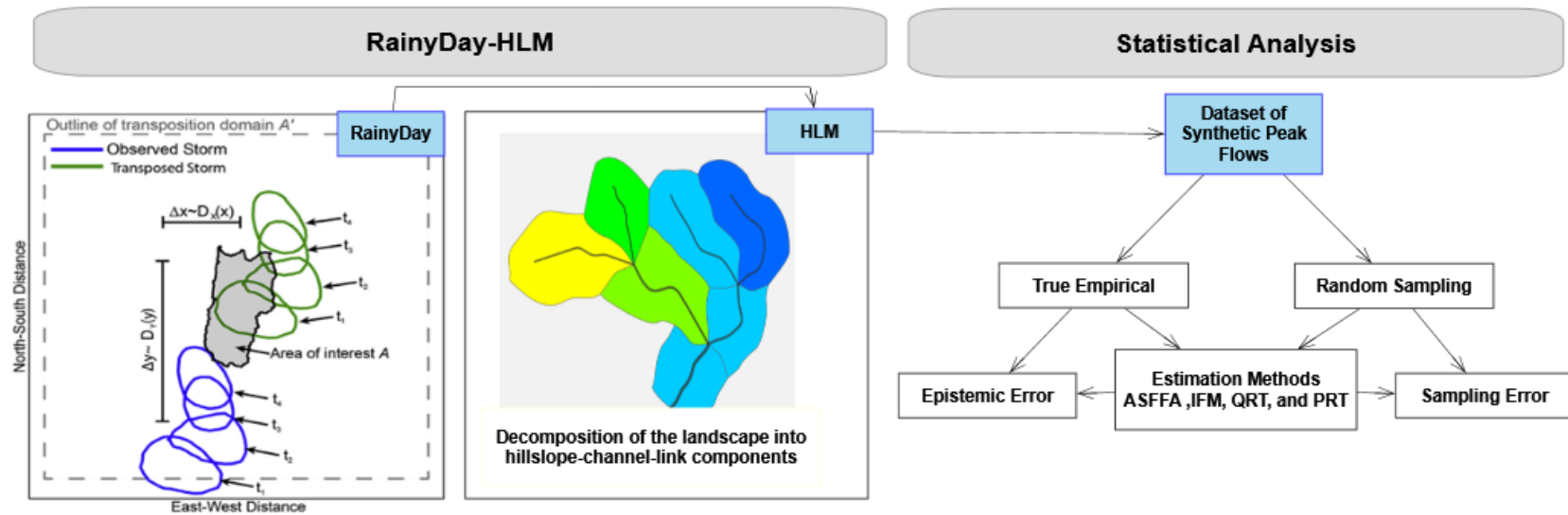
Figure 5-2. Flowchart describing the processes in the evaluation of the model and sampling errors in the estimation of peak flow quantiles. RainyDay panel is adapted from *Wright et al. (2017)*.
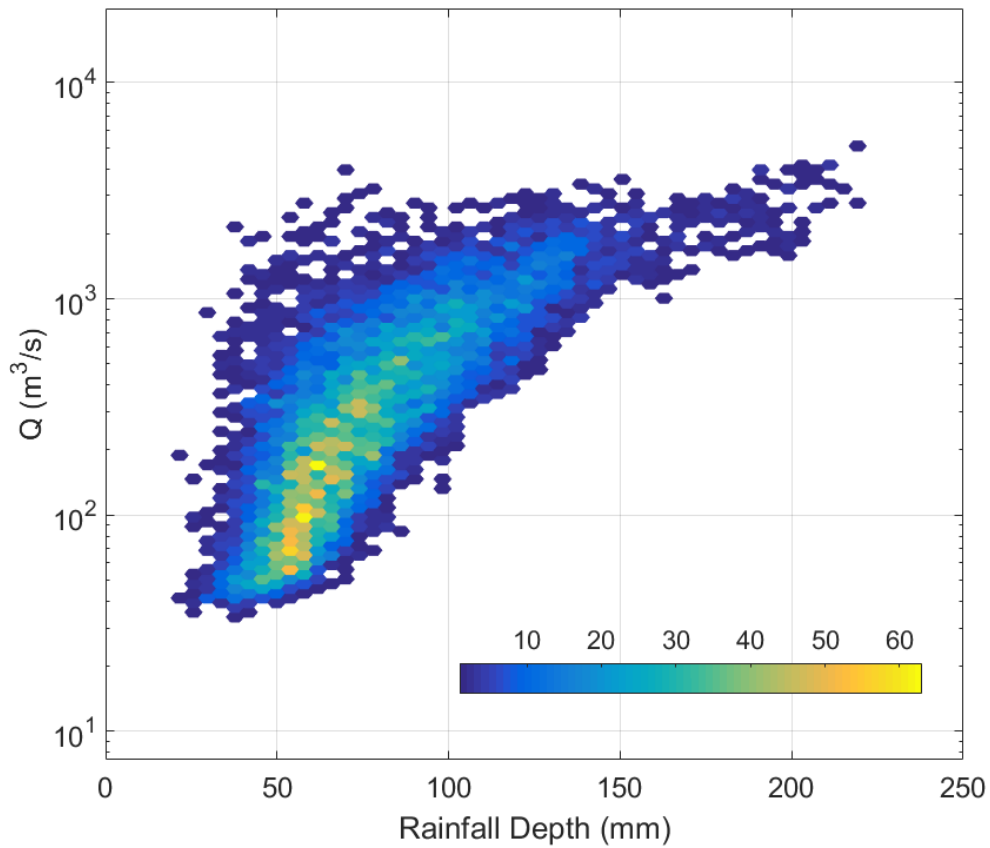
Figure 5-3. Precipitation depths and peak flows in the outlet of the Turkey River basin for all the 10,000 simulations of RainyDay-HLM. The precipitation depth is calculated over the rainfall duration of 72 hours. Shading indicates the number of overlaying points.
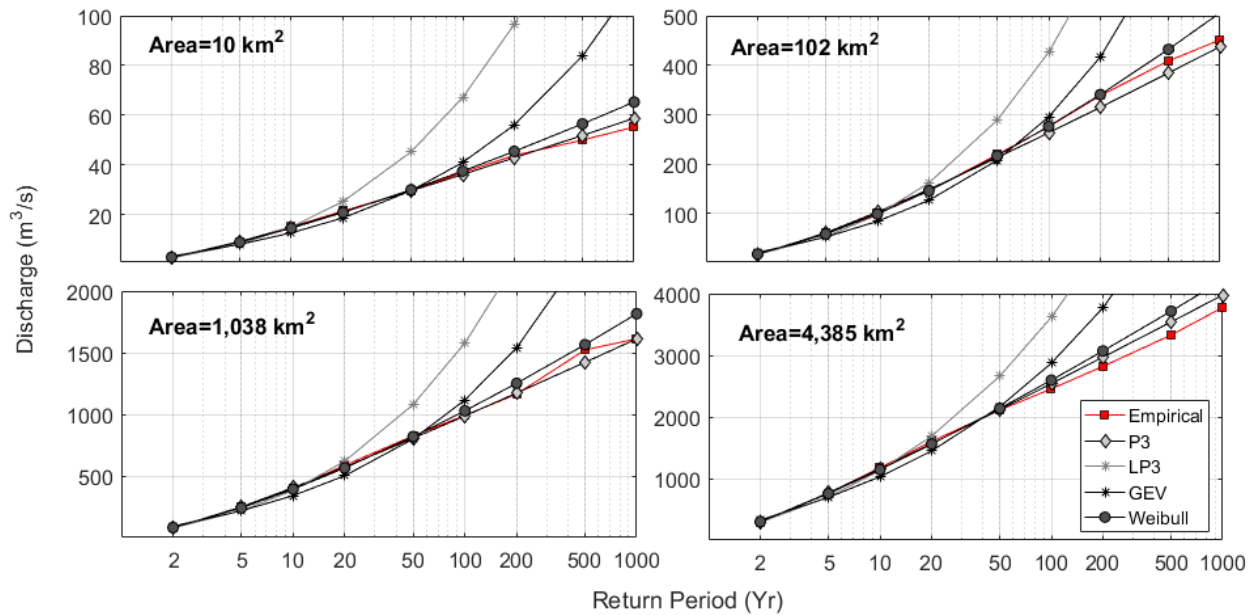
Figure 5-4. Probability distribution fitting for four sites representing different spatial scales of the peak flow population (10,000 peak flows per site). The fitted frequency curves are from the Pearson Type III (P3), Log Pearson Type III (LP3), Generalized Extreme Value (GEV), and 3 parameter Weibull distributions. The empirical frequency curve is included as reference.

150
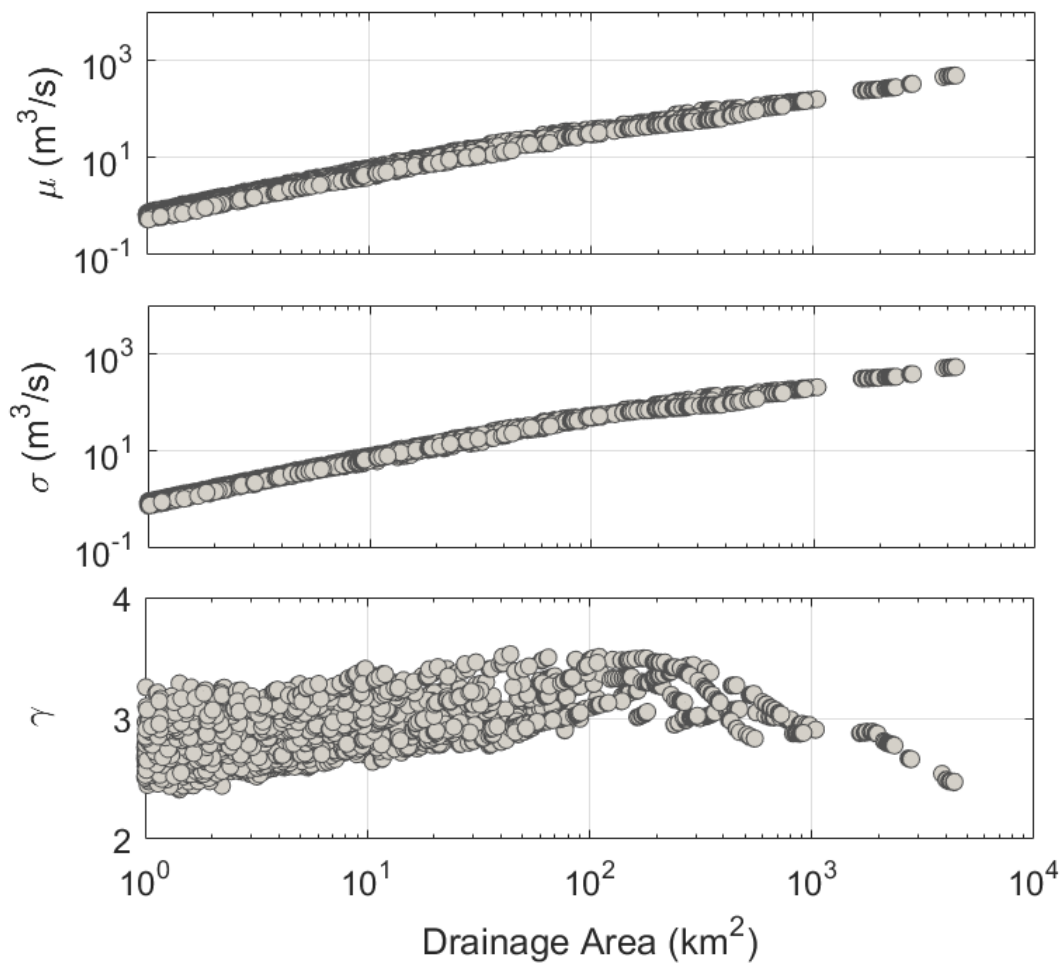
Figure 5-5. Mean, standard deviation, and skewness of the peak flow population of each of the 5,000 sites in the Turkey River watershed as a function of drainage area.
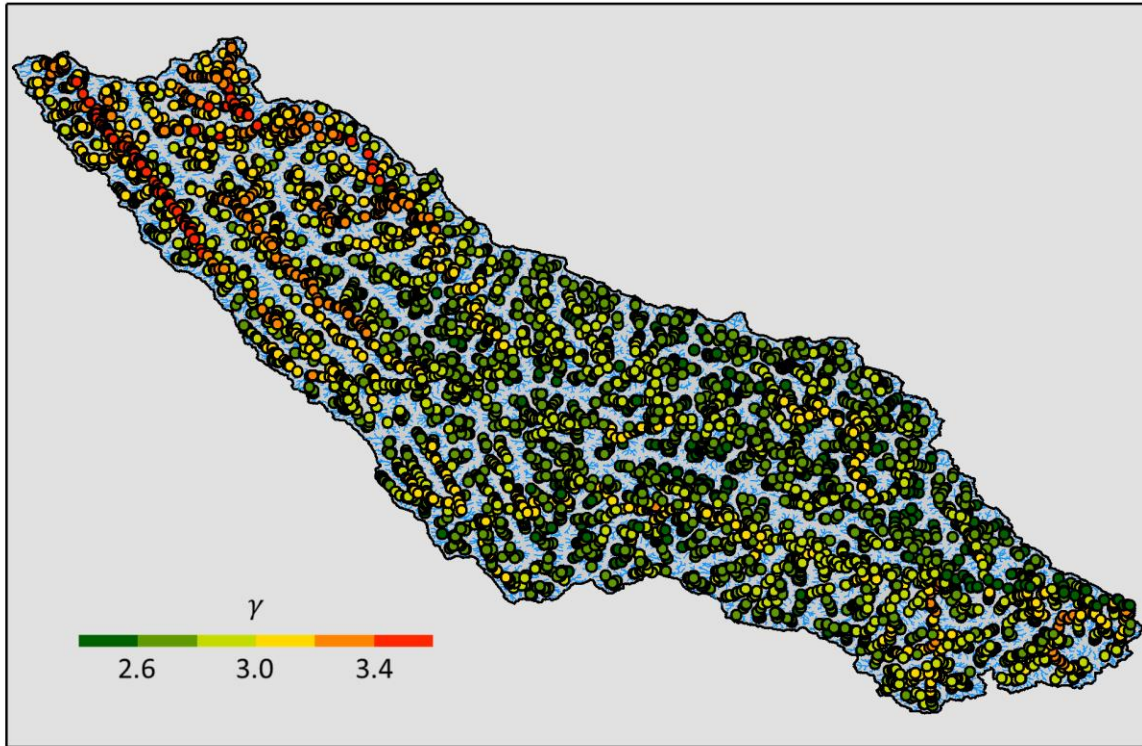
Figure 5-6. Spatial distribution of the skewness of the peak flow distribution using the RainyDay-HLM framework.
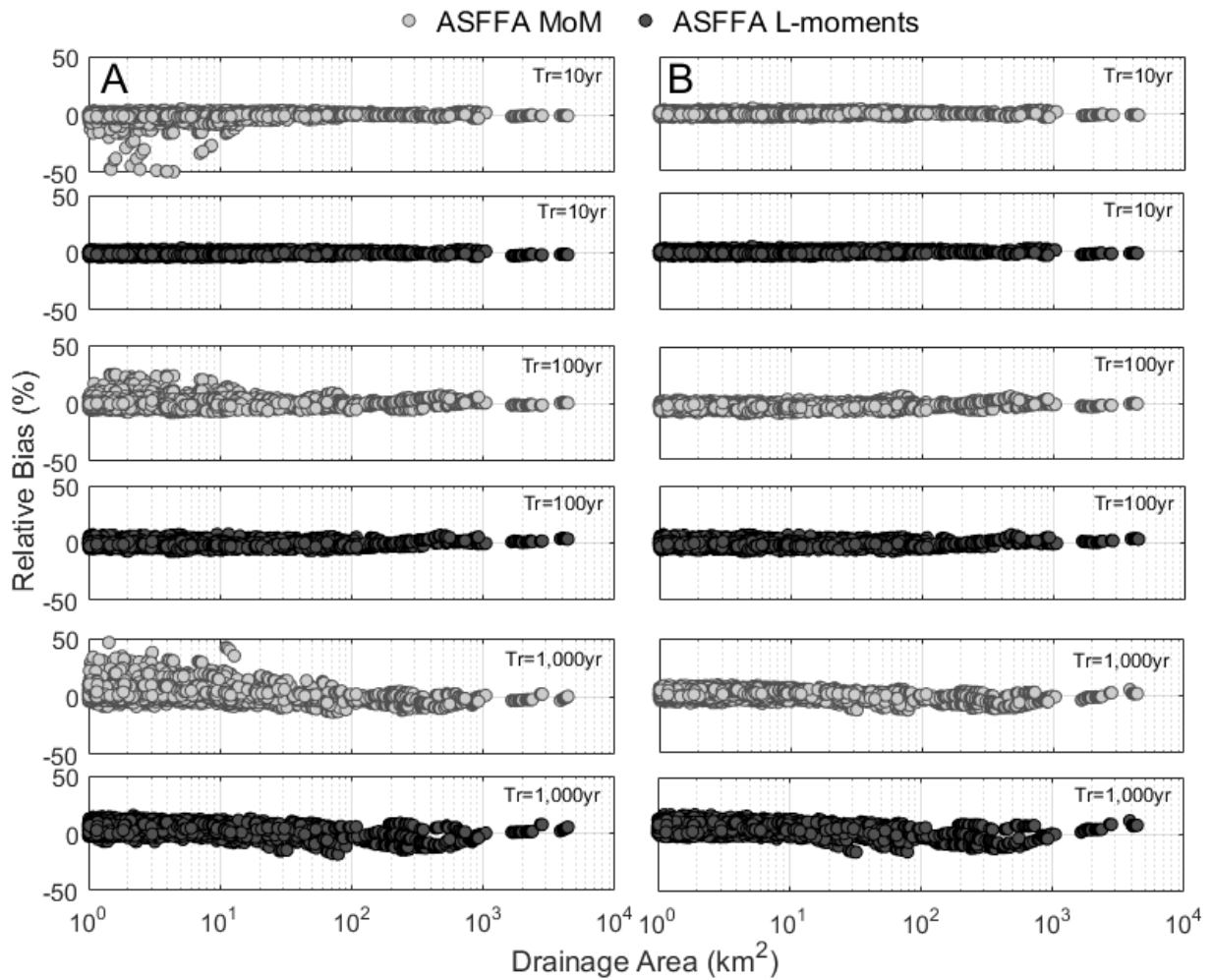
Figure 5-7. Epistemic error in the 10- , 100- , and 1,000-year PFQs estimates using the P3 distribution fitted via MoM (gray circles) and L-moments (black circles) for the 5,000 sites. Column A contains the relative bias using the entire population (10,000 peak flows), and Column B contains the relative bias after removing the 2 largest peak flows at each site.

153
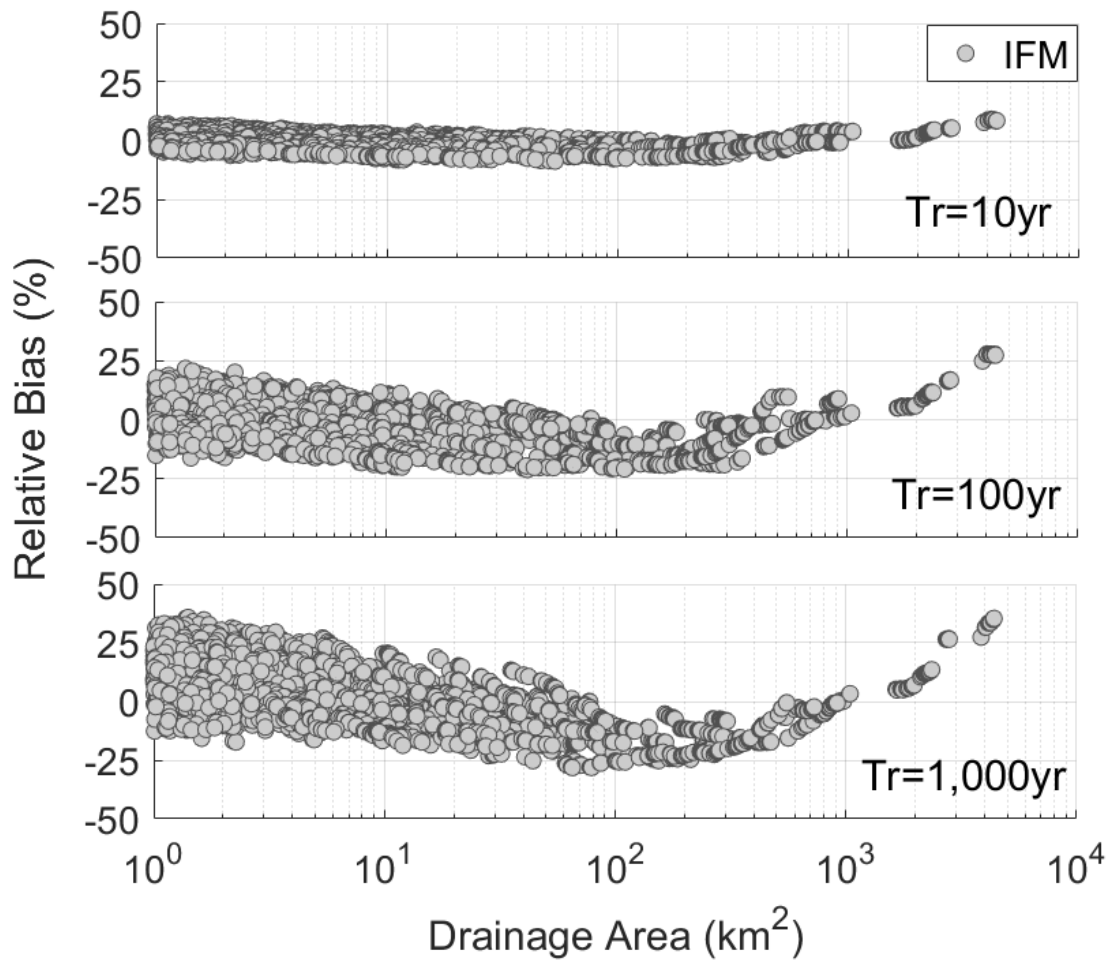
Figure 5-8. Epistemic error in the 10-, 100-, and 1,000-year PFQ estimates using IFM for the 5,000 sites.
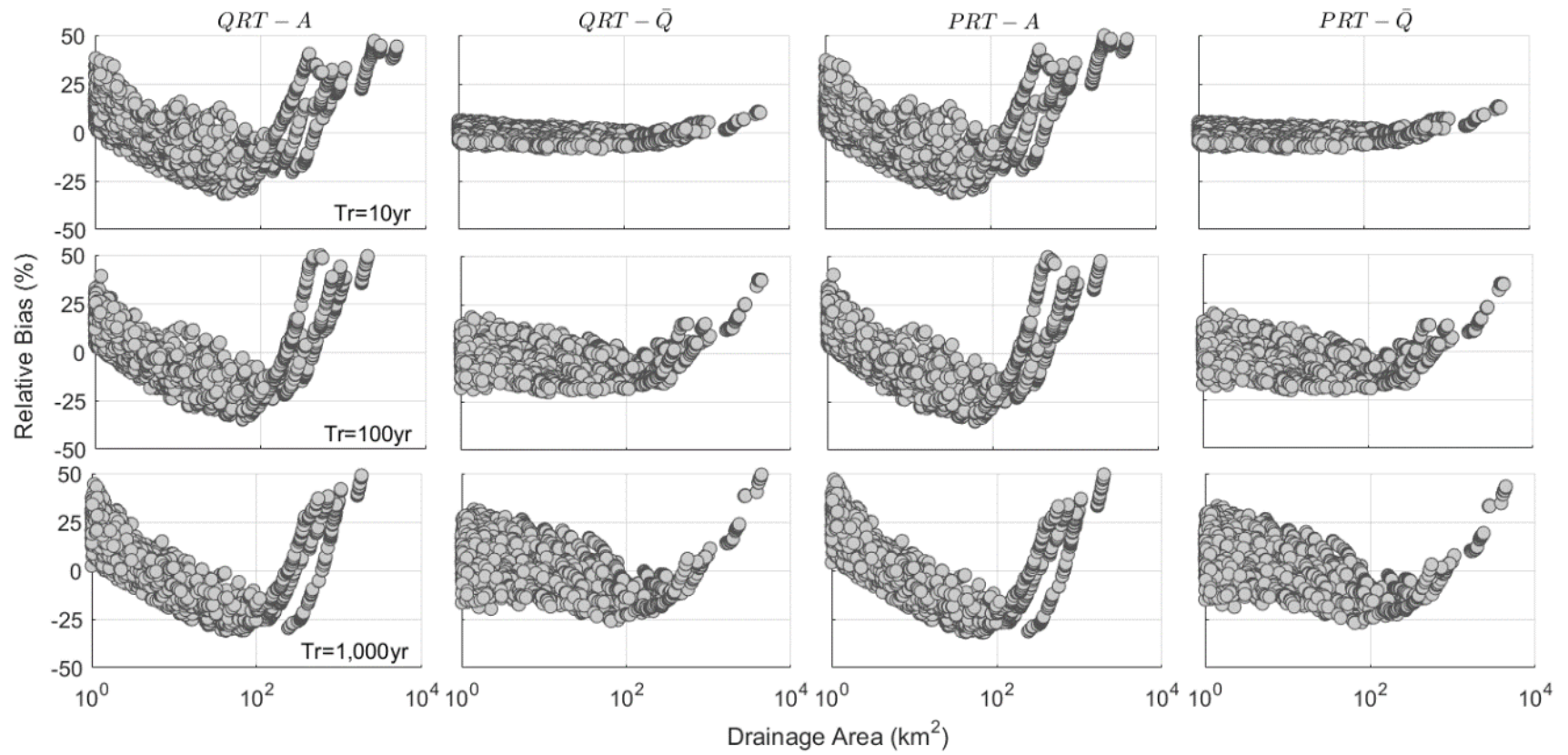
Figure 5-9. Epistemic error in the 10-, 100-, and 1,000-year PFQ estimates using the QRT-A, QRT-$\bar{Q}$, PRT-A, and PRT-$\bar{Q}$ for the 5,000 sites.
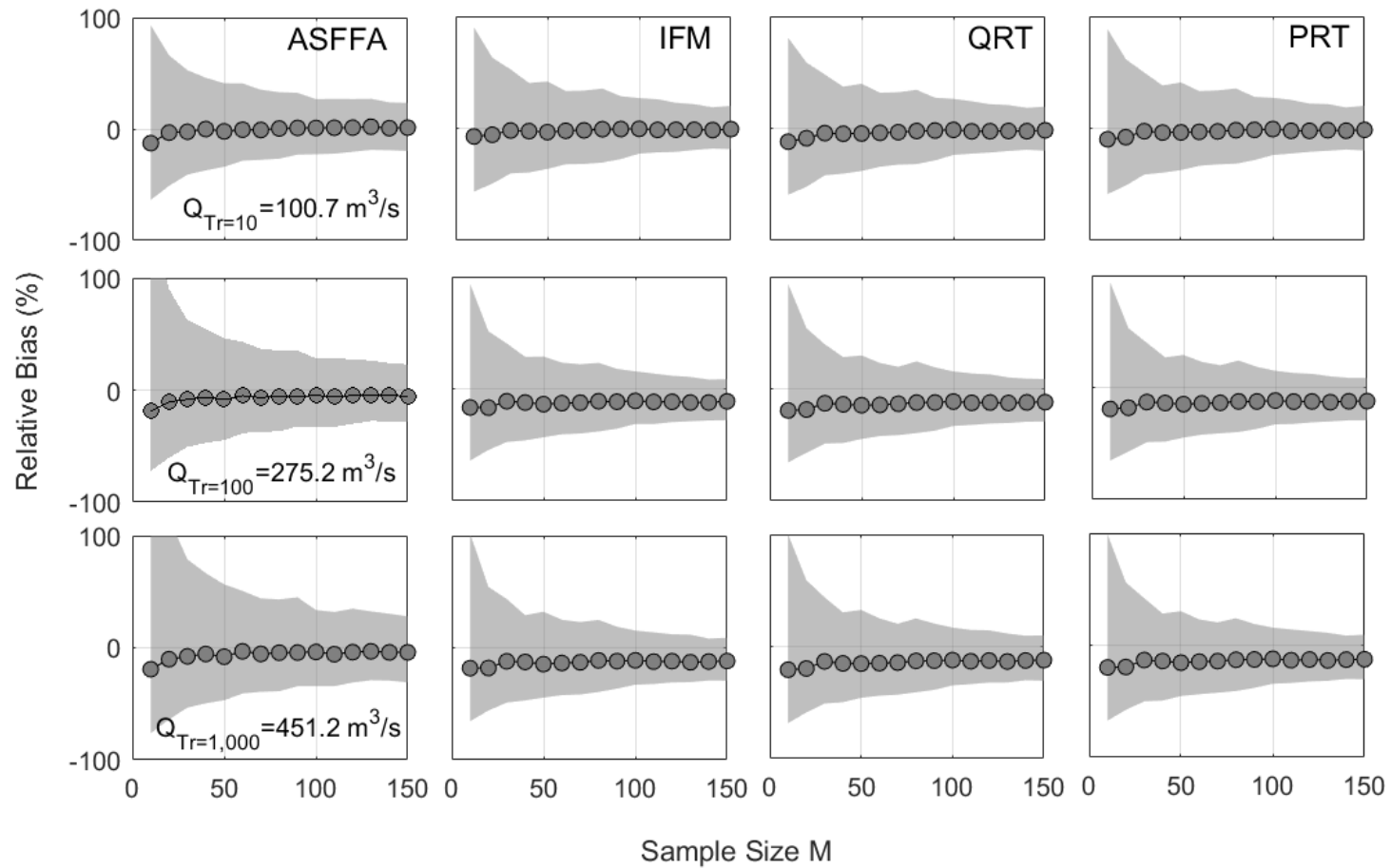
Figure 5-10. Example of the total error in the 10-, 100-, and 1,000-year PFQ estimates with ASFFA (with P3 and L-moments), IFM, QRT, and PRT for an arbitrary site with a drainage area of 100 km^2. The results are presented as a function of the peak flow sample size $M = \{10, 20, \ldots, 150\}$. Shaded regions denote the 0.05-0.95 quantile range from the 1,000 Monte Carlo simulations for each M. The simulation uses $N = 20$ sites with Partial Dependence.
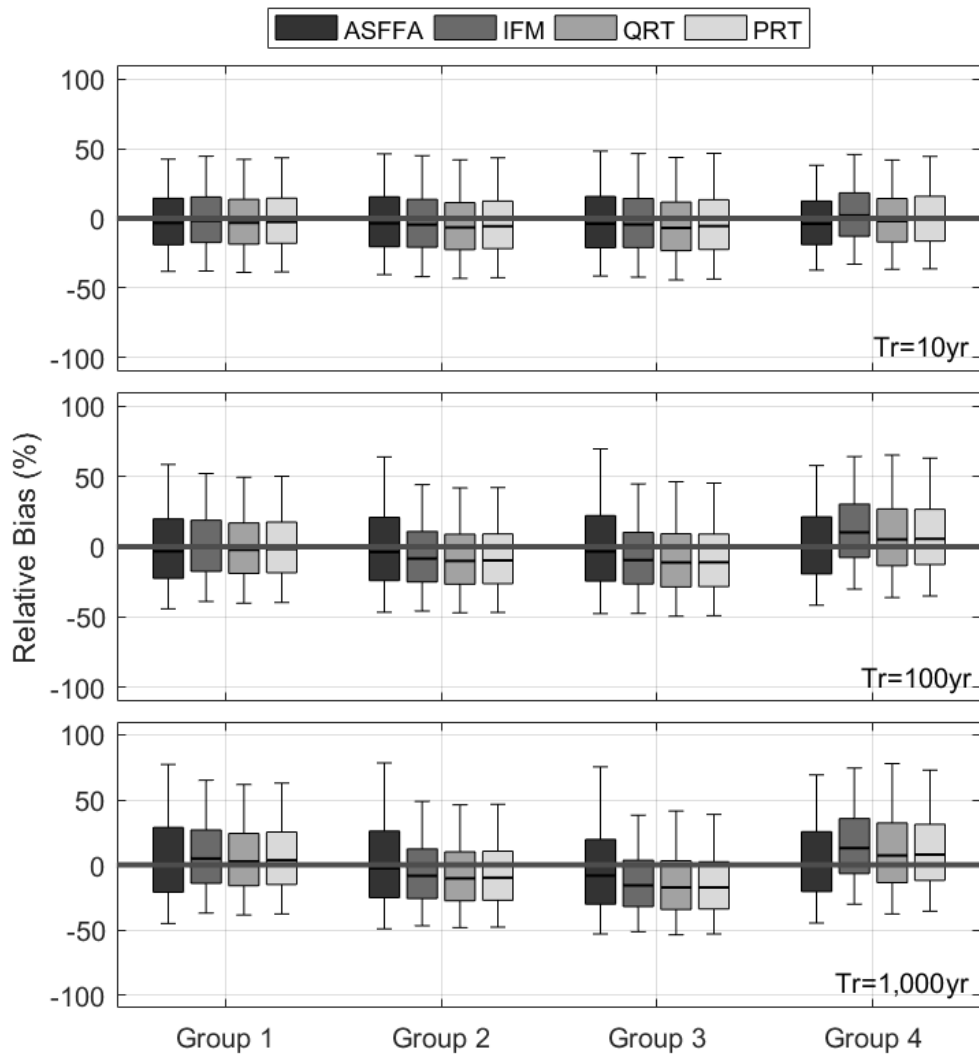
Figure 5-11. Total error distribution of ASFFA, IFM, QRT, and PRT for four different spatial scales and 10-, 100-, and 1,000-year return periods. Group 1: 1 to 10 km^2, Group 2: 10 to 100 km^2, Group 3:100 to 1,000 km^2; and Group 4: 1,000 to 4,385 km^2. Group 1, Group 2, Group 3, and Group 4 have 3,250, 1,131, 469, and 150 sites, respectively. The error distribution is obtained via aggregation of all the sites that belong to that spatial scale; each site has 1,000 independent Monte Carlo realizations. The simulation uses $M = 30$, $N=20$ with Partial Dependence. The whiskers represent the 0.05-0.95 quantile range.
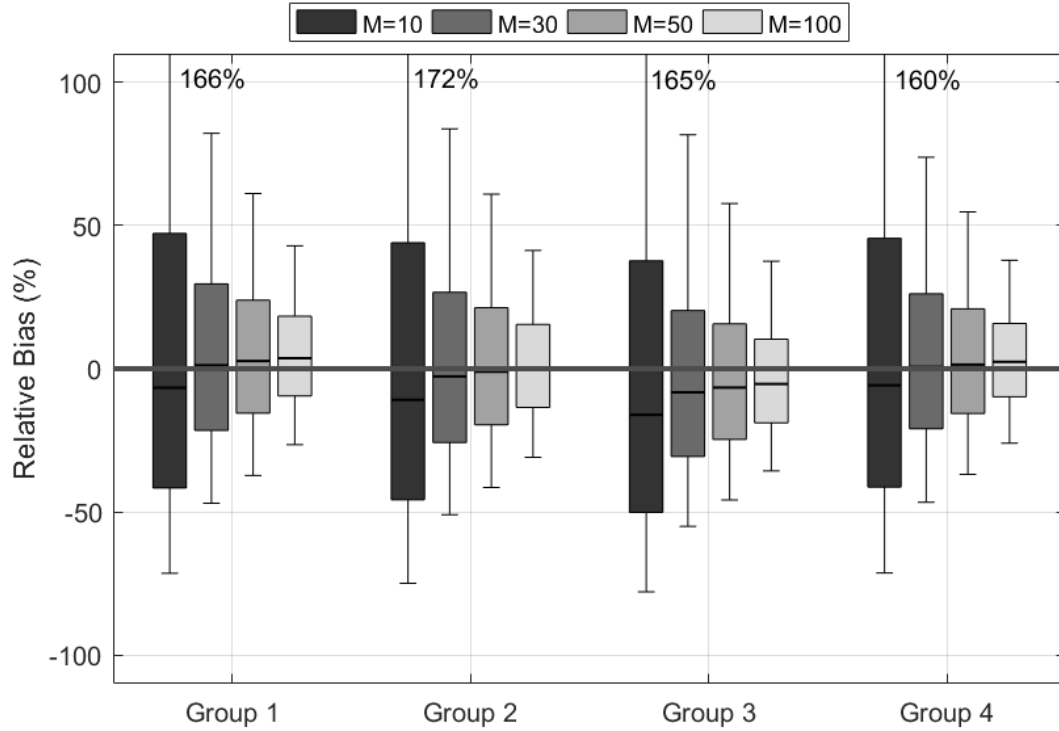
Figure 5-12. Distribution of total errors for the 1,000-year PFQ estimates using ASFFA for the four different groups. The results are presented for simulations with samples sizes of *M=* {10,30,50,100} with Partial Dependence. The whiskers represent the 0.05-0.95 quantile range. The percentages indicate the values outside of the plot range
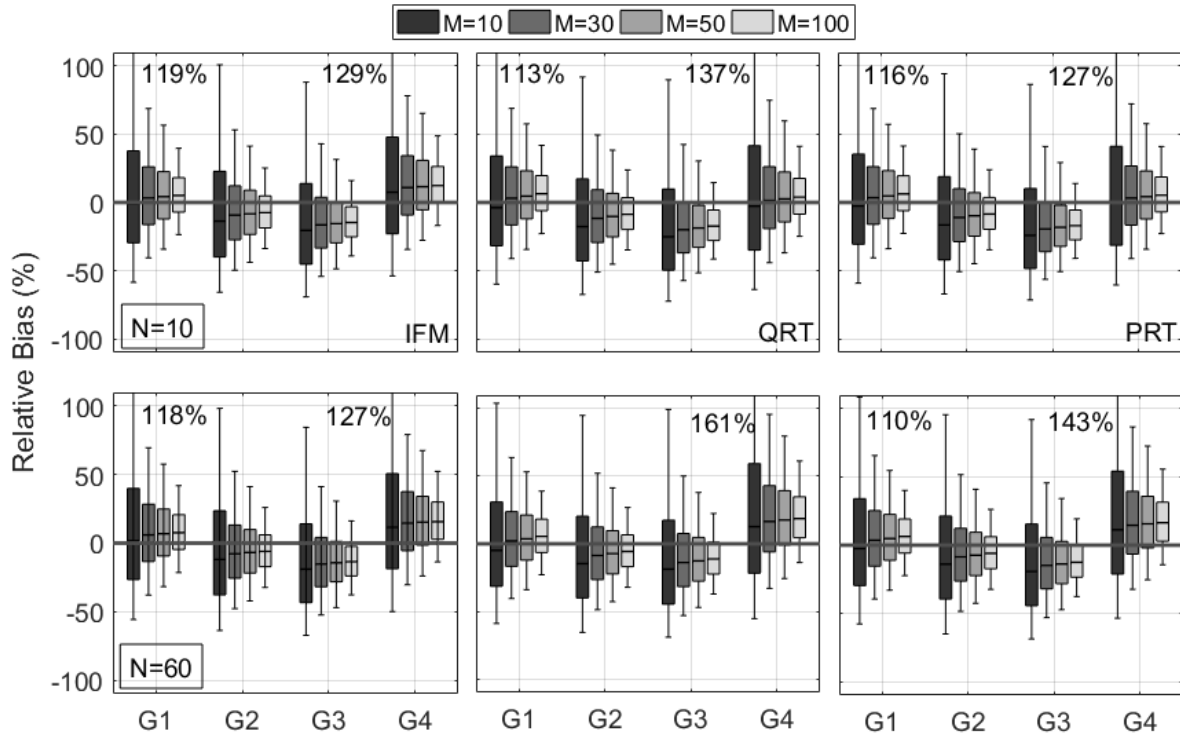
Figure 5-13. Distribution of total errors for the 1,000-year PFQ estimates using IFM, QRT, and PRT for the four different groups. Each column represents a specific method, and each row represents a different number of pooled sites for the regional methods. The results are presented for simulations with samples sizes of *M*= {10,30,50,100} with Partial Dependence. The whiskers represent the 0.05-0.95 quantile range. The percentages indicate the values outside of the plot range

159
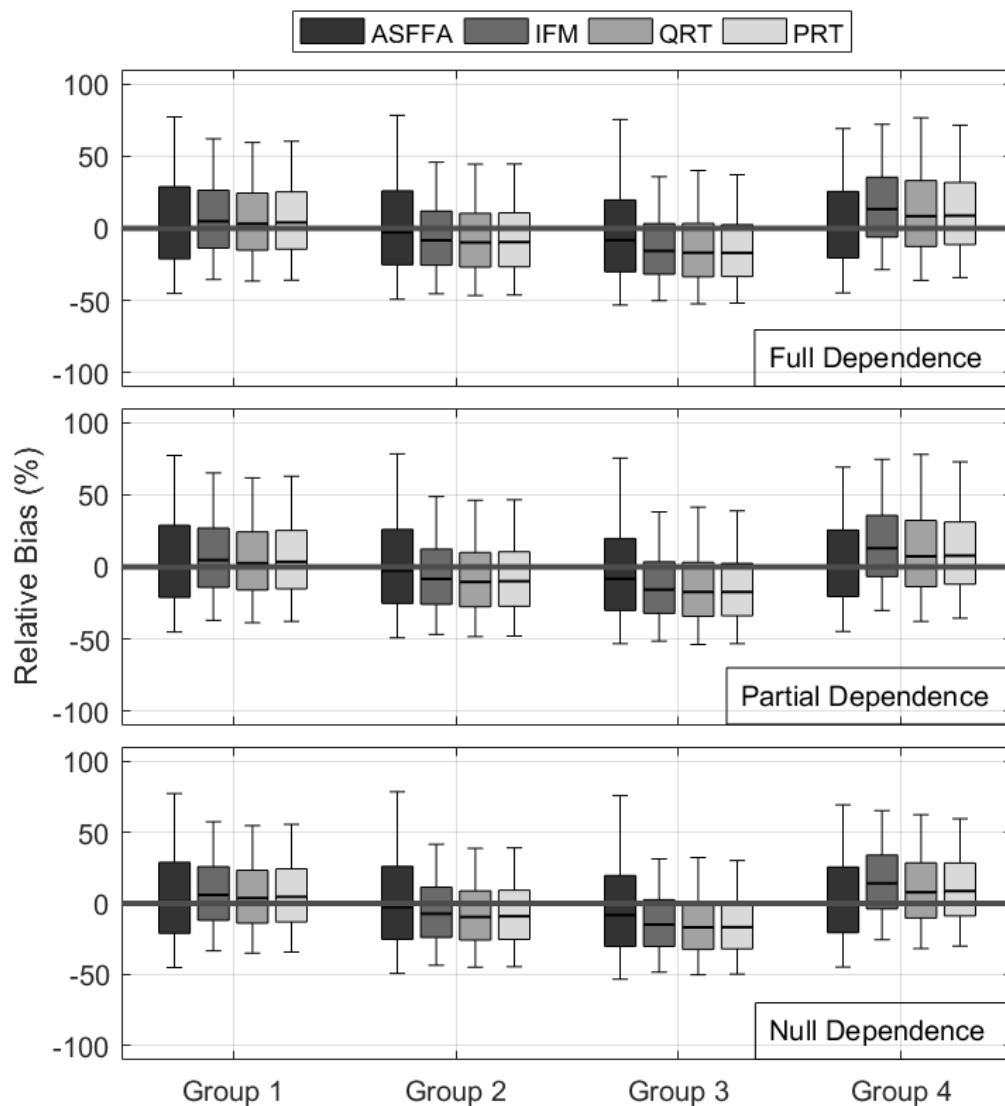
Figure 5-14. Distribution of total errors for 1,000-year PFQ estimates using ASFFA, IFM, QRT, and PRT for four different spatial scales. Each row represents a different type of intersite dependence for the selection of peak flows for the regional methods. The Monte Carlo simulation uses M=30, N= 20. The whiskers represent the 0.05-0.95 quantile range.
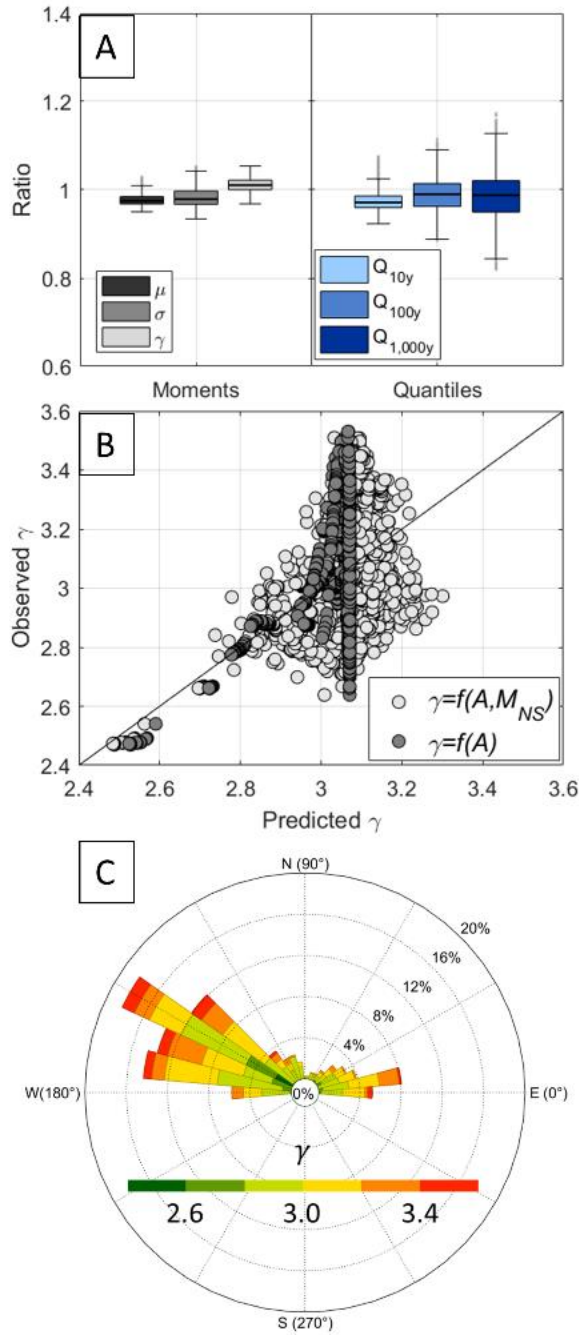
Figure 5-15. Evidence for the evaluation of hypotheses to explain the spatial variability of the skewness. A) Sampling effect: Ratios of moments and quantiles of peak flows for two different simulation sets. B) River network structure: Regression analysis between skewness and Width Function descriptors $(f(A, M_{NS}) = -0.00013A + 1.31M_{NS} + 1.78$ with $R^2_{adj} = 0.34)$, the regression using just the drainage area is used as a reference $(f(A) = -0.00012A + 3.07$ with $R^2_{adj} = 0.22)$ C) Main orientation of each sub-basin within the Turkey River Basin as a directional histogram of the skewness. M_{NS}:Mass of the Width Function at region.
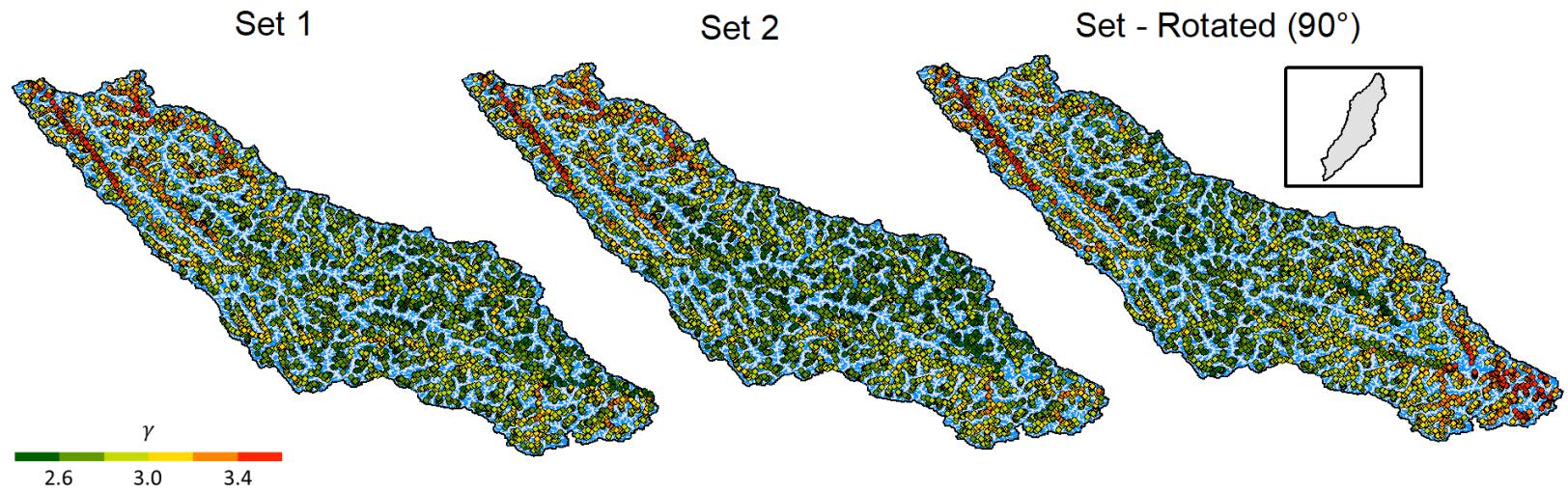
Figure 5-16. Spatial variability of the skewness from three separate simulation sets (i.e. populations) using the RainyDay-HLM framework. Sets 1 and 2 use identical configurations to highlight that stochastic variability is minimal between the two populations. "Set – Rotated (90)" has a rotation of 90° counterclockwise (see inset panel).

6.1. Introduction

This chapter presents an extension of the scaling theory of floods applied to streamflow distributions as Flow Duration Curves (FDCs). A FDC is a plot that shows the percentage of time when streamflow is likely to exceed or equal a given discharge value over a specific period of observation. The FDC provides a picture of streamflow temporal variability for a specific location. Its interpretation in terms of recurrence depends on the time scale of flow averages (days, weeks, months, or years), and the sampling period of streamflow records. The most conventional FDCs are the historical and the median-annual. Researchers calculate the historical FDC using the entire period of record utilizing historical daily flows. On the other hand, the median-annual FDC is calculated as the median of FDCs for independent water year records of daily flows. These FDCs have a wide application range in water resources, including hydro power design, water-quality management, sediment load estimates, and infrastructure design (Hickox & Wessenauer, 1933; Mitchell, 1957; Vogel & Fennessey, 1995). A deficiency of the historical FDC and the median-annual FDC is that they do not describe changes in flow likelihood because of the seasonal variability of the streamflow throughout the year. For example, extremely low flows caused by droughts during the month of June can be comparable in value to very high streamflow values typical for the month of December. Alternatively, we can describe this type of variability by constructing FDCs from daily flow records associated with specific months. For instance, if the historical daily flow records are separated by month, then an FDC can be estimated for every month (e.g., the January's FDC is constructed with all

the daily records observed that month), and these 12 monthly FDCs can more accurately represent the seasonal variability in probability of occurrence month by month.

When streamflow data are available for a specific site, the FDC can be straightforwardly estimated using parametric or non-parametric fitting procedures. However, streamflow records are limited around the world, and the prediction of FDC at ungauged locations is one of the challenges for the hydrologic community (Sivapalan et al., 2003). In response to this problem, researchers have proposed and implemented regionalization methods to estimate FDCs. The effectiveness of these regionalization methods depends on their ability to capture the spatial and temporal hydrological variability in a region using independent explanatory variables such as precipitation, land cover, evapotranspiration, and geometric properties of the basin and drainage network. In cases where hydrological heterogeneity cannot be fully captured or described by independent variables, the region is partitioned into hydrologic sub-regions. The presence of these sub-regions creates a disadvantage in the estimations of FDC for large domains, both in terms of the development of regional equations, as the primary explanatory variables need to be identified independently, and in terms of applications, because in many cases a catchment of interest can include many sub-regions.

One of the most recent motivations for the estimation of FDC at ungauged sites came from the need to classify streamflow outputs from distributed hydrological models (DHM) that provide streamflow estimations at local, regional, and national scales. The USGS provides classified streamflow maps for the nation using observed streamflow values and historical FDCs for sites with long-term records (http://waterdata.usgs.gov/ia/nwis/rt). USGS scientists classify the flow condition as a function of the percentile of the streamflow for a particular day of the year with a total of 365 references. However, this classification, based on historical observations,

164

is for gauged sites only. An alternative is to estimate the FDC based on the model outputs; however, this requires an extensive simulation of long periods (more than 30 years), which is a difficult task for large regions. The USGS maps with classified streamflow are useful to us because they provide an immediate visual assessment of the state of rivers in different regions of the country. However, when there is a need to analyze a region or state in more detail, the sparsity of information makes the picture incomplete (see Figure 6-1). In contrast, DHMs provide current and future streamflow estimates across the entire drainage network in the domain, including ungauged locations. However, actual streamflow values on a map are difficult to interpret because of the multiple scales and regional heterogeneity in space and time. A value of 100 m^3/s on a map would be difficult to interpret correctly: is it a high flow for a small basin or a low flow for a large basin? The correct interpretation of streamflow outputs from hydrologic models is crucial for water-use decision-making. The potential use of these streamflow outputs requires interpretation associated with the flow conditions related to flow magnitude. Without such tools, providing discharge estimates at locations where there is no reference data is not very meaningful. The simplest interpretation tool is the translation of flow magnitudes into flow frequencies using an FDC. Researchers can establish flow frequency thresholds to determine if the streamflow is in very low, low, normal, or high condition at an arbitrary location. This hydrologic information is not only relevant for the scientific community, but also for the general public because local communities can better understand streamflow conditions in a stream channel of interest, identifying impacts to the community either by droughts, floods, agricultural practices, recreational uses, or water supply activities.

Examples of the extensive use of regional hydrologic distributed models include the Iowa Flood Center (IFC) Hillslope Link Model (HLM) for the state of Iowa (Mantilla & Gupta, 2005;

165

Quintero et al., 2016) and the National Water Model (NWM) for the entire continental United States (Maidment, 2016). The HLM estimates the current and future streamflow for 420,000 stream channels embedded in Iowa's drainage domain. The Iowa Flood Information System web platform (Krajewski et al. 2017; Demir & Krajewski, 2013) disseminates this information, providing access for local authorities and the public. At a national scale, the National Oceanic and Atmospheric Administration (NOAA) launched the National Water Model, which provides streamflow forecasting for 2.7 million rivers in the United States based on the National Hydrography Dataset NHDPlusV2. These hydrologic models make important contributions to support water-use decision-making for current and future scenarios.

The literature documents a broad range of methodologies to estimate FDCs at ungauged locations. These methodologies can be classified in two broad categories. The first estimates streamflow distributions based on parametric statistical distributions, in which the distribution parameters are approximated from explanatory variables for estimations at ungauged sites (Doulatyari et al., 2015; Fennessey & Vogel, 1990; Li, Shao, Zhang, & Chiew, 2010; Longobardi & Villani, 2013). The second approach uses regression analyses performed between specific streamflow quantiles or distribution-moments with respect to a set of explanatory variables. This method is well described in work by Farmer et al. (2015); Flynn (2003); Singh (1971); and Yue & Gan (2004), among others.

The USGS has developed a methodology to estimate streamflow quantiles for the construction of FDCs at ungauged sites in Iowa (Linhart et al., 2012). They used independent streamflow quantile regressions employing 113 streamflow gauges with at least 10 complete years of daily mean streamflow, without regulation or diversion. The method uses a regression analysis between discharge for a particular quantile and independent variables that describe

166

physical and climatic basin characteristics. In total, they explored 57 physical and climate basin characteristics as explanatory variables. They used the stepwise selection method to identify the significant independent variables in the regression analysis. Once researchers had filtered the independent variables, they performed an Ordinary Least Square (OLS) regression analysis and Weighted Least Squares (WLS) to determine the best set of regression equations. They conducted this regression analysis with an imposed limit of three independent variables for each equation to minimize overfitting of the regression models. The WLS multiple linear regression's advantage is that it accounts for differences in record length. In addition, the study uses left-censored regression for streamflows with a 99% probability of exceedance (low flow), with a censoring threshold of 0.1 ft^3/s, and the goal of reducing the standard error in the regression analysis. They fitted 15 equations for 15 quantiles: 0.01, 0.05, 0.10, 0.15, 0.20, 0.30, 0.50, 0.60, 0.70, 0.80, 0.85, 0.90, 0.95, and 0.99. Each equation includes up to three independent variables, accounting for the following: drainage area; mean annual precipitation; percent area underlain by hydrologic soil type B, C, and D; relative stream density; hydrograph separation; streamflow-variability index; and a measure of the steepness of the slope of a duration curve. The web-based tool StreamStats (Ries et al., 2009) implements this method, allowing for reconstruction of the FDC from the 15 streamflow quantiles.

Although the rigorous statistical analysis presented in Linhart et al. (2012) provides convenient estimations of 15 streamflow quantiles that allow us to reconstruct the FDC, the estimation of FDC could be improved and compacted for easier implementation in larger domains. I identified three main drawbacks in Linhart et al. (2012). First, the changes to the physical and climatic variables used to describe different streamflow quantiles make it difficult to track the overall role of an explanatory variable in the entire streamflow distribution. Second,

167

the fitting of independent equations for specific streamflow quantiles (Q_p) with different explanatory variables does not guarantee a monotonic decreasing trend in the FDC ($Q_{p_i} > Q_{p_j}$ with $p_i < p_j$), which implies that $Q_{p_i} < Q_{p_j}$ for $p_i < p_j$ could occur. Third, the authors of Linhart et al. (2012) were only concerned with the historical FDC, which does not capture the streamflow seasonality described at a monthly scale.

This chapter is organized as follows: the Section 6.2 describes the research objectives of this study; the Section 6.3 describes the information and methods used to estimate FDCs at ungauged sites (this section will describe the regression analysis, the selection of the explanatory variables, the validation test, and the final construction of a piecewise continuous monotonic FDC); in Section 6.4, I discuss the results and examine the outcomes of the FDC estimations for the state of Iowa at ungauged sites; and finally, the main results are synthetized in the closing comments.

6.2. Research Objectives

In this study, our primary objective is to estimate historical-annual and historical-monthly FDCs at ungauged sites in Iowa. I define the following specific objectives in the construction of FDCs: 1) estimate FDCs with a single explanatory variable for an easy implementation; 2) fit a continuous and monotonic FDC for a representative range of quantiles; and 3) estimate FDCs for both historical and monthly scales to capture the streamflow variability during the year.

For the development of research objectives, the following hypothesis is stated: the long-term mean annual streamflow ($\bar{Q}$) captures most of the hydrological heterogeneities of streamflow quantiles across space and watershed scales. I explore this hypothesis recognizing that the mean annual flow integrates the spatial variability of two hydrologic fields (precipitation

168

and evapotranspiration) across the watershed through the relationship given by the long-term water balance equation. This concept is expanded in Section 6.3.1. I use power-law regressions following the existent literature on the connection between peak flow quantiles and drainage area (Gupta & Dawdy, 1995; Gupta & Waymire, 1990, 1998; Mantilla et al., 2011; Ogden & Dawdy, 2003) as well as other studies showing the connection between drainage area and mean annual flow within a scale-invariant framework (Vogel & Sankarasubramanian, 2000; Yue & Yew Gan, 2004). This hypothesis is reinforced by Poveda et al. (2007), who uncovered the scaling connections between peak flow quantiles and mean annual flow. While Poveda et al. (2007) made the connections with peak flow quantiles rather than streamflow quantiles, their results suggest that the mean annual flow contains valuable information to describe different streamflow frequencies.

6.3. Materials and Methods

In this study, I calculate the empirical non-parametric historical-annual FDCs for gauged sites by sorting the daily streamflow record of *n* values from the largest to the smallest and assigning each position a rank (*R*). Each ranked position is associated with a probability (*p*), which represents the chance that the sample exceeds or equals the corresponding streamflow. The cumulative probability *p* associated with *R* can be calculated with different approaches (Beard, 1974; Blom, 1958). I calculated *p* using the Weibull plotting position (Weibull, 1939), which is approximately unbiased for quantiles:

$$p = \frac{R}{n+1}$$
Equation 6-1

This study uses daily mean streamflow records from 114 streamflow gauges not affected by regulation or diversions (see Figure 6-2) and located across Iowa up to September 2014, employing only complete water years. Data flags provided by the USGS help identify the sites

with regulation or diversion. These gauges are grouped in two different data sets for different analyses. The first, called the calibration set, included 74 streamflow gauges with more than 30 years of records; I used these in the regression analysis section. The remaining 40 streamflow gauges are used for a validation test and have streamflow record durations ranging from 10 to 30 years. Tables 6-1 and 6-2 show some climatologic features and duration of records for the calibration and validation gauge sets.

To construct the historical-annual FDC, I estimate the streamflow quantiles with the complete daily streamflow record for each streamflow gauge using Equation 6-1. For the historical-monthly FDC, I divided the streamflow records by months and again used Equation 6-1. The streamflow quantiles are defined for probabilities of exceedance ranging from 0.01 to 0.99 with a step of 0.001, for a total of 981 quantiles. By selecting streamflow gauges with more than 30 years with small step (0.001) between frequencies. In the case of monthly FDCs, I grouped the data by months; therefore, there is a significant reduction in the number of streamflow observations. Thus, the streamflow gauges in the calibration set must have more than 30 years of records to guarantee at least 980 daily streamflow observations per month. In cases where the data are not sufficient, Equation 6-1 does not give frequency values for the exact quantile in the range of 0.01 to 0.99 with step of 0.001. Therefore, I use a linear interpolation between frequencies obtained from Equation 6-1 to get the desired streamflow quantiles estimate for every streamflow gauge. I censored streamflow records with zero flow values at 0.001 ft^3/s ($\approx$0.0003 m^3/s) to avoid problems with the logarithmic transformation in the regression equations described in the next section.

6.3.1. FDC Scaling Models and Regression Analysis

I fit four different regression models to estimate quantiles in the gauges calibration set. The model configurations result from assumptions of statistical simple-scaling or multi-scaling, in which the intercept (α_p) and scaling exponent (θ_p) are the "scaling parameters" for a specific probability of exceedance (p). Simple-scaling arises when the scaling exponent in the power law relations are constant for all frequencies (quantiles), and multi-scaling arises when they are not (Vijay K. Gupta & Waymire, 1990). One of the specific objectives was to come up with a simple structure of FDC described by a single explanatory variable. In the literature, it is well recognized that the drainage area (A) captures a large part of the streamflow variability; however, other variables may be relevant in the representation of the streamflow distributions, especially in heterogeneous regions (Farmer et al., 2014; Farmer et al., 2015). I decided to explore the A and the long-term mean annual streamflow ($\bar{Q}$) as independent explanatory variables. The $\bar{Q}$ is selected as explanatory variable because by definition, it integrates the spatial variability of precipitation and evapotranspiration across the watershed. The mean annual flow ($\bar{Q}$) can be estimated from the long-term water balance equation,

$$\bar{Q} = A(\bar{P} - \overline{ET})$$
<div align="right">Equation 6-2</div>

where $\bar{P}$ is mean annual precipitation and $\overline{ET}$ is mean annual evapotranspiration. The long-term water balance is used to estimate the mean annual flow because we can estimate this quantity at gauged and ungauged sites. For this estimation, I used the drainage area reported by the USGS, the mean annual precipitation from the PRISM product (Oregon State University, 2016), and evapotranspiration from a continuous global record of land surface evapotranspiration from 1983 to 2006 (Zhang et al., 2010) (see Tables 6-1 and 6-2 for these values in every streamflow gauge).

The four scaling models and their corresponding regression equations are given by

171

$SSA\ Model:\quad \frac{Q_p}{\alpha_p A} \overset{d}{=} Z_1\ which\ implies \quad E[Q_p|A] = \alpha_p\,A \qquad$ Equation 6-3

$SSQ\ Model:\quad \frac{Q_p}{\alpha_p \bar{Q}} \overset{d}{=} Z_2\ which\ implies \quad E[Q_p|A] = \alpha_p\,\bar{Q} \qquad$ Equation 6-4

$MSA\ Model:\quad \frac{Q_p}{\alpha_p A^{\theta_p}} \overset{d}{=} Z_3\ which\ implies \quad E[Q_p|A] = \alpha_p\,A^{\theta_p} \qquad$ Equation 6-5

$MSQ\ Model:\quad \frac{Q_p}{\alpha_p \bar{Q}^{\theta_p}} \overset{d}{=} Z_4\ which\ implies \quad E[Q_p|A] = \alpha_p\,\bar{Q}^{\theta_p} \qquad$ Equation 6-6

where the $\overset{d}{=}$ symbol indicates equality in distribution with respect to the random variable Z_i, which is assumed to be scale invariant, with expected value equal to 1, and independent from the explanatory variable. The model acronyms refer to SSA: Simple-Scaling with A; SSQ: Simple-Scaling with $\bar{Q}$; MSA: Multi-Scaling with A; and MSQ: Multi-Scaling with $\bar{Q}$.

The SSA and SSQ models evaluate the streamflow quantile relation with respect to A and $\bar{Q}$ in a simple scaling framework, respectively, for which the θ_p is constant and equal to one. The MSA and MSQ models are the multi-scaling versions of the SSA and SSQ models, respectively, allowing changes in the θ_p across streamflow quantiles. The four proposed equations can be interpreted in the context of regional homogeneity of the streamflow distribution with respect to the explanatory variable. The A does not depend on climatic variability, so for this reason SSA and MSA models assume homogeneity in the streamflow distribution across the domain as defined by Gupta et al., 1995, in the context of peak flows. However, models SSQ and MSQ are based on the $\bar{Q}$ and include variability in the precipitation and evapotranspiration across the domain. Therefore, we can assume that these models better describe the non-homogeneous regional features in the representation of the streamflow distribution.

I fit these models to observations using a WLS regression for values of p ranging from 0.01 to 0.99 with a step of 0.001, for a total of 981 independent streamflow quantile regressions

172

per model. The WLS regression accounts for differences in the sample size caused by the differences in record periods in the streamflow gauges, but it does not compensate for cross-correlation among the streamflow gauges. Future studies could include generalized least squares methods to account for streamflow dependence among sites in the development of the regression analysis. The use of independent regression can lead to the failure of the monotonic property of a FDC. However, the use of the same explanatory variable and a small step between the streamflow frequencies in the regressions make it unlikely that the monotonic property in the estimated FDC will fail. To enforce monotonicity, I connect the shape of the parameters α_p and θ_p as a function of the probability of exceedance (p) (see Section 6.3.4).

I use the coefficient of determination (R^2) as model selection criteria since the four models use a single explanatory variable and the log-transform of any of the four models makes them close to linear. In addition, the performance of each regression is evaluated with the Mean Average Percentage Error (MAPE), Symmetric Mean Percentage Error (SMAPE), and Mean Square Accuracy Ratio (MSAR). The MAPE is a common statistic used to measure the relative error in models; however, the MAPE is not symmetric because the interchange of Q_p and $\widehat{Q_p}$ leads to different values in which $\widehat{Q_p}$ is the estimated streamflow for a specific p based on the regression equation. This disadvantage is overcame by adding the symmetric version SMAPE to the analysis. Additionally, I included the MSAR statistic (Tofallis, 2015) to recognize the scale dependence in the models because it evaluates the differences in the logarithmic space, balancing the errors for small and large basins.

$$R^2 = 1 - \frac{\sum_{i=1}^{n}(Q_{p_i} - \widehat{Q_p})^2}{\sum_{i=1}^{n}(Q_{p_i} - \overline{Q_p})^2} \qquad \text{Equation 6-7}$$

$$MAPE = \frac{1}{n}\sum_{i=1}^{n}\left|\frac{Q_{p_i} - \widehat{Q_p}}{Q_{p_i}}\right|$$

Equation 6-8

$$SMAPE = \frac{1}{n}\sum_{i=1}^{n}\frac{\left|Q_{p_i} - \widehat{Q_p}\right|}{(\left|Q_{p_i}\right| + \left|\widehat{Q_p}\right|)/2}$$

Equation 6-9

$$MSAR = \frac{1}{n}\sum_{i=1}^{n}[log\left(\frac{\widehat{Q_p}}{Q_{p_i}}\right)]^2$$

Equation 6-10

6.3.2. Assessment of the Explanatory Variables

I begin by explaining the rationale for selecting A and $\bar{Q}$ as explanatory variables in the construction of a scale-invariant streamflow distribution for Iowa. Scale-invariance in the streamflow distribution requires that the explanatory variable captures the scale dependence of the Q_p throughout the spatial domain. In a homogeneous region, this scale dependence is captured by *A* alone (Gupta et al., 1995). However, in a non-homogeneous region, it is insufficient to explain the broad range of hydrologic variability (Farmer et al., 2015). In those cases, splitting the region into sub-regions and/or finding additional explanatory variables that explain the non-homogeneities are the preferred approaches. The variable $\bar{Q}$ includes both the scale dependence of *A* through Equation 6-2, as well as the regional variability in precipitation and evapotranspiration. For this reason, $\bar{Q}$ seems to be a better representation of the streamflow distribution with a scale-invariant property.

To explore the characteristics of the *A* and the $\bar{Q}$ as explanatory variables in a scale-invariant framework, I focused the analysis on the multi-scaling relationships expressed in the MSA and MSQ models. If the explanatory variable captures most of the streamflow variability across the domain, it would not be necessary to define the hydrologic regions. The regional dependence in the explanatory variable can be identified when clusters in the regression analysis are associated with specific regions in the domain of study. If a regional dependency exists,

174

regional domains should be delimited to perform a separate analysis that will capture the streamflow distribution in the region. The purpose of this study is to define a FDC for the entire domain of the state of Iowa; therefore, the definition of different hydrologic regions needs to be avoided.

To test the scale-invariance of the MSA and MSQ models, possible hydrologic regions in the domain of study need to be identified. With the regions defined, I use a hypothesis test to determine whether the scaling parameters (α_p and θ_p) for different regions differ significantly. The null hypothesis for the scaling exponent is $H_0: \theta_p^{[i]} = \theta_p^{[j]}$; for the intercept it is $H_0: \alpha_p^{[i]} = \alpha_p^{[j]}$; the index *[i]* or *[j]* refers to different regions. I tested the null hypothesis using the Potthoff method (Potthoff, 1966) to determine if there was a significant difference in the linear regression parameters when the data is separated into different groups (regions in this case) by performing a multi-linear regressions. To apply the Potthoff analysis, I transformed Equation 6-5 (for the MSA model) and Equation 6-6 (for the MSQ model) to linear equations expressed by

$$ln(Q_p) = ln\left(\alpha_p^{[i]}\right) + \theta_p^{[i]}ln(A) \qquad \text{Equation 6-11}$$

$$ln(Q_p) = ln\left(\alpha_p^{[i]}\right) + \theta_p^{[i]}ln(\bar{Q}) \qquad \text{Equation 6-12}$$

Subsequently, we defined the linear expression

$$Y^{[i,j]} = a + bX^{[i,j]} + cG^{[i]} + dG^{[i]}X^{[i,j]} \qquad \text{Equation 6-13}$$

and performed a multi-linear regression to estimate its coefficients. Here Y is the dependent variable for the regions i and j; X is the independent variable for the regions i and j; and G is the dichotomous grouping variable (dummy variable) with the coding one for the region i and zero for the region j. The dependent variable $Y^{[i,j]} = \ln(Q_p{}^{[i,j]})$, and the independent variable $X^{[i,j]} =$

$\ln(\bar{Q}^{[i,j]})$ for the approach with the mean annual flow, and $X^{[i,j]} = \ln(A^{[i,j]})$ for the approach with the drainage area.

The coefficients a, b, c, and d in Equation 6-13 evaluate the difference in coefficients for Equation 6-11 (or Equation 6-12 for the mean annual flow) between the regions i and j. The coefficient a represents the intercept for the region i ($\ln\left(\alpha_p^{[i]}\right)$); the coefficient b is the slope for the region i ($\theta_p^{[i]}$); the coefficient c is the difference between the intercepts of the region i and j ($\ln(\alpha_p^{[i]}) - \ln(\alpha_p^{[j]})$); and the coefficient d is the difference between the exponents of the region i and j ($\theta_p^{[i]} - \theta_p^{[j]}$).

Using this procedure, the p-value for each parameter in the multi-linear regression is estimated. The p-value is used to test the null hypothesis that the parameter is equal to zero. Therefore, the p-value for c and d in the multi-linear regression is testing the null hypothesis $H_0: \theta_p^{[i]} = \theta_p^{[j]}$ and $H_0: \alpha_p^{[i]} = \alpha_p^{[j]}$, respectively. With a significance level of 5%, we can conclude that if the p-value is less than 0.05, the null hypothesis is rejected, concluding that the intercepts or scaling exponents are statistically different in both regions. But if the p-value is greater than 0.05, we cannot reject the null hypothesis and come to the conclusion that the intercepts or scaling exponents are probably the same in both regions. This test is key to determine if it is necessary to use more than one region to develop regional regressions for the proposed models.

6.3.3. FDC Validation

As a validation test, I calculated the MAPE, SMAPE, and MSAR to compare the FDCs estimated from the models SSA, SSQ, MSA, and MSQ with the observed FDC on 40 gauges.

176

These 40 gauges have streamflow records between 10 and 30 years and were not included in the set of the 74 gauges used for the construction of our four models. I did not include these 40 gauges for the construction of the four models because the regressions for the monthly FDCs must have more than 30 years of records to guarantee at least 980 daily streamflow observations per month. Although these gauges do not have more than 30 years as the calibration streamflow gauges do, we could use them as a good proxy to evaluate the performance of our results with respect to the observed FDC and the standard method that the USGS developed for the state of Iowa using the web-platform tool StreamStats. For the models SSA and MSA the A is the drainage area reported by the USGS. For the models SSQ and MSQ the $\bar{\bar{Q}}$ is estimated with the long-term water balance equation.

6.3.4. FDC as a Piecewise Continuous Function

To facilitate the potential practical use of FDCs using the SSA, SSQ, MSA, or MSQ models, I had to find a functional and continuous form to estimate the regression parameters ($\hat{\alpha}$ and $\hat{\theta}$) of these models as a continuous function of p. Because of the structure of $\hat{\alpha}$ and $\hat{\theta}$ for low, normal, and high flows, I found that $\hat{\theta}$ and the logarithm of $\hat{\alpha}$ can be described as a piecewise continuous function with respect to p as

$$ln(\hat{\alpha}) = Ap^B + C \qquad\qquad\qquad \text{Equation 6-14}$$

$$\hat{\theta} = Ap^B + C \qquad\qquad\qquad \text{Equation 6-15}$$

I fitted Equations 6-14 and 6-15 into three intervals: High Flows (sub-index H) with p between 0.01 and 0.3; Normal Flows (sub-index N) with p between 0.3 and 0.9; and low flows (sub-index L) with p between 0.9 and 0.99. For instance, the Equations 6-16, 6-17, and 6-18 show the relations for the three intervals of the logarithm of $\hat{\alpha}$ (similar procedure for $\hat{\theta}$). The

177

break values of 0.3 and 0.9 on p for the definition of these intervals was based on a trial-and-error process, to ensure a good fit.

$$ln(\widehat{\alpha_H}) = A_1 p^{B_1} + C_1 \ for \ p \in [0.01 \ 0.3] \qquad \text{Equation 6-16}$$

$$ln(\widehat{\alpha_N}) = A_2 p^{B_2} + C_2 \ for \ p \in [0.3 \ 0.9] \qquad \text{Equation 6-17}$$

$$ln(\widehat{\alpha_L}) = A_3 p^{B_3} + C_3 \ for \ p \in [0.9 \ 0.99] \qquad \text{Equation 6-18}$$

An individual regression analysis for each range could be performed; however, the estimated parameters for each function do not guarantee continuity at the interval end points of p at 0.3 and 0.9. To overcome this problem, the piecewise function based on the three functions described above is necessary to enforce continuity.

To enforce continuity at the interval end points, the conditions $A_1 0.3^{B_1} + C_1 = A_2 0.3^{B_2} + C_2$ and $C_2 = A_1 0.3^{B_1} + C_1 - A_2 0.3^{B_2}$ is imposed. Thus, Equation 6-17 can be rewritten as

$$ln(\widehat{\alpha_N}) = A_2 p^{B_2} + A_1 0.3^{B_1} + C_1 - A_2 0.3^{B_2} \qquad \text{Equation 6-19}$$

Similarly, Equations 6-17 and 6-18 must preserve continuity at p equal to 0.9. This can be achieved by imposing the condition $A_2 0.9^{B_2} + C_2 = A_3 0.9^{B_3} + C_3$ and $C_3 = A_2 0.9^{B_2} + C_2 - A_3 0.9^{B_3}$, and replacing C_2, $C_3 = A_2 0.9^{B_2} + A_1 0.3^{B_1} + C_1 - A_2 0.3^{B_2} - A_3 0.9^{B_3}$. As a result, Equation 6-18 can be rewritten as

$$ln(\widehat{\alpha_L}) = A_3 p^{B_3} + A_2 0.9^{B_2} + A_1 0.3^{B_1} + C_1 - A_2 0.3^{B_2} - A_3 0.9^{B_3} \qquad \text{Equation 6-20}$$

Now the logarithm of $\hat{\alpha}$ can be estimated as a piecewise continuous function with the simultaneous fit of Equations 6-16, 6-19, and 6-20 based on an OLS regression. I used the same procedure to fit the parameter $\hat{\theta}$ in the three regions.

6.4. Results and Discussion

Figure 6-3 shows the R^2, MAPE, SMAPE, and MSAR for the 981 independent streamflow quantile regressions for the historical-annual FDC using the SSA, SSQ, MSA, and MSQ models. The model selection criteria R^2 suggest that the models based on the $\bar{Q}$ (SSQ and MSQ) explain more the total variation of the streamflow quantiles than the models based on the A (SSA and MSA). Although the SSQ and MSQ models have similar values of R^2, the MAPE, SMAPE, and MSAR display lower errors for the MSQ model than the SSQ model; hence we select the MSQ model as the best basis to construct the historical-annual FDC.

In the four models, the streamflow estimations for low probabilities of exceedance (high flows) fit better in comparison with the streamflow with higher probabilities (low flows). Here, it is interesting to observe that the p of the $\bar{Q}$ varies between 0.2 and 0.3 (See Table 6-1 and Table 6-2), which is close to the range where the regression models show better performance. However, moving away from this range toward high frequencies (low flows), the performance decreases. In general, the decreasing in performance for low flows can be attributed to the fact that A or $\bar{Q}$ do not fully capture the streamflow variability in this range of frequencies. I found similar results for the historical-monthly FDCs, which show a better performance for the MSQ model. Figure 6-4 shows the statistic for the historical-monthly FDCs using the MSQ model. The error metrics change from month to month. Based on the R^2, the months with lower performance correspond to the winter season. Similarly, the other error metrics show that the months in fall show lower performance, with higher MAPE, SMAPE, and MSAR values for the months of September and October. Certainly, the MSQ model fits better than the other models explored in this study. Figure 6-5 shows the Mean Error and the Root Mean Square Error (RMSE) for the MSQ model for the historical-annual FDC and the 12 historical-monthly FDCs.

The MSQ model works much better than the MSA model because the MSQ model is region independent in the domain of the state of Iowa, while the model MSA is regionally

179

dependent. For an example of this idea, we normalized the Q_p for the 981 quantiles with respect to its A or $\bar{Q}$ (see Figure 6-6, left panel). This plot allowed us to visualize the presence of regional dependence. A visual inspection grouping the data by 4-digit HUCs reveals spatial clusters between the normalized variable and the A. The right-hand panel in Figure 6-6 shows an example; I fixed p=0.1 and plotted the normalized variables against the A. Here I identified a clear regional dependency in $Q_{0.1}/A$ by observing that most of the rescaled streamflow values for region 1 (black dots) were above 0.016; values for region 2 (gray squares) are between 0.011 and 0.016; and values for region 3 are below 0.011. Note that these clusters are not evident in the $Q_{0.1}/\bar{Q}$ plot. Figure 6-7 shows the location of the three regions based on the clusters found in the relation Q_p/A and A. Although the identification of these clusters is a function of the frequency evaluated and its delineation can be redefined with clustering techniques, we can be satisfied with the visual identification of the three regions shown in Figure 6-7 because they illustrate how Q_p/A depends on the region, while $Q_p/\bar{Q}$ does not.

I used the procedure explained in Section 6.3.2 to evaluate whether the scaling parameters of the MSA and MSQ models were changing significantly in the three regions identified above. Figure 6-8 shows the results for the p-values that assess the null hypothesis related to the θ_p of the MSA and MSQ models for the historical-annual FDC. For the MSA model, we can observe that the paired regions 1-3 and 2-3 differ in the θ_p, with p-values of less than 0.05 for low and high frequencies ($p<0.1$ and $p>0.9$). For the regions 1-2, I found p-values of less than 0.05 in probabilities of exceedance less than 0.1. On the other hand, the same analysis for $\bar{Q}$ as explanatory variable (MSQ model) indicated that for all the frequencies, the p-value is greater than 0.05; therefore, we cannot reject the hypothesis that the θ_p is the same along

180

the three regions identified in Iowa. Figure 6-9 shows the same analysis for the α_p; here the p-values for the MSA model in the regions 1-2 showed a wide range ($0.2<p<0.7$), with p-values of less than 0.05. The comparison for the sets of regions 1-3 and 2-3 shows p-values of less than 0.5 in low and high frequencies; thus, we concluded that the α_p are significantly different in these frequencies. On the other hand, the test for the α_p using the $\bar{Q}$ as explanatory variable showed p-values above 0.05 for the three sets of regions. Therefore, the hypothesis that the MSQ model is region independent cannot be rejected. In conclusion, the MSA model with the A as explanatory variable exhibited a significant regional dependency in Iowa.

I replicated the hypothesis test for monthly scale FDCs, with a total of three pairs of regions, 12 months, and 981 quantiles. The results for the α_p and θ_p are shown in Figure 6-10 and Figure 6-11, respectively. The results show that there is not a significant signature of regional dependency when the $\bar{Q}$ is used as explanatory variable for the regression analysis at monthly scale. However, by looking at the results for the α_p and θ_p for A, we can recognize large ranges for diverse months in which the p-value is less than 0.05. Hence, we can determine that the MSA model also presents a regional dependency at monthly scale, with a prevalence in low and high flows; the MSQ model does not exhibit such dependence.

Regarding the validation test, Figure 6-12 shows the error metrics for quantile estimations at 40 streamflow gauges for the historical-annual FDCs using the four models explored in this study and the standard method obtained from StreamStats based on Linhart et al., 2012. The MAPE results show that the MSQ model performed best in estimating streamflow quantiles among the four proposed models. StreamStats outperforms the MSQ model in low streamflows. The MAPE results show that the MSQ model performs in a similar manner in the

181

range of frequencies from 0.01 to 0.6, and the MSAR indicates that the performance is comparable for the ranges 0.01 to 0.4. This result is consistent with the statistics shown in the regression analysis in which lower performances were obtained at low flows, with an increase in performance near the frequency range of 0.2 to 0.3. Of the four methods explored in this study, we observed that the MSQ model with multi-scaling approach and explanatory variable $\bar{Q}$ is the best option to replicate some quantiles of the FDC. I replicated the same validation test for FDC at monthly scales; however, in this case, it was not possible to compare the FDC with StreamStats results because the USGS method only provides estimates for the historical-annual FDC. Figure 6-13 shows the MAPE, SMAPE, and MSAR statistics at a monthly scale for the MSQ model. The results indicate that the historical-monthly FDC is well described in all the months with decreasing performance for low flows. The months of February, March, and April show a better model performance for most frequencies. On the other hand, the months with lower performance (July, August, and September) also show the largest errors over the range of low flows. These results show the variability in time (months) and frequency (percentage of time exceeded) in the model performance.

With the MSQ model selected as the best model for the estimation of the historical-annual and historical-monthly FDCs, I fit the α_p and θ_p of the MSQ model to a piecewise continuous function with respect to the *p*. The results show that the sum of squared errors and the RMSE in these regressions are small (see Table 6-3). Therefore, the estimated scaling parameters ($\hat{\theta}$ and $\hat{\alpha}$) from the piecewise continuous function can be consider an accurate representation of θ_p and α_p (see Figure 6-14). I replicated this analysis at the monthly scale and again had the low sum of squared errors and RMSE (see Table 6-3), which allowed us to calculate piecewise continuous functions for the estimation of $\hat{\theta}$ and $\hat{\alpha}$ for each month. I synthesized the final

182

historical-annual and historical-monthly FDCs based on these piecewise continuous functions as a set of equations for the three different ranges of p (see Table 6-4, Table 6-5, and Table 6-6). Based on the streamflow gauges used in this study, reasonable values of $\bar{Q}$ for the state of Iowa range from 0 to 200 m^3/s. I verified the monotonic property of these piecewise continuous FDCs in the range of $\bar{Q}$ between 0 and 200 m^3/s, checking the existence of negative derivatives on the final equation with respect to the probability of exceedance p. Then, we can confirm that the monotonic property emerges because of the small steps between frequencies in the streamflow regression, and because of the use of a single explanatory variable in the regression analysis.

6.4.1. Scale Invariant FDC Application for the State of Iowa

Figure 6-15 shows the historical-annual and historical-monthly FDCs estimated from the piecewise continuous functions for three different basins in the validation sites. These sites have drainage areas equal to 290 km^2, 580 km^2, and 2,079 km^2. Figure 6-15 also shows the FDC from the streamflow observations and the FDC obtained with the StreamStats tool. The results confirm that the estimated historical-annual FDCs from the piecewise function match the observed FDC well. Figure 6-15 also shows the estimated streamflow quantiles from monthly FDCs and observed FDC for seven specific quantiles (0.99, 0.9, 0.75, 0.5, 0.25, 0.1, and 0.01). The graphs show the strong differences in streamflow distribution for different months, which are not captured by a historical-annual FDC.

One of the main motivations to develop this study was the need to translate streamflow outputs from real-time hydrologic distributed models to streamflow frequencies to help the public interpret the hydrologic model flow estimates and predicted estimates. To demonstrate the applicability of these results, I used streamflow outputs from the distributed hydrologic model implemented by the IFC and classified these outputs into streamflow conditions along Iowa's drainage network. In this case, I defined the following streamflow conditions: $p<0.1$ Near Bankfull; $0.1<p<0.25$ High; $0.25<p<0.75$ Normal; $0.75<p<0.9$ Low; and $p>0.9$ Very Low. Figure 6-16 shows the streamflow condition classification along

183

the drainage network for Sept. 20, 2016. Note that for the construction of this map, I used the set of equations in Tables 6-4, 6-5, and 6-6 for the month of September. GIS techniques were used to estimate the A for every site in the hydrologic model domain (Mantilla & Gupta, 2005). I estimated the mean annual flow with long-term water balance, again using the PRISM product for precipitation and evapotranspiration from a continuous global record of land surface evapotranspiration from 1983 to 2006. Overall, this example demonstrates the convenience of implementing this methodology into hydrologic distributed models that can be presented as regional maps.

6.5. Conclusions

The method presented in this chapter for estimating FDCs can be characterized as follows: 1) the FDC is described by a scale-invariant power law; 2) the power law are constructed using the multi-scaling framework, with variation in the scaling exponent and intercept across frequencies; 3) the FDC captures regional non-homogeneities in Iowa via the $\bar{Q}$, which captures changes in precipitation and evapotranspiration across the domain; 4) the FDC is region independent in the sense that we can implement the method anywhere in the state of Iowa; 5) we can calculate the FDC using a piecewise continuous function based on the $\bar{Q}$ and p; and 6) we can estimate the FDC for historical annual and monthly scales, which allows us to represent more accurately the seasonal variability in the streamflow distribution.

The proposed methodology provides reasonable FDC estimates with respect to estimates from streamflow observations at historical annual and monthly scales. The historical-annual FDC comparison with respect to the FDC estimated with StreamStats shows that the proposed approach demonstrates a similar performance in streamflow quantiles for probabilities of exceedance less than 0.6. I found that the errors in our FDC estimations are larger for low flows with *p>0.6*, but well within the margin of error of many engineering applications. This methodology is valid for unregulated rivers within the state of Iowa, excluding the Mississippi River and Missouri River, which are heavily regulated. Reasonable values of $\bar{Q}$ for Iowa range from 0 to 200 m^3/s across all watershed scales.

184

A few caveats on this analysis include the following. (1) The results of performance in the regression estimates for the calibration and the validation sets suggest that the variance in the estimates is higher in low flows, and the StreamStats methodology shows better performance at the annual scale for these low flows. (2) The proposed method uses the mean annual flow and therefore, the performance of the FDC estimation depends on the accuracy of its estimation. (3) Other basin characteristics or hydrological processes not captured by the mean annual flow drive the description of variability in low flow quantiles. This can be explained by noting that the mean annual flow has a probability of exceedance between 0.2 and 0.3; therefore, the information contained in $\bar{Q}$ in the representation of the streamflow distribution decreases toward frequencies closer to 1 (low flows). (4) The suitability to translate streamflow outputs from real-time hydrologic distributed models to streamflow frequencies relies on the performance of the hydrologic model to represent the observed streamflow distribution, since if the outputs of the hydrologic model are biased the streamflow classification based on the FDC will be biased as well.

Although I developed this study for Iowa, this approach can easily be extended to other regions. This makes it an attractive technique for the classification of streamflow outputs from regional or national hydrologic distributed models to streamflow frequencies in order to create regional maps that can be easily used to interpret streamflow conditions at ungauged sites.

Table 6-1. Description of the 74 streamflow gauges used in the regression analysis in the SSA, SSQ, MSA, and MSQ models.

USGS stream gauge number	Drainage area USGS (km²)	$\overline{P}$ (mm/year)	$\overline{ET}$ (mm/year)	$\overline{Q}$ (m³/s)	p for $\overline{Q}$	% Zero records	Water years
5387500	1323.5	885.9	617.5	11.3	0.22	0.00%	44
5388250	1994.3	885.8	614.1	17.2	0.29	0.00%	40
5411600	458.4	899.3	618.8	4.1	0.22	0.00%	35
5412500	4001.5	911.0	618.9	37.1	0.20	0.00%	94
5418500	4022.3	929.9	631.8	38.0	0.21	0.00%	101
5421000	2714.3	915.1	617.9	25.6	0.21	0.00%	81
5422000	6050.2	922.9	622.5	57.6	0.26	0.00%	80
5422470	46.1	914.0	588.0	0.5	0.23	0.00%	31
5449500	1111.1	846.4	610.4	8.3	0.22	0.00%	73
5451500	3967.9	873.6	625.1	31.3	0.24	0.00%	96
5451700	305.6	908.5	644.2	2.6	0.24	0.09%	65
5451900	145.3	904.6	642.9	1.2	0.23	0.06%	65
5452000	520.6	904.7	639.1	4.4	0.23	0.00%	69
5452200	183.6	908.8	646.2	1.5	0.23	0.86%	65
5453000	489.5	913.9	646.2	4.2	0.24	0.13%	69
5453100	7236.4	888.6	634.7	58.3	0.29	0.00%	58
5454000	65.5	930.5	636.7	0.6	0.19	5.27%	77
5454300	254.1	924.2	635.7	2.3	0.22	0.08%	62
5455100	520.6	930.9	648.2	4.7	0.20	0.00%	44
5455500	1486.7	930.2	650.3	13.2	0.20	0.00%	75
5457700	2729.8	870.5	596.6	23.7	0.24	0.00%	45
5458000	792.5	886.8	615.4	6.8	0.19	0.00%	60
5458500	4302.0	879.1	604.4	37.5	0.19	0.00%	94
5459500	1362.3	859.1	609.5	10.8	0.22	0.00%	82
5462000	4522.1	871.0	601.7	38.6	0.24	0.00%	61
5463000	898.7	893.0	625.7	7.6	0.22	0.00%	69
5463500	784.8	899.1	622.3	6.9	0.22	0.00%	56
5464000	13328.1	879.6	609.9	114.0	0.25	0.00%	74
5465000	20168.2	893.8	612.9	179.6	0.26	0.00%	75
5470000	815.8	891.5	624.3	6.9	0.20	0.98%	88
5470500	528.4	907.1	637.5	4.5	0.23	3.04%	57
5471050	2079.8	903.8	636.2	17.6	0.28	0.00%	29
5471200	714.8	906.3	638.4	6.1	0.26	0.00%	46
5471500	4234.6	907.9	642.2	35.7	0.25	0.00%	69
5472500	1890.7	923.5	658.2	15.9	0.23	0.00%	69
5473400	1372.7	956.5	647.0	13.5	0.17	0.00%	37
5474000	11168.0	927.8	648.5	98.9	0.22	0.00%	100
5476750	5843.0	763.2	608.2	28.7	0.32	0.00%	50
5479000	3387.7	810.5	602.5	22.3	0.24	0.00%	74
5481000	2185.9	854.7	612.5	16.8	0.22	0.00%	74

186

Table 6-1 – Continued

5481950	927.2	891.7	632.5	7.6	0.24	0.44%	54
5482300	1813.0	831.9	599.4	13.4	0.22	0.03%	56
5482500	4193.2	844.4	616.2	30.3	0.22	0.00%	74
5483450	971.2	866.2	643.1	6.9	0.28	0.00%	35
5484000	2574.4	880.5	654.1	18.5	0.20	0.00%	74
5484500	8912.1	862.8	632.2	65.2	0.20	0.00%	99
5484800	203.1	899.1	545.0	2.3	0.21	0.46%	43
5485640	240.1	905.7	584.7	2.4	0.24	0.61%	43
5486000	903.9	895.2	681.1	6.1	0.22	0.38%	74
5486490	1267.5	901.9	678.2	9.0	0.20	0.00%	74
5487470	1191.4	923.8	659.0	10.0	0.13	0.09%	74
5487980	862.5	940.0	660.1	7.7	0.15	0.00%	52
5488200	233.4	930.0	666.7	1.9	0.15	0.30%	29
5489000	968.7	948.9	650.2	9.2	0.12	0.08%	67
5494300	227.1	978.6	689.8	2.1	0.11	0.28%	33
6483500	4123.3	723.8	620.5	13.5	0.26	0.16%	66
6600000	168.6	714.0	629.9	0.4	0.28	0.39%	47
6600100	694.1	753.1	618.6	3.0	0.22	0.34%	59
6600500	2294.7	736.1	619.2	8.5	0.22	0.00%	79
6605000	1103.3	752.3	619.5	4.6	0.35	0.44%	37
6605850	4009.3	763.9	622.5	18.0	0.33	0.00%	42
6606600	6475.0	770.3	628.2	29.2	0.26	0.00%	87
6607200	1732.7	802.8	634.8	9.2	0.25	0.01%	73
6607500	9132.3	801.9	637.8	47.5	0.23	2.74%	71
6608500	1054.1	798.0	650.6	4.9	0.23	0.00%	74
6609500	2255.9	821.9	642.9	12.8	0.21	0.01%	82
6807410	1577.3	847.7	646.1	10.1	0.27	0.00%	55
6808500	3434.3	858.3	648.9	22.8	0.24	0.00%	66
6809210	1129.2	878.0	657.6	7.9	0.25	0.00%	54
6809500	2315.4	881.5	659.8	16.3	0.20	0.00%	84
6810000	7267.5	870.9	654.7	49.8	0.21	0.00%	87
6898000	1815.6	920.0	684.9	13.5	0.16	0.00%	79
6903400	471.4	955.1	680.5	4.1	0.14	1.34%	49
6903700	435.1	970.6	702.1	3.7	0.13	0.11%	47

Table 6-2. Description of the 40 streamflow gauges used in the validation analysis.

USGS stream gauge number	Drainage area USGS (km²)	$\overline{P}$ (mm/year)	$\overline{ET}$ (mm/year)	$\overline{Q}$ (m³/s)	p for $\overline{Q}$	% Zero records	Water years
5387440	950.5	884.7	613.7	8.2	0.33	0.00%	12
5388000	1471.1	882.2	613.4	12.5	0.17	0.00%	26
5388500	110.9	884.4	638.1	0.9	0.06	0.00%	21
5389400	88.4	879.0	619.0	0.7	0.24	0.00%	23
5411400	71.5	879.1	594.5	0.6	0.26	0.00%	10
5411850	1660.2	901.7	624.7	14.6	0.26	0.00%	14
5412000	2307.7	894.1	619.8	20.1	0.16	0.00%	10
5412020	2338.8	893.7	619.7	20.3	0.28	0.00%	13
5412400	901.3	899.5	565.1	9.6	0.22	0.00%	15
5416900	712.2	932.2	599.7	7.5	0.28	0.00%	13
5417700	158.8	916.3	614.5	1.5	0.19	0.00%	19
5418400	1307.9	912.9	633.8	11.6	0.32	0.00%	16
5418450	1336.4	911.5	632.4	11.8	0.18	0.00%	14
5420680	896.1	921.6	631.8	8.2	0.25	0.00%	14
5421740	4079.2	953.4	654.0	38.7	0.30	0.00%	12
5422560	41.7	918.2	627.0	0.4	0.25	0.00%	20
5422600	148.4	911.2	509.1	1.9	0.17	0.00%	20
5448500	290.1	844.6	625.2	2.0	0.09	0.00%	10
5451210	580.2	888.5	641.8	4.5	0.27	0.00%	18
5452500	6358.4	900.1	647.8	50.9	0.18	0.00%	20
5454220	151.3	919.7	642.1	1.3	0.27	0.00%	20
5460500	3413.6	887.8	617.3	29.3	0.18	0.00%	11
5464220	774.4	907.8	636.7	6.7	0.27	0.00%	15
5464640	461.0	910.0	642.2	3.9	0.23	0.15%	16
5471040	47.7	908.7	662.6	0.4	0.26	0.00%	10
5473450	150.2	948.5	650.6	1.4	0.20	0.41%	17
5478000	1196.6	805.6	622.2	7.0	0.15	0.46%	23
5482135	603.5	840.2	616.1	4.3	0.32	0.00%	13
5484650	9140.1	905.2	674.4	66.9	0.29	0.00%	18
5485605	160.6	901.8	628.1	1.4	0.32	0.00%	11
5487540	17.6	909.8	663.7	0.1	0.28	0.37%	10
5487550	52.6	912.4	633.9	0.5	0.20	0.00%	11
5488000	984.2	908.8	630.9	8.7	0.12	0.00%	17
5494500	417.0	963.3	670.7	3.9	0.10	0.30%	11
6483270	2040.9	714.8	616.3	6.4	0.12	0.00%	15
6483290	2209.3	714.7	615.6	6.9	0.39	0.00%	13
6605600	3455.0	793.7	655.9	15.1	0.18	0.00%	15
6607000	101.8	798.6	631.1	0.5	0.19	0.00%	18
6808000	27.5	866.6	638.0	0.2	0.09	0.11%	15
6818750	562.0	914.9	711.8	3.6	0.17	0.01%	23

Table 6-3. Measurements of errors in the fit of the piecewise continuous function of θ and α.
SSE: sum of squared errors. RMSE: root-mean-square error

| | θ | | α | |
Period	SSE	RMSE	SSE	RMSE
Jan	4.929	0.07	0.175	0.013
Feb	1.39	0.037	0.036	0.006
Mar	2.364	0.049	0.04	0.006
Apr	1.185	0.035	0.023	0.005
May	1.492	0.039	0.023	0.005
Jun	1.548	0.039	0.037	0.006
Jul	2.96	0.055	0.039	0.006
Aug	3.76	0.062	0.104	0.01
Sep	3.619	0.06	0.113	0.011
Oct	3.687	0.061	0.064	0.008
Nov	0.557	0.024	0.133	0.012
Dec	1.036	0.032	0.072	0.009
Historic	1.038	0.032	0.042	0.006

189

Table 6-4, Table 6-5, and Table 6-6 are the fitted equations for the piecewise continuous FDC. Because of the long decimal precision, these equations are not completely continuous in the quantiles 0.3 and 0.9; however, the error caused by the decimal precision presented in the below tables is less than 2%.

Table 6-4. FDC for the Range of High Flows Q_p (m^3/s): $p \in 0[0.01, 0.3]$ $with$ $\bar{Q}$ in m^3/s

Annual	$Q_p = \left(e^{-8.2874p^{0.17448}+6.2045}\right)\bar{Q}^{\left(-0.033369p^{-0.44814}+1.1032\right)}$
Jan	$Q_p = \left(e^{-7.2464p^{0.1385}+4.9096}\right)\bar{Q}^{\left(-0.02314p^{-0.42977}+1.0296\right)}$
Feb	$Q_p = \left(e^{-9.5577p^{0.14276}+7.3535}\right)\bar{Q}^{\left(-0.23795p^{-0.16362}+1.2533\right)}$
Mar	$Q_p = \left(e^{-6.8543p^{0.27272}+4.9471}\right)\bar{Q}^{\left(-2.3482p^{-0.031583}+3.4959\right)}$
Apr	$Q_p = \left(e^{-6.1301p^{0.20205}+5.000}\right)\bar{Q}^{\left(-0.1064p^{-0.23894}+1.1936\right)}$
May	$Q_p = \left(e^{-6.841p^{0.18141}+5.7478}\right)\bar{Q}^{\left(-0.11855p^{-0.26169}+1.1892\right)}$
Jun	$Q_p = \left(e^{-8.451p^{0.16674}+7.0607}\right)\bar{Q}^{\left(-0.19006p^{-0.22559}+1.3257\right)}$
Jul	$Q_p = \left(e^{-9.1678p^{0.17473}+6.8023}\right)\bar{Q}^{\left(-8.7076p^{-0.009692}+9.9458\right)}$
Aug	$Q_p = \left(e^{-10.421p^{0.17116}+7.0758}\right)\bar{Q}^{\left(0.95518p^{0.13605}+0.34082\right)}$
Sep	$Q_p = \left(e^{-7.982p^{0.29306}+4.0195}\right)\bar{Q}^{\left(0.54661p^{0.32954}+0.77356\right)}$
Oct	$Q_p = \left(e^{-6.402p^{0.33205}+3.0477}\right)\bar{Q}^{\left(0.45314p^{0.27173}+0.77025\right)}$
Nov	$Q_p = \left(e^{-5.3556p^{0.2415}+3.1321}\right)\bar{Q}^{\left(-0.056636p^{-0.27264}+1.0983\right)}$
Dec	$Q_p = \left(e^{-5.2069p^{0.22562}+2.9578}\right)\bar{Q}^{\left(-0.11892p^{-0.18339}+1.1418\right)}$

190

Table 6-5. FDC for the Range of Normal Flows Q_p (m^3/s): $p \in [0.3, 0.9]$ with $\bar{Q}$ in m^3/s

Annual	$Q_p = \left(e^{-4.681p^{1.8189}+0.011191}\right)\bar{Q}^{(0.41077p^{2.8303}+1.0324)}$
Jan	$Q_p = \left(e^{-4.4163p^{1.8954}-0.77303}\right)\bar{Q}^{(0.46338p^{2.4184}+0.9656)}$
Feb	$Q_p = \left(e^{-4.267p^{2.0548}-0.33528}\right)\bar{Q}^{(0.41219p^{3.642}+0.95836)}$
Mar	$Q_p = \left(e^{-3.3558p^{1.9773}+0.3218}\right)\bar{Q}^{(0.12431p^{4.7135}+1.0563)}$
Apr	$Q_p = \left(e^{-3.2572p^{1.8738}+0.53492}\right)\bar{Q}^{(0.15369p^{3.4107}+1.0492)}$
May	$Q_p = \left(e^{-3.3821p^{2.0642}+0.5307}\right)\bar{Q}^{(0.17573p^{2.3192}+1.0159)}$
Jun	$Q_p = \left(e^{-3.7196p^{1.9925}+0.48461}\right)\bar{Q}^{(0.22026p^{2.1528}+1.0598)}$
Jul	$Q_p = \left(e^{-3.8816p^{2.0222}-0.28611}\right)\bar{Q}^{(0.32633p^{3.0773}+1.1279)}$
Aug	$Q_p = \left(e^{-3.9659p^{1.361}-0.96985}\right)\bar{Q}^{(0.44026p^{2.0457}+1.1142)}$
Sep	$Q_p = \left(e^{-4.6853p^{1.3536}-0.67115}\right)\bar{Q}^{(0.6086p^{1.2049}+0.99847)}$
Oct	$Q_p = \left(e^{-5.1126p^{1.2704}-0.13713}\right)\bar{Q}^{(0.54816p^{1.7235}+1.028)}$
Nov	$Q_p = \left(e^{-4.6008p^{1.293}+0.09765}\right)\bar{Q}^{(0.49555p^{1.0543}+0.8803)}$
Dec	$Q_p = \left(e^{-4.5552p^{1.7252}-0.43975}\right)\bar{Q}^{(0.46776p^{1.7962}+0.9397)}$

Table 6-6. FDC for the Range of Low Flows $Q_p (m^3/s)$: $p \in [0.9, 0.99]$ $with$ $\bar{Q}$ in m^3/s

|	
Annual	$Q_p = \left(e^{-3.7633p^{13.776}-2.972}\right)\bar{Q}^{(0.45486p^{17.36}+1.2642)}$
Jan	$Q_p = \left(e^{-4.8963p^{10.107}-2.7018}\right)\bar{Q}^{(0.69032p^{10.198}+1.0891)}$
Feb	$Q_p = \left(e^{-4.0703p^{21.932}-3.3679}\right)\bar{Q}^{(0.63714p^{36.682}+1.2258)}$
Mar	$Q_p = \left(e^{-3.0216p^{12.189}-1.5684}\right)\bar{Q}^{(0.30487p^{33.91}+1.1234)}$
Apr	$Q_p = \left(e^{-2.9957p^{12.879}-1.3675}\right)\bar{Q}^{(0.33232p^{45.799}+1.1538)}$
May	$Q_p = \left(e^{-3.3561p^{11.587}-1.2003}\right)\bar{Q}^{(0.26413p^{29.894}+1.1423)}$
Jun	$Q_p = \left(e^{-4.1585p^{26.324}-2.2709}\right)\bar{Q}^{(0.67024p^{53.786}+1.2331)}$
Jul	$Q_p = \left(e^{-4.4844p^{11.566}-2.097}\right)\bar{Q}^{(0.53367p^{14.263}+1.2452)}$
Aug	$Q_p = \left(e^{-3.6738p^{10.155}-2.978}\right)\bar{Q}^{(0.40043p^{8.6684}+1.3084)}$
Sep	$Q_p = \left(e^{-3.3683p^{18.422}-4.2501}\right)\bar{Q}^{(0.56343p^{40.483}+1.5266)}$
Oct	$Q_p = \left(e^{-3.2238p^{11.477}-3.6471}\right)\bar{Q}^{(0.33409p^{17.549}+1.4327)}$
Nov	$Q_p = \left(e^{-2.6267p^{18.00}-3.5229}\right)\bar{Q}^{(0.32068p^{27.14}+1.3054)}$
Dec	$Q_p = \left(e^{-3.5668p^{11.401}-3.1648}\right)\bar{Q}^{(0.47741p^{11.517}+1.185)}$
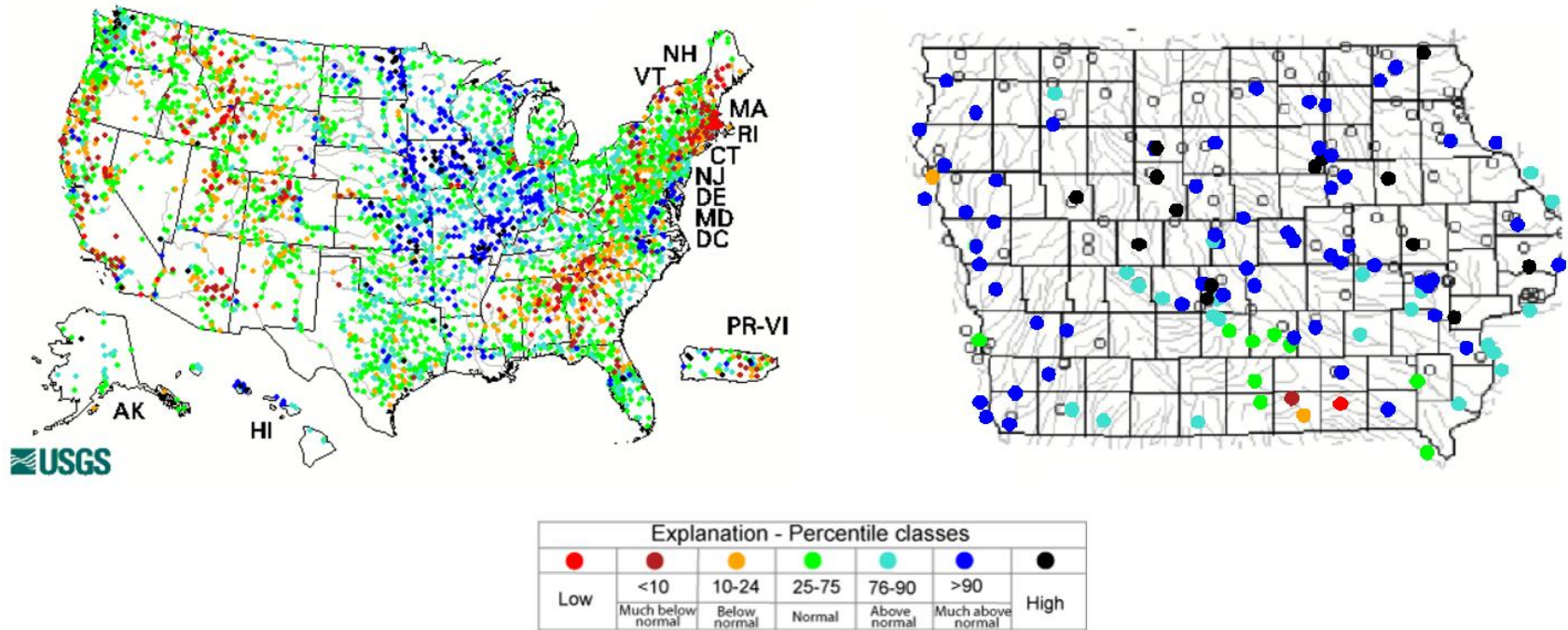
Figure 6-1. USGS classification of daily streamflow conditions for the United States and the state of Iowa on Sept. 20, 2016.
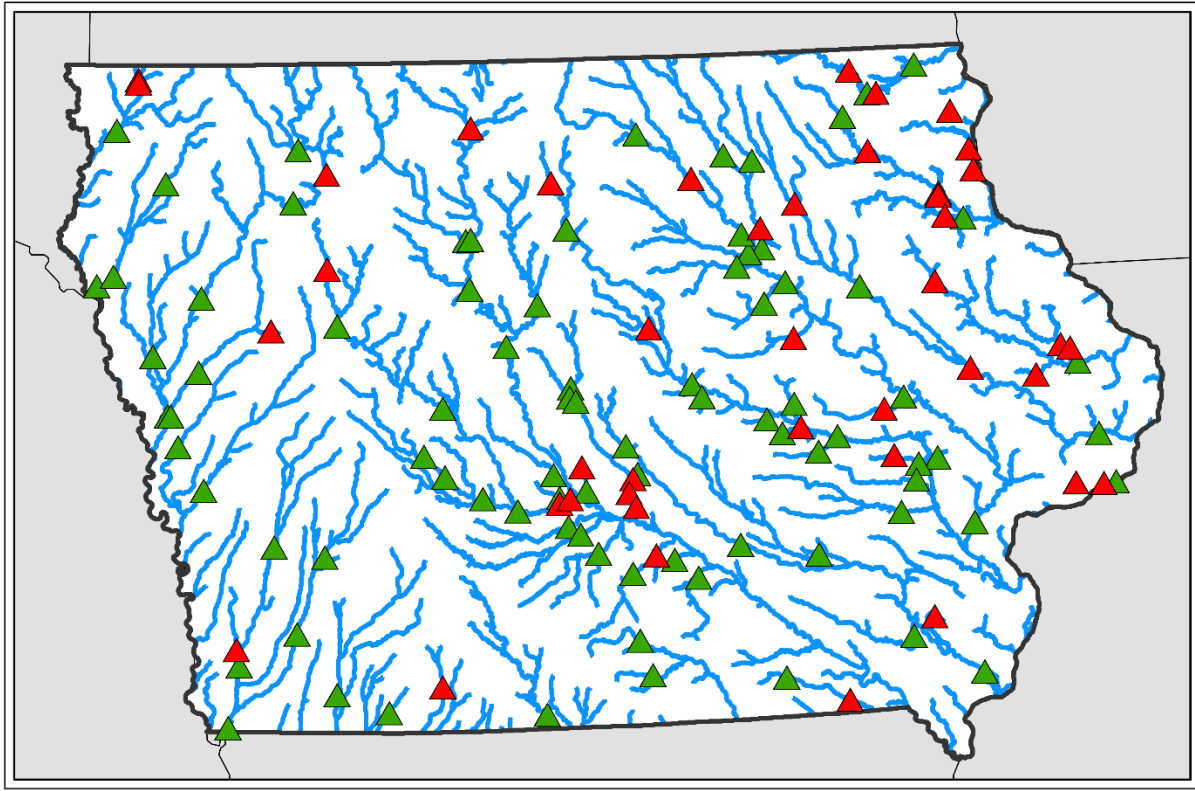
Figure 6-2. Location of the streamflow gauges in Iowa. The green triangles are the USGS gauges used for the model development. The red triangles are the USGS gauges used for the validation test.

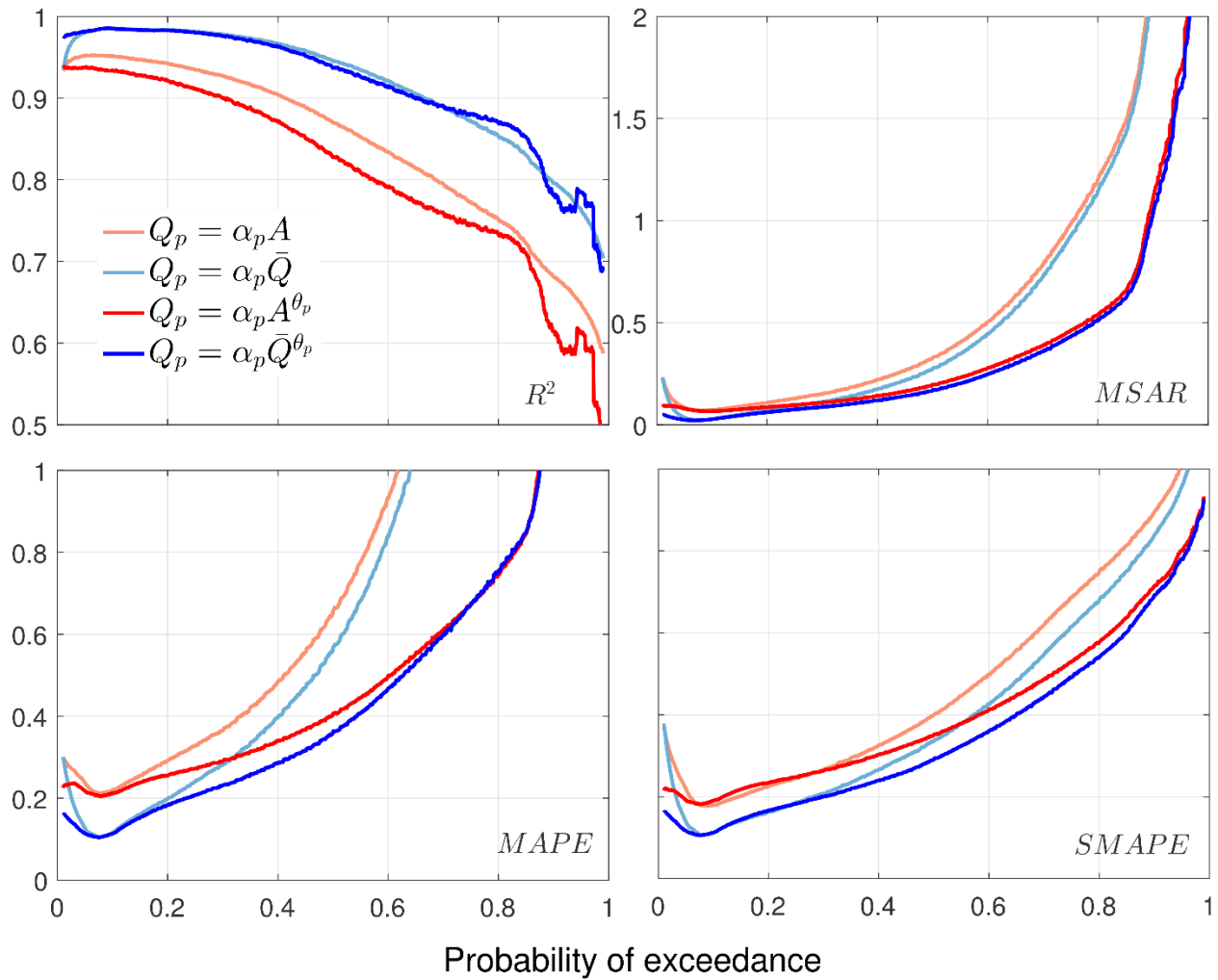Figure 6-3. Statistics R^2, MAPE, SMAPE, and MSAR for quantiles ranging from 0.01 to 0.99 for the four models describing the historical FDC.
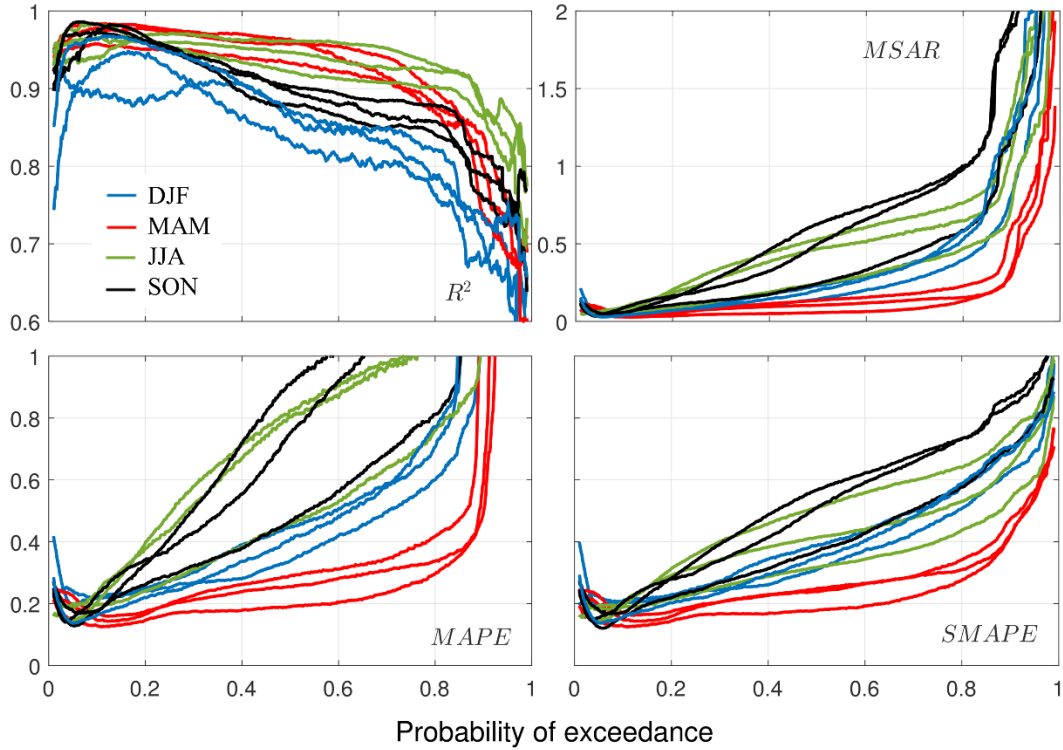
Figure 6-4. Statistics R^2, MAPE, SMAPE, and MSAR for quantiles ranging from 0.01 to 0.99 for the MSQ model describing the monthly FDCs. Winter months (DJF) are shown in blue, spring months (MAM) in red, summer months (JJA) in green, and fall months (SON) in black.
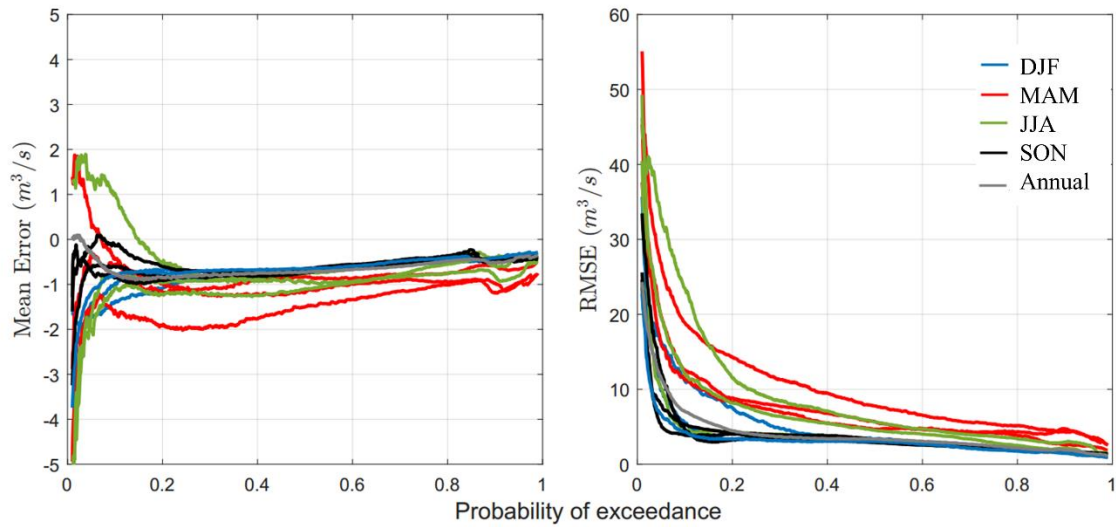
Figure 6-5. Mean Error and RMSE for quantiles ranging from 0.01 to 0.99 for the MSQ model describing the annual and monthly FDCs. Annual result is shown in gray. Winter months (DJF) are shown in blue, spring months (MAM) in red, summer months (JJA) in green, and fall months (SON) in black.
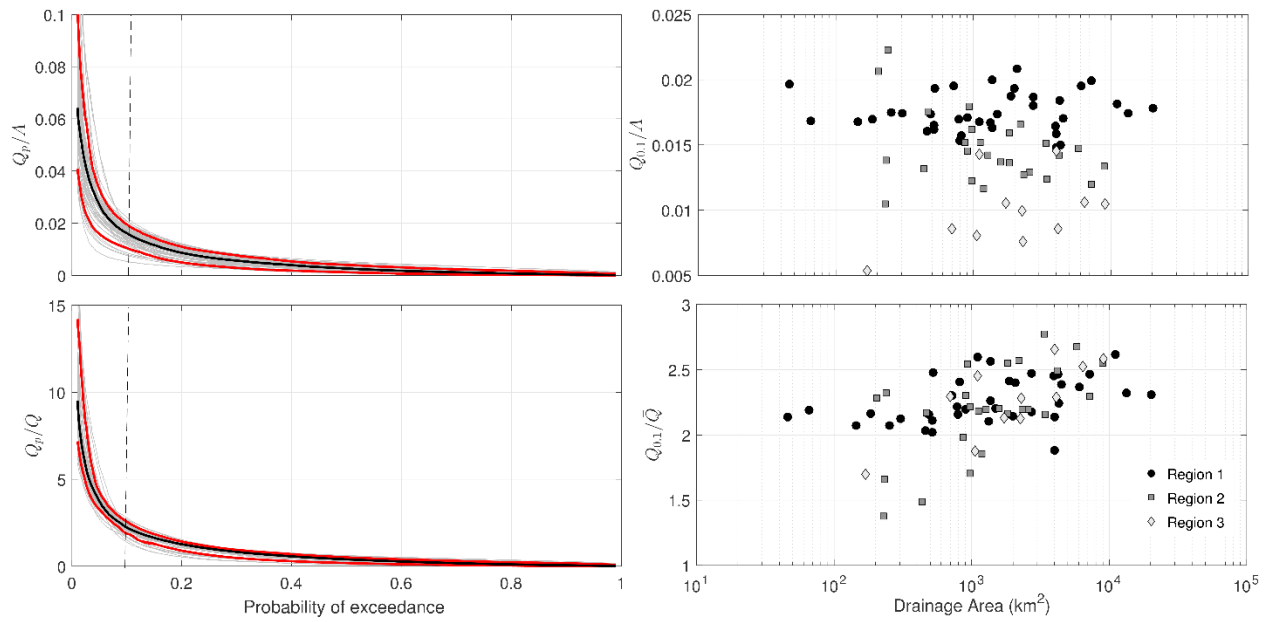
Figure 6-6. Streamflow quantiles normalized with respect to A and $\bar{Q}$ for the 74 streamflow gauges used for the model development; the red lines represent the percentile 5 and 95 (left panel). Normalized streamflow with p equal to 0.1 associated to three regions in the state of Iowa (right panel).
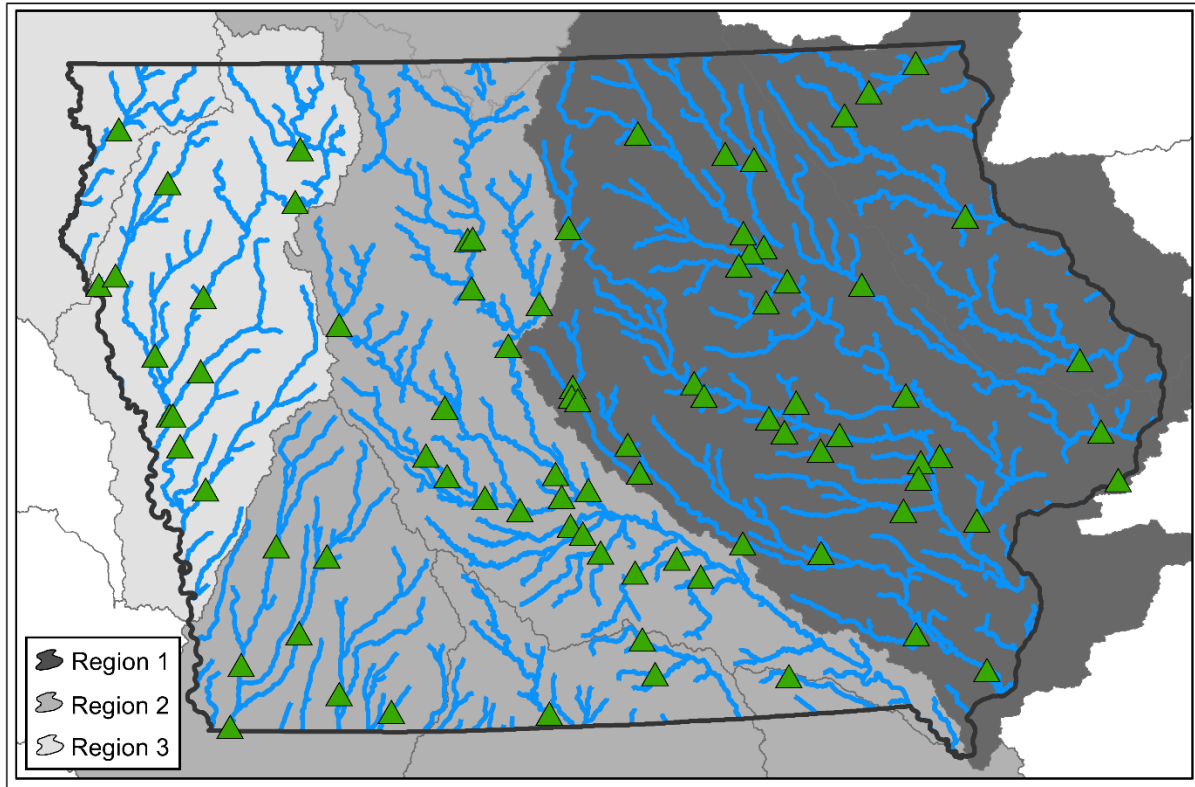
Figure 6-7. Definition of the three regions detected in the relation Q_p/A and A. The green triangles are the USGS gauges used for the model development.

Figure 6-8. This figure illustrates the p-value for testing of the null hypothesis $H_0: \theta_{p,Region\ i}^{[MSA]} = \theta_{p,Region\ j}^{[MSA]}$ and $H_0: \theta_{p,Region\ i}^{[MSQ]} = \theta_{p,Region\ j}^{[MSQ]}$ in the historical FDC with quantiles ranging from 0.01 to 0.99.
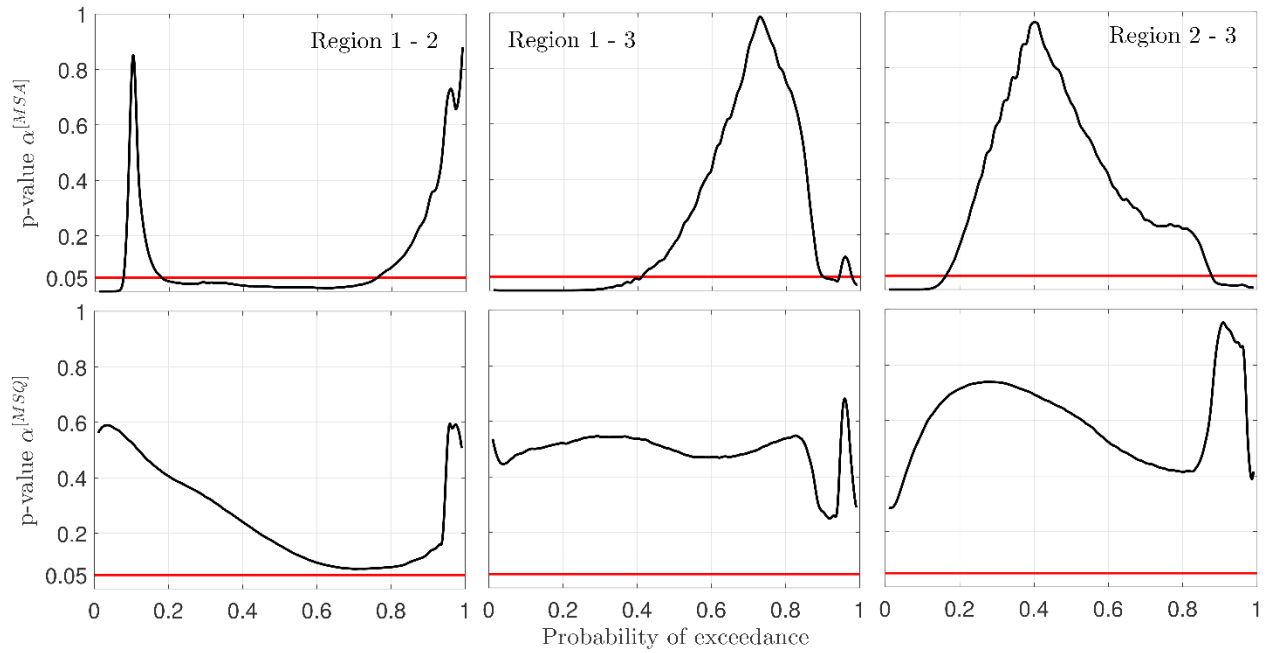
Figure 6-9. This figure illustrates the p-value for testing of the null hypothesis $H_0: \alpha_{p,Region\ i}^{[MSA]} = \alpha_{p,Region\ j}^{[MSA]}$ and $H_0: \alpha_{p,Region\ i}^{[MSQ]} = \alpha_{p,Region\ j}^{[MSQ]}$ in the historical FDC with quantiles ranging from 0.01 to 0.99.
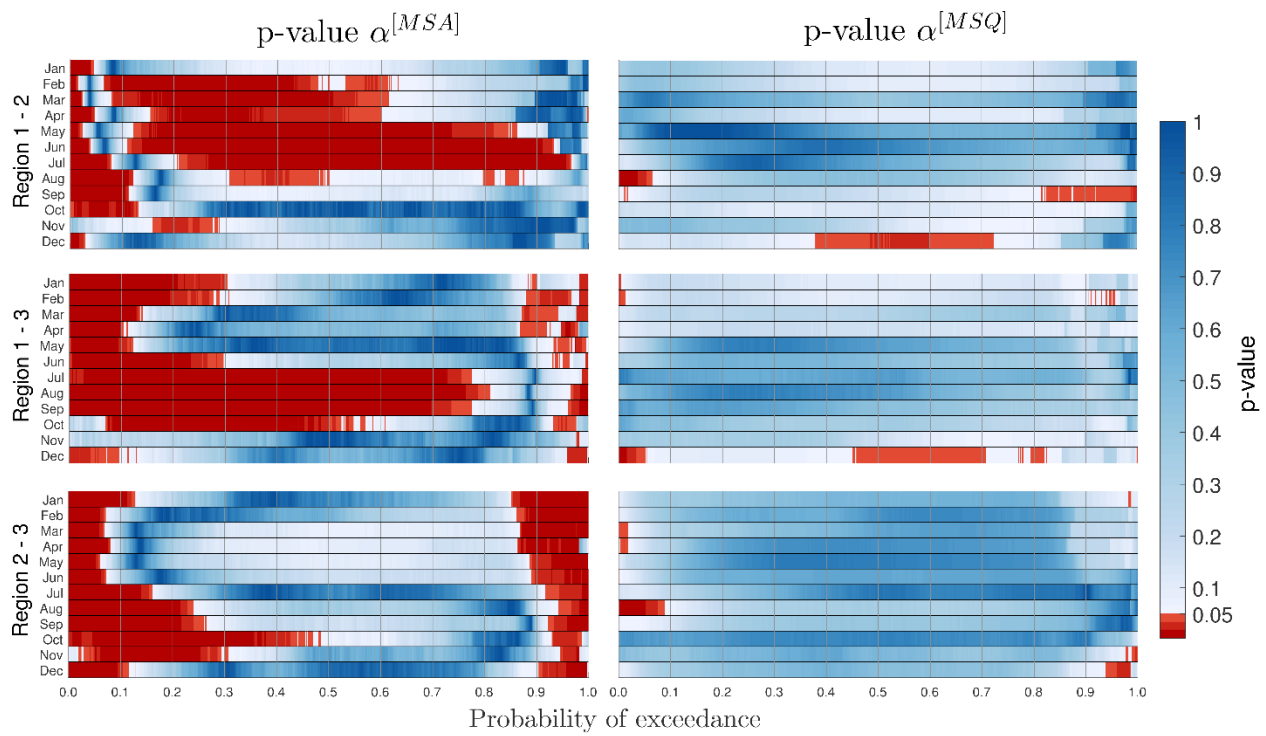
Figure 6-10. This figure illustrates the p-value for the null hypothesis $H_0: \alpha_{p,Region\ i}^{[MSA]} = \alpha_{p,Region\ j}^{[MSA]}$ and $H_0: \alpha_{p,Region\ i}^{[MSQ]} = \alpha_{p,Region\ j}^{[MSQ]}$ at monthly scale with quantiles ranging from 0.01 to 0.99.

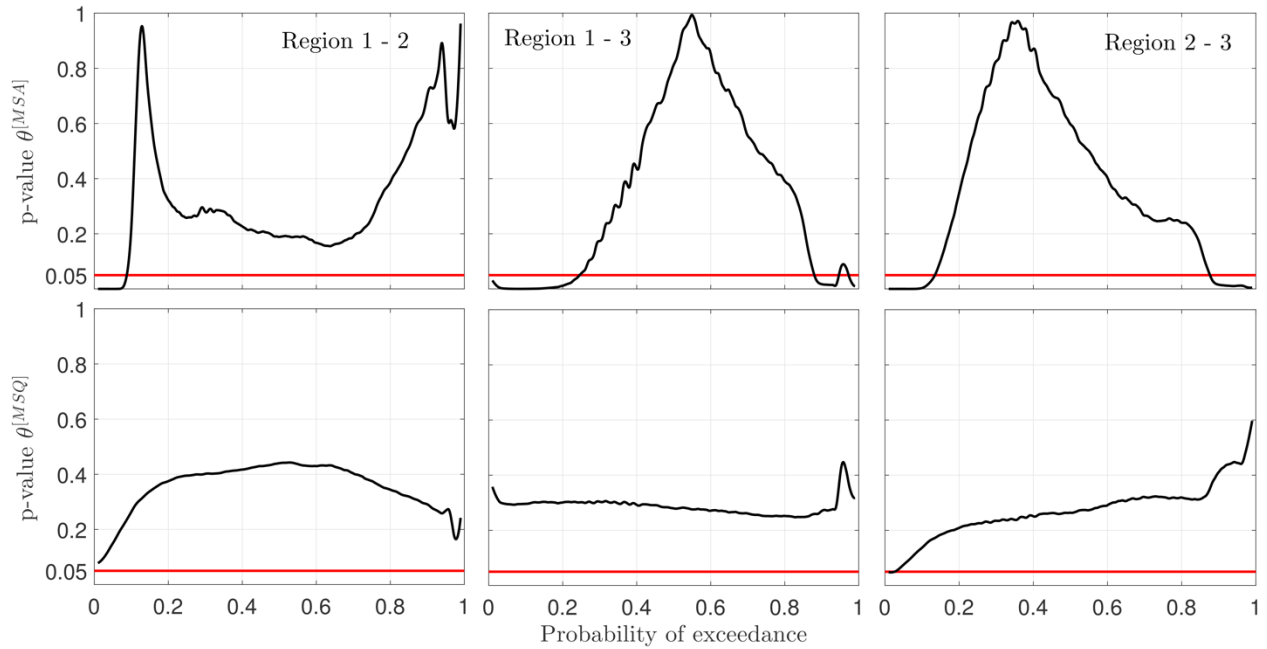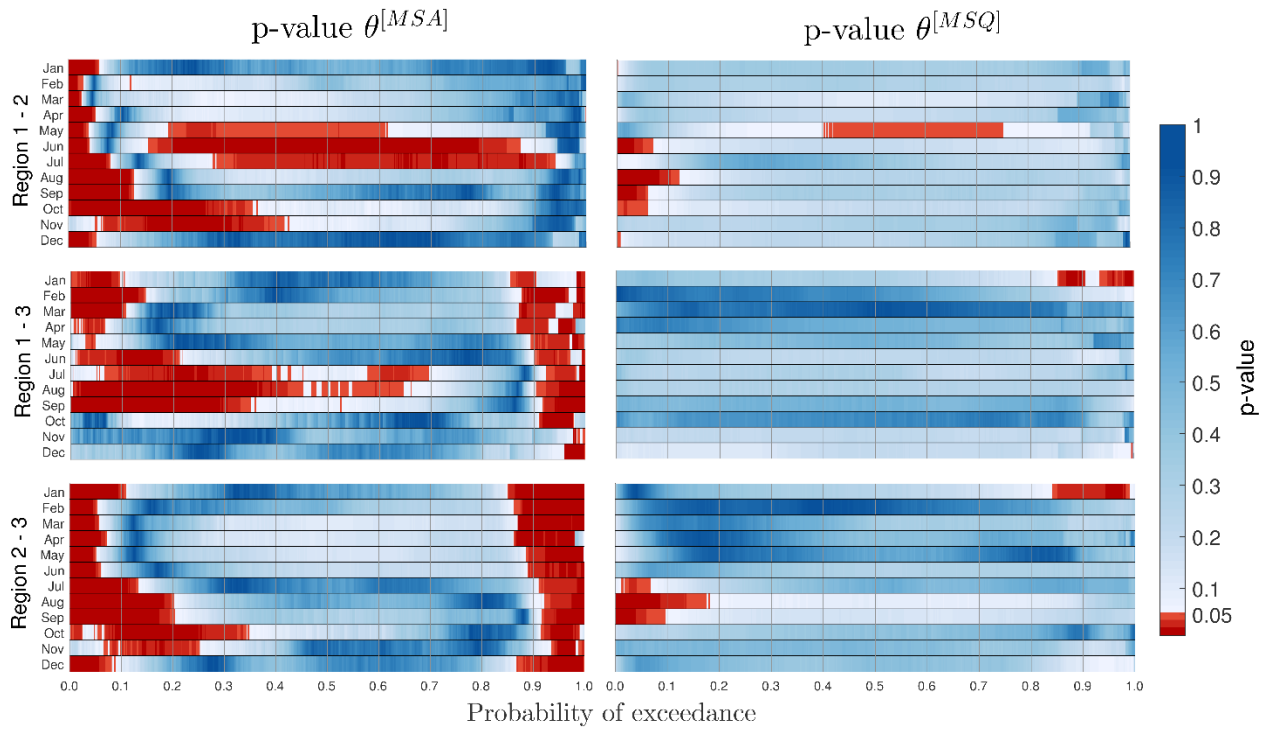Figure 6-11. This figure illustrates the p-value for the null hypothesis $H_0: \theta_{p,Region\ i}^{[MSA]} = \theta_{p,Region\ j}^{[MSA]}$ and $H_0: \theta_{p,Region\ i}^{[MSQ]} = \theta_{p,Region\ j}^{[MSQ]}$ at monthly scale with quantiles ranging from 0.01 to 0.99.
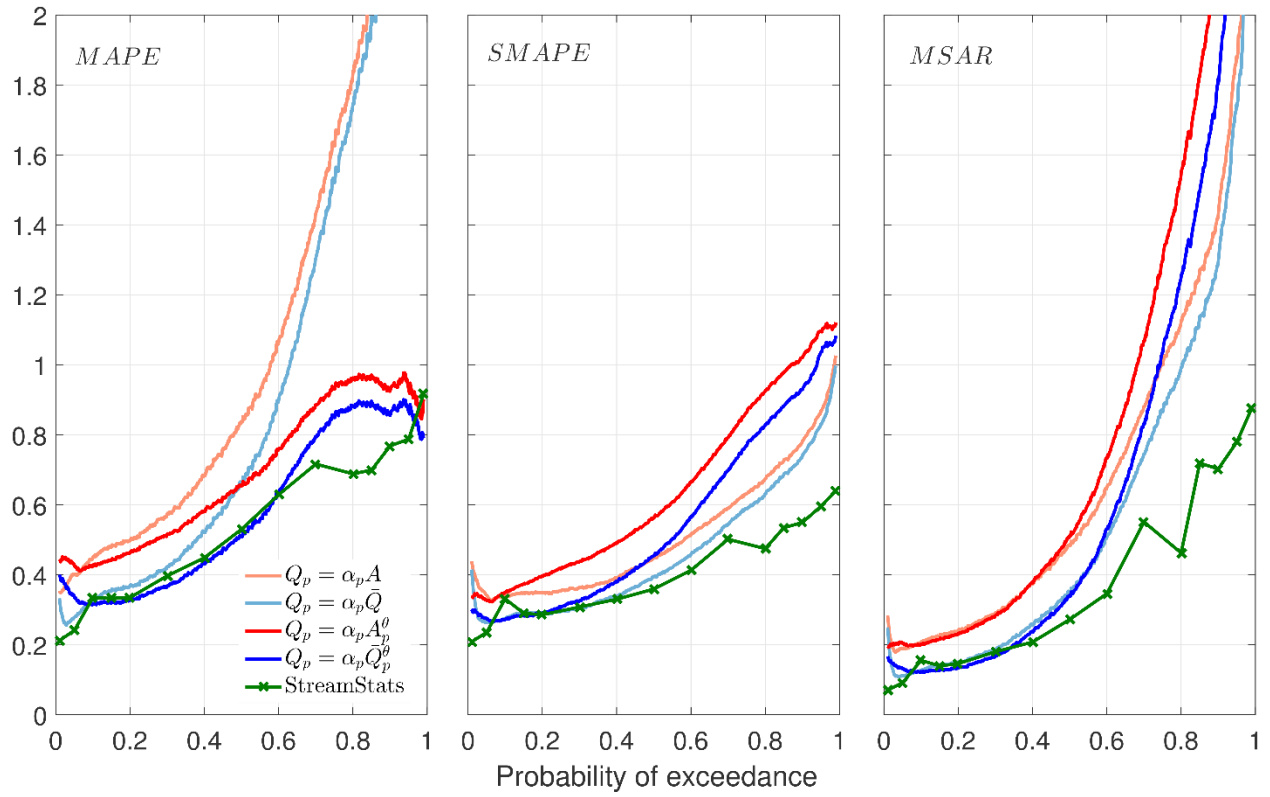
Figure 6-12. Statistics MAPE, SMAPE, and MSAR using the 42 validation gauges at historical annual scale and quantiles ranging from 0.01 to 0.99 for the four models and the StreamStats results.
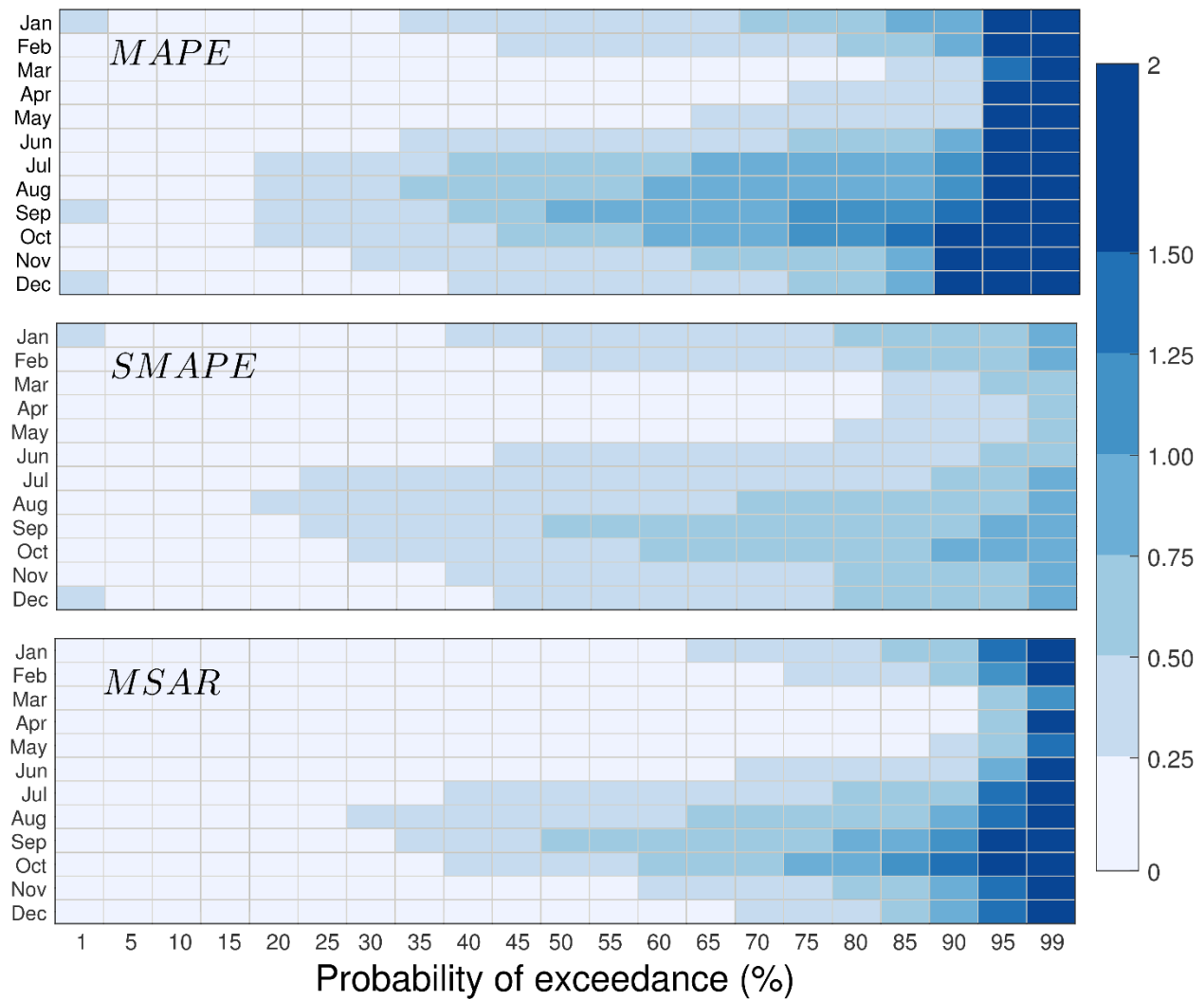
Figure 6-13. Statistics MAPE, SMAPE, and MSAR for the 42 validation gauges at monthly scale and quantiles ranging from 0.01 to 0.99 for the MSQ model.
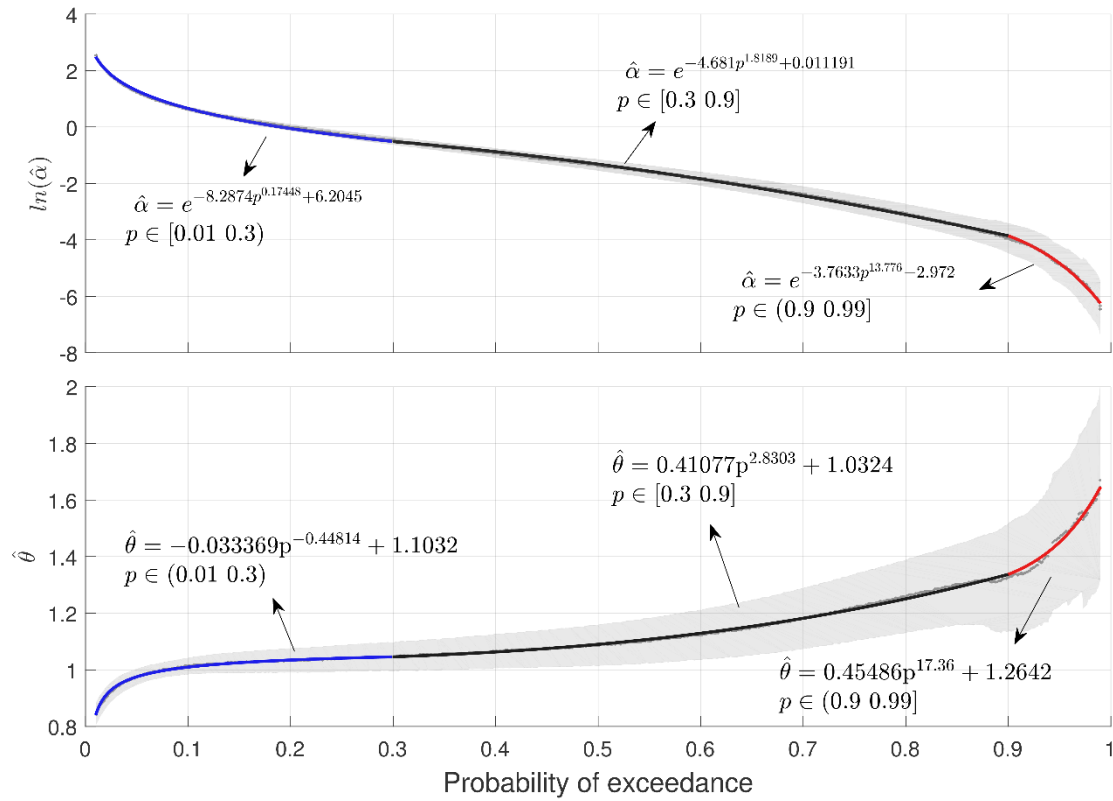
Figure 6-14. Piecewise continuous function for $\hat{\theta}$ and $ln(\hat{\alpha})$ at annual scale for quantiles ranging from 0.01 to 0.99 over the MSQ model. The shaded region represents the 95% confidence intervals from the independent regression analysis performed in each of the 981 streamflow quantiles.
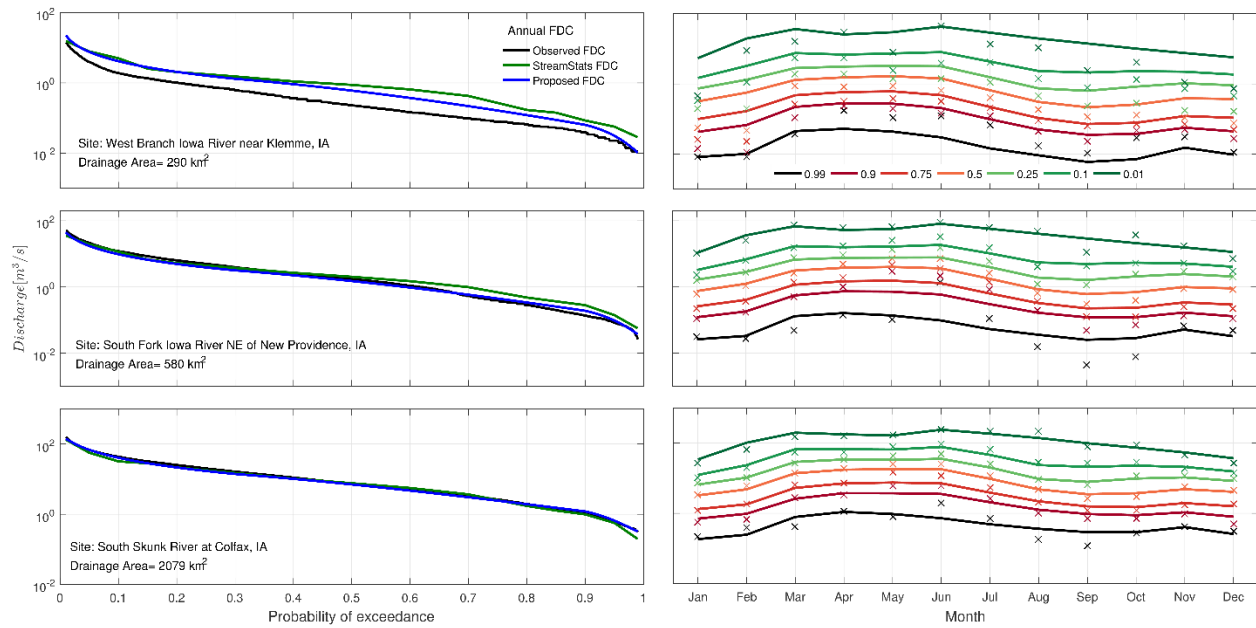
Figure 6-15. Estimation of the FDC for three validations sites based on the fitted piecewise continuous function for MSQ model. The left figure shows the proposed FDC (MSQ model), the StreamStats FDC, and the observed historical FDC. The right figure shows the monthly FDC for the quantiles of 0.99, 0.9, 0.75, 0.5, 0.25, 0.1, and 0.01. The continuous lines are the estimation from the monthly piecewise continuous function using the MSQ model, and the cross points are the data from the observed FDC.
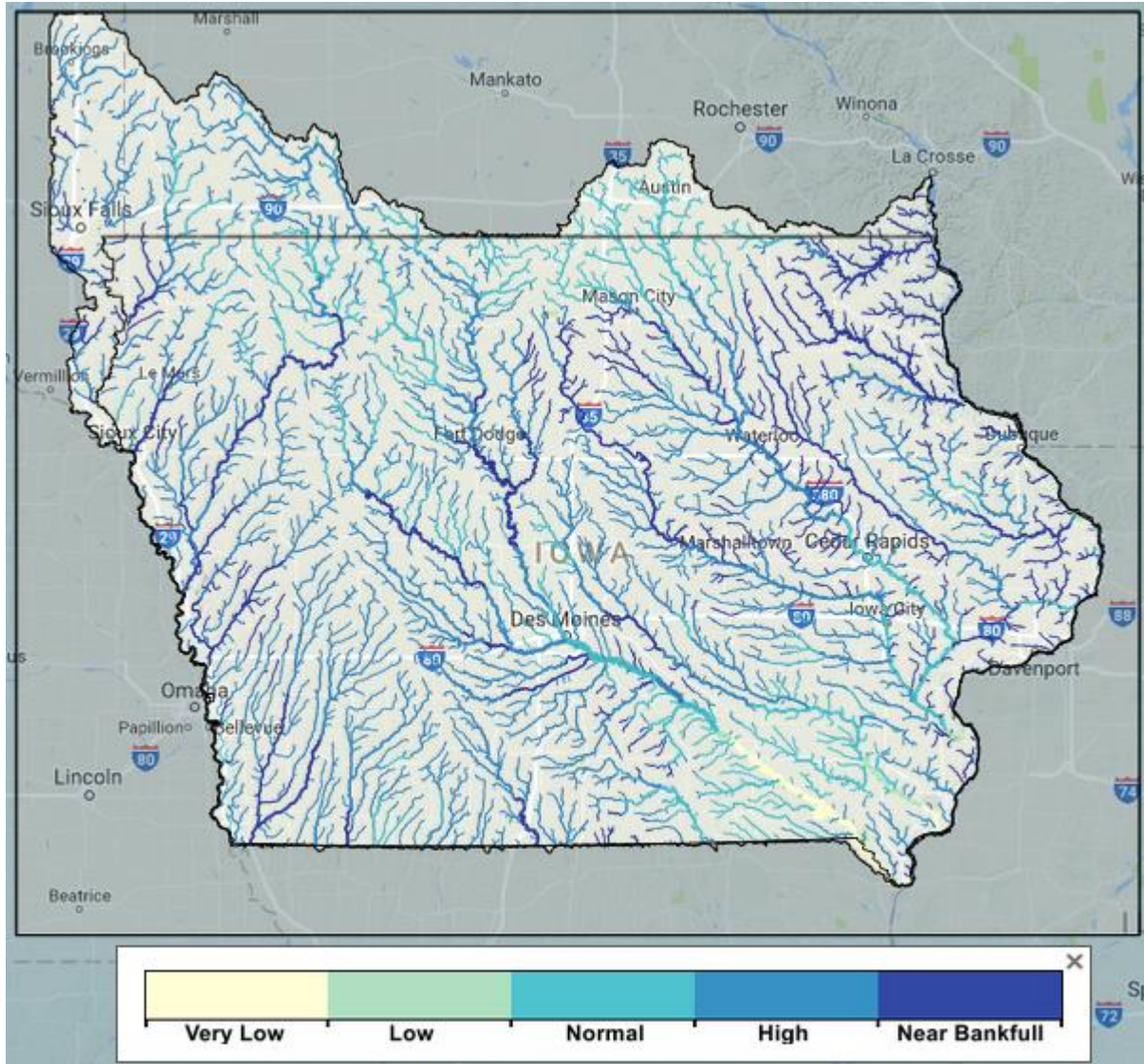
Figure 6-16. An example of translating streamflow magnitudes to streamflow conditions in Iowa on Sept. 20, 2016.

CHAPTER 7: FINAL REMARKS AND FUTURE DIRECTIONS

This dissertation was inspired by multiple works that contributed to the development of a scaling theory of floods. The adoption of a scaling model ($Q = \alpha A^{\theta}$) to represent the variability of peak flows across scales is not only because this structure seems to reflect a fundamental symmetry of nature, but also because it provides a simple and reliable framework supported by empirical and experimental analysis for hypothesis testing of physical mechanisms behind peak flow variabilities. An engaging description of the outlines and future directions of this theory is provided by Gupta et al., (2007). However, it has been more than 10 years since this overview was reported. Therefore, we recognize the need to review and bring together =new advances in the scaling theory of floods. Mainly, these recent advances focus on the interpretation of scaling parameters with respect to rainfall properties and geomorphologic attributes (e.g., Ayalew et al., 2015; Ayalew et al., 2014a; Ayalew et al., 2014b; Gupta et al., 2015; Mandapaka et al., 2009; Mantilla et al., 2011; Mantilla, 2012). However, little attention was devoted to understanding the interplay of sampling errors/epistemic errors with respect to this scaling theory, which is essential if this theory is to be adopted as a feasible alternative for real engineering applications to estimate peak flow quantiles. We believe this dissertation contributes to this greater understanding, starting with the regional analysis of scaling parameter at different spatial scales (Chapter 2); definition of river network descriptors (Chapter 3); inclusion of river network descriptor to improve the peak flow scaling (Chapters 3 and 4); and evaluation of sampling errors and different model structures in the estimation of peak flows (Chapters 4 and 5). Nevertheless, a long but promising path remains if we are to refine this scaling theory of floods to serve as a solid framework to predict peak flows at ungauged sites that have experienced dramatic changes in land use or climate.

The overall hypothesis presented in "The Scaling Theory of Floods" is that scaling in peak flows emerges from the physical mechanisms involved in rainfall-runoff generation and the river network directing flow toward the outlet. The work performed here provides meaningful guidance to develop physics-informed methodologies to estimate peak flow quantiles at ungauged sites, and it shows that the theory can be extended to all flows in the river. Based on the various findings in this dissertation, I assert five future directions for continued progress toward an improved scaling theory of floods.

(1) I demonstrated that the Width Function Descriptors can explain part of the regional peak flow variability (see Chapters 3 and 4). This result opens an avenue to evaluate whether the inclusion of these descriptors improves the regional peak flow equations estimated in the USGS' official flood frequency equations (Eng. et al., 2009). Subsequent studies must evaluate whether the standard regional regression analysis presented by the USGS is improved by the inclusion of WFDs.

(2) The Scaling Theory of Floods is evaluated based on the conventional regression techniques such as Ordinary Least Squares. However, more sophisticated and appropriate techniques such as Generalized Least Squares must be implemented in order to consider the correlation between concurrent peak flow observations. In the same way, the scaling theory must be also compared with spatial techniques that take advantage of the peak flow dependencies between sites, such as topological kriging or canonical kriging.

(3) The findings in Chapters 3 and 4 are tied to inner variabilities of river network structures in Iowa. Hence, a broader analysis with different geomorphologic variabilities (e.g., mountain regions) must be performed to validate and expand the application of Width Function Descriptors as an explanatory variable for regional regression analysis.

(4) The findings in Chapters 3, 4, and 5 focused on the evaluation of natural variabilities (by means of width function descriptors) and stochastic variabilities (by means of sampling error) of regional peak flow structures. However, other natural variabilities, such as antecedent soil moisture, rainfall structure, soil cover, and channel network geometry, can dominate a region's peak flow variability. Therefore, we recognize the need to perform numerical simulations to evaluate the combined interplay of these processes in order to dissect their contributions to regional peak flow variability.

(5) The physical principles behind the scaling theory of floods are not unique to extreme events. This fact is detailed in Chapter 6 with the use of the scaling theory in the estimation of Flow Duration Curves. This result opens new avenues to explore whether Width Function Descriptors can improve the estimation of Flow Duration Curves, just as they do in peak flows.

REFERENCES

Ahn, K. H., & Palmer, R. (2016). "Regional flood frequency analysis using spatial proximity and basin characteristics: Quantile regression vs. parameter regression technique." *Journal of Hydrology*, 540, 515–526. https://doi.org/10.1016/j.jhydrol.2016.06.047

Alexander, G. N. (1963). "Using the probability of storm transposition for estimating the frequency of rare floods." *Journal of Hydrology*, 1(1), 46–57. https://doi.org/10.1016/0022-1694(63)90032-5

Archfield, S. A., Pugliese, A., Castellarin, A., Skoien, J. O., & Kiang, J. E. (2013). "Topological and canonical kriging for design flood prediction in ungauged catchments: an improvement over a traditional regional Solid Earth regression approach?", 1575–1588. https://doi.org/10.5194/hess-17-1575-2013

Ayalew, T. B., & Krajewski, W. (2017). "Effect of river network geometry on flood frequency : A tale of two watersheds in Iowa", 22(8), 1–7. https://doi.org/10.1061/(ASCE)HE.1943-5584.0001544.

Ayalew, T. B., Krajewski, W., & Mantilla, R. (2014a). "Connecting the power-law scaling structure of peak-discharges to spatially variable rainfall and catchment physical properties." *Advances in Water Resources*, 71, 32–43. http://doi.org/10.1016/j.advwatres.2014.05.009

Ayalew, T. B., Krajewski, W., Mantilla, R., & Small, S. J. (2014b). "Exploring the effects of hillslope-channel link dynamics and excess rainfall properties on the scaling structure of peak-discharge." *Advances in Water Resources*, 64, 9–20. http://doi.org/10.1016/j.advwatres.2013.11.010

212

Ayalew, T. B., Krajewski, W., & Mantilla, R. (2015). "Analyzing the effects of excess rainfall properties on the scaling structure of peak discharges: Insights from a mesoscale river basin." *Water Resources Research*, 51, 3900–3921. http://doi.org/10.1002/2014WR016258

Beard, L. R. (1943). "Statistical analysis in hydrology." *Trans. Amer. Soc. Civ. Eng.*, 108, 1110–1160.

Black, P. E. (1972). "Hydrograph responses to geomorphic and precipitation variables", 17, 309–329.

Blom, G. (1958). "Statistical Estimates and Transformed Beta-Variables." *John Wiley and Sons*, 146 pp.

Bras, R. L., & Rodriguez-Iturbe, I. (1989). "A review of the search for a quantitative link between hydrologic response and fluvial geomorphology." *New Directions for Surface Water Modeling*, (181), 149–163.

Brown, M. E., Escobar, V., Moran, S., Entekhabi, D., O'Neill, P. E., Njoku, E. G., Entin, J. K. (2013). "NASA's Soil Moisture Active Passive (SMAP) Mission and Opportunities for Applications Users." *Bulletin of the American Meteorological Society*. https://doi.org/10.1175/bams-d-11-00049

Burns, D. A., Smith, M. J., & Freehafer, D. A. (2015). "Development of flood regressions and climate change scenarios to explore estimates of future peak flows." *U.S. Geological Survey Open-File Report*, (2015–1235), 11.

Corporation, H. S. (2016). "NHD Plus Version 2." Retrieved from http://www.horizon-systems.com/NHDPlus/NHDPlusV2_data.php

Cunha, L. K., Mandapaka, P. V., Krajewski, W. F., Mantilla, R., & Bradley, A. A. (2012). "Impact of radar-rainfall error structure on estimated flood magnitude across scales: An investigation based on a parsimonious distributed hydrological model." *Water Resources Research*, 48(10), 1–22. https://doi.org/10.1029/2012WR012138

Dawdy, D. R., Griffis, V. W., & Gupta, V. K. (2012). "Regional Flood-Frequency Analysis: How We Got Here and Where We Are Going." *Journal of Hydrologic Engineering*, 17(9), 953–959. http://doi.org/10.1061/(ASCE)HE.1943-5584.0000584

Doulatyari, B., Betterle, A., Basso, S., Biswal, B., Schirmer, M., & Botter, G. (2015). "Predicting streamflow distributions and flow duration curves from landscape and climate." *Advances in Water Resources*, 83, 285–298. https://doi.org/10.1016/j.advwatres.2015.06.013

Eash, D. A., Barnes, K. K., & Veilleux, A. G. (2013). "Methods for estimating annual exceedance-probability discharges for streams in Iowa , based on data through water year 2010" *USGS scientific investigations report* 2013 – 5086.

England, J., Cohn, T., Faber, B., Stedigen, J., Wilbert, T., Veilleux, A., Mason, R. (2015). "Bulletin 17C: guidelines for determining flood flow frequency." *USGS, USACE, ACWI, US Department of the Interior*, 156. https://doi.org/http://dx.doi.org/10.3133/tm4–BXX/

Eng, K., Chen, Y.-Y., & Kiang, J. E. (2009). "User's Guide to the Weighted-Multiple-Linear Regression Program (WREG version 1.0).." Retrieved from http://pubs.usgs.gov/tm/tm4a8/

Farmer, W. H., Over, T. M., & Vogel, R. M. (2015). "Multiple regression and inverse moments improve the characterization of the spatial scaling behavior of daily streamflows in the

Southeast United States." *Water Resources Research*, 51(3), 1775–1796.

https://doi.org/10.1002/2014WR015924

Farmer, W.H., Archfield, S.A., Over, T.M., Hay, L.E., LaFontaine, J.H., and Kiang, J. (2014). A

"Comparison of Methods to Predict Historical Daily Streamflow Time Series in the

Southeastern United States." Manual. https://doi.org/10.3133/sir20145231

Fennessey, N., & Vogel, R. M. (1990). "Regional flow -duration curves for ungauged sites in

Massachusetts." *Journal of Water Resources Planning and Management* (ASCE), 116(4),

530–549.

Fenton, T. E., Duncan, E. R., Shrader, W. D., & Dumenil, L. C. (1971). "Productivity levels of

some Iowa soils." *Iowa State Univ*. Ext. Special Report No. 66 Iowa State Univ., Ames,

IA.

Flynn, K. M., Kirby, W. H., Hummel, P. R., & Geological, S. (2006). "User's manual for

Program PeakFQ, annual flood-frequency analysis using Bulletin 17B guidelines."

Retrieved from http://purl.access.gpo.gov/GPO/LPS97012

Flynn, R. H. (2003). "Development of Regression Equations to Estimate Flow Durations and

Low-Flow- Frequency Statistics in New Hampshire Streams", 77.

Fontaine, T. A., & Potter, K. W. (1989). "Estimating Probabilities of Extreme Rainfalls."

Journal of Hydraulic Engineering, 115(11), 1562–1575.

https://doi.org/10.1061/(ASCE)0733-9429(1989)115:11(1562)

Foufoula-Georgiou, E. (1989). "A probabilistic storm transposition approach for estimating

exceedance probabilities of extreme precipitation depths." *Water Resources Research*,

25(5), 799–815. https://doi.org/10.1029/WR025i005p00799

Franchini, M., Helmlinger, K. R., Foufoula-Georgiou, E., & Todini, E. (1996). "Stochastic storm transposition coupled with rainfall-runoff modeling for estimation of exceedance probabilities of design floods." *Journal of Hydrology*, 175(1–4), 511–532. https://doi.org/10.1016/S0022-1694(96)80022-9

Fuller, W. E. (1914). "Flood flows." *Trans. ASCE*, 77, 564–617.

Furey, P. R., & Gupta, V. K. (2005). "Effects of excess rainfall on the temporal variability of observed peak-discharge power laws." *Advances in Water Resources*, 28(11), 1240–1253. https://doi.org/10.1016/j.advwatres.2005.03.014

Furey, P. R., & Gupta, V. K. (2007). "Diagnosing peak-discharge power laws observed in rainfall-runoff events in Goodwin Creek experimental watershed." *Advances in Water Resources*, 30(11), 2387–2399. http://doi.org/10.1016/j.advwatres.2007.05.014

Furey, P. R., Troutman, B. M., Gupta, V. K., Krajewski, W., & Asce, M. (2016). "Connecting event-based scaling of flood peaks to regional flood frequency relationships", 21(10), 1–11. https://doi.org/10.1061/(ASCE)HE.1943-5584.0001411.

Gado, T. A., & Nguyen, V.-T.-V. (2016). "Regional Estimation of Floods for Ungauged Sites Using Partial Duration Series and Scaling Approach." *Journal of Hydrologic Engineering*, 21(12), 04016044. https://doi.org/10.1061/(asce)he.1943-5584.0001439

Greenwood, J. A., Landwehr, J. M., Matalas, N. C., & Wallis, J. R. (1979). "Probability weighted moments: Definition and relation to parameters of several distributions expressible in inverse form." *Water Resources Research*, 15(5), 1049–1054. https://doi.org/10.1029/WR015i005p01049

Griffis, V., & Stedinger, J. (2007). "Log-Pearson Type 3 Distribution and Its Application in Flood Frequency Analysis. I: Distribution Characteristics." *Journal of Hydrologic Engineering*, 12(5), 482–491. https://doi.org/10.1061/(ASCE)1084-0699(2007)12:5(482)

Gupta, V. K., & Dawdy, D. R. (1995). "Physical interpretations of regional variations in the scaling exponents of flood quantiles." *Hydrological Processes*, 9(September 1994), 347–361. https://doi.org/10.1002/hyp.3360090309

Gupta, V. K., & Mesa, O. J. (1988). "Runoff generation and hydrologic response via channel network geomorphology - Recent progress and open problems." *Journal of Hydrology*, 102(1–4), 3–28. https://doi.org/10.1016/0022-1694(88)90089-3

Gupta, V. K., & Mesa, O. J. (2014). "Horton laws for hydraulic-geometric variables and their scaling exponents in self-similar Tokunaga river networks." *Nonlinear Processes in Geophysics*, 21(5), 1007–1025. https://doi.org/10.5194/npg-21-1007-2014

Gupta, V. K., & Waymire, E. (1990). "Multiscaling properties of spatial rainfall and river flow distributions." *Journal of Geophysical Research*, 95(D3), 1999. https://doi.org/10.1029/JD095iD03p01999

Gupta, V. K., & Waymire, E. (1998). "Spatial variability and scale invariance in hydrologic regionalization" *Scale Dependence and Scale Invariance in Hydrology*. Cambridge University Press.

Gupta, V. K., Castro, S. L., & Over, T. M. (1996). "On scaling exponents of spatial peak flows from rainfall and river network geometry." *Journal of Hydrology*, 187(1–2), 81–104. http://doi.org/10.1016/S0022-1694(96)03088-0

Gupta, V. K., Mesa, O. J., & Dawdy, D. R. (1994). "Multiscaling theory of flood peaks: Regional quantile analysis." *Water Resources Research*, 30(12), 3405–3421. https://doi.org/10.1029/94WR01791

Gupta, V. K., Troutman, B. M., & Dawdy, D. R. (2007). "Towards a Nonlinear Geophysical Theory of Floods in River Networks : An Overview of 20 Years of Progress", (1997).

Gupta, V. K., Waymire, E., & Wang, C. T. (1980). "A representation of an instantaneous unit hydrograph from geomorphology." *Water Resources Research*, 16(5), 855–862. https://doi.org/10.1029/WR016i005p00855

Hack, J. T. (1957). "Studies of longitudinal stream profiles in Virginia and Maryland." *USGS Professional Paper* 249, 97.

Haddad, K., & Rahman, A. (2012). "Regional flood frequency analysis in eastern Australia: Bayesian GLS regression-based methods within fixed region and ROI framework - Quantile Regression vs. Parameter Regression Technique." *Journal of Hydrology*, 430–431, 142–161. https://doi.org/10.1016/j.jhydrol.2012.02.012

Haddad, K., Rahman, A., & Kuczera, G. (2011). "Comparison of ordinary and generalised least squares regression models in regional flood frequency analysis : A case study for New South Wales." *Australasian Journal of Water Resources*, 16(1), 59–70.

Haddad, K., Rahman, A., & Stedinger, J. R. (2012). "Regional flood frequency analysis using Bayesian generalized least squares: A comparison between quantile and parameter regression techniques." *Hydrological Processes*, 26(7), 1008–1021. http://doi.org/10.1002/hyp.8189

Hailegeorgis, T. T., & Alfredsen, K. (2016). "Studies Regional flood frequency analysis and prediction in ungauged basins including estimation of major uncertainties for mid-

218

Norway." *Journal of Hydrology: Regional Studies*, 9, 104–126.

https://doi.org/10.1016/j.ejrh.2016.11.004

Haktanir, T., & Horlacher, H. B. (1993). "Evaluation of various distributions for flood frequency

analysis." *Hydrological Sciences Journal*, 38(1), 15–32.

https://doi.org/10.1080/02626669309492637

Halbert, K., Nguyen, C. C., Payrastre, O., & Gaume, E. (2016). "Reducing uncertainty in flood

frequency analyses: A comparison of local and regional approaches involving

information on extreme historical floods." *Journal of Hydrology*, 541, 90–98.

https://doi.org/10.1016/j.jhydrol.2016.01.017

Heine, R.A.; Lant, C.L.; Sengupta, R. R. (2004). "Development and comparison of approaches

for automated mapping of stream channel networks." *Annals of the American

Geographers*, 94(August 2003), 477–490.

Hickox, G. H., Wessenauer, G. O. (1933). "Application of duration curves to hydroelectric

studies." *Trans. ASCE*, 98(2), 1276–1308.

Horton, R. E. (1932). "Drainage basin characteristics." *Eos, Transactions American Geophysical

Union*, 13(1), 350–361. https://doi.org/10.1029/TR013i001p00350

Hosking, J. R. M. (1990). "L-Moments : Analysis and Estimation of Distributions Using Linear

Combinations of Order Statistics." *American Statistician*, 52(1), 105–124. Retrieved from

http://www.jstor.org/stable/2345653

Huff, F. A., & Angel, J. R. (1992). "Rainfall frequency atlas of the Midwest." *MCC Research

Report* 92-03, 71, 141. https://doi.org/ISSN 0360-9804

Ignacio Rodríguez-Iturbe, A. R. (2001). "Fractal river basins: chance and Self-Organization."
Cambridge University Press. Retrieved from
https://books.google.com/books?id=_xjhtl7zeB8C

J. R. M. Hosking, & Wallis, J. R. (1997). "Regional Frequency Analysis: An Approach Based on
L-Moments." (C. U. Press, Ed.).

Jothityangkoon, C., & Sivapalan, M. (2001). "Temporal scales of rainfall - runoff processes and
spatial scaling of flood peaks : space - time connection through catchment water
balance." *Advances in Water Resources*, 24(9–10), 1015–1036.
http://doi.org/10.1016/S0309-1708(01)00044-6

Jothityangkoon, C., & Sivapalan, M. (2001). "Temporal scales of rainfall - runoff processes and
spatial scaling of flood peaks : space - time connection through catchment water
balance." *Advances in Water Resources*, 24(9–10), 1015–1036.
https://doi.org/10.1016/S0309-1708(01)00044-6

Kirshen, D. M., & Bras, R. L. (1983). "The linear channel and its effect on the geomorphologic
IUH." *Journal of Hydrology*, 65(1–3), 175–208. https://doi.org/10.1016/0022-
1694(83)90216-0

Kjeldsen, T. R., & Jones, D. A. (2009). "An exploratory analysis of error components in
hydrological regression modeling." *Water Resources Research*, 45(2), 1–13.
https://doi.org/10.1029/2007WR006283

Krajewski, W. F., Ceynar, D., Demir, I., Goska, R., Kruger, A., Langel, C., Young, N. C. (2017).
"Real-time flood forecasting and information system for the state of Iowa." *Bulletin of
the American Meteorological Society*, 98(3), 539–554. https://doi.org/10.1175/BAMS-D-
15-00243.1

Kroll, C. (2014). "The prediction of hydrologic statistics in nested watersheds across the United States." *World Environmental and Water Resources Congress*, 2326–2335. Retrieved from http://earthjustice.org/features/campaigns/fracking-across-the-united-states

Kroll, C. N. (1998). "Regional hydrologic analysis : Ordinary and generalized least squares revisited", 34(1), 121–128.

Lavers, D. A., & Villarini, G. (2013). "Atmospheric rivers and flooding over the central United States." *Journal of Climate*, 26(20), 7829–7836. http://doi.org/10.1175/JCLI-D-13-00212.1

Lee, M. T., & Delleur, J. W. (1976). "A variable source area model of the rainfall-runoff process based on the watershed stream network." *Water Resources Research*, 12(5), 1029–1036. https://doi.org/10.1029/WR012i005p01029

Li, M., Shao, Q., Zhang, L., & Chiew, F. H. S. (2010). "A new regionalization approach and its application to predict flow duration curve in ungauged basins." *Journal of Hydrology*, 389(1–2), 137–145. https://doi.org/10.1016/j.jhydrol.2010.05.039

Lim, Y. H., & Voeller, D. L. (2009). "Regional flood estimations in Red River using L-moment-based index-flood and Bulletin 17B procedures." *Journal of Hydrologic Engineering*, 14(9), 1002–1016. https://doi.org/10.1061/(ASCE)HE.1943-5584.0000102

Lin, Y., & Mitchell, K. E. (2005). "The Ncep Stage Ii / Iv Hourly Precipitation Analyses : Development and Applications." *19th Conf. on Hydrology, American Meteorological Society*, 2–5. https://doi.org/10.1111/j.1651-2227.2007.00250.x

Linhart, S. M., Nania, J. F., Sander Jr., C. L., & Archfield, S. A. (2012). "Computing daily mean streamflow at ungaged locations in Iowa by using the Flow Anywhere and flow duration

curve transfer statistical methods." *U.S. Geological Survey Scientific Investigations Report*, (2012–5232), 50.

Longobardi, A., & Villani, P. (2013). "A statistical, parsimonious, empirical framework for regional flow duration curve shape prediction in high permeability Mediterranean region." *Journal of Hydrology*, 507, 174–185. https://doi.org/10.1016/j.jhydrol.2013.10.019

Maidment, D. R. (2016). "Conceptual Framework for the National Flood Interoperability Experiment." *Journal of the American Water Resources Association*, 78758. https://doi.org/10.1111/1752-1688.12474

Malamud, B. D., & Turcotte, D. L. (2006). "The applicability of power-law frequency statistics to floods." *Journal of Hydrology*, 322(1–4), 168–180. https://doi.org/10.1016/j.jhydrol.2005.02.032

Malekinezhad, H., Nachtnebel, H. P., & Klik, A. (2011). "Comparing the index-flood and multiple-regression methods using L-moments." *Physics and Chemistry of the Earth*, 36(1–4), 54–60. https://doi.org/10.1016/j.pce.2010.07.013

Mandapaka, P. V., Krajewski, W., Mantilla, R., & Gupta, V. K. (2009). "Dissecting the effect of rainfall variability on the statistical structure of peak flows." *Advances in Water Resources*, 32(10), 1508–1525. http://doi.org/10.1016/j.advwatres.2009.07.005

Mantilla, R., & Gupta, V. K. (2005). "A GIS Numerical Framework to Study the Process Basis of Scaling Statistics in River Networks." *IEEE Geoscience and Remote Sensing Letters*, 2(4), 404–408. https://doi.org/10.1109/LGRS.2005.853571

Mantilla, R., Cunha, L. K., Krajewski, W. F., Small, S. J., Jay, L. O., Fonley, M., & Curtu, R. (2012). "Simulation of a Distributed Flood Control System using a Parallel

Asynchronous Solver for Systems of ODEs." *Applied Simulation and Modelling: Artificial Intelligence and Soft Computing*, (Asm), 158–164. https://doi.org/10.2316/P.2012.776-042

Mantilla, R., Gupta, V. K., & J. Mesa, O. (2006). "Role of coupled flow dynamics and real network structures on Hortonian scaling of peak flows." *Journal of Hydrology*, 322, 155–167. http://doi.org/10.1016/j.jhydrol.2005.03.022

Mantilla, R., Gupta, V. K., & Troutman, B. M. (2011). "Scaling of peak flows with constant flow velocity in random self-similar networks." *Nonlinear Processes in Geophysics*, 18(4), 489–502. https://doi.org/10.5194/npg-18-489-2011

Martin P. Wanielista, Robert Kersten, R. E. (1996). "Hydrology: Water quantity and quality control" (2nd Edition).

Mastin, M. C., Konrad, C. P., Veilleux, A. G., & Tecca, A. E. (2016). "Magnitude , frequency , and trends of floods at gaged and ungaged sites in Washington , based on data through water year 2014." *U.S. Geological Survey Scientific Investigations Report* 2016 – 5118, (October), 70.

Medhi, H., & Tripathi, S. (2015). "On identifying relationships between the flood scaling exponent and basin attributes." *Chaos*, 25(7). http://doi.org/10.1063/1.4916378

Melton, M. A. (1957). "An analysis of the relations among elements of climate, surface properties, and geomorphology." *Department of Geology, Columbia University*. Retrieved from https://books.google.com/books?id=ZZl6QQAACAAJ

Menabde, M., & Sivapalan, M. (2001). "Linking space-time variability of river runoff and rainfall fields: A dynamic approach." *Advances in Water Resources*, 24(9–10), 1001–1014. http://doi.org/10.1016/S0309-1708(01)00038-0

Mesa O.J., Mifflin E.R. (1986) "On the Relative Role of Hillslope and Network Geometry in
Hydrologic Response." In: Gupta V.K., Rodríguez-Iturbe I., Wood E.F. (eds) *Scale
Problems in Hydrology*. Water Science and Technology Library, vol 6. Springer,
Dordrecht

Micevski, T., & Kuczera, G. (2009). "Combining site and regional flood information using a
Bayesian Monte Carlo approach", 45(April), 1–11.
https://doi.org/10.1029/2008WR007173

Miller, V. (1953). "A quantitative geomorphic study of drainage basin characteristics in the
clinch mountain area. Virginia and Tennessee." *Technical Report. Office of Naval
Research*. Department of Geology. Columbia University. Geography Branch, New York.

Mitchell, W. D. (1957). "Flow duration of Illinois streams." *Department of Public Works and
Buildings Division and Waterways*.

Mohssen, M. (2009). "Partial duration series in the annual domain", (July), 2694–2700.

Moran, P. A. . (1950). "Notes on continuous stochastic phenomena." *Biometrika*, 17:37.

Morisawa, M. (1958). "Measurement of drainage-basin outline source." *The Journal of Geology*.
The University of Chicago Press, 66(5), 587–591.

Morrison, J. E., & Smith, J. a. (2001). "Scaling properties of flood peaks. Extremes, 4, 5–22.
http://doi.org/10.1023/A:1012268216138

Moussa, R. (1997). "Geomorphological transfer function calculated from digital elevation
models for distributed hydrological modelling." *Hydrological Processes*, 11(5), 429–449.
https://doi.org/10.1002/(SICI)1099-1085(199704)11:5<429::AID-HYP471>3.0.CO;2-J

Moussa, R. (2003). "On morphometric properties of basins, scale effects and hydrological
response." *Hydrological Processes*, 17(1), 33–58. https://doi.org/10.1002/hyp.1114

Moussa, R. (2008). "What controls the width function shape, and can it be used for channel network comparison and regionalization?" *Water Resources Research*, 44(8), 1–19. https://doi.org/10.1029/2007WR006118

Muelle, J. E. (1968). "An introduction to the hydraulic and topographic sinuosity indexes." *Annals of the Association of American Geographers*., 58(2), 371–385.

Naden, P. S. (1992). "Spatial variability in flood estimation for large catchments: The exploitation of channel network structure." *Hydrological Sciences Journal*, 37(1), 53–71. https://doi.org/10.1080/02626669209492561

Nguyen, C. C., Gaume, E., & Payrastre, O. (2014). "Regional flood frequency analyses involving extraordinary flood events at ungauged sites: Further developments and validations." *Journal of Hydrology*, 508, 385–396. https://doi.org/10.1016/j.jhydrol.2013.09.058

Odry, J., & Arnaud, P. (2017). "Comparison of Flood Frequency Analysis Methods for Ungauged Catchments in France." *Geosciences*, 7(3), 88. https://doi.org/10.3390/geosciences7030088

Ogden, F. L., & Dawdy, D. R. (2003). "Peak Discharge Scaling in Small Hortonian Watershed." *Journal of Hydrologic Engineering*, 8(2), 64–73. https://doi.org/10.1061/(ASCE)1084-0699(2003)8:2(64)

Orlandini, S., Tarolli, P., Moretti, G., & Dalla Fontana, G. (2011). "On the prediction of channel heads in a complex alpine terrain using gridded elevation data." *Water Resources Research*, 47(2), 1–12. https://doi.org/10.1029/2010WR009648

Paretti, N. V., Kennedy, J. R., & Cohn, T. A. (2014). "Evaluation of the Expected Moments Algorithm and a Multiple Low-Outlier Test for Flood Frequency Analysis at Streamgaging Stations in Arizona." *Scientific Investigation Report* 2014-5026. USGS.

Parrett, C., Carlson, D. D., & Craig S. Grodon, J. (1984). "Floods of May 1978 in Southeastern Montana and Northeastern Wyoming." *U.S Geological Survey Professional Paper*.

Parrett, C., Veilleux, A., Stedinger, J.R., Barth, N.A., Knifong, D.L., and Ferris, J. C. (2010). "Regional skew for California, and flood frequency for selected sites in the Sacramento-San Joaquin river basin , based on data through water year 2006." *Scientific Investigations Report* 2010 - 5260.

Pavlopoulos, H., & Krajewski, W. (2014). "A diagnostic study of spectral multiscaling on spatio-temporal accumulations of rainfall fields based on radar measurements over Iowa." *Advances in Water Resources*, 74, 258–278. https://doi.org/10.1016/j.advwatres.2014.10.001

Perez, G., Mantilla, R., & Krajewski, W. (2018a). "Spatial Patterns of Peak Flow Quantiles Based on Power-Law Scaling in the Mississippi River Basin." *Advances in Nonlinear Geosciences*, 497–518. https://doi.org/10.1007/978-3-319-58895-7_23

Perez, G., Mantilla, R., & Krajewski, W. (2018b). "The Influence of Spatial Variability of Width Functions on Regional Peak Flow Regressions." *Water Resources Research*, 54(10). https://doi.org/10.1029/2018WR023509

Perez, G., Mantilla, R., & Krajewski, W. (2018c). "Estimation of Historical-Annual and Historical-Monthly Scale-Invariant Flow Duration Curves with Implementation for Iowa." *Journal of Hydrologic Engineering*. https://doi.org/10.1061/(asce)he.1943-5584.0001707

Potthoff, R. F. (1966). "Statistical aspects of the problem of biases in psychological tests." *Institute of Statistics Mimeo Series*. (D. of S. Chapel Hill: University of North Carolina, Ed.),.

Poveda, G., Vélez, J. I., Mesa, O. J., Cuartas, A., Barco, J., Mantilla, R. I., Quevedo, D. I. (2007). "Linking Long-Term Water Balances and Statistical Scaling to Estimate River Flows along the Drainage Network of Colombia." *Journal of Hydrologic Engineering*, 12(1), 4–13. https://doi.org/10.1061/(ASCE)1084-0699(2007)12:1(4)

Puente, C. E., & Sivakumar, B. (2003). "A deterministic width function model." *Nonlinear Processes in Geophysics*, 10(6), 525–529. https://doi.org/10.5194/npg-10-525-2003

Quintero, F., & Krajewski, W. (2018). "Mapping outlets of Iowa Flood Center and National Water Center river networks for hydrologic model comparison." *Journal of the American Water Resources Association*, 54(1), 28–39. https://doi.org/10.1111/1752-1688.12554

Quintero, F., Krajewski, W., Mantilla, R., Small, S., & Seo, B.-C. (2016). "A Spatial–dynamical framework for evaluation of satellite rainfall products for flood Prediction." *Journal of Hydrometeorology*, 17(8), 2137–2154. https://doi.org/10.1175/JHM-D-15-0195.1

Quintero, F., Mantilla, R., Anderson, C., Claman, D., & Krajewski, W. (2018). "Assessment of Changes in Flood Frequency Due to the Effects of Climate Change: Implications for Engineering Design." *Hydrology*, 5(1), 19. https://doi.org/10.3390/hydrology5010019

Rai, P. K., Chaubey, P. K., Mohan, K., & Singh, P. (2017). "Geoinformatics for assessing the inferences of quantitative drainage morphometry of the Narmada Basin in India." *Applied Geomatics*, 9(3), 167–189. https://doi.org/10.1007/s12518-017-0191-1

Ries, K. G., Steeves, P. A., Guthrie, J. D., Rea, A. H., & Stewart, D. W. (2009). "Stream-Network navigation in the U.S. geological survey streamStats web application."

Proceedings of the International Conference on Advanced Geographic Information Systems and Web Services, GEOWS 2009, 80–84. https://doi.org/10.1109/GEOWS.2009.35

Rigon, R., Bancheri, M., Formetta, G., & deLavenne, A. (2016). "The geomorphological unit hydrograph from a historical-critical perspective." *Earth Surface Processes and Landforms*, 41(1), 27–37. https://doi.org/10.1002/esp.3855

Rinaldo, A., Marani, A., & Rigon, R. (1991). "Geomorphological dispersion." *Water Resources Research*, 27(4), 513–525. https://doi.org/10.1029/90WR02501

Rinaldo, A., Vogel, G. K., Rigon, R., & Rodriguez-Iturbe, I. (1995). "Can one gauge the shape of a basin?" *Water Resources Research*, 31(4), 1119–1127. https://doi.org/10.1029/94WR03290

Robinson, J. S., & Sivapalan, M. (1997). "Temporal scales and hydrological regimes: Implications for flood frequency scaling." *Water Resources Research*, 33(12), 2981. http://doi.org/10.1029/97WR01964

Rodríguez-Iturbe, I., & Valdes, J. B. (1979). "The geomorpholic structure of hydrologic response." *Water Resources Research*, 15(6), 1409–1420. https://doi.org/10.1029/WR015i006p01409

Saf, B. (2009). "Regional Flood Frequency Analysis Using L-Moments for the West Mediterranean Region of Turkey." *Water Resources Management*, 23(3), 531–551. https://doi.org/10.1007/s11269-008-9287-z

Schilling, K. E., & Helmers, M. (2008). "Effects of subsurface drainage tiles on streamflow in Iowa agricultural watersheds: Exploratory hydrograph analysis." *Hydrological Processes*, 22(23), 4497–4506. https://doi.org/10.1002/hyp.7052

Schroeder, M. R. (2012). "Fractals, chaos, power laws: Minutes from an infinite paradise."
Courier Corporation.

Schumm, S. A. (1956). "Evolution of drainage systems and slopes in badlands at Perth Amboy,
New Jersey." *Bulletin of the Geological Society of America*, 67(5), 597–646.
https://doi.org/10.1130/0016-7606(1956)67[597:EODSAS]2.0.CO;2

Seaber, P. R., Kapinos, F. P., & Knapp, G. L. (1987). "Hydrologic Unit Maps: U.S. Geological
Survey." *Water-Supply Paper* 2294, 63.

Seo, B.-C., Quintero, F., Krajewski, W. F. (2018). "High-Resolution QPF Uncertainty and Its
Implications for Flood Prediction: A Case Study for the Eastern Iowa Flood of 2016."
Journal of Hydrometeorology, 19(8), 1289–1304. https://doi.org/10.1175/JHM-D-18-
0046.1

Sherman, L. R. K. (1932). "The relation of hydrographs of runoff to size and character of
drainage basins." *Eos, Transactions American Geophysical Union*, 13(1), 332–339.
https://doi.org/10.1029/TR013i001p00332

Shreve, R. L. (1969). "Stream lengths and basin areas in topologically random channel
networks." *The Journal of Geology*, 77(4), 397–414. https://doi.org/10.1086/628366

Singh, K. P. (1971). "Model Flow Duration and Streamflow Variability." *Water Resources
Research*, 7(4), 1031–1036. https://doi.org/10.1029/WR007i004p01031

Sivapalan, M., Takeuchi, K., Franks, S. W., Gupta, V. K., Karambiri, H., Lakshmi, V., Connell,
P. E. O. (2003). "IAHS Decade on Predictions in Ungauged Basins (PUB), 2003 –
2012 : Shaping an exciting future for the hydrological sciences", 48(December 2003),
2003–2012.

Sloan, B. P. (2013). "Hydrologic impacts of tile drainage in Iowa." Retrieved from

http://ir.uiowa.edu/etd/5060

Small, S. J., Jay, L. O., Mantilla, R., Curtu, R., Cunha, L. K., Fonley, M., & Krajewski, W. F.

(2013). "An asynchronous solver for systems of ODEs linked by a directed tree

structure." *Advances in Water Resources*, 53, 23–32.

https://doi.org/10.1016/j.advwatres.2012.10.011

Smart, J. S., & Surkan, A. J. (1967). "The relation between mainstream length and area in

drainage basins." *Water Resources Research*, 3(4), 963–974.

https://doi.org/10.1029/WR003i004p00963

Smith, A., Sampson, C., & Bates, P. (2015). "Regional flood frequency analysis at the global

scale." *Water Resources Research*, 51, 539–553. http://doi.org/10.1002/2014WR015829

Smith, M. B., Koren, V. I., Zhang, Z., Reed, S. M., Pan, J. J., & Moreda, F. (2004). "Runoff

response to spatial variability in precipitation: An analysis of observed data." *Journal of

Hydrology*, 298(1–4), 267–286. https://doi.org/10.1016/j.jhydrol.2004.03.039

Snell, J. D., & Sivapalan, M. (1994). "On geomorphological dispersion in natural catchments and

the geomorphological unit hydrograph." *Water Resources Research*, 30(7), 2311–2323.

https://doi.org/10.1029/94WR00537

Sofia, G., Tarolli, P., Cazorzi, F., & Dalla Fontana, G. (2011). "An objective approach for

feature extraction: Distribution analysis and statistical descriptors for scale choice and

channel network identification." *Hydrology and Earth System Sciences*, 15(5), 1387–

1402. https://doi.org/10.5194/hess-15-1387-2011

Srinivas, V. V., Tripathi, S., Rao, A. R., & Govindaraju, R. S. (2008). "Regional flood frequency analysis by combining self-organizing feature map and fuzzy clustering." *Journal of Hydrology*, 348(1–2), 148–166. http://doi.org/10.1016/j.jhydrol.2007.09.046

Stedinger, J. R., & Tasker, G. D. (1985). "Regional Hydrologic Analysis: 1. Ordinary, Weighted, and Generalized Least Squares Compared." *Water Resources Research*, 21(9), 1421–1432. https://doi.org/10.1029/WR021i009p01421

Stedinger, J. R., & Tasker, G. D. (1986). "Regional Hydrologic Analysis, 2, Model-Error Estimators, Estimation of Sigma and Log-Pearson Type 3 Distributions." *Water Resources Research*, 22(10), 1487–1499. https://doi.org/10.1029/WR022i010p01487

Strahler, A. N. (1964). "Quantitative geomorphology of drainage basins and channel networks." *In Chow, V.T. (Ed.) Handbook of Applied Hydrology*, McGraw-Hill, New York., pp 439-476.

Strupczewski, W. G., Kochanek, K., Markiewicz, I., Bogdanowicz, E., Weglarczyk, S., & Singh, V. P. (2011). "On the tails of distributions of annual peak flow." *Hydrology Research*, 42(2–3), 171. https://doi.org/10.2166/nh.2011.062

Sveinsson, O. G. B., Boes, D. C., & Salas, J. D. (2001). "Population index flood method for regional frequency analysis." *Water Resources Research*, 37(11), 2733–2748. https://doi.org/10.1029/2001WR000321

Tarboton, D., Bras, R., & Rodriguez-Iturbe, I. (1991). "On the extraction of channel networks from digital elevation data." *Hydrological Processes*, 5(1), 81–100. https://doi.org/10.1002/hyp.3360050107

Taylor, A. B., & Schwarz, H. E. (1952). "Unit hydrograph lag and peak flow related to basin characteristics." *Eos, Transactions American Geophysical Union*, 33(2), 235–246. https://doi.org/10.1029/TR033i002p00235

Thorndahl, S., Smith, J. A., Baeck, M. L., & Krajewski, W. F. (2014). "Analyses of the temporal and spatial structures of heavy rainfall from a catalog of high-resolution radar rainfall fields." *Atmospheric Research*, 144, 111–125. https://doi.org/10.1016/j.atmosres.2014.03.013

Tofallis, C. (2015). "A better measure of relative prediction accuracy for model selection and model estimation." *Journal of the Operational Research Society*, 66(8), 1352–1362. https://doi.org/10.1057/jors.2014.103

Troutman, B. M., & Karlinger, M. R. (1985). "Unit hydrograph approximations assuming linear flow through topologically random channel networks." *Water Resources Research*, 21(5), 743–754. https://doi.org/10.1029/WR021i005p00743

University Oregon State. (2016). PRISM Climate Group. Retrieved from http://www.prism.oregonstate.edu/normals/

Veitzer, S. A., & Gupta, V. K. (2001). "Statistical self-similarity of width function maxima with implications to floods." Advances in Water Resources, 24(9–10), 955–965. https://doi.org/10.1016/S0309-1708(01)00030-6

Veneziano, D., Moglen, G. E., Furcolo, P., & Iacobellis, V. (2000). "Stochastic model of the width function." *Water Resources Research*, 36(4), 1143–1157. https://doi.org/10.1029/2000WR900002

Villarini, G., Goska, R., Smith, J. A., & Vecchi, G. A. (2014). "North Atlantic Tropical Cyclones and U.S. Flooding." *Bulletin of the American Meteorological Society*, 95(9), 1381–1388. http://doi.org/10.1175/BAMS-D-13-00060.1

Vivekanandan, N. (2015). "Flood frequency analysis using method of moments and L-moments of probability distributions." *Cogent Engineering*, 2(1). https://doi.org/10.1080/23311916.2015.1018704

Vogel, R. M., & Fennessey, N. M. (1995). "Flow duration curves II: a review of applications in water resources planning." *Journal of the American Water Resources Association*, 31(6), 1029–1039. https://doi.org/10.1111/j.1752-1688.1995.tb03419.x

Vogel, R., Wilbert, T., & Mcmahon, T. (1993). "Flood-Flow Frequency Model Selection in Southwestern United States." *Water Resources*, 119(3), 353–366.

Wan Jaafar, W. Z., & Han, D. (2012). "Calibration Catchment Selection for Flood Regionalization Modeling." *Journal of the American Water Resources Association*, 48(4), 698–706. http://doi.org/10.1111/j.1752-1688.2012.00648.x

Weibull, W. (1939). "A Statistical Theory of the Strength of Materials." *Royal Swedish Institute for Engineering Research*. Anstalts Förlag, Stockholm: Generalstabens Litografiska.

Wright, D. B., Mantilla, R., & Peters-Lidard, C. D. (2017). "A remote sensing-based tool for assessing rainfall-driven hazards." *Environmental Modelling and Software*, 90, 34–54. https://doi.org/10.1016/j.envsoft.2016.12.006

Wright, D. B., Smith, J., & Baeck, M. (2014). "Flood frequency analysis using radar rainfall fields and stochastic storm transposition." *Water Resources Research*, 1592–1615. https://doi.org/10.1002/2013WR014224.Received

Yue, S., & Yew Gan, T. (2004). "Simple scaling properties of Canadian annual average streamflow." *Advances in Water Resources*, 27(5), 481–495. https://doi.org/10.1016/j.advwatres.2004.02.019

Zhang, K., Kimball, J. S., Nemani, R. R., & Running, S. W. (2010). "A continuous satellite-derived global record of land surface evapotranspiration from 1983 to 2006." *Water Resources Research*, 46(9), 1–21. https://doi.org/10.1029/2009WR008800

235

Descriptors for the geometric WF using $\Delta x = 1\ km$

$$W_{max} = max(W(x)) \tag{A1}$$

$$D(W_{max}) = D(x), with\ x\ such\ that\ max(W(x)) \tag{A2}$$

$$D_B = max(D(C_L)) \tag{A3}$$

$$M = \sum_{d=1}^{D_B} W(d) \cdot \Delta x = \sum_{d=1}^{D_B} W(d) = T_L \tag{A4}$$

$$\bar{d} = \frac{\sum_{d=1}^{D_B} d \cdot \Delta x \cdot W(d)}{\sum_{d=1}^{D_B} \Delta x \cdot W(d)} = \frac{\sum_{d=1}^{D_B} d \cdot W(d)}{\sum_{d=1}^{D_B} W(d)} \tag{A5}$$

$$\bar{W} = \frac{\sum_{d=1}^{D_B} \frac{1}{2} W(d) \cdot \Delta x \cdot W(d)}{\sum_{d=1}^{D_B} \Delta x \cdot W(d)} = \frac{\sum_{d=1}^{D_B} W(d)^2}{2 \sum_{d=1}^{D_B} W(d)} \tag{A6}$$

$$V_W = 2\pi \sum_{d=1}^{D_B} d \cdot W(d) \cdot \Delta x = 2\pi \sum_{d=1}^{D_B} d \cdot W(d) \tag{A7}$$

$$M_{[0,D(W_{max})]} = \sum_{d=1}^{D(W_{max})} W(d) \cdot \Delta x = \sum_{d=1}^{D(W_{max})} W(d) \tag{A8}$$

$$M_{[D(W_{max}),D_B]} = \sum_{d=D(W_{max})}^{D_B} W(d) \cdot \Delta x = \sum_{d=D(W_{max})}^{D_B} W(d) \tag{A9}$$

$$T_D = \frac{T_L}{D_B} \tag{A10}$$

$$M_{WD} = W_{max} \cdot D(W_{max}) \tag{A11}$$

$$M_{\overline{WD}} = \bar{W} \cdot \bar{d} \tag{A12}$$

236

Descriptors for the WF-at-site

$$\overline{D^{[N]}} = \frac{1}{T_L} \sum_{C_L=1}^{T_L} D^{[N]}(C_L) \tag{A13}$$

$$Var\left(D^{[N]}\right) = \frac{1}{T_L-1} \sum_{C_L=1}^{T_L} (D^{[N]}(C_L) - \overline{D^{[N]}})^2 \tag{A14}$$

$$Sk\left(D^{[N]}\right) = \frac{\frac{1}{T_L}\sum_{C_L=1}^{T_L}(D^{[N]}(C_L)-\overline{D^{[N]}})^3}{\left(\sqrt{\frac{1}{T_L}\sum_{C_L=1}^{T_L}(D^{[N]}(C_L)-\overline{D^{[N]}})^2}\right)^3} \tag{A15}$$

$$K\left(D^{[N]}\right) = \frac{\frac{1}{T_L}\sum_{C_L=1}^{T_L}(D^{[N]}(C_L)-\overline{D^{[N]}})^4}{(\frac{1}{T_L}\sum_{C_L=1}^{T_L}(D^{[N]}(C_L)-\overline{D^{[N]}})^2)^2} \tag{A16}$$

$$q_{25}\left(D^{[N]}\right) \text{ such as } \Pr\left[D^{[N]} \leq q_{25}\left(D^{[N]}\right)\right] = 0.25 \tag{A17}$$

$$q_{50}\left(D^{[N]}\right) \text{ such as } \Pr\left[D^{[N]} \leq q_{50}\left(D^{[N]}\right)\right] = 0.50 \tag{A18}$$

$$q_{75}\left(D^{[N]}\right) \text{ such as } \Pr\left[D^{[N]} \leq q_{75}\left(D^{[N]}\right)\right] = 0.75 \tag{A19}$$

$$D_{W_{max}}^{[N]} = \frac{D(W_{max})}{D_B} \tag{A20}$$

$$M_{[0,D_{W_{max}}^{[N]}]}^{[N]} = \frac{M_{[0,D(W_{max})]}}{M} \tag{A21}$$

$$M_{[D_{W_{max}}^{[N]},1]}^{[N]} = \frac{M_{[D(W_{max}),1]}}{M} = 1 - M_{[0,D_{W_{max}}^{[N]}]}^{[N]} \tag{A22}$$

237

Descriptors for the WF-at-region using $\Delta x = 1 \, km$

$$W_{max}^{[NS]} = max(W^{[NS]}(x)) \tag{A23}$$

$$D(W_{max}^{[NS]}) = D^{[NS]}(x), with \ x \ such \ that \ max(W^{[NS]}(x)) \tag{A24}$$

$$A_r = \frac{E[D_B] \cdot E[\overline{W}]}{M} \tag{A25}$$

$$D_B^{[NS]} = \frac{D_B}{E[D_B]} \tag{A26}$$

$$M^{[NS]} = \sum_{d=1/D_B}^{D_B^{[NS]}} W^{[NS]}(d) \cdot \frac{\Delta x}{D_B} = \frac{1}{D_B} \sum_{d=1/D_B}^{D_B^{[NS]}} W(d) \tag{A27}$$

$$\overline{d^{[NS]}} = \frac{\sum_{d=1/D_B}^{D_B^{[NS]}} d \cdot \frac{\Delta x}{D_B} \cdot W^{[NS]}(d)}{\sum_{d=1/D_B}^{D_B^{[NS]}} \frac{\Delta x}{D_B} \cdot W^{[NS]}(d)} = \frac{\sum_{d=1/D_B}^{D_B^{[NS]}} d \cdot W^{[NS]}(d)}{\sum_{d=1/D_B}^{D_B^{[NS]}} W^{[NS]}(d)} \tag{A28}$$

$$\overline{W^{[NS]}} = \frac{\sum_{d=1/D_B}^{D_B^{[NS]}} \frac{1}{2} W^{[NS]}(d) \cdot \frac{\Delta x}{D_B} \cdot W^{[NS]}(d)}{\sum_{d=1/D_B}^{D_B^{[NS]}} \frac{\Delta x}{D_B} \cdot W^{[NS]}(d)} = \frac{\sum_{d=1/D_B}^{D_B^{[NS]}} W^{[NS]}(d)^2}{2 \sum_{d=1/D_B}^{D_B^{[NS]}} W^{[NS]}(d)} \tag{A29}$$

$$V^{[NS]}{}_W = 2\pi \sum_{d=\frac{1}{D_B}}^{D_B^{[NS]}} d \cdot W^{[NS]}(d) \cdot \Delta x = 2\pi \sum_{d=\frac{1}{D_B}}^{D_B^{[NS]}} d \cdot W^{[NS]}(d) \cdot \frac{1}{E[D_B]} \tag{A30}$$

$$M^{[NS]}{}_{[0,D(W_{max}^{[NS]})]} = \sum_{d=1/D_B}^{D(W_{max}^{[NS]})} W^{[NS]}(d) \cdot \frac{\Delta x}{D_B} = \frac{1}{D_B} \sum_{d=1/D_B}^{D(W_{max}^{[NS]})} W^{[NS]}(d) \tag{A31}$$

$$M^{[NS]}{}_{[D(W_{max}^{[NS]}),D_B^{[NS]}]} = \sum_{d=D(W_{max}^{[NS]})}^{D_B^{[NS]}} W^{[NS]}(d) \cdot \frac{\Delta x}{D_B} = \frac{1}{D_B} \sum_{d=D(W_{max}^{[NS]})}^{D_B^{[NS]}} W^{[NS]}(d) \tag{A32}$$

$$M_{WD}^{[NS]} = W_{max}^{[NS]} \cdot D(W_{max}^{[NS]}) \tag{A33}$$

$$M_{\overline{WD}}^{[NS]} = \overline{W^{[NS]}} \cdot \overline{d^{[NS]}} \tag{A34}$$

.